

**NANO-STRUCTURED SORBENTS FOR
RAPID RESPONSE INTERIOR AIR
HUMIDITY BUFFERING APPLICATIONS**

Sean Casey

**Thesis submitted to the University of
Nottingham for the degree of
Doctor of Philosophy**

February 2013

ABSTRACT

Within a closed environment, (e.g. building, car, aircraft) that is thermally and hygrically isolated from the exterior climate, one approach that can help reduce the energy required for indoor mechanical climate control whilst increasing comfort levels for occupants is to use hygrothermal coatings on top of existing materials. Hygrothermal coatings can re-introduce both thermal and hygric buffering within the isolated envelope. Understanding of the behaviour of these coatings allows them to be optimized for different environments.

The overall aim of the research is to design the functional properties of inorganic, nano structured surface coatings *i.e.* mesoporous silica (MS) to produce desired hygrothermal behavioural responses to climatic variables in a controlled environment. This can be achieved through correlation of the hygrothermal properties of desiccant materials with their microstructural characteristics and understanding the hygrothermal behaviour of the materials under representative psychrometric conditions.

Stage 1 was to characterise the hygrothermal properties of the MS and other conventional desiccant materials *i.e.* Silica Gel, Molecular Sieve, Clinoptilolite and Bentonite to produce a ‘Template of functional properties’ and provide material input data for the numerical models. These tests included dynamic vapour sorption (DVS) techniques for moisture absorption including cyclic adsorption/desorption and sorption isotherms, wet-cup tests for vapour permeability, partial immersion tests for liquid water absorption, modified transient plane source (MTPS) tests for thermal conductivity and differential scanning calorimetry (DSC) for heat capacity.

Stage 2 utilised techniques to classify the pore geometry of the desiccants, including

helium pycnometry for solid density, gravimetric testing for bulk density, N₂ physisorption for specific surface area, mesopore volume and mean pore diameter with small angle X-ray scattering and transmission electron microscopy used to corroborate the N₂ results. Scanning electron microscopy (SEM) was used to confirm material composition and purity and to indicate macropore distribution. A correlation between the hygrothermal properties from Stage 1 with their microstructural characteristics was then sought.

Stage 3 was a parametric analysis of the candidate materials hygrothermal behaviour using the validated 1D numerical simulation software WUFI Pro v5.1. Further analysis was carried out to assess how the numerical model could be used to tune the functional properties of the MS materials to suit differing psychrometric conditions in closed environments. A series of simulations using a representative climate (Nottingham) were also run to compare the hygrothermal behaviour of the MS materials to the conventional desiccants

A series of energetic 3D physical and numerical models (WUFI Plus v 2.1) were designed to study the resultant relative humidity levels in both occupied and unoccupied spaces and under different air exchange rates due to the presence of the hygrothermal materials in a closed environment. The 3D model was also used to compare the operational energy usage of different retrofitting cases under the same representative climate used in Stage 3 with three different heating, cooling humidification and dehumidification (HCHD) control scenarios.

The MS materials displayed significantly higher Moisture Buffer Values (MBV), equilibrium moisture contents (EMC) and faster response rates when compared to the conventional desiccants. It was shown that WUFI Pro can be used as a design tool for material functional properties, with the sorption isotherm, and in particular

adjustment of the $w_{50} - w_{80}$ gradient of the absorption branch isotherm being by far the most sensitive parameter. In the MS samples, the dynamic vapour sorption (DVS) response time has a significant and positive logarithmic relationship with both the mesopore diameter and the mesopore volume implying that mesopore geometry can be tuned in order to give the desired dynamic vapour sorption/desorption response rate and storage capacity to suit a given set of interior psychrometric conditions. It is therefore possible to tune an MS material to suit a particular set of psychrometric conditions using WUFI Pro.

The MS materials displayed outstanding passive buffering performance across a range of exterior climate conditions combined with numerous internal moisture and ventilation overloading scenarios, providing constant humidity buffering within the American Society of Heating, Refrigerating and Air Conditioning Engineers (ASHRAE) comfort limits. When compared against a retro-fitted gypsum-lined indoor environment there was a potential reduction in humidification/dehumidification energy demand of up to 100% when using an MS material coating.

ACKNOWLEDGEMENTS

I wish to gratefully acknowledge the support of the Engineering and Physical Sciences Research Council (EPSRC) and E.ON (UK) Ltd. for funding the research presented in this thesis as part of a larger project (EP/G000387/1 ‘CALEBRE’).

I offer my grateful thanks to my friend and supervisor, Dr. Matthew Hall for providing me with this opportunity and his endless guidance and patience throughout the course of my research. Our many hours of discussion have always been appreciated and very helpful, you opened my eyes to a microscopic world.

In addition, I wish to thank Prof. Mark Gillott and Prof. Paul Brown for their assistance in both keeping me focused and seeing the broader picture. Mrs Nicola Weston, Dr Nigel Neate, and Dr Keith Dinsdale in Wolfson with Ian Richardson, Mike Langford, Chris Fox, Craig Cox and Andrew Maddison in NCG for their technical support and advice. I am grateful to Rich Blakemore, Mick Winfield and Jon Watson in NTEC for their support. I would also like to acknowledge Dr. Hartwig Künzel and the team at IBP Fraunhofer for providing me with assistance whilst conducting my numerical modelling work.

My sincere thanks are also extended to my two colleagues Khalid Najim and Pejman Keikhaei for our great discussions, both academic and cultural that provided much needed interludes during the longer days.

Finally, to my parents Colm & Mary, my family; Michelle & Dermot, Rachel, Rebecca and Grace, Colm and Kathy, and Caz. Thank you so very much for all the support and belief you have shown me from the start.

“Go raibh maith agat, mo chairde”

DECLARATION

I declare that, unless otherwise cited in the text, the contents of this thesis are the results of my own work conducted at The University of Nottingham, Faculty of Engineering between October 2009 and September 2012. No part of this thesis has been submitted to any other University or other educational institution for a Degree, Diploma or other qualifications.

Sean Casey

February 2013

PUBLICATIONS

Journal Articles

CASEY, SP, & HALL, MR, 2013. Energetic and hygrothermal analysis of a nano-structured material for rapid-response humidity buffering in closed environments. *Building and Environment*. 60, 24-36

CASEY, SP, HALL, MR, TSANG, SCE, KHAN, MA. 2012. Nanocomposite materials for rapid-response interior air humidity buffering in closed environments. *Journal of Building Performance Simulation*. 1-13.

HALL, MR, TSANG, SCE, CASEY, SP, KHAN, MA, & YANG, H. 2012. Synthesis, characterization and hygrothermal behaviour of mesoporous silica high-performance desiccants for relative humidity buffering in closed environments. *Acta Materialia*, 60, 89-101.

DEHDEZI, PK, HALL, MR, DAWSON, AR & CASEY SP. 2012. Thermal, mechanical, and microstructural analysis of concrete containing microencapsulated phase change materials. *International Journal of Pavement Engineering*, 1-14.

LIUZZI, S, Hall, MR, STEFANIZZI, P & CASEY, SP. 2013. Hygrothermal behaviour and relative humidity buffering of unfired and hydrated lime-stabilised clay composites in a Mediterranean climate. *Building and Environment*. 61, 82-92

Conference Papers

DEHDEZI, PK, HALL, MR, DAWSON, AR & CASEY, SP. 2012. Investigate the feasibility of using asphalt pavements as a source of heating. *2nd International Symposium on Asphalt Pavements & Environment*, 1st-3rd October, Fortaleza, Brazil.

WANG, X, CASEY, SP, BOUZALAKOS, S, CAMPS, A, PERRY, R, MAROTO-VALER, MM, HALL, MR, & GILLOTT, M, 2010. Mineral sequestration of CO₂ by aqueous carbonation of incinerator sewage sludge ash (ISSA) *In: 8th European Conference on Coal Research and its Applications: ECCRIA 8*, 6th – 8th September, Leeds.

Book Chapter

HALL, MR. & CASEY, SP. 2012. Chapter 3: Hygrothermal behaviour and thermal comfort in modern earth buildings. In: HALL M R, LINDSAY R, AND KRAYENHOFF M, ed., *Modern earth buildings: Materials, engineering, construction and applications*, Woodhead Publishing, Cambridge.

LIST OF FIGURES

Figure 1 - Hygrothermal fluxes and their alternating directions across a building envelope. Adapted from: (ASHRAE, 2009a)	3
Figure 2 - A simplified psychrometric chart.	12
Figure 3 - Factors influencing health and hygiene showing comfort range for RH_{ie} (40% to 70%). Adapted from: (Simonson et al., 2001).	15
Figure 4 - A three phase model for porous materials adapted from: (Barnes, 2000).	17
Figure 5 - Cross section of a porous solid showing typical pore types.....	17
Figure 6 - A typical moisture vapour isotherm showing pore filling stages and transport mechanisms.....	19
Figure 7 – Adsorption isotherm classification. Adapted from: (Sing et al., 1985)....	21
Figure 8 - Isotherm hysteresis loop classification. Adapted from: (Sing et al., 1985)	22
Figure 9 - Moisture vapour molecular diffusion mechanisms in porous solids.....	25
Figure 10 - Graphical representation showing the reversal of moisture transfer during the transition from vapour diffusion to capillary flow in a pore. Adapted from: (Künzel, 1995).....	28
Figure 11 - Capillary rise in a pore showing meniscus formation.	29
Figure 12 - Figure illustrating Fourier's law of steady state heat conduction. Adapted from: (Incropera et al., 2007).	31
Figure 13 - Figure illustrating increased heat flow due to increasing moisture content.....	31
Figure 14 - Figure showing sensible and latent heat storage.	34
Figure 15 - Categorisation of Hygrothermal materials by hygrothermal function. ...	35
Figure 16 - SEM images of softwood cellular structure. Adapted from: (Koch., 1972, UoT, 2012).....	36
Figure 17 - Formation of clays showing Kaolinite and Smectite.....	39
Figure 18 - Framework of natural zeolite showing silicon tetrahedra (BZA, 2006)..	42
Figure 19 - Sorption isotherms for experimental silica gels (ASHRAE, 2009a).....	45
Figure 20 - Figure showing regeneration temperatures and desorption for three silica gels(Ng et al., 2001).	45
Figure 21 - SEM and TEM images of mesoporous silica MCM-41 (Yang et al., 2008).	47
Figure 22 - Water vapour sorption isotherms for microstructured silica. Adapted from (Ohashi et al., 1999).	48
Figure 23 - Photograph of a vacuum insulation panel (Tenpierik and Cauberg, 2006).	49
Figure 24 - Flowchart of inputs, calculation technique and outputs for the WUFI	

group of programs. Adapted from: (Künzel, 1995).	59
Figure 25 – Process flow chart outlining the research approach.	63
Figure 26 - Schematic diagram of Gas Pycnometry technique.....	67
Figure 27 - Classification of density types for porous particles. Adapted from: (Webb, 2001).....	68
Figure 28 - Schematic diagram of a scanning electron microscope where (1) electron column, (2) electron gun, (3) electron beam, (4) lenses, (5) apertures, (6) deflector coils, (7) sample, (8) sample chamber, (9, 10) SE and BSE detectors, (11) vacuum unit and (12) computer.	70
Figure 29 - Schematic representation of the sample/ beam interaction for an SEM..	71
Figure 30 - Graphical representation of 'full width half maximum' for EDS.	72
Figure 31 - Schematic of N ₂ physisorption process where (1) sample, (2) Dewar vessel containing liquid Nitrogen, (3) vacuum generation pump, (4) calibrated volume and (5) manometer. Adapted from: (BSi, 1996)	73
Figure 32 - Graphical representation of Bragg diffraction. Adapted from (Koughia et al., 2006).	77
Figure 33 - Schematic diagram of a transmission electron microscope where (1) electron beam, (2) electron gun, (3) beam column, (4) condensing, objective and projection electromagnetic lenses (5) apertures, (6) sample stage, (7) fluorescent screen, (8) vacuum unit and (9) printer.	79
Figure 34 - Schematic of experimental setup using a desiccator jar for sorption/ desorption moisture vapour isotherm tests.....	81
Figure 35 - Schematic of experimental setup using the climate chamber for sorption/ desorption moisture vapour isotherm tests.....	83
Figure 36 - Characteristic dynamic moisture uptake result graph showing change in mass against time.	84
Figure 37 - Schematic of experimental setup for vapour permeability tests.....	86
Figure 38 - Figure showing Type 1 and Type 2 water absorption plots.	87
Figure 39 - Schematic of experimental setup for water absorption tests.	88
Figure 40 - Schematic diagram of a differential scanning calorimeter where (1) sample, (2) empty pan, (3) crucible, (4) lid, (5 & 6) heating elements (7) connecting cables and (8) computer.	90
Figure 41 - Example heat flow curves and temperature profile from a DSC test.....	91
Figure 42 - Schematic diagram of a modified transient plane source test kit where (1) powder sample, (2) locating ring, (3) sensor, (4) compacting mass, (5) computer and (6) control unit.....	92
Figure 43 - Methodology for determining $t_{75\%}$ for thermal comfort range step testing (Hall et al., 2012b).	95
Figure 44 – Step variation of RH_{ie} for thermal comfort range step testing.	96
Figure 45 - Sinusoidal variation of RH_{ie} for cyclic response testing (Casey et al., 2012).	98

Figure 46 - Graph showing the MBV classification system for materials. Adapted from (Rode et al., 2005).	99
Figure 47 - Schematic of experimental setup for water evaporation tests.	102
Figure 48 - Schematic of experimental setup for RH_{ie} buffering tests.....	103
Figure 49 - Schematic diagram of the ventilation assembly for the isolated box where (1) Perspex tube, (2) backing plate, (3) sealant, (4) M6 bolts, (5) orifice plate, (6) ventilation hole and (7) M6 nuts.	105
Figure 50 - Moisture generation schedule for humidity buffering testing.	106
Figure 51 - Variation of RH for sorption isotherm numerical modelling.	108
Figure 52 - Component assembly for the numerical sorption isotherm model showing monitor positions and grid spacing.	109
Figure 53- Component assembly for the numerical vapour permeability model showing monitor positions and grid spacing.....	110
Figure 54 - Component assembly for the numerical sinusoidal cyclic response model showing monitor positions and grid spacing.....	111
Figure 55 - Methodology for calculating variance occurrence inside and outside limits (Casey et al., 2012b).	112
Figure 56 - Methodology for determining variance range and model confidence (Casey et al., 2012b).....	113
Figure 57 - Sinusoidal variation of RH_{ie} for sensitivity analysis model.	114
Figure 58 – Case 1 assembly for the numerical building retrofit model showing monitor positions and grid spacing.	116
Figure 59 - Case 2 assembly for the numerical building retrofit model showing monitor positions and grid spacing.	116
Figure 60 - Case 3 assembly for the numerical building retrofit model showing monitor positions and grid spacing.	117
Figure 61 - Case 4 assembly for the numerical building retrofit model showing monitor positions and grid spacing.	117
Figure 62 - External climate for the 3D building retrofit model generated from the Nottingham CIBSE TRY file.	118
Figure 63 - Schematic representation of the 3D numerical model volume showing a central monitoring node and the hygrothermal fluxes.	119
Figure 64 - Envelope assembly for the 'non-visualised attachment' in the humidity buffering model.....	122
Figure 65 - Graph showing 'over-loading' occupancy schedules and sinusoidal variation of RH_{oe} for the increased moisture load model.	126
Figure 66 - Graph showing window opening schedules and sinusoidal variation of RH_{oe} for the increased air exchange rate model.	127
Figure 67 – N_2 adsorption/desorption isotherms of all candidate materials.	133
Figure 68 - BJH pore size distribution of the MS samples (Hall et al., 2012b).....	134

Figure 69 - BJH ($C = 90$) pore size distribution of the four non-MS samples.....	135
Figure 70 - SAXRS diffractograms of the MS samples obtained by the University of Oxford (Hall et al., 2012b).....	136
Figure 71 - TEM bright field micrographs of the MS samples obtained by the University of Oxford (Hall et al., 2012b).....	137
Figure 72 - SEM micrographs of the four MS samples (Hall et al., 2012b).....	138
Figure 73 - Mufti-scale SEM micrographs of MMS 4.8.....	139
Figure 74 - EDX spectral analysis of MS 4.7.	140
Figure 75 - EDX spectral analysis of MMS 4.8.....	140
Figure 76 - EDX spectral analysis of MS 8.3.	140
Figure 77 - Graph showing the relative proportion of mesopore and macropore volume to total pore volume for the eight candidate materials (Hall et al., 2012b).	143
Figure 78 - Graph showing the moisture vapour sorption isotherms determined using the desiccator jar method for six candidate materials.	144
Figure 79 - Graph showing the cycle to cycle degradation in EMC for the two MS materials.	145
Figure 80 - Graph showing the moisture vapour sorption isotherms determined using the climate chamber for all candidate materials (Hall et al., 2012b).	146
Figure 81 - Graph showing the linear mass loss from the wet- cup assembly in the vapour permeability tests (Hall et al., 2012b).	148
Figure 82 - Graph showing the liquid water absorbed per exposed surface area against square root of time.	149
Figure 83 - Graph showing the kinetic moisture uptake curves between 40% and 70%RH used to determine $t_{75\%}$	151
Figure 84 - Vapour sorption response for all candidate materials measured between 40% and 70% RH at 23 °C (Hall et al., 2012b).	151
Figure 85 - Mean and total range of moisture uptake in the thermal comfort range with normalized time scale for all materials at 23 °C (Hall et al., 2012b).....	153
Figure 86 - Graph showing $MBV_{\text{practical}}$ levels of the candidate and traditional materials (Hall et al., 2012b).....	155
Figure 87 - Graph showing the logarithmic relationship between mean pores diameter and t_{emc} (Hall et al., 2012b).....	156
Figure 88 - Graph showing physical and numerical kinetic moisture uptake results for the three MS materials.....	161
Figure 89 - Graph showing numerically predicted interior and exterior vapour fluxes for the three MS materials.....	162
Figure 90 - Graph showing the physical and numerical cyclic response results (Casey et al., 2012).....	163
Figure 91 - Graph showing variance and occurrence within limits for the three MS materials (Casey et al., 2012).....	165

Figure 92 - Graph showing 1D model sensitivity of RH_{coat} and w_{coat} to increasing ΔRH_{ie} amplitudes (Casey et al., 2012).	166
Figure 93 - Graph showing the controlling factor of hygrothermal material properties using WUFI for material tuning (Casey et al., 2012).....	167
Figure 94 – Graph showing simulated yearly w_{coat} levels for all interior coating materials (Casey et al., 2012).	169
Figure 95 - Graph showing normalised yearly range of w_{coat} for all interior coating materials (Casey et al., 2012).	170
Figure 96 – Graph showing change in mass (loss) from evaporation for dish $\varnothing = 28, 49, 65$ and 77mm	174
Figure 97 – Graph showing water evaporation rate plotted against dish diameter. .	174
Figure 98 - Graph showing the physical and numerical material humidity buffering results.	176
Figure 99 - Graph showing the variance and occurrence within limits for all interior coating materials.	177
Figure 100 - Graph showing ΔRH_{ie} reduction for increasing hygrothermal material ratio under four air exchange rates without moisture loading.....	180
Figure 101 - Graph showing RH_{ie} dwell time for increasing hygrothermal material ratio under four air exchange rates without moisture loading.....	181
Figure 102 - Graph showing ΔRH_{ie} reduction for increasing hygrothermal material ratio under four air exchange rates with moisture loading.....	182
Figure 103 - Graph showing RH_{ie} dwell time for increasing hygrothermal material ratio under four air exchange rates with moisture loading.....	182
Figure 104 - Graph showing sensitivity of ΔRH_{ie} to varying amplitudes of ΔRH_{oe} under four air exchange rates.	183
Figure 105 - Graph showing variation of RH_{ie} for increased occupancy moisture loads under five air exchange rates.	185
Figure 106 - Graph showing variation of RH_{ie} under increasing air exchange rates.	187
Figure 107 - Graph showing variation of ΔRH_{ie} and ASHRAE comfort zone for the six test cases at four material depths with no HCHD control.	188
Figure 108 - Graph showing 2 nd year RH_{ie} profiles for the six test cases with constant HCHD control at $45\% \leq RH_{ie} \leq 65\%$ and $21^\circ\text{C} \leq T_{ie} \leq 25^\circ\text{C}$	190
Figure 111 - Graph showing variation of ΔRH_{ie} for the six test cases with constant HCHD control at $45\% \leq RH_{ie} \leq 65\%$ and $21^\circ\text{C} \leq T_{ie} \leq 25^\circ\text{C}$	191
Figure 112 - Graph showing RH_{ie} dwell time for the six test cases with constant HCHD control at $45\% \leq RH_{ie} \leq 65\%$ and $21^\circ\text{C} \leq T_{ie} \leq 25^\circ\text{C}$	192
Figure 113 - Graph showing 2 nd year RH_{ie} profiles for the six test cases with partial HCHD control at $45\% \leq RH_{ie} \leq 65\%$ and $21^\circ\text{C} \leq T_{ie} \leq 25^\circ\text{C}$	193
Figure 114 - Graph showing RH_{ie} dwell time for the six test cases with partial HCHD control at $45\% \leq RH_{ie} \leq 65\%$ and $21^\circ\text{C} \leq T_{ie} \leq 25^\circ\text{C}$	193

Figure 115 - Graph showing 2 nd year RH_{ie} profiles for the six test cases with partial HCHD control at ASHRAE limits.	195
Figure 116 - Graph showing RH_{ie} dwell time for the six test cases with partial HCHD control at ASHRAE limits.	195

LIST OF TABLES

Table 1 - Types and sources of indoor pollutants (Spengler et al., 2001).....	14
Table 2 - Range of pore types and shapes (IUPAC, 1994)	18
Table 3 – Range and classification of pore sizes.	18
Table 4 - Principle moisture mechanisms, states and driving potentials. Adapted from: (Trechsel, 1994)	24
Table 5 - Properties of woods & man-made timber products (IBP, 2012b).	36
Table 6 - Chemical analysis of Clinoptilolite (Zalba et al., 2009).....	42
Table 7 - Pore size and formulae for molecular sieves (Haixin, 2010).....	43
Table 8 - Physical properties of experimental silica gels (ASHRAE, 2009a).	44
Table 9 - Characteristic data for microstructured silica (Ohashi et al., 1999).	47
Table 10 - Source and application of existing hygrothermal numerical models in published literature (Hall et al., 2012a).....	57
Table 11 - Summary of the pore network characterisation techniques.	66
Table 12 - Summary of material properties and characterisation techniques.	80
Table 13 - Relative humidity above saturated salt solutions prepared in accordance with BS ISO 12571.	82
Table 14 - Time periods for Δm recording of for water absorption testing.	88
Table 15 - Occupant loads obtained from WUFI Plus v2.1.1.73 (IBP, 2012a) and ^a BS 5250 (BSi, 2011).	101
Table 16 - Volume adjusted loads for the physical model calculated from Table 15.	101
Table 17 - Volume adjusted occupant loads for the 1m ³ numerical model calculated from Table 15.	102
Table 18 - Input parameters for the numerical sorption isotherm model.....	109
Table 19 - Input parameters for the numerical vapour permeability model.	110
Table 20 - Input parameters for the numerical sinusoidal cyclic response model. ..	111
Table 21 - Input parameters for the numerical building retrofit model.	119
Table 22 - Unchanged input parameters for all 3D numerical models.	120
Table 23 - Input parameters for the material humidity buffering model.	121
Table 24 - Common input parameters for all cyclic response 3D numerical models.	124
Table 25 - Input parameters for the cyclic response model - Case 1: Standard Wall.	124
Table 26 - Input parameters for the cyclic response model - Case 2: Retrofitted Wall.	124

Table 27 - Input parameters for the cyclic response model - Case 3: Spruce Cladding.....	125
Table 28 - Input parameters for the cyclic response model - Case 4: MS Coating..	125
Table 29 - Morning and evening moisture profiles for the increased occupancy numerical model.....	126
Table 30 - Morning and evening ACH profiles for the increased air exchange numerical model.....	127
Table 31 - Results of N ₂ physisorption measurements of the candidate materials (Hall et al., 2012).	133
Table 32 - Solid density for the eight candidate materials.....	141
Table 33 - Bulk density for the eight candidate materials.	142
Table 34 - Summary of the porous network properties for the eight candidate materials.	142
Table 35 - Comparison of dynamic vapour sorption (DVS) and desiccator (DJ) EMC levels.	146
Table 36 - Summary of changes in mass with corresponding response times and moisture storage functions for all candidate materials.....	147
Table 37 - Water vapour transmission properties for all candidate materials.....	148
Table 38 - Liquid water absorption properties for all candidate materials.	150
Table 39 - Kinetic moisture data for calculation of $t_{75\%}$ and $t_{40-70-40}$	150
Table 40 - MBV, liquid diffusivity and EMPD for candidate and traditional materials. ^A Values adapted from (Rode et al., 2005).	154
Table 41 - Thermal conductivity of candidate materials measured at 50%RH.	157
Table 42 - Dry-state specific heat capacity of the eight candidate materials (Hall et al., 2012b).	158
Table 43 - Comparison of the numerically predicted and experimentally calculated vapour fluxes for the three MS materials.....	162
Table 44 - Variance and occurrence within limits for all three MS materials at 30% and 70% RH amplitudes.....	165
Table 45 - Controlling factors for material tuning using WUFI.	168
Table 46 - Summary of w_{coat} levels for all interior coating materials.....	170
Table 47 - Water evaporation rate calculation data.	175
Table 48 - Variance and occurrence for all interior coating materials.....	178
Table 49 - Comparative energy usage and potential savings for the four post-retrofitted cases under constant HCHD control at $45\% \leq RH_{ie} \leq 65\%$ and $21^{\circ}\text{C} \leq T_{ie} \leq 25^{\circ}\text{C}$	196
Table 50 - Comparative energy usage and potential savings for the four post-retrofitted cases under partial HCHD control at $45\% \leq RH_{ie} \leq 65\%$ and $21^{\circ}\text{C} \leq T_{ie} \leq 25^{\circ}\text{C}$	197

Table 51 - Comparative energy usage and potential savings for the four post-retrofitted cases under partial HCHD control at the ASHRAE limits. 198

LIST OF ACRONYMS

1D	One Dimensional
3D	Three Dimensional
ACH	Air Changes per Hour
ASHRAE	American Society of Heating, Refrigerating and Air Conditioning Engineers
BET	Brunauer-Emmett-Teller
BJH	Barrett-Joyner-Halenda
BSE	Back Scatter Electrons
CFD	Computational Fluid Dynamics
DSC	Differential Scanning Calorimetry
DVS	Dynamic Vapour Sorption
EMC	Equilibrium Moisture Content
EMPD	Effective Moisture Penetration Depth
HAM	Heat and Moisture
HCHD	Heating Cooling Humidification and Dehumidification
HVAC	Heating Ventilation and Air Conditioning
MBV	Moisture Buffer Value
MCM	Mobil Crystalline Material
MS	Mesoporous Silica
MTPS	Modified Transient Plane Source
MVHR	Mechanical Ventilation and Heat Recovery
PIR	polyisocyanurate
PTFE	Polytetrafluoroethylene
RH	Relative Humidity
SAXRS	Small Angle X-Ray Scattering
SBA	Santa Barbara Amorphous type material
SEM	Scanning Electron Microscopy
SE	Secondary Electrons
SSA	Specific Surface Area
TEM	Transmission Electron Microscopy
VIP	Vacuum Insulation Panel
WUFI	Wärme Und Feuchte Instationär

NOMENCLATURE

A	area	m^2
A_w	liquid water absorption rate	$kg/m^2 s^{0.5}$
c_p	constant pressure specific heat capacity	$J/(kg K)$
c_p^*	moisture content-dependent specific heat capacity	$J/(kg K)$
C_v	mass concentration of water vapour	kg/m^3
D	diffusion coefficient for water vapour in still air	m^2/s
d	thickness, depth	m
d_p	penetration depth	m
d_v	absolute humidity	kg/m^3
g	total rate of mass transfer	$kg/s m^2$
g_g	evaporation/moisture generation rate	g/h
g_l	rate of liquid water transfer	$kg/s m^2$
g_v	rate of water vapour transfer	$kg/s m^2$
$g_{v,air}$	rate of water vapour diffusion in still air	$kg/s m^2$
G	water vapour flow rate	kg/s
H	enthalpy	J
h	specific enthalpy	J/kg
L	effective length	m
m	mass	kg
n	bulk porosity	m^3/m^3
P	pressure	Pa
Q	heat flow	W
q	total heat flux	W/m^2
r	radius	m
RH	relative humidity	$\%$
RH_{coat}	near surface relative humidity of coating	$\%$
RH_{ie}	indoor environment relative humidity	$\%$
RH_{oe}	outdoor environment relative humidity	$\%$
R	thermal resistance	$m^2 K/W$
R_o	universal gas constant	$J/kg mol K$
R_{vap}	individual gas constant of water vapour	$J/kg K$
t	time	s
t_{emc}	time interval to reach equilibrium moisture content	hr
T	thermodynamic temperature	K
V	volume	m^3
w	specific moisture content	kg/m^3
w_c	capillary saturation specific moisture content	kg/m^3
w_{coat}	specific moisture content of coating	kg/m^3
w_r	specific moisture content at hygroscopic limit	kg/m^3
w_s	saturation specific moisture content	kg/m^3
W	Humidity ratio	kg/kg
W	water vapour permeance	$kg/m^2 s Pa$
x	1-dimensional distance	m
α	thermal diffusivity	m^2/s
β	thermal effusivity	$W s^{1/2}/m^2 K$
δ_a	water vapour permeability of still air	$kg/m s Pa$

δ	water vapour permeability	kg/m s Pa
ε	emissivity	-
γ	surface tension	N/m
λ	wavelength	m
λ	dry state thermal conductivity	W/(m K)
λ^*	moisture-dependent thermal conductivity	W/(m K)
μ	water vapour diffusion resistance factor	-
ξ	moisture storage function	kg/kg
ξ_a	moisture capacity during absorption (from wetting curve)	kg/kg
ξ_d	moisture capacity during desorption (from drying curve)	kg/kg
ρ	density	kg/m ³
ϕ	angle of friction	°
φ	relative humidity (decimal)	-
Ψ	capillary potential	Pa

Subscripts

<i>ie</i>	indoor environment
<i>oe</i>	outdoor environment
<i>db</i>	dry bulb
<i>wb</i>	wet bulb
<i>sat</i>	saturation

TABLE OF CONTENTS

TITLE PAGE	i
ABSTRACT	iii
ACKNOWLEDGEMENTS.....	vi
DECLARATION	vii
PUBLICATIONS	viii
LIST OF FIGURES	ix
LIST OF TABLES	xv
LIST OF ACRONYMS	xviii
NOMENCLATURE	xix
TABLE OF CONTENTS.....	xxi
1 CHAPTER 1: Introduction	1
1.1 Introduction	1
1.2 Hygrothermal Behaviour	2
1.3 Overall Aim	5
1.4 Hypothesis	6
1.5 Research Objectives	6
1.6 Limitations of the study	7
2 CHAPTER 2: Scientific Background	9
2.1 Introduction	9
2.2 Psychrometrics	9
2.3 Occupant Comfort	12
2.4 Hygric Theory	16
2.4.1 Porosity	16
2.4.2 Moisture Storage	19
2.4.3 Moisture Transport.....	24
2.4.3.1 Vapour Transport	24
2.4.3.2 Transition from Vapour to Capillary Transfer	27
2.4.3.3 Capillary Transfer.....	28
2.5 Thermal Theory	30
2.5.1 Heat Transfer.....	30
2.5.2 Heat Storage	32

2.6	Hygic Materials	34
2.6.1	Conventional Building Materials	35
2.6.1.1	Timber	35
2.6.1.2	Earth	37
2.6.1.3	Clay	38
2.6.2	Zeolites (Natural & Synthetic)	41
2.6.3	Silica Gel	44
2.6.4	Mesoporous Silica	46
2.7	Materials for Thermal Regulation	48
2.8	Hygrothermal Investigations	49
2.8.1	Material Level	50
2.8.2	Physical Models	52
2.8.3	Full Scale Testing	54
2.8.4	Numerical Investigations	56
2.9	Summary	60
3	CHAPTER 3: Methodology	62
3.1	Introduction	62
3.1.1	Mesoporous Silica Synthesis	63
3.2	Characterisation of the Pore Network and Microstructure	65
3.2.1	Porosity and Density	66
3.2.1.1	Gas Pycnometry	66
3.2.1.2	Gravimetric Testing	67
3.2.2	The Macropore Network	68
3.2.2.1	Scanning Electron Microscopy	69
3.2.3	The Mesopore Network	72
3.2.3.1	N ₂ Physisorption	73
3.2.3.1.1	Specific Surface Area	74
3.2.3.1.2	Mesopore Volume and Mean Pore Diameter	75
3.2.3.2	Small Angle X-Ray Scattering	76
3.2.3.3	Transmission Electron Microscopy	78
3.3	Characterisation of Hygrothermal Functional Properties	80
3.3.1	Dynamic Vapour Sorption	80
3.3.1.1	Desiccators	80
3.3.1.2	Climate Chamber	83

3.3.2	Vapour Permeability	85
3.3.3	Liquid Water Absorption	86
3.3.4	Specific Heat Capacity	89
3.3.5	Thermal Conductivity	91
3.4	Physical Modelling	93
3.4.1	1D Physical Modelling	93
3.4.1.1	ASHRAE Comfort Range Step Test	94
3.4.1.2	Sinusoidal Cyclic Response Test	96
3.4.1.3	Moisture Buffer Value	98
3.4.2	3D Physical Modelling	100
3.4.2.1	Moisture Generation Rates	100
3.4.2.1.1	Scaling factor for the physical model volume	101
3.4.2.1.2	Scaling factor for the 1m ³ numerical model volume	101
3.4.2.2	Evaporation rates	102
3.4.2.3	Humidity Buffering Experiments	103
3.5	Numerical Modelling	107
3.5.1	1D Numerical Models	107
3.5.1.1	Sorption Isotherm Model	108
3.5.1.2	Vapour Permeability Model	109
3.5.1.3	Sinusoidal Cyclic Response Model	110
3.5.1.4	ΔRH_{ie} Sensitivity Analysis Model	113
3.5.1.5	Material Tuning Model	114
3.5.1.6	1D Building Retrofit Model	115
3.5.2	3D Numerical Models	119
3.5.2.1	Material Humidity Buffering Model	120
3.5.2.2	Increased Hygrothermal Area/ Volume Ratio Model	122
3.5.2.3	Cyclic Response Testing Model	123
3.5.2.4	Increased Moisture Load Model	125
3.5.2.5	Increased Air Exchange Rate Model	126
3.5.2.6	3D Representative Climate Model	128
3.6	Experimental Error	129
3.6.1	Pore Network Characterisation	129
3.6.2	Hygrothermal Characterisation	130
3.6.3	Physical Modelling	130

3.7	Summary	130
4	CHAPTER 4: Material Characterisation Results.....	132
4.1	Introduction	132
4.2	Characterisation of the Porous Network Results.....	132
4.2.1	N ₂ Physisorption	132
4.2.2	Corroboration of N ₂ Physisorption Results.....	135
4.2.2.1	Small Angle X-Ray Scattering	135
4.2.2.2	Transmission Electron Microscopy.....	136
4.2.3	Scanning Electron Microscopy	137
4.2.4	Density and Porosity	141
4.3	Characterisation of Hygric Functional Properties Results	143
4.3.1	Sorption Isotherms	143
4.3.1.1	Desiccator Jars.....	143
4.3.1.2	Climatic Chamber.....	145
4.3.2	Vapour Permeability	147
4.3.3	Liquid Water Absorption	149
4.3.4	Vapour Sorption Response.....	150
4.3.5	Moisture Buffer Value	153
4.3.6	Mean Pore Diameter & Response Time Relationship	155
4.4	Characterisation of Thermal Functional Properties Results.....	157
4.4.1	Thermal Conductivity	157
4.4.2	Specific Heat Capacity	157
4.5	Summary	158
5	CHAPTER 5: Results of 1D Hygrothermal Modelling	160
5.1	Introduction	160
5.2	Sorption Isotherm Model.....	160
5.3	Vapour Permeability Model	161
5.4	Cyclic Response Experiments	162
5.4.1	1D Numerical Model Validation.....	163
5.4.2	Variance Testing	164
5.5	Sensitivity Analysis for Variation of ΔRH_{ie}	165
5.6	Sensitivity Analysis for Material tuning	167
5.7	1D Building Retrofit Model	168

5.8	Summary	171
6	CHAPTER 6: Results of Energetic 3D Hygrothermal Modelling	173
6.1	Introduction	173
6.2	Moisture Generation Rates Experiment	173
6.3	Material Humidity Buffering Model	175
6.3.1	3D Numerical Model Validation.....	175
6.3.2	Variance Testing	177
6.4	Increased Hygrothermal Area/ Volume Ratio Model	178
6.4.1	No Internal Moisture Load.....	179
6.4.2	With Internal Moisture Load.....	181
6.5	Cyclic Response Model.....	183
6.6	Increased Moisture Loads Model	184
6.7	Increased Air Exchange Rate Model.....	186
6.8	Representative Climate Modelling.....	187
6.8.1	Material Depth Analysis	188
6.8.2	Full HCHD Control.....	189
6.8.3	Partial HCHD Control.....	192
6.8.4	Partial HCHD Control at ASHRAE Limits	194
6.8.5	Energy Analysis	196
6.9	Summary	198
7	CHAPTER 7: Discussion.....	200
8	CHAPTER 8: Conclusions & Further Research	205
8.1	Concluding Remarks	205
8.2	Recommendations for future research.....	207
	REFERENCES.....	209
	APPENDICES	220
	A1 - Photographs of experimental apparatus	220
	A2 - WUFI Material Datasheets	225

CHAPTER 1: Introduction

1.1 Introduction

The current stock of UK housing (≈ 25 million) consists of approximately 8.1 million (32%) ‘solid-wall’ type dwellings. With poor envelope materials and construction techniques there are large energy losses due to increased heat and mass transfer through the envelope and air infiltration and can result in space heating dominating domestic energy usage in temperate climates (Hong et al., 2006, Yoshino et al., 2006). As a consequence of this, these domestic buildings account for approximately 50% of total UK domestic sector CO₂ emissions (CALEBRE, 2010).

To improve occupant comfort and counteract operational losses, reducing energy consumption and CO₂ emissions there has been a Government-led push in recent years to increase the insulative performance of these buildings (DCLG, 2007). The nature of UK domestic housing stock however, dictates that, in the majority of cases this insulation coupled with vapour barriers can only be placed on the internal surfaces of the building envelope, requiring high performance insulation technologies that are also thin to minimise interior space losses. Cases where this is applicable are:

- Listed historic buildings where the outside appearance of the structure is protected and cannot be altered, for example by external insulation cladding systems
- Buildings where local planning permission is unlikely to be accepted due to changes in the external appearance, e.g. housing estates
- Terraced buildings where fitting external insulating to one building in

isolation would not be acceptable.

Installation of insulation and vapour barriers to the interior of these buildings (*i.e.* retrofitting) can effectively create an internal closed environment. An internal closed environment can be classified as any internal space isolated from its external environment *i.e.* an isolated system (Brewster 2009), and can include domestic buildings, containers (storage & transportation), vehicles (air, motor, shipping), museums, heritage sensitive structures and archives. In the context of this research domestic buildings will be the focus.

1.2 Hygrothermal Behaviour

As building envelopes are subject to hygrothermal loads, the HCHD load of a buildings internal environment is sensitive to both the external and internal environmental loads experienced by the envelope. These include:

- Heat transfer to and from the material arising from short and long wave radiation and sensible/latent heat gains
- Heat storage within the material
- Liquid and vapour moisture transfer to and from the material
- Moisture storage within the material

Internal hygrothermal loads can include sensible/latent heat gains and moisture vapour from occupants, heat-emitting devices or moisture generating devices whilst external loads include solar radiation, ground water, wind driven rain and moisture generation. Each of these hygrothermal loads does not act independently or in 1-dimension (1D), but simultaneously as illustrated in Figure 1. The hygrothermal behaviour of a material can be defined as the change in a material's physical

properties as a result of the simultaneous absorption, storage and release of liquid and vapour in the form of heat and moisture (Künzel, 1995). This behaviour is determined by the materials hygrothermal properties (BSi, 2007a) and can be considered as a ‘template of functional properties’:

- Dry-state thermal conductivity, λ in W/(m K) and its moisture-dependency, $\lambda^* = f(w)$
- Specific heat capacity, c_p in J/(kg K) and its moisture-dependency, $c_p^* = f(w)$
- Bulk density, ρ_d in kg/m³
- Apparent porosity, n in m³/m³
- Sorption isotherm(s) for water vapour and capillary water, where $w = f(\phi)$ in kg/m³
- Water vapour permeability, W in kg/(m² s Pa)
- Liquid water absorption, A_w in kg/m² s^{0.5}

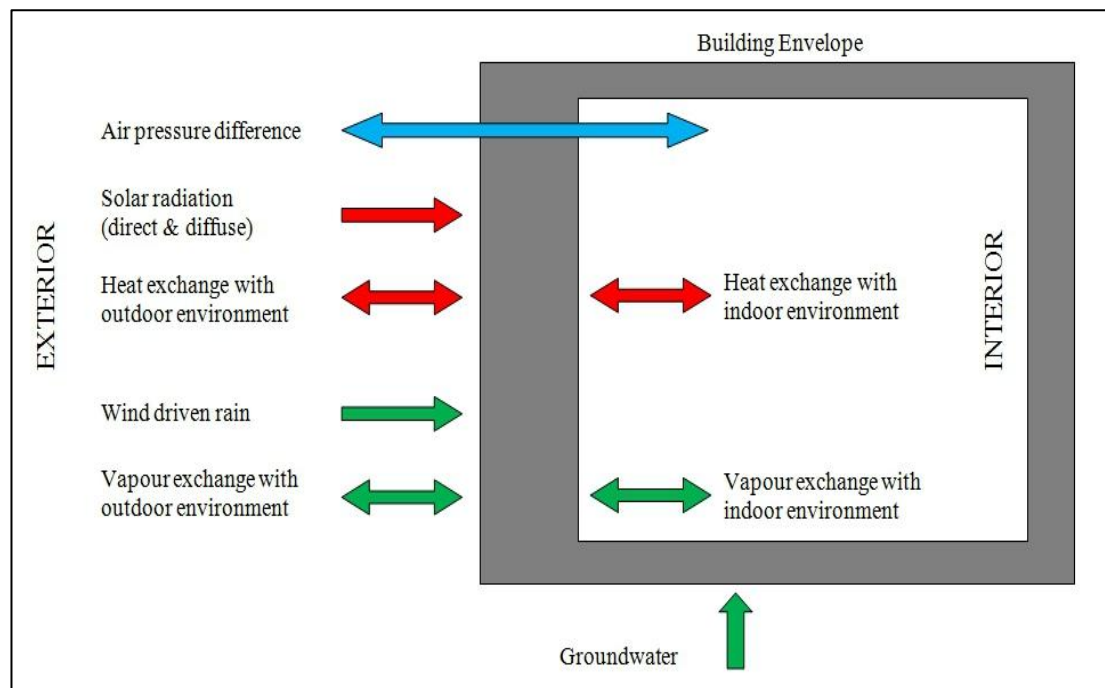


Figure 1 - Hygrothermal fluxes and their alternating directions across a building envelope. Adapted from: (ASHRAE, 2009a)

In a building specific internal closed environment the hygroscopic fabrics that were previously exposed (e.g. brick, masonry, gypsum, plaster or timber surfaces) are now thermally and hygrically isolated from the internal hygrothermal loads due to the retrofitting of the insulation/ vapour barriers. This can give rise to amplified maxima and minima in air temperature and relative humidity (*RH*) variations, negatively affecting occupant health and comfort (CIBSE, 2006, Hall, 2010, Jayamaha, 2006). Poor occupant health can manifest as “sick building syndrome” caused by reduced levels of *RH*, whilst elevated *RH* levels can lead to irritation of the upper respiratory tract. Energy penalties can also be incurred due to the additional interior climate control required from mechanical systems such as Heating Ventilation and Air Conditioning (HVAC) (Kalamees et al., 2009, Liddament and Orme, 1998, Orme, 2001).

It has been shown that hygrothermal materials can be used to reduce the HCHD load by reducing temperature and relative humidity variations *i.e.* creating a passive buffering effect (Allinson and Hall, 2010, Cerolini et al., 2009, Hameury, 2005, Künzeli et al., 2004, Osanyintola and Simonson, 2006, Ramos et al., 2010). Conventional humidity buffering materials (*i.e.* timber, natural fibres and clay) can require large material depths to effectively eliminate any significant variation in relative humidity as a function of time *i.e.* passive humidity buffering, incurring interior space losses. Many desiccants (*i.e.* natural and synthetic zeolites, molecular sieves and silica gels) have high specific surface area (SSA) and high porosity and exhibit good moisture vapour absorption however, predefined microstructural characteristics result in set levels of moisture uptake and storage (Gao et al., 2006, Ng et al., 2001).

Hall and Allinson (2009a) concluded that it is not the moisture storage capacity of

hygrothermal materials, but the rate at which they respond to fluctuations in humidity variations that is key to providing humidity buffering. The performance of hygrothermal materials in this regard is related to optimising their response rate through manipulation of the pore structure to match any anticipated humidity fluctuations. It would therefore be advantageous to have a material that exhibits high specific surface area and high porosity to provide elevated moisture vapour storage levels, but where the pore geometry could be precision engineered to alter its hygrothermal behaviour and response rate, providing humidity buffering to suit different climates *i.e.* fluctuations of *RH*. With regard to health and safety in a domestic context, a material that is inorganic, non-combustible and inert would also be advantageous.

Mesoporous Silica (MS) materials are inorganic and exhibit very high porosities (typically > 90%) coupled with large specific surface areas (from 750 – 1500 m²/g). More importantly, they can also be synthesized using the surfactant method (see: Section 3.1.1) with a finely controlled, pre-determined pore geometry *i.e.* shape, diameter (Jana et al., 2004).

1.3 Overall Aim

The aim for this research is to characterise the functional properties of inorganic, nano-structured surface coatings and correlate these with mesopore geometry to produce desired hygrothermal behavioural response and buffering of changes in climatic variables within a closed environment.

1.4 Hypothesis

The hypothesis as set out for this research is threefold;

1. Pore geometry of mesoporous silica materials can be correlated with their hygrothermal behaviour.
2. 1D hygrothermal numerical software (WUFI Pro v 5.1) can be used as a material selection tool by ‘tuning’ material properties.
3. Mesoporous silica materials can provide occupant comfort in closed spaces by maintaining relative humidity levels within ASHRAE comfort limits.

1.5 Research Objectives

To achieve this aim, the following research objectives have been set out;

1. To identify (specific) candidate desiccant materials and appropriate experimental characterisation techniques, a state of the art literature review on the current use of hygrothermal materials, behaviour, modelling, theory and research in the field will be undertaken.
2. To correlate pore geometry with hygrothermal behaviour by producing a ‘template of functional properties’ using experimental characterisation of the hygrothermal functional properties and pore networks of the materials as set out in Section 1.3.
3. To determine the materials hygrothermal behaviour in terms of moisture uptake and response rate and tune behavioural response to climatic variables through parametric analysis, using the 1D hygrothermal numerical modelling package WUFI Pro v 5.1 (IBP, 2012b) validated using 1D physical modelling.

4. To determine *RH* buffering potential when using hygrothermal materials in a notional domestic building environment under different occupancies and ventilation scenarios with both parametrically varied and representative external climates using the 3D energetic numerical modelling package WUFI Plus v2.1.1.73 (IBP, 2012a) validated using 3D physical models.
5. To determine occupant comfort conditions and any potential HCHD energy savings when using hygrothermal materials compared to standard retrofitting cases using the validated WUFI Plus v2.1.1.73 model.

1.6 Limitations of the study

Due to the time scale of the research, limitations will be set for this study. This research project is primarily focussed on gaining fundamental understanding of the structure-property relationships of desiccants so that response rate of interior hygrothermal material coatings can be tuned to suit varying climatic conditions. In this regard, this study does not focus on research into the manufacturing methods, including R&D, which may be used to produce a useable product for various markets. Areas such as product appearance (colour, texture etc.) and costs are also excluded, allowing the research to focus primarily on the functionality of the desiccants.

For the numerical modelling used in this research it is assumed a thin powder coating of hygrothermal material will be used that will be attached to the building's interior envelope wall. There are several manufacturing methods that could be used to apply this coating:

- bonding to a supportive substrate surface using glue
- sintering of the particles to form a rigid lattice

- containment of the powder particles within a permeable enclosure

Manufacturing methods and product development including investigation of mechanical and structural properties of the coatings (*i.e.* stiffness, compressive strength etc.) however, does not form part of this research.

CHAPTER 2: Scientific Background

2.1 Introduction

This chapter provides a background to the research including a state of the art literature review on the current use of hygrothermal materials, behaviour, modelling, theory and research in the field, whilst also setting out the impetus for the use of MS materials over more traditional materials supported by relevant fundamental theory.

2.2 Psychrometrics

The air that occupies any environment is composed of many individual gases including nitrogen, oxygen, carbon dioxide and water vapour. There are also other constituents including other gases, air borne contaminants and pollutants (*i.e.* particulate matter and dust mites etc.). The field of psychrometrics is the study of the thermodynamic properties of air containing water vapour *i.e.* moist air.

There are many terms associated with the study of moist air, with definitions often being misused. As there is extensive use of these terms in this thesis clarification is provided here:

- **Dry Air** is atmospheric air without any water vapour or contaminants present.
- **Moist air** can be defined as a binary mixture of dry air and water vapour. The amount of water vapour present can vary from zero (no water vapour) to a maximum level (saturated) that is dependent on temperature and pressure (ASHRAE, 2009a).
- **Humidity Ratio (W)**. Can be referred to as the mixing ratio or moisture content and is defined as the ratio of the mass of water vapour, m_v to the mass of ‘dry’

air, m_a in the mixture:

$$W = \frac{m_v}{m_a} \quad \text{Eq 2.1}$$

- **Absolute Humidity (d_v)** or vapour concentration is the mass of water vapour, m_v per unit volume of ‘moist’ air, V_a and is given by:

$$d_v = \frac{m_v}{V_a} \quad \text{Eq 2.2}$$

- **Atmospheric Pressure (P_0)** is the pressure exerted by the air surrounding us and can vary with temperature, altitude, localised geographical position and weather conditions. At sea level (altitude = 0 m) and $T = 15^\circ\text{C}$ $P_0 = 101.325$ kPa (Kaye and Laby, 2012).
- **Saturation Vapour Pressure (p_{sat})** can be defined as the upper limit for a given temperature at which an equilibrium exists between the condensed and vapour water phases (Trechsel, 1994). For $T > 0^\circ\text{C}$, p_{sat} can be obtained from moist air property tables or calculated using Eq. 2.3 (ASHRAE, 2009a):

$$\ln p_{sat} = C_1/T + C_2 + C_3T + C_4T^2 + C_5T^3 + C_6 \ln T \quad \text{Eq 2.3}$$

Where T is absolute temperature ($^\circ\text{C} + 273$), $C_1 = -5.80 \cdot 10^3$, $C_2 = 1.392$, $C_3 = -4.86 \cdot 10^{-2}$, $C_4 = 4.18 \cdot 10^{-5}$, $C_5 = -1.45 \cdot 10^{-8}$ and $C_6 = 6.546$.

- **Partial Vapour Pressure (p_v)** is defined as the partial pressure of the water vapour portion of the moist air mixture. For any given T , p_v cannot exceed p_{sat} . When $p_v = p_{sat}$ the moist air is described as saturated air.
- **Partial Air Pressure (p_a)** is the partial pressure of the dry air portion of the moist air mixture such that the total pressure of the mixture is the sum of the two

partial pressures, *i.e.* $p_a + p_v$.

- **Relative humidity (RH)** can be defined as the ratio of partial vapour pressure to saturation vapour pressure within a finite volume at a given temperature. RH is commonly expressed as a percentage and it follows that at its highest level ($RH = 100\%$), the air is saturated. RH can be calculated using:

$$RH = \frac{p_v}{p_{sat}} \cdot 100 \quad \text{Eq 2.4}$$

- **Dry Bulb Temperature (T_{db})** is a measure of the heat content (*i.e.* internal energies of the gas and vapour) of ambient air. It can have units of Celsius ($^{\circ}\text{C}$) or Fahrenheit ($^{\circ}\text{F}$) with SI units of Kelvin ($\text{K} = ^{\circ}\text{C} + 273.15$).
- **Wet Bulb Temperature (T_{wb})** is the temperature of adiabatic saturation. If a bulb thermometer is wrapped in a saturated wick (continuous water supply), evaporation will occur at constant T and RH from the wick until an equilibrium is reached with the surrounding air. When placed alongside a bare bulb thermometer, a depression in measured T_{wb} will be evident in the wet-bulb due to evaporative cooling at the bulb surface. The $\downarrow\Delta T$ from T_{db} to T_{wb} corresponds to relative humidity (%RH). For example, if $T_{wb} = T_{db}$ then $RH = 100\%$ with no evaporation possible as the air is already at saturation.
- **Dew-Point (D_p)** is the temperature at which the partial vapour pressure is equal to the saturation vapour pressure. It is the temperature at which condensation begins to occur under normal conditions when the moist air is cooled at constant pressure (BSi, 1981). At $RH = 100\%$ then $D_p = T_{db}$.

The psychrometric chart is used as a tool to ‘map’ changes in the conditions of moist air. It is a plot of the relationship between T_{db} , T_{wb} and RH and can be used to determine any of the other psychrometric conditions. On the simplified chart (see

Figure 2), if the two parameters $T_{db} = 27^\circ\text{C}$ and $RH = 30\%$ are chosen, the values for T_{wb} and W can be estimated at $\approx 7.5^\circ\text{C}$ and $\approx 0.0065 \text{ kg/kg}$ respectively. This compares well with calculated values of 7.99°C and 0.0066 kg/kg . The chart can also be utilised to display extended periods of data for occurrence of T_{db} and RH .

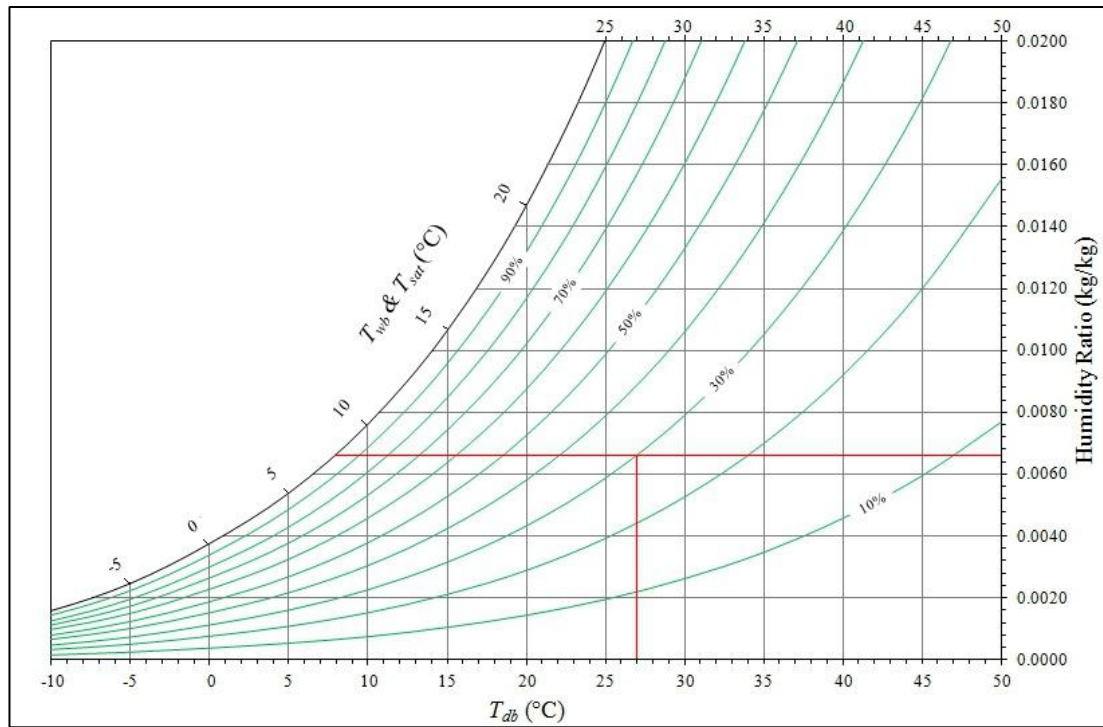


Figure 2 - A simplified psychrometric chart.

2.3 Occupant Comfort

Occupant/ thermal comfort is a person's perceived comfort level in relation to their environment. According to the standard BS EN ISO 7730:2005 (BSi, 2005a) comfort can be defined as the condition of mind which expresses satisfaction with the thermal environment. In the context of this research the environment is a closed space (see: Section 1.1). Comfort is not determined from temperature only (Parsons, 2003), but from the interaction of other parameters including:

1. air temperature
2. mean radiant temperature

3. relative humidity
4. air velocity
5. metabolic heat generation
6. clothing

The human body is constantly subjected to the influences of the environmental factors (1, 2, 3 and 4) with utilisation of the personal factors (5 and 6) to achieve comfort. In an attempt to regulate itself at a constant temperature, the body uses biological thermoregulation processes to act against these influences; evaporation of sweat, respiratory evaporation, conduction, convection via the blood, radiation and metabolic storage. The thermoregulation process may be represented by the heat balance equation (ASHRAE, 2009a).

$$M - W = q_{sk} + q_{res} + S \quad \text{Eq 2.5}$$

Where M is the total metabolic heat production rate, W is the rate of mechanical work accomplished, q_{sk} and q_{res} are the rates of heat loss from the skin and respiration respectively and S is the heat stored (all units are W/m^2). Whilst it is possible to easily measure and monitor the environmental and personal factors contributing towards thermal comfort, it is less simple to measure the physiological phenomena as comfort is a subjective measure. There are two measures for comfort analysis:

1. Personal and environmental - how the person feels (hot/cold)
2. Acceptance and/or tolerance of the thermal environment.

The Predicted Mean Vote (PMV) and Percentage of People Dissatisfied (PPD) are used to give a qualitative indication of the person's response. PMV and PPD can be calculated using the standard BS EN ISO 7730 (BSi, 2005a), whilst subjective

judgement scales can be found in BS EN ISO 10551 (BSi, 2001a).

In addition to thermal comfort, there is also an expectation that an acceptable level of indoor air quality (IAQ), with respect to pollution, be provided for occupants. The causes of pollution will generally stem from one of (or a combination of) poorly maintained environments, poor ventilation, biological contamination, internal pollutant generation and external pollution ingress (Maroni et al., 1995). Typical pollutants found in the indoor environment can be seen in Table 1. The affect of poor IAQ can be manifested as poor health, with symptoms including dryness of the eyes, nasal cavity, mucous membranes and skin *i.e.* “sick building syndrome” caused by reduced levels of RH , whilst elevated RH levels can lead to irritation of the upper respiratory including nasal congestion, sneezing, runny or itchy nose and throat irritation, as well as coughing, wheezing and asthma. Other health effects such as tiredness and headaches are also common.

Type	Pollutant	Source
Organic	Volatile Organic Compounds (VOCs)	Cleaning agents, Cosmetics, Furnishings, Tobacco
	Pesticides	Agricultural spraying
	Formaldehyde	Tobacco, Lacquers, Varnish
Inorganic	Carbon Dioxide (CO ₂)	Breathing, Combustion
	Carbon Monoxide (CO)	Combustion, Tobacco
	Nitrogen Dioxide (NO ₂)	Combustion, Tobacco
Physical	Particulate Matter (PM)	Combustion, Biological, Tobacco, Aerosols
Biological	Man Made Mineral Fibre (MMMF)	Furnishings, Insulation
	Dust Mites	Bedding, Furnishings
	Allergens	Pets, Vermin, Pollen
	Bacteria	HVAC, Humans, Animals, Dust Aerosols
	Fungi/Mould	Damp Organic Matter

Table 1 - Types and sources of indoor pollutants (Spengler et al., 2001).

As discussed in Section 1.1, an occupied closed environment can result in increased fluctuations of T and RH . Combining these can lead to moisture accumulation within

the indoor space due to decreased air exchange with the exterior environment, reducing IAQ. The relative impact of various pollutants, their associated biological problems and sources across the RH range can be seen in Figure 3. For this research the ASHRAE comfort zone is described as the acceptable range of RH at $T \approx 23^\circ\text{C}$ that will provide occupant comfort whilst minimising pollution and improve IAQ. It should be noted that whilst the ASHRAE standard (55-2004) recommends an upper limit $RH = 70\%$ at 23°C , it does not specify a lower RH limit but recommends a minimum dew-point temperature of 2°C . Many studies have suggested various RH ‘comfort bands’ such as 30% to 60% at 18 to 24°C (Crump et al., 2002), 40% to 60% (Hines et al., 1993) and 40% to 70% (Tsutsumi et al., 2007). The lower limit of $RH = 40\%$, as suggested by Tsutsumi has been adopted here for a UK climate.

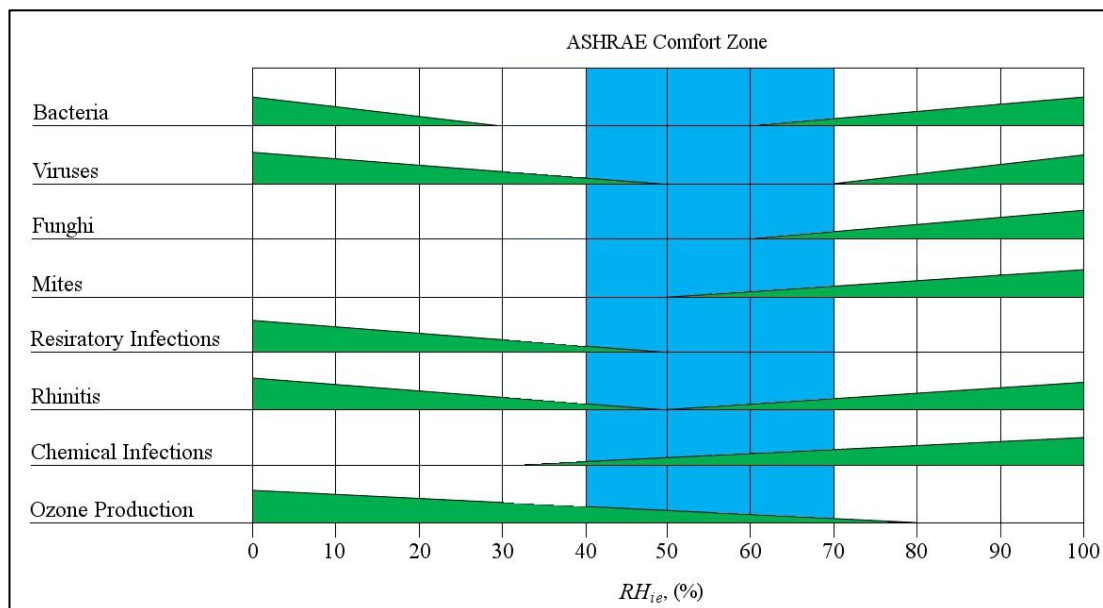


Figure 3 - Factors influencing health and hygiene showing comfort range for RH_{ie} (40% to 70%). Adapted from: (Simonson et al., 2001).

Guidelines for IAQ measurement can be found in the international standard BS ISO 16814:2008 (BSi, 2008). With IAQ expressed either in terms of the health risk to the occupants or in terms of the acceptability, based on the occupants Perception of Air Quality (PAQ). The PAQ method of expressing IAQ uses subjective scales derived

from questionnaires similar to those used for PPD.

2.4 Hygric Theory

As discussed in Section 1.2, there are functional properties that influence the hygric behaviour of a material. These include bulk density, ρ_{bulk} apparent porosity, n sorption isotherm(s) for water vapour and capillary water, water vapour permeability, δ and the liquid water absorption, A_w . The following sections present theory relevant to these properties.

2.4.1 Porosity

A material that is described as hygroscopic (*i.e.* porous and permeable) will allow moisture to be transported into and within it. In order to accurately determine the moisture content of any specific material, it is necessary to understand the pore structure of that material. Considering a finite volume of porous material as a system, the soil model (Barnes, 2000) can be adapted from soil mechanics principles to show the relationship between mass, volume and constituents (see: Figure 4). Moisture entering the system can be classified as ‘absorbed’ whilst moisture leaving the system is classified as ‘desorbed’.

A material will have a total volume, V_t made up of solids, V_s and void spaces, V_v . When a liquid (*i.e.* water) enters the system it can displace any gas (*i.e.* air) present, V_g with an equivalent amount of liquid. Likewise the material has masses equivalent to the volumes with the exception that the mass of air is assumed to be zero, $m_a = 0$ where the total mass, m_t as the sum of the solid mass, m_s and liquid mass, m_l only.

Volumes			Constituents	Masses	
Total volume V_t	Voids V_v	Air V_a	AIR	Air m_a	$M_a = 0$
		Water V_w	WATER	Water m_w	Total mass m_t
	Solid V_s		SOLIDS	Solids m_s	

Figure 4 - A three phase model for porous materials adapted from: (Barnes, 2000).

There are many types of pores that are common in materials and a description of these are shown in Figure 5 and classified in Table 2.

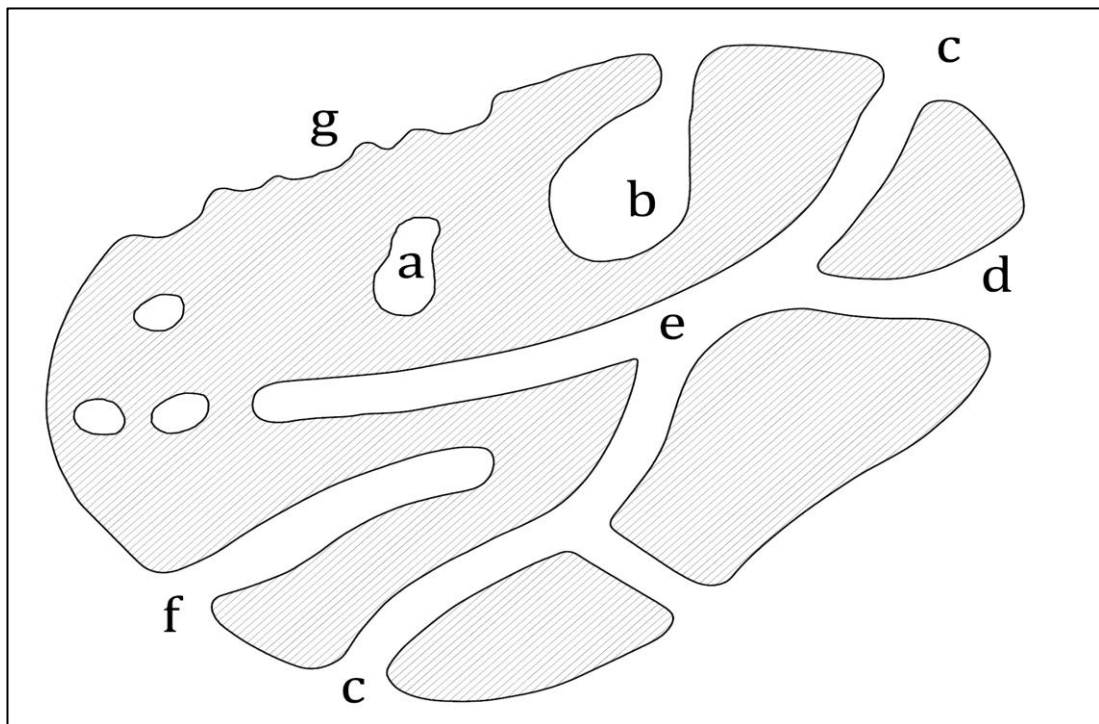


Figure 5 - Cross section of a porous solid showing typical pore types.

Pore Type	Designation in Figure 5
Open	b, c, d, e, f
Closed	a
Blind / Saccate	b, f
Through	c, d
Cylindrical	c, f
Funnel	d
Ink-bottle	b

Table 2 - Range of pore types and shapes (IUPAC, 1994)

Porosity can be defined as the ratio of the total pore volume to the apparent volume of the particle or powder (IUPAC, 1994). It is important to note that this excludes inter-particle voids. In this research it is the open porosity that will be stated at all times (*i.e.* the volume of pores that are accessible to moisture vapour) as it is the open porosity that determines the maximum water content at saturation, w_c of a material. Open porosity, n can be calculated if the solid density, ρ_s and bulk density, ρ_{bulk} are known. Solid density will be measured using gas pycnometry (see: Section 3.2.1.1) and bulk density will be measured using gravimetric testing (see: Section 3.2.1.2). Equation 2.6 is used to calculate n (%):

$$n = 1 - \left(\frac{\rho_s}{\rho_{bulk}} \right) \cdot 100 \quad \text{Eq 2.6}$$

According to the International Union of Pure and Applied Chemistry (IUPAC) (McNaught and Wilkinson, 1997, Lal and Shukla, 2004) pores can be characterised as shown in Table 3.

Pore Description	Pore Size
Ultra-micropore	$\leq 0.7\text{nm}$
Micropore	$\leq 2\text{nm}$
Mesopore	$\geq 2\text{nm}, \leq 50\text{nm}$
Macropore	$\geq 50\text{nm}$

Table 3 – Range and classification of pore sizes.

2.4.2 Moisture Storage

Moisture can be stored in a material as vapour, liquid or solid (ice) or a mixture of all three states. Depending on the environmental conditions, the moisture can undergo phase transitions between these states. As the relative humidity of air surrounding a hygroscopic, capillary active material increases, the moisture content, w of the material will also increase due to vapour and liquid transfer (*i.e.* absorption) to the material and storage within the pore network. The classification of this moisture within the porous material is governed by internal void geometry and electrostatic surface charge for a given temperature and partial vapour pressure (Hall and Allinson, 2009a). A material will absorb and store moisture in three domains;

1. Hygroscopic domain - Moisture vapour absorption
2. Capillary domain – Liquid water absorption
3. Gravitational (Super Saturated) domain – Liquid water absorption under an external pressure gradient.

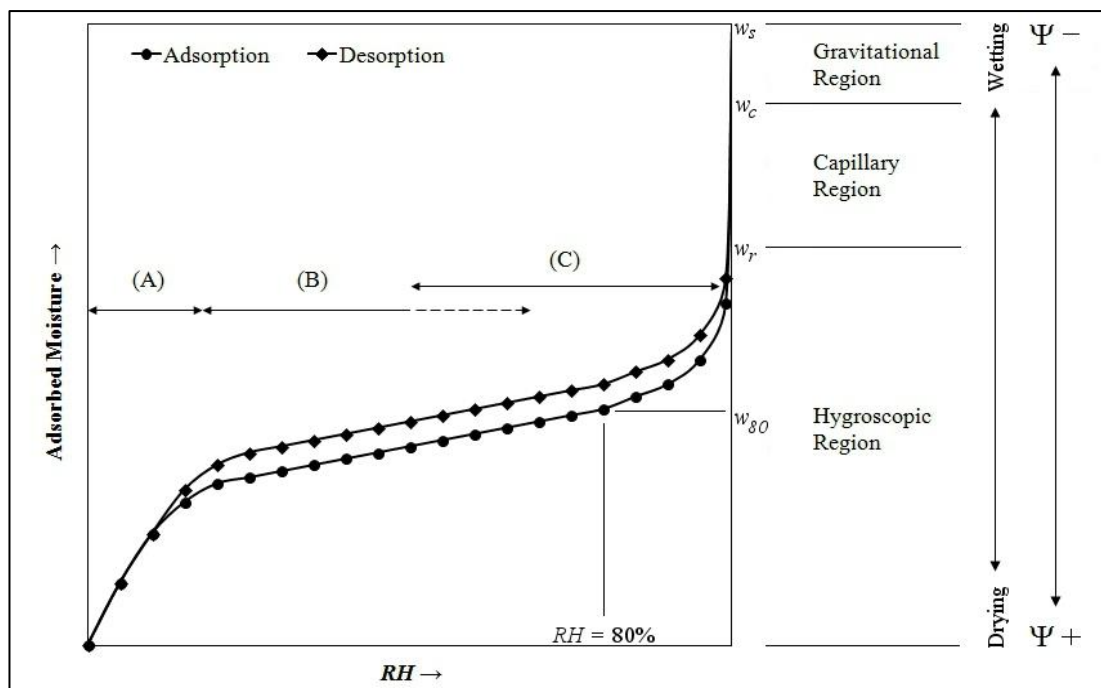


Figure 6 - A typical moisture vapour isotherm showing pore filling stages and transport mechanisms

Moisture vapour absorption data can be represented with a sorption isotherm (See: Figure 6) which defines the relationship between the external psychrometric conditions (*i.e.* RH and T) and moisture uptake. The absorption process occurs through monolayer adsorption to the pore walls (A), followed by multi-molecular formation (B) as p_v increases followed by pore filling (C) occurring due to capillary (Kelvin) condensation. There are a number of different isotherm types which are characteristic of the porous nature of the materials being tested (see: Figure 7).

A Type I isotherm typically has a concave curve, is usually reversible *i.e.* no hysteresis, and has a defined limiting value as $p/p_0 \rightarrow 1$. Type I isotherms are representative of microporous solids with relatively small external surfaces where the limiting uptake value is determined by the accessible micropore volume rather than by the internal surface area. Type II isotherms display unrestricted monolayer-multilayer adsorption as evidenced by the increasing adsorption as $p/p_0 \rightarrow 1$ and are representative of a non-porous or macroporous adsorbent. Point B on the isotherm indicates the stage at which monolayer adsorption is complete and multilayer adsorption begins. Type III isotherms with convex curves over the entire range do not exhibit a Point B and are not common.

Typically, for solids with pores in the mesoporous range and a tightly controlled mean pore diameter, a type IV isotherm would be expected. Type IV isotherms usually have characteristic hysteresis loops, which are associated with capillary condensation taking place in mesopores, and have a limiting uptake as $p/p_0 \rightarrow 1$. Type V isotherms display characteristics common to Type III and Type IV with weak adsorbent/adsorbate interaction but strong capillary condensation and associated hysteresis. Type VI isotherms are characteristic of stepwise multilayer adsorption on a uniform non-porous surface and are not common. Classification of

the full range of isotherms can be found in British and international standards (BSi, 1996, IUPAC, 2004).

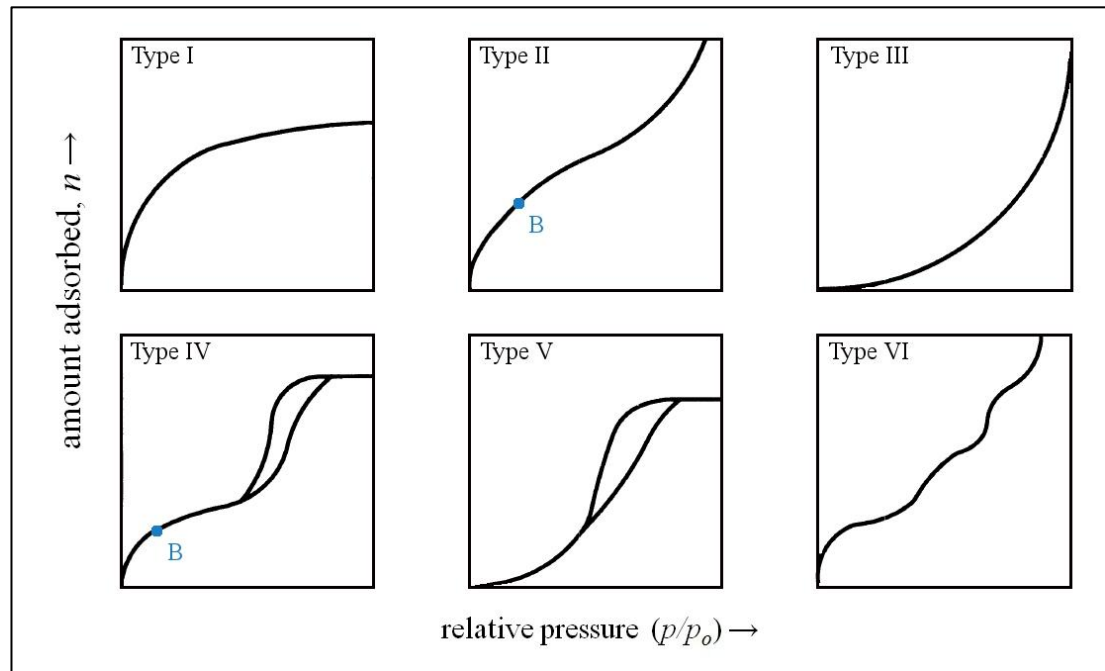


Figure 7 – Adsorption isotherm classification. Adapted from: (Sing et al., 1985)

As discussed, some isotherms display hysteresis loops between the adsorption and desorption branches of the isotherm. This hysteresis is usually associated with capillary condensation in the mesoporous solids however it can also occur due to adsorption of the moisture vapour on the pore walls having a high enthalpy of vaporisation, requiring greater energy to desorb from the pore volume when $\Delta p/p_0$ is negative. As with isotherm shape, hysteresis can be indicative of many pore types. H1 hysteresis loops (see: Figure 8) typically seen in mesoporous solids are indicative of agglomerates (*i.e.* rigidly bound clusters of particles) and have near vertical and parallel isotherm branches due to their narrow pore size distribution. H2 loops have traditionally been associated with the difference between the condensation and evaporation mechanisms occurring within ‘ink-bottle’ type pores (see: Section 2.4.1) and are difficult to interpret correctly. Type H3 hysteresis loops are associated with Type III isotherm whilst H4 loops are associated with Type I isotherms. These loops

are often indicative of aggregates of plate-like particles which give rise to slit-shaped pores within the material. Many microporous solids display non reversible low pressure hysteresis as $p/p_0 \rightarrow 0$ as indicated by the dashed line in Figure 8. This can be due to the adsorption of molecules through pore entrances of about the same width as that of the adsorbate molecule or in some cases irreversible chemisorption of the molecules with the pore wall. Regeneration of these solids to a dry state is only possible by outgassing at high temperatures.

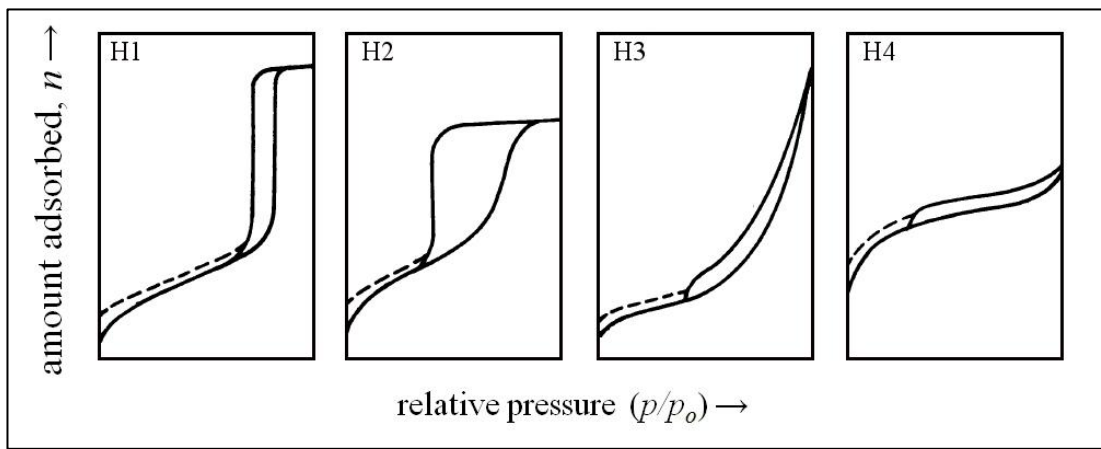


Figure 8 - Isotherm hysteresis loop classification. Adapted from: (Sing et al., 1985)

In the hygroscopic region of the adsorption isotherm, below the residual moisture content, ($w < w_r$) (see: Figure 6) moisture is adsorbed as vapour through inter-molecular adhesion to the pore wall surfaces (*i.e.* adsorbent – adsorbate) and cohesion to other molecules (*i.e.* adsorbate – adsorbate). This is due to both dispersion and dipole-dipole forces (known as Van der Waals forces and including hydrogen bonding). Where the adsorbent – adsorbate forces are greater than the intermolecular forces of the water molecules, adsorbent or surface wetting occurs.

The saturation vapour pressure, p_{sat} above a flat surface of liquid water is dependent upon the pressure applied by the air surrounding it (at $r = \infty$) and at a given ΔPa the p_{sat} can be calculated using Eq. 2.7 (Atkins and de Paula, 2006):

$$p_{sat} = p_{sat}^* e^{V_m \Delta P / R_o T} \quad \text{Eq 2.7}$$

Equation 2.7 can be expanded to give Kelvin's equation (see: Eq. 2.8) where, in a pore of radius r , the water will form a meniscus and be curved, also to a known radius, r . The condition $p_{sat} < p_{sat}^*$ now exists where the saturation vapour pressure of liquid water inside the pore is less than that for a flat surface.

$$p_{sat} = p_{sat}^* e^{-2\gamma V_m \Delta P / r R_o T} \quad \text{Eq 2.8}$$

The Kelvin equation can be rearranged to determine either the critical radius of a void (r_{crit}) for a given RH ($p_v/p_{sat} \cdot 100$) or the RH for a given r_{crit} at which condensation occurs in the pores (see Eq. 2.9). According to Kelvin's law vapour entering a porous solid will begin to condense and pore filling occurs when the pore radius r is less than the critical pore radius ($r < r_{crit}$).

$$RH\% = \exp\left(\frac{2\gamma}{r} \frac{1}{R_{vap} \rho_w T}\right) \cdot 100 \quad \text{Eq 2.9}$$

If the RH surrounding the solid increases with a corresponding increase of moisture vapour within the pore volume then it follows that r_{crit} also increases leading to greater pore condensation (filling) and therefore increased w . There is an equilibrium moisture content (EMC) reached for any given value of RH (0 to 100%) at a constant T for a particular material. EMC can be plotted against increasing (adsorption) and decreasing (desorption) levels of RH to give a material's sorption isotherm. The moisture storage function ξ_u , is calculated from the slope of the linear portion of the sorption isotherm below $w = w_{80}$ as, when RH passes 80% capillary condensation increasing more rapidly.

In the capillary region ($w_r < w < w_c$), as the vapour pressure increases above the

hygroscopic range, where $RH \rightarrow 100\%$, capillarity becomes dominant increasing moisture storage. Moisture content within the pores increases due to capillary action where the water rises in the pore to achieve pressure equilibrium with the pore air (see: Section 2.4.3.3). In the gravitational region ($w_c < w < w_s$), where capillary potential approaches zero, $\Psi \rightarrow 0$ the material is at capillary saturation. As no more moisture can enter the volume through capillarity, any further moisture storage can only occur with increased external pressure or by gravity (Hall and Allinson, 2009a).

2.4.3 Moisture Transport

As a fluid is absorbed, the nature of the porous network (geometry, radius, surface charge and temperature) determines its fluid phase and its associated transport mechanism. Similarly to moisture storage, there are different forms of mass transport mechanisms, vapour, capillary and solid transport. In the context of this research vapour and capillary transport will be considered. For any transport mechanism to occur there must be a driving potential. Table 4 contains the principle driving potentials for mass transport.

Transport Mechanism	Fluid State	Driving Potential
Vapour diffusion	Vapour	Vapour Pressure (ΔRH)
Surface diffusion	Adsorbate	Concentration
Capillary flow	Liquid	Capillary potential, Ψ
Gravitational flow	Liquid	Height (pressure)

Table 4 - Principle moisture mechanisms, states and driving potentials. Adapted from: (Trechsel, 1994)

2.4.3.1 Vapour Transport

Due to the complex pore structures found in most materials, vapour transport may occur by any one, or a combination of:

- Fickian diffusion

- Knudsen diffusion
- Surface diffusion

In general, Fickian diffusion occurs in larger pore sizes (macropores) that are air filled, with Knudsen diffusion occurring in very small pores. Surface diffusion occurs along the surfaces of the pore walls.

The pore classification mentioned in the Section 2.4.1 is derived from the adsorption performance of a pore. In micropores the overlapping surface forces are dominant, whereas the surface force and capillary forces pervade in the mesoporous range (Roque-Malherbe, 2007). In the macroporous range the pore geometry contributes little to the adsorption due to the reduced specific surface area and greater pore size.

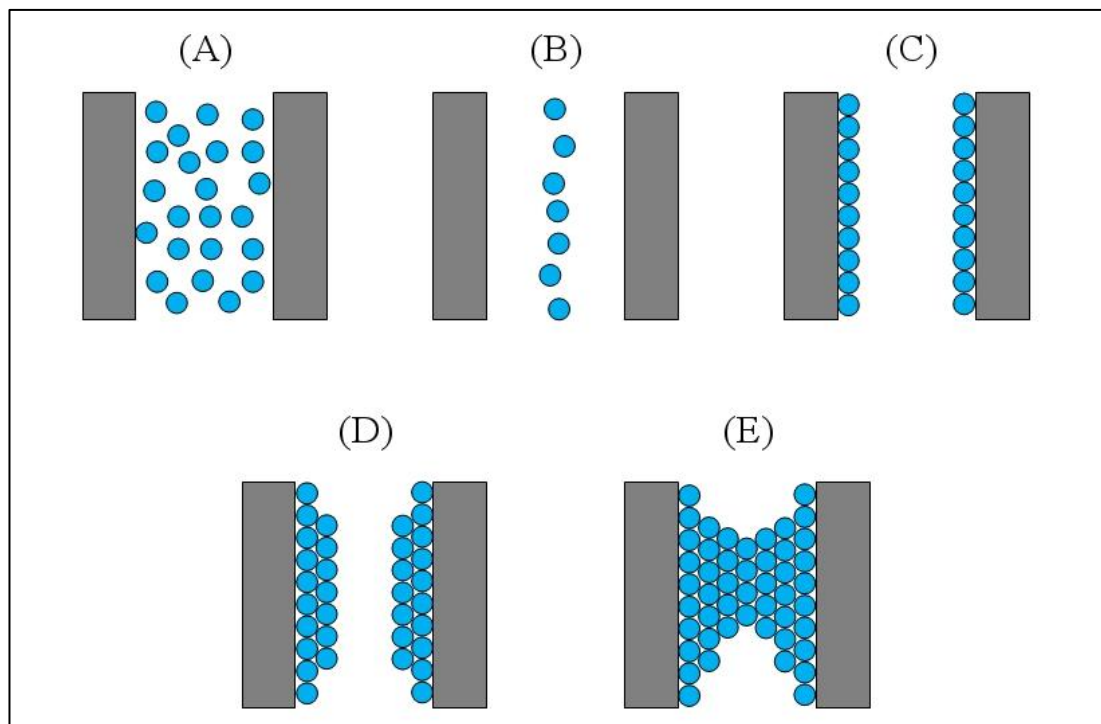


Figure 9 - Moisture vapour molecular diffusion mechanisms in porous solids.

Figure 9 shows that in larger pores (A) transport is by Fickian diffusion as the pore radius is larger than the mean molecular free path (MMFP) which is the average distance it travels before colliding with another molecule (Bird et al., 2001). Here

collisions between molecules are more frequent than collisions with the pore walls. As the pore size decreases (B) Knudsen diffusion becomes dominant where the MMFP increases and collisions with the pore walls becomes more frequent. Monolayer and multilayer adsorption can be seen in C and D with surface diffusion occurring as the molecules migrate along the pore walls. The molecules can also fill the pore (E) due to capillary condensation.

Fickian or molecular diffusion is the redistribution of a gas from a high concentration to a low concentration (Δp_v) through pores or void spaces in or above the macropore range. Fick's law of diffusion is given as:

$$g_{v,air} = -D \frac{\partial C_v}{\partial x} \quad \text{Eq 2.10}$$

Where $g_{v,air}$ is the mass flux, D is the coefficient of diffusion and C_v is the mass concentration of water vapour in air. In ideal gas behaviour C_v can be expressed in terms of pressure; $C_v = p_v M_w / R_o T$. Substituting this into Eq. 2.10 gives:

$$g_{v,air} = -D \frac{M_w}{R_o T} \frac{\partial p_v}{\partial x} \quad \text{Eq 2.11}$$

Where M_w is the molar mass of water. The water vapour permeability of still air, δ_a is given as $D \cdot M_w / R_o T$. This allows Fick's law to be rewritten for water vapour flow in quiescent air as:

$$g_{v,air} = -\delta_a \frac{\partial p_v}{\partial x} \quad \text{Eq 2.12}$$

The vapour permeability of a specific material, δ is the moisture transport that occurs within the material via Fickian diffusion. The vapour flow is given by:

$$g_v = -\delta \frac{\partial p_v}{\partial x} \quad \text{Eq 2.13}$$

In practice the product of the materials water vapour permeance, W and its thickness, d (see: Eq. 2.15) is used to calculate δ . The water vapour permeance is defined as the water vapour flow rate, G (*i.e.* $\Delta m/t$) through the material divided by the product of the water vapour pressure difference, Δp_v between its two exposed surfaces and the exposed surface area, A :

$$W = \frac{g_v}{A \cdot \Delta p_v} \quad \text{Eq 2.14}$$

$$\delta = W \cdot d \quad \text{Eq 2.15}$$

The water vapour diffusion resistance factor, μ is also used to indicate a material's permeability to moisture vapour. It can be defined as the ratio of water vapour permeability of air, δ_{air} to that of the material, δ (See: Eq. 2.17). The resistance factor indicates the ratio of a material's vapour resistance to that of an equally thick layer of quiescent air under identical conditions. Calculation of μ is necessary as it is used as a primary material property input in the WUFI numerical models used later. Use of μ requires the calculation of δ_{air} using Eq. 2.16 and Eq. 2.17 (Trechsel, 1994).

$$\mu = \frac{\delta_{air}}{\delta} \quad \text{Eq 2.16}$$

$$\delta_{air} = \frac{0.00002306 \cdot p_0}{R_v \cdot T \cdot p} \left(\frac{T}{273.15} \right)^{1.81} \quad \text{Eq 2.17}$$

2.4.3.2 Transition from Vapour to Capillary Transfer

As discussed previously, when the RH and thus w increases, a transition from the vapour diffusion to capillary flow occurs (see: Figure 10). Considering a typical

winter scenario, it can be seen from the figure that, even when interior RH levels (RH_{int}) are lower than the exterior (RH_{ext}), Fickian diffusion will occur from interior to exterior due to the higher T and thus p_v in the interior (Künzel, 1995). As w increases in the pore ($w \rightarrow w_r$), monolayer and multilayer adsorption occurs with surface diffusion occurring in the opposite direction to the vapour diffusion as the molecules migrate along the pore walls from the thicker sorbate film on the exterior side (higher RH) to the thinner interior film. With the onset of capillary flow as w increases ($w_r < w < w_c$) moisture flow is completely reversed from vapour diffusion.

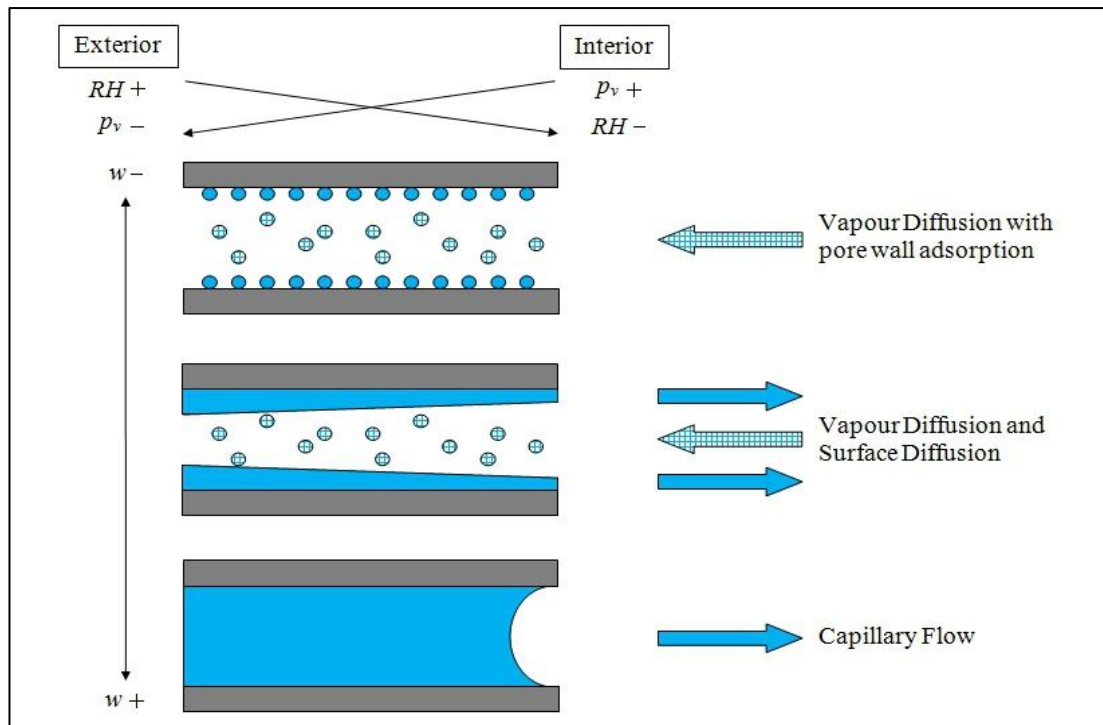


Figure 10 - Graphical representation showing the reversal of moisture transfer during the transition from vapour diffusion to capillary flow in a pore. Adapted from: (Künzel, 1995).

2.4.3.3 Capillary Transfer

Capillary flow or capillarity (sometimes referred to as suction) is the process of water rising in a capillary or pore in order to equilibrate the pressure differential caused by p_{sat} at the curved surface of water inside the pore being less than that of

the surrounding air. In a pore or capillary tube, the adhesion forces at the surface of the pore wall are greater than the intermolecular cohesion forces within the liquid. This gives rise to the characteristic ‘upward’ curve (see: Figure 11). Increased surface tension alongside an increased ratio of adhesion to cohesion will result in increased capillarity.

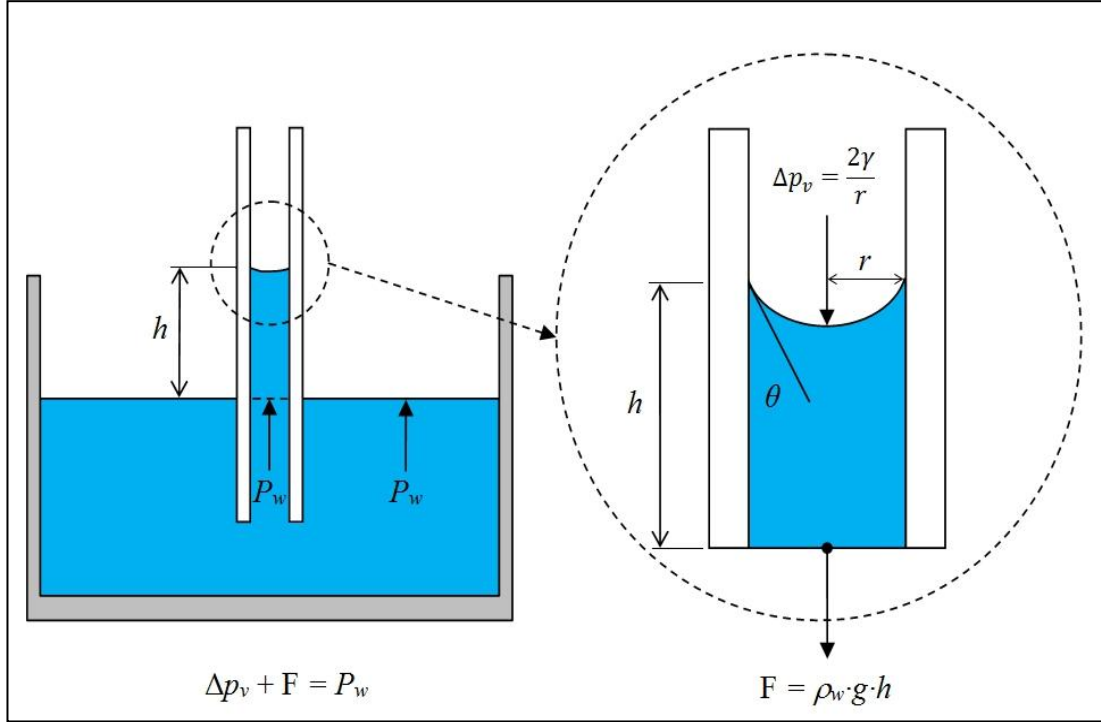


Figure 11 - Capillary rise in a pore showing meniscus formation.

The height of a water column in a pore can be calculated using Eq. 2.18 (Hall and Hoff, 2002) assuming pressure equilibrium has been reached ($P_w = P_a$):

$$h = \frac{2\gamma}{r\rho_w g} \quad \text{Eq 2.18}$$

Liquid water absorption or water absorption coefficient, A_w by capillary action, is the ability of a homogenous permeable material to absorb and transfer liquid water. It can be defined as the mass of water absorbed by a sample per exposed surface area and per square root of time ($\text{kg/m}^2\text{s}^{0.5}$).

2.5 Thermal Theory

As outlined in Section 1.2 the dry-state thermal conductivity, λ and specific heat capacity, c_p (including their moisture-dependencies, λ^* and c_p^* respectively) are functional properties of a material that contribute to its hygrothermal behaviour. Theory relevant to these properties is presented in the following sections.

2.5.1 Heat Transfer

Although heat transfer occurs through many mechanisms within the context of this research it is transfer by conduction that is of interest. Heat transfer via convection and thermal radiation are considered during the numerical modelling however, it was not necessary to investigate these properties experimentally. Heat transfer by conduction, Q is the transfer of energy between neighbouring molecules due to a temperature gradient (Baehr and Stephan, 2006). Thermal conductivity, λ is the ability of a material to conduct energy in the form of heat. It can be defined as the quantity of heat transmitted, due to unit temperature gradient, in unit time under steady conditions in a direction normal to a surface of unit area, when the heat transfer is dependent only on the temperature gradient (Kaye and Laby, 1995). It is derived from Fourier's law (see: Figure 12) and can be expressed by Eq. 2.19:

$$\lambda = \frac{q_x x}{\Delta T} \quad \text{Eq 2.19}$$

Where q_x is the heat flow, x is the depth and ΔT is the temperature difference.

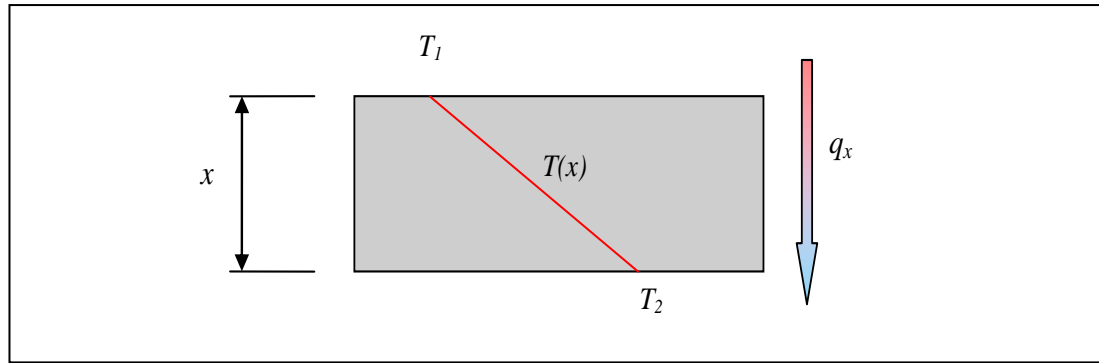


Figure 12 - Figure illustrating Fourier's law of steady state heat conduction. Adapted from: (Incropera et al., 2007).

From the definition it can be seen that λ is dependent on the surrounding psychrometric conditions. In a hygroscopic, permeable material an increase in RH results in an increase in w (see: Section 2.4.2). Increasing w , results in gradual capillary filling of the void spaces with formation of inter-particle menisci (Hall and Allinson, 2009b). Due to the higher thermal conductivity of liquid moisture over that of air, and the increased inter-particle contact from menisci bridging, there is an increase in the heat flow, q_x of the moist sample (see: Figure 13).

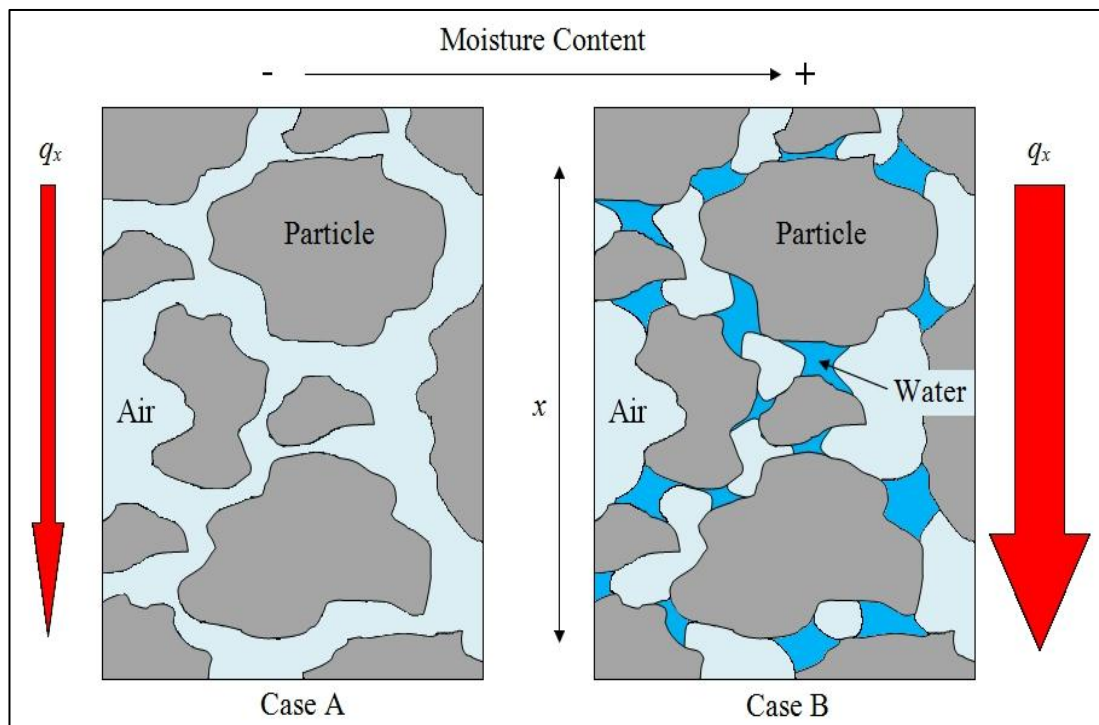


Figure 13 - Figure illustrating increased heat flow due to increasing moisture content.

A greater increase in heat flow, q_x can also occur due to convective heat transfer in the vapour phase within pore networks. As discussed in Hall M, 2010 when a temperature differential ($\Delta T = T_2 - T_1$) is placed across a material, moisture vapour on the higher temperature side (T_2) will vaporise and migrate towards the cooler side (T_1) via diffusion (see: Section 2.4.3.2). This combination of sensible transport via conduction in the material, convection in the vapour and latent transport when the vapour condenses at T_1 significantly increases q_x . This can be further increased as ΔT increases where liquid water can accumulate at T_1 resulting in increased capillary potential, Ψ and liquid transfer back to T_2 . These mechanisms can become cyclic resulting in significantly higher q_x over that of a dry or inter particle wetted material.

The thermal diffusivity, α is the rate at which heat diffuses through the material via conduction. Materials with high diffusivity will reach equilibrium with their surrounding environment more quickly. The diffusivity is a function of thermal conductivity, bulk density (for hygroscopic materials) and specific heat capacity:

$$\alpha = \frac{\lambda}{\rho_{bulk} c_p} \quad \text{Eq 2.20}$$

The thermal effusivity, β is the magnitude of heat transferred on contact *i.e.* when touching a piece of steel and a piece of plastic, at equal temperatures, the steel will feel colder as there is a greater magnitude of heat transfer on contact due to its higher effusivity over that of the plastic. It can be calculated using Eq. 2.21:

$$\beta = \sqrt{\lambda \rho_{bulk} c_p} \quad \text{Eq 2.21}$$

2.5.2 Heat Storage

Specific heat capacity (at constant pressure), c_p is the ability of a material of selected

mass to store energy in the form of heat. It can be defined as the quantity of heat necessary to raise the temperature of a unit mass of material by 1 K at constant pressure. It can be expressed by Eq. 2.22;

$$c_p = m \left(\frac{\Delta Q}{\Delta T} \right) \quad \text{Eq 2.22}$$

Whilst it is the sensible heat storage of materials that is of interest here, a brief description of the theory surrounding latent heat storage is also presented. Sensible heat storage, Q_s is the amount of heat stored due to heat transfer to a substance resulting in a temperature increase, as in (A), Figure 14. If there is an increase from an initial temperature, T_i to a final temperature, T_f molecules within a material will possess higher kinetic energy in the form of heat. Sensible heat is a function of the specific heat and mass of a substance. Most common building materials can be used as sensible heat stores providing c_p is sufficiently high. The formula for Q_s is given as:

$$Q_s = mc_p(T_f - T_i) \quad \text{Eq 2.23}$$

Latent heat is the internal energy change associated with a change of phase of a material due to a temperature change. This phase change can occur as solid-liquid, liquid-gas or solid-solid. At the molecular level the internal energy is associated with the intermolecular forces between molecules. These forces are progressively weaker from solid – liquid – gas. Phase change will occur at an onset temperature, T_o when sufficient energy is added to a solid (or liquid) to break these intermolecular forces causing the substance to change to a gas. The portion of added energy is stored in the substance in the gaseous state and is termed the latent heat. It is difficult to achieve an isothermal phase change in experimental conditions where there is usually a small

ΔT due to thermal gradients (see: B, Figure 14). Materials that undergo phase change (PCMs) can be used to either store energy (heat) with little ΔT , or to control ΔT . The latent heat is a function of the sensible and latent phase and is given by:

$$Q_l = m[c_s(T_m - T_i) + a_m\Delta h_m + c_l(T_f - T_m)] \quad \text{Eq 2.24}$$

Where a_m is the fraction of the material melted and Δh_m is the change in enthalpy associated with the phase change.

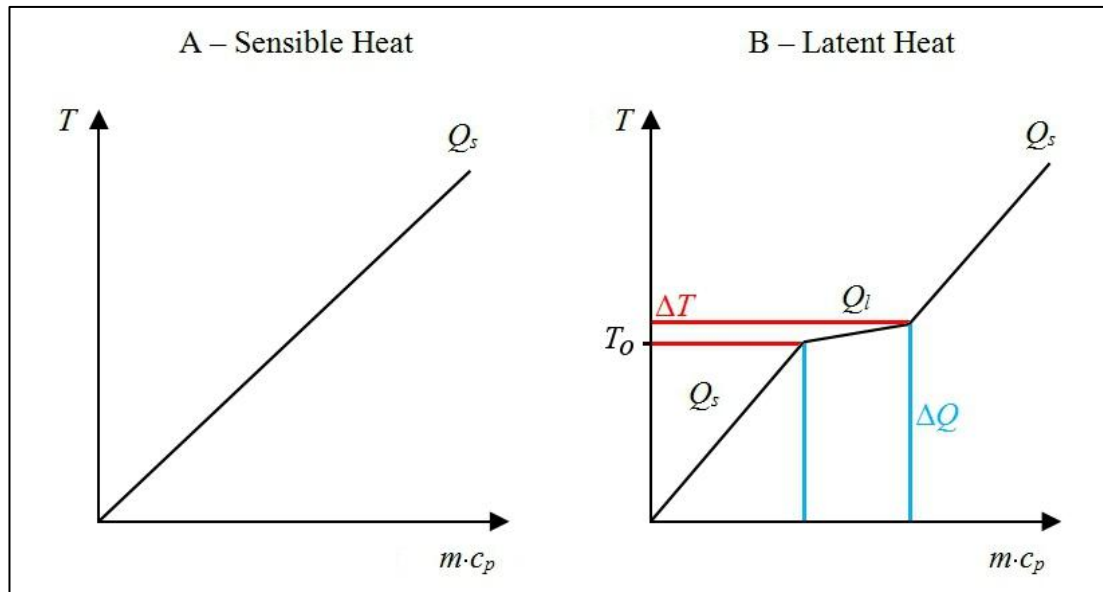


Figure 14 - Figure showing sensible and latent heat storage.

2.6 Hygric Materials

Figure 15 contains a summary of many construction materials categorized by hygrothermal function. Both the ‘hygrothermal’ and ‘thermal’ sets of materials are routinely evidenced as building envelope materials (both internally and externally in certain cases) however, it is not common to discover those materials classed as ‘hygric’ within the context of building physics.

As stated in Section 2.4.1 only solids that have a porous network which is available for the adsorption of moisture vapour from its external environment (*i.e.*

hygroscopic) will be considered as candidate materials for this research. The following sections provide a review of the materials that fit this criterion.

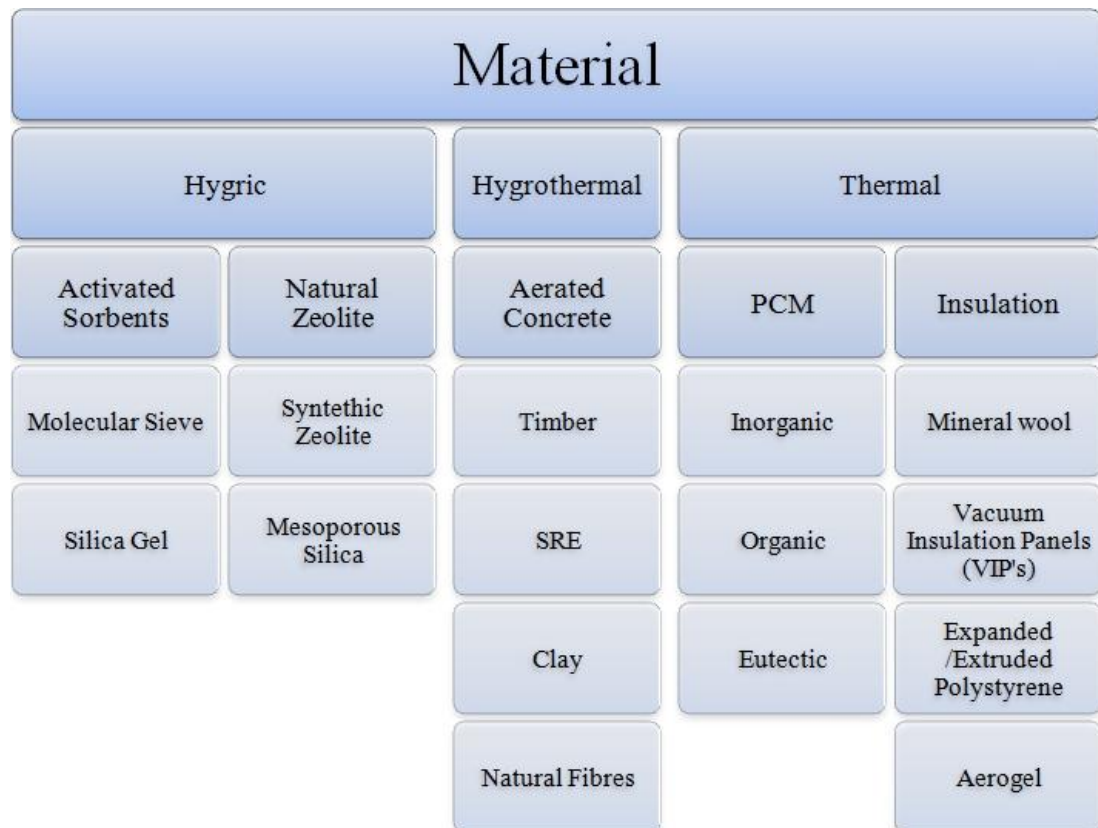


Figure 15 - Categorisation of Hygrothermal materials by hygrothermal function.

2.6.1 Conventional Building Materials

Many conventional or traditional building materials perform both hygric and thermal functions. These materials can be classified as hygrothermal as they provide some level of enthalpy buffering *i.e.* the buffering of sensible and latent heat energy simultaneously with moisture (Hall, 2010). They include gypsum plaster, timber, concrete, clay/brick and other earthen materials.

2.6.1.1 Timber

Timber is a natural fibrous material consisting of lignin, ash-forming minerals and extractives formed in a cellular structure (USDA, 1989) occurring in many different

varieties which can be manufactured into various types of solid boards, composites and other products. Some of the hygrothermal properties of hardwoods, softwoods and boards are shown in Table 5.

	ρ_{bulk}	c_p	λ	μ
Hardwoods				
Oak	685	1500	0.13	140
Beech	650	1500	0.13	200
Softwoods				
Red Cedar	350	1880	0.084	1963
Spruce	455	1500	0.09	130
White Pine	460	1880	0.093	4427
Manmade Boards				
Chipboard	600	1500	0.11	70
MDF	508	1700	0.12	15
Plywood	500	1500	0.1	700

All properties will vary depending on age, moisture level etc.

Table 5 - Properties of woods & man-made timber products (IBP, 2012b).

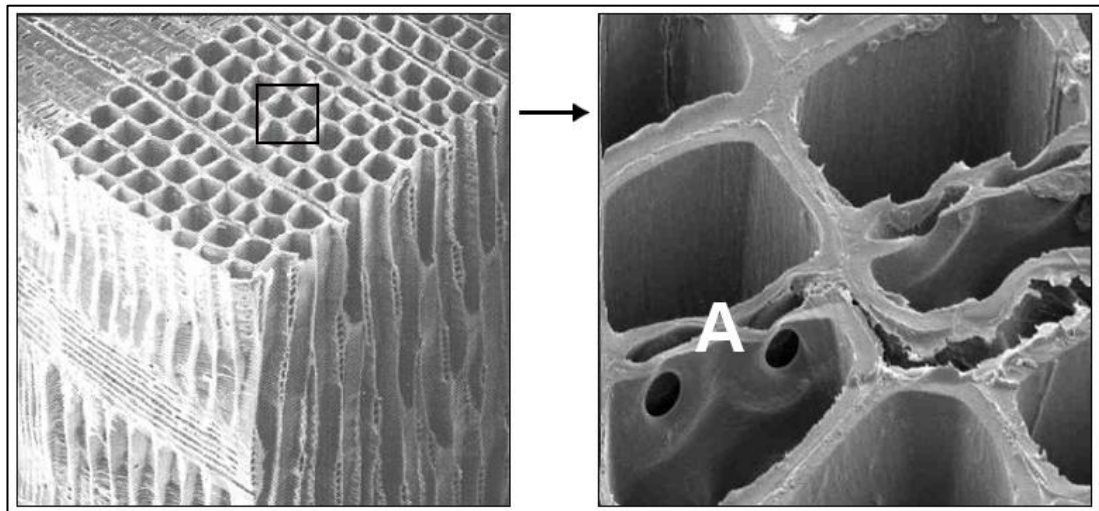


Figure 16 - SEM images of softwood cellular structure. Adapted from: (Koch., 1972, UoT, 2012)

Generally hardwoods exhibit much higher density due to their slow growing nature and tightly packed cellular structure, whilst softwoods are faster growing resulting in a more open cellular structure, lower density and also a lower thermal conductivity than the hardwoods. It is the cellular structure within softwood that allows the transport of moisture to and from the material whilst according to Hall, 2010 in

hardwoods moisture transport occurs within large purpose grown vessels. Within the cellular structure, timber has torus (see: A, Figure 16) between the cells which act as valves for moisture transport.

Timber and wood based materials have been shown to have good ΔRH amplitude buffering in numerous studies (Künzel et al., 2004, Padfield, 1998, Simonson et al., 2002, Svennberg et al., 2007, Hameury, 2005). Künzel et al., 2004 demonstrated that untreated Scandinavian spruce and pine wall linings can provide an RH reduction of >50% when compared to gypsum plaster in a room with moisture generation and an air exchange rate of 0.5ACH (air changes per hour). Wood fibre-board displayed better ‘short-term’ reductions, however these would require an additional surface finish in practice, reducing the hygric performance. The numerical investigations carried out by Simonson et al., 2002 showed a reduction in ΔRH from 45% to 10% in an occupied bedroom (with ACH = 0.5) constructed from wooden materials when the surface finish (paint) permeability was increased allowing the moisture vapour to transfer to the hygroscopic timber. It is noted however that the study has no experimental validation of the results. Svennberg et al., 2007 present a review of experimental studies carried out on wooden materials in Sweden and Germany which concur with Simonson that, any potential ΔRH buffering effect can be negated when high vapour resistant finishes are used. Wood fibre-board and plywood have also been found to improve the ΔRH buffering considerably in other studies (Woloszyn et al., 2009, Osanyintola and Simonson, 2006).

2.6.1.2 Earth

Rammed Earth (RE) materials have been traditionally used to create stable, warm and low-impact structures. It is said that up to a half of the total world population

live or work in RE buildings (Rael, 2008). RE can constitute many different materials including sand, gravel and clay, mixed as earth (Hall and Allinson, 2009a). Recently, stabilizing agents have been introduced (typically Portland cement) to act as a binder and to produce stabilized Rammed Earth (SRE). SRE materials act as thermal mass (ΔT buffering) by absorbing heat during high temperature periods and releasing heat stored when the temperature drops. SRE is also hygroscopic, due to the presence of clay in the earth (see: Section 2.6.1.3) and therefore can also act as hygric mass providing ΔRH buffering.

An investigation carried out by the Hall and Allinson (Allinson and Hall, 2010) using the numerical hygrothermal simulation software WUFI Plus (IBP, 2012a) validated in field tests, demonstrated that SRE has very good potential for passive indoor climate control by significantly reducing the amplitude of RH fluctuations, when compared to standard building materials (*i.e.* unpainted and painted plaster board). In Hall and Allinson, 2009a the authors demonstrate that there is no significant variation of moisture capacity (EMC) across three different SRE mix designs however, the response rate (t_{emc}) to changes in RH vary significantly highlighting the importance of response rate in relation to pore geometry when considering ΔRH buffering applications. They propose that by fully understanding the hygrothermal behaviour of SRE (and other materials) through precise characterisation of the hygrothermal functional properties, the response rate of materials to ΔRH and ΔT fluctuations can be optimised (Hall and Allinson, 2009a).

2.6.1.3 Clay

Clays are defined as a naturally occurring material composed primarily of fine-grained minerals, which is generally plastic at appropriate water contents and will

harden when dried or fired (Guggenheim and Martin, 1995). Clay constitutes phyllosilicates formed of layers of silicate and aluminate minerals to form lamellar structures, although it can also contain other materials that may aid plasticity. The lamellar structure will either be of the ratio 1:1 or 2:1 and it is the ‘stacking’ of these that dictate the final clay type.

Clays are strong desiccants due to their high specific surface area (SSA), high net surface potential and corresponding formation of a double diffuse water layer (Hall et al., 2012b). The hygrothermal properties of individual clay types can vary significantly however. For example Kaolinite has little moisture sorption capacity due to its strong hydrogen bonds where as Smectite (Montmorillonite) will absorb large volumes of water due to weak layer bonding and high SSA (see: Figure 17).

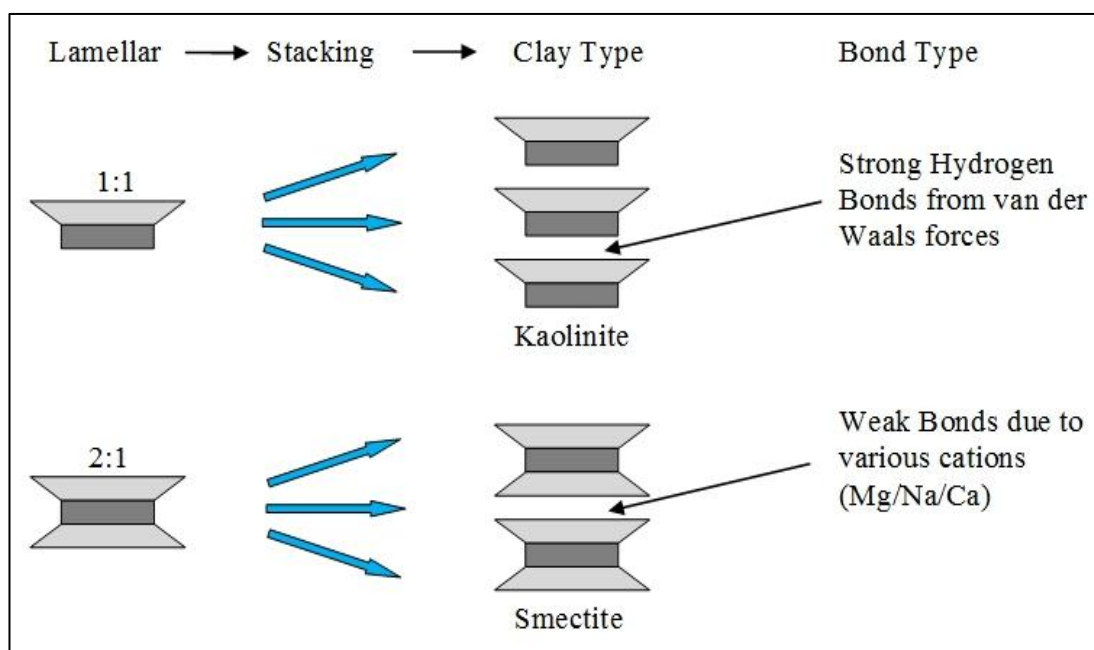


Figure 17 - Formation of clays showing Kaolinite and Smectite

Mesoporous clay materials were prepared by hydrothermally treating composites of metakaolin, quartz and slaked lime using different forming pressures (Maeda and Ishida, 2009b, Maeda and Ishida, 2009a) with the authors suggesting that introducing a pore size range of 3.2nm to 7.4nm to the clay structure could control

RH in the 40% to 70% range. These clays were found to have good humidity buffering performance with a ΔRH reduction from $\approx 42\%$ to 18% in a 6L airtight container with an exposed sample surface area of $1.8 \cdot 10^{-3} \text{m}^2$. Whilst this initially appears impressive, the moisture vapour sorption isotherms for the materials show very little EMC based on %mass without any initial mass stated suggesting the results may be questionable. There is also a large degree of hysteresis present which would suggest that whilst ΔRH reduction may be significant in the ‘short-term’ it is not sustainable over extended periods.

In an investigation of sepiolite (Caturla et al., 1999) which is a fibrous clay mineral with fine microporous channels running parallel to the fibres, the authors report the good humidity buffering potential of the material, particularly in environments with high *RH* levels ($>95\%$). The minimal EMC levels, slow response rates and hysteresis of the materials shed doubt on the conclusions however.

Other clays of the smectite group have been used in applications such as montmorillonite for water retention agents for soil hydration and bentonite as a seal in various guises from radioactive waste repositories (Villar and Rivas, 1994), to boreholes, shafts, mine drifts, and tunnels (Akgün, 2009). Bentonite exhibits a high swelling potential during water absorption, which will effectively seal the clay by forming an impermeable barrier (Dueck et al., 2008). Sodium Carbonate has been used to treat bentonite to improve its adsorption isotherm capacity (D’Orazio and Quagliarini, 2009), to increase the buffering capacity in an ‘inter-space’ cavity between wooden beams and a masonry wall. The authors use a volumetric (m^3/m^3) measure for adsorption which is not commonly used and prevents like for like comparison with other materials as ρ_{bulk} for the materials was not quoted. The treated bentonites showed an elevated isotherm when compared to brick and spruce which

does suggest increased buffering potential against these materials. No desorption or hysteresis data was presented for the bentonites and therefore any ‘long term’ buffering potential, as suggested using numerical modelling is in doubt.

Montmorillonite clay has also been treated with water-glass and sulphuric acid, which coats the clay with silica. This was then formed into pellets called ‘Kaken Gel’ or ‘Nikka Pellets’ (Toishi, 1959). These pellets show rapid absorption and desorption with hysteresis, however they respond poorly to temperature fluctuations. Pulverising the pellets and combining them with tissue paper using a hygrophillic binder such as Polyvinyl Alcohol, however, partly overcame this problem (Kenjo, 1982).

2.6.2 Zeolites (Natural & Synthetic)

Natural zeolites are microporous crystalline aluminosilicates comprising a three-dimensional structure composed of Si–O and Al–O tetrahedroids. Interconnected micropores of different size dependent on classification (~ 3 to 10 \AA) result in large specific surface areas. They are formed when tetrahedra link together to construct a framework, as in the case of the silicate tetrahedra illustrated in Figure 18. This framework structure can contain linked cages, cavities or channels, which serve to limit the passage of certain molecules through the structure. There are approximately forty natural zeolites that are commercially mined including analcime, chabazite, clinoptilolite, erionite, ferrierite, heulandite, laumontite, mordenite and phillipsite (Hall et al., 2012b) and have exhibited good moisture storage capacity when used as an admixture for aerated concrete (Feng and Peng, 2005). The zeolite (mordenite) was calcined at 300°C for 1 h before adding to the cement paste. The authors claim that the addition of the zeolite results in a reduction of ΔRH_{ie} from $\approx 70\%$ to $\approx 20\%$

over a period $t = 84\text{h}$. No experimental parameters or design is presented to support the results, which leads to some doubt in the conclusions.

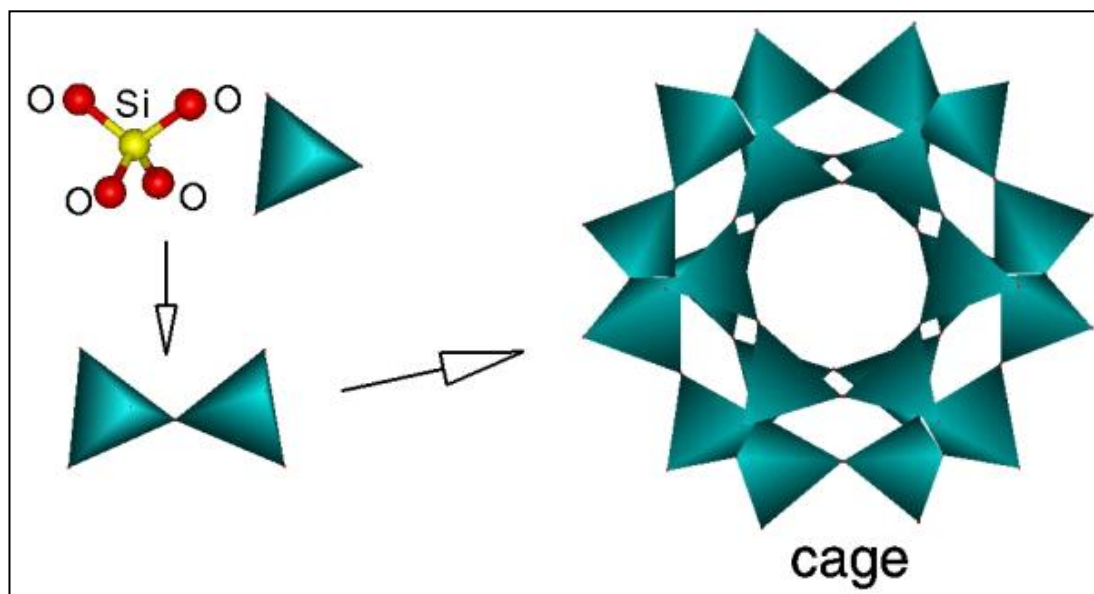


Figure 18 - Framework of natural zeolite showing silicon tetrahedra (BZA, 2006).

Zeolites have also been used as a humidity buffering agent in ceiling paint (Zalba et al., 2009) where after being activated at 350°C for four hours, $\approx 11\%$ wt of clinoptilolite was added to the paint providing a slight increase ($\approx 1\%$ wt) in moisture adsorption at $RH = 79.5\%$. The chemical analysis of the clinoptilolite is given in Table 6, with a more comprehensive list for other zeolites available in Wang and Peng, 2010. As zeolites have a high cation exchange capacity (CEC) they are also used in the field of water purification to filter out various organic and inorganic pollutants (Wang and Peng, 2010) where the H^+ in the water molecule is attracted to the O^- in the zeolite. With a high SSA and thus high surface potential, there is a corresponding higher attraction.

Clinoptilolite - $(\text{Na}_2, \text{K}_2)\text{O} \cdot \text{Al}_2\text{O}_3 \cdot 10\text{SiO}_2 \cdot 8\text{H}_2\text{O}$

SiO_2	Al_2O_3	Na_2O	K_2O	CaO	MgO	Fe_2O_3
63.22	12.64	3.37	1.45	2.51	1.03	1.21

Table 6 - Chemical analysis of Clinoptilolite (Zalba et al., 2009)

Synthetic zeolites or molecular sieves are crystalline alumina-silicates, similar to natural zeolites, but are manufactured using thermal processes. The frameworks of molecular sieves are negatively charged, which is counter-balanced by positive cations. It is the exchange of these cations during thermal processing that controls pore size. A 4A molecular sieve (Sodium form of zeolite 4A) has a pore diameter ≈ 4 Å ($4 \cdot 10^{-10}$ m). Exchanging the Sodium ion with a Potassium ion, (see: Table 7) will result in a pore diameter of ≈ 3 Å giving a 3A molecular sieve. In a 5A molecular sieve, one calcium ion replaces two sodium ions giving a diameter of ≈ 5 Å.

	Pore Size	Chemical Formula
Mol Sieve 3Å	3×10^{-10}	$0.4\text{K}_2\text{O} \cdot 0.6\text{Na}_2\text{O} \cdot \text{Al}_2\text{O}_3 \cdot 2\text{SiO}_2 \cdot 4.5\text{H}_2\text{O}$
Mol Sieve 4Å	4×10^{-10}	$\text{Na}_2\text{O} \cdot \text{Al}_2\text{O}_3 \cdot 2.0\text{SiO}_2 \cdot 4.5\text{H}_2\text{O}$
Mol Sieve 5Å	5×10^{-10}	$0.7\text{CaO} \cdot 0.3\text{Na}_2\text{O} \cdot \text{Al}_2\text{O}_3 \cdot 2\text{SiO}_2 \cdot 4.5\text{H}_2\text{O}$
Mol Sieve 10Å	1×10^{-9}	$\text{Na}_2\text{O} \cdot \text{Al}_2\text{O}_3 \cdot 2.45\text{SiO}_2 \cdot 6.\text{OH}_2\text{O}$

Table 7 - Pore size and formulae for molecular sieves (Haixin, 2010).

An advantage of molecular sieves is that they can be fabricated from industrial wastes (Gao et al., 2005, Gao et al., 2006). Zeolite/carbon molecular sieve composites were synthesised using a combined process of calcination of coal fly ash and sawdust at 600–850 °C for $t = 1$ h under N_2 gas followed by a hydrothermal treatment in 2M NaOH aqueous solution at 120 °C for $t = 24$ h. All samples displayed ‘Type IV’ isotherms for N_2 and moisture adsorption (see: Section 2.4.2) however in the range where $30\% < RH < 80\%$ there is limited adsorption evident which can be indicative a ‘Type I’ isotherm (*i.e.* rapid adsorption in the micropore range with little or no uptake in the mesopore range). The composites displayed a slight increase in moisture uptake of $18 \cdot 10^{-3}$ g/cm³ over a step in RH from 60 – 65% when compared to commercial zeolites which the authors claim provides excellent humidity buffering capabilities. However, the RH step change is minimal and not

indicative of realistic conditions. Based on the adsorption isotherm presented it is evident that the EMC at $RH = 60\%$ is only about 10wt% and shows pronounced hysteresis suggesting that over repeated cycling of RH the sieves would prove ineffective. Molecular sieves have also found applications in the nuclear industry to remove fission ions from eutectic molten salt (Garcia and Bulbulian, 1991, Harjula and Lehto, 1986) and widely in adsorption refrigeration (Dieng and Wang, 2001).

2.6.3 Silica Gel

Silica Gels are manufactured by the process of condensing soluble silicates from solutions of water or other solvents and have the chemical composition $\text{SiO}_2 \cdot n\text{H}_2\text{O}$. An example of the range of silica gel performance can be seen in the ASHRAE handbook where the sorption isotherms and porous characteristics of three variants of silica gel were tested. Each of the gels presented had a different internal structure, but similar surface adsorption characteristics. It can be seen that there is a trade off between pore volume and surface area in that Gel 1 has large pores *i.e.* large volume but small specific surface area. In Figure 19, Gel 1 displays large EMC at $RH > 80\%$, but very poor uptake in the hygroscopic range. This is indicative of the larger pore size (see: Section 2.4.2) and lower SSA as presented in Table 8. Gel 8, on the other hand, has much smaller pore size and volume, but much larger surface area than Gel 1 and displays much better sorption capacity across the full range of RH , but with little capillary uptake.

Type	Pore Size (10^{-9} m)	Specific Surface Area (m^2/g)	Pore Volume (mm^3/g)
Gel # 1	21	315	1700
Gel # 5	3.8	575	490
Gel # 8	2.2	540	250

Table 8 - Physical properties of experimental silica gels (ASHRAE, 2009a).

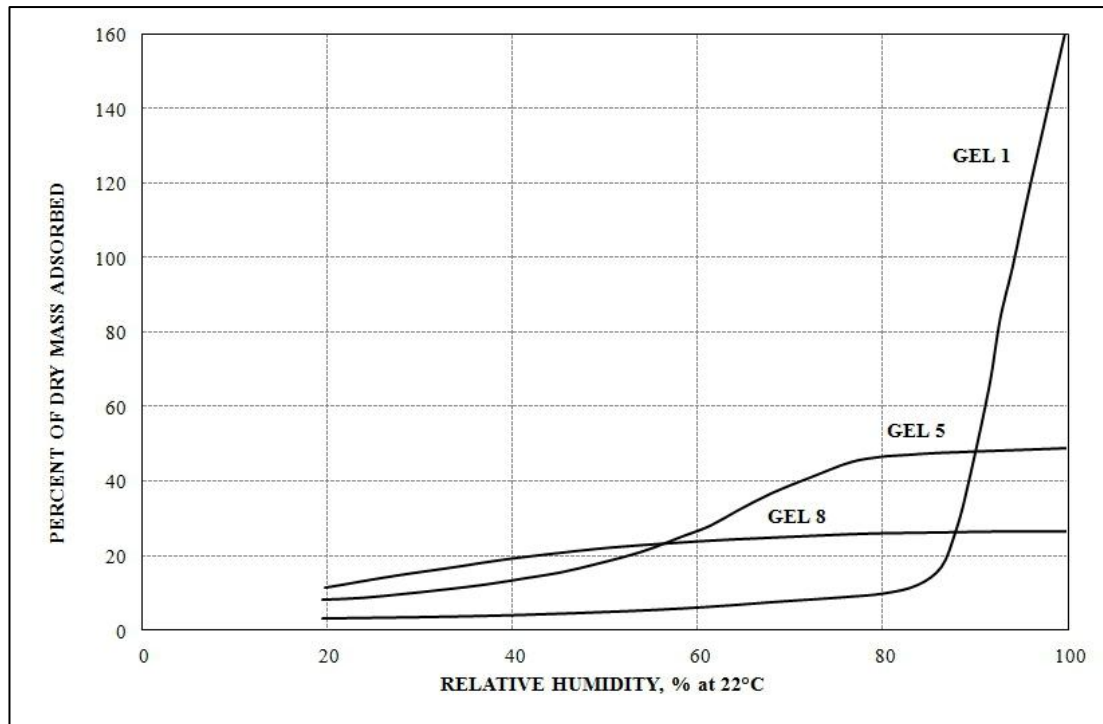


Figure 19 - Sorption isotherms for experimental silica gels (ASHRAE, 2009a).

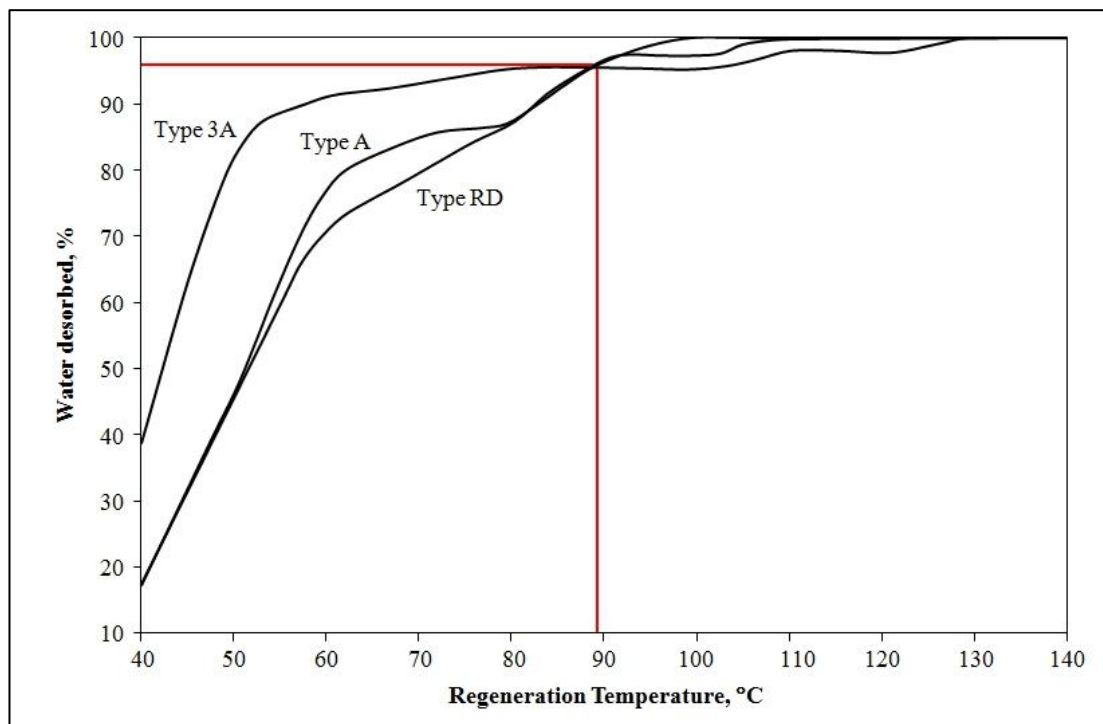


Figure 20 - Figure showing regeneration temperatures and desorption for three silica gels (Ng et al., 2001).

Two of the major problems with using commercially available silica gels as humidity buffering materials are that they have comparatively poor sorption capacity

in the hygroscopic range when compared to other sorbents and display large hysteresis requiring regeneration at elevated temperatures necessitating an independent heat source. Figure 20 shows the regeneration temperatures and amount desorbed for three silica gels (Ng et al., 2001) where, to achieve desorption levels of $\approx 95\%$ requires $T \approx 90\text{ }^{\circ}\text{C}$. In an effort to overcome this, silica gel composite materials have been developed that somewhat overcome the limited sorption capacity of silica gel, whilst reducing the regeneration temperature, but only under high airflow rates (Daou et al., 2006, La et al., 2010).

2.6.4 Mesoporous Silica

Mesoporous silica (MS) materials are highly porous silica solids with tightly controlled pore size distributions in the mesopore range (see: Section 2.4.2). Ordered MS materials were first developed during the 1990s with the well researched variants MCM-41 (Beck et al., 1992) and SBA-15 (Zhao et al., 1998) developed as larger pore size variants of molecular sieves. Mesoporous silica (MS) materials typically display very high porosity ($>90\%$) and SSA (typically $750\text{--}1500\text{ m}^2/\text{g}$) and have the significant advantage of being synthesized with a controllable pore geometry (shape, diameter) (Jana et al., 2004).

MS materials exhibit high moisture vapour EMC levels across the hygroscopic regions of their adsorption isotherms, but with pronounced hysteresis on desorption in the first isotherm cycle. This reduces in subsequent cycles due to the highly ordered narrow pore size distributions and irreversible initial adsorption (Inagaki et al., 1996, Inagaki and Fukushima, 1998). This can be indicative of a slight decrease of pore size due to chemisorption of the water molecules over the initial sorption cycles. They also show rapid t_{emc} response to amplitude variations of RH .

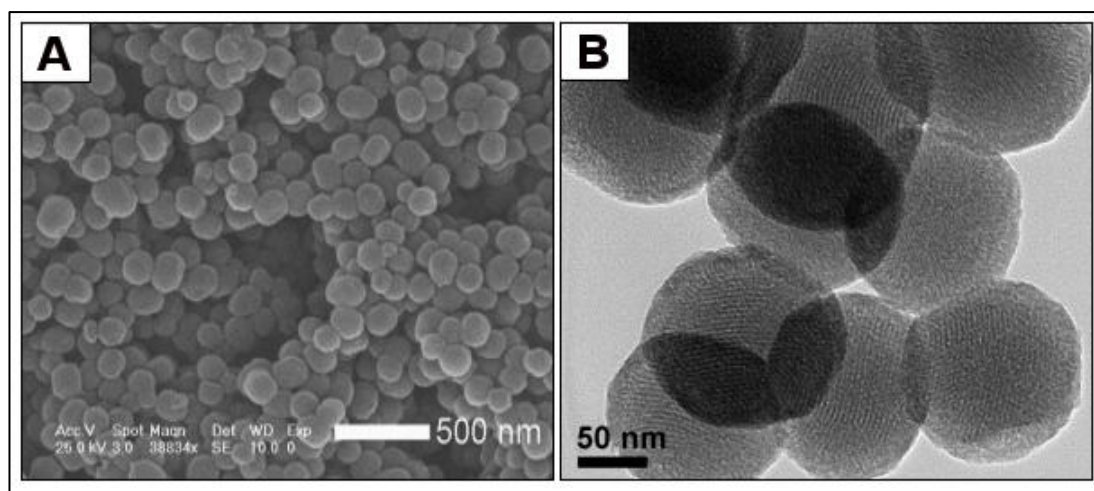


Figure 21 - SEM and TEM images of mesoporous silica MCM-41 (Yang et al., 2008).

Virtually all early research for MS application is focused in the biomedical field of drug delivery with reviews by Tang et al., 2012 and Li et al., 2012 presenting detailed discussions. A study by Ohashi et al., 1999 discussed MS synthesized using fumed silica as the base material for humidity control applications. The authors present a rigorous experimental analysis of pore geometry and moisture sorption characteristics. Two of the four MS materials that were investigated are shown in Figure 21 with a summary of all materials properties in Table 9.

	Specific surface area (m ² /g)	Total pore volume (ml/g)	Average pore diameter (nm)
Mesostructured Silica-10	965	0.54	2.14
Mesostructured Silica-12	1233	0.62	2.36
Mesostructured Silica-14	1137	0.65	2.70
Mesostructured Silica-16	1344	1.10	3.20

Table 9 - Characteristic data for microstructured silica (Ohashi et al., 1999).

The moisture vapour sorption analysis showed very high EMC for all materials with microstructured silica-16 peaking at >80% at $RH \approx 95\%$. The response within the hygroscopic range is excellent for all materials however, as reported by Inagaki previously there is a decline in EMC over repeated cycling. As before, hysteresis is also reduced after the initial cycle (see: Figure 22). Ohashi et al., 1999 suggests that

the material be used for humidity control in buildings, however no further studies regarding this could be found.

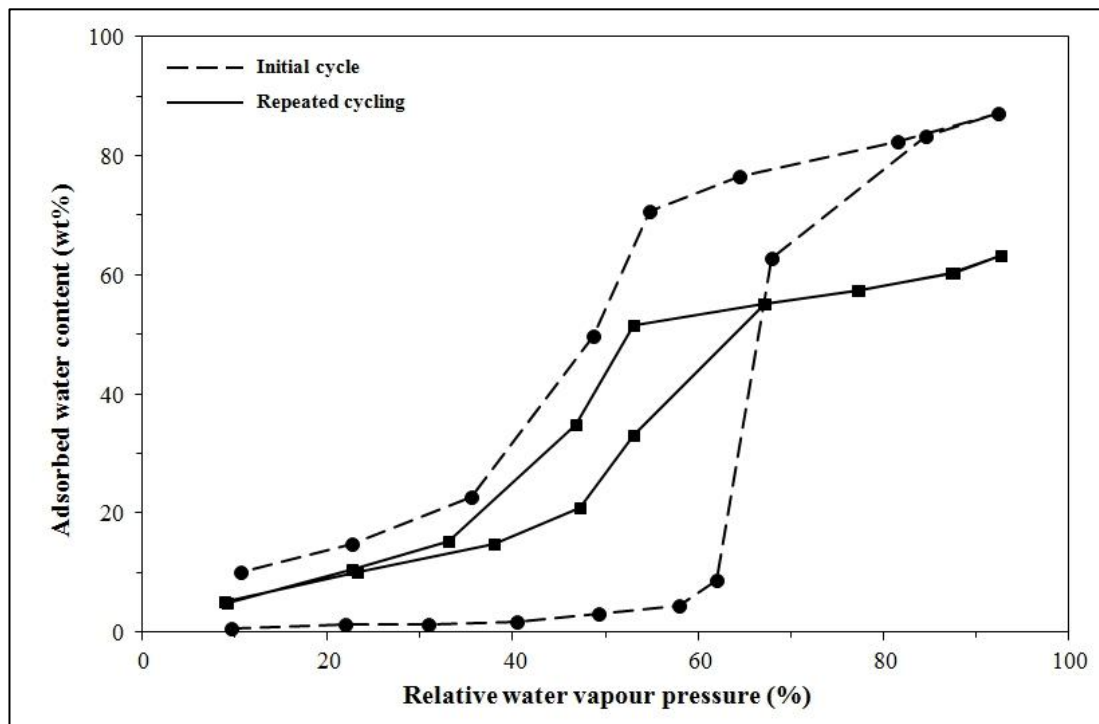


Figure 22 - Water vapour sorption isotherms for microstructured silica. Adapted from: (Ohashi et al., 1999).

2.7 Materials for Thermal Regulation

As this thesis is not primarily concerned with the insulative properties of the environmental envelope, the thermal class of materials is disregarded here however, a brief review is provided to form some context for the discussion in Chapter 6.

The range of thermal materials is split into two distinct areas in building physics *i.e.* those that reduce the conduction of heat through an envelope (Insulative) and those that allow conduction coupled with high heat capacity in order to cyclically store and release heat using the ‘thermal mass’ concept, see (Kalogirou et al., 2002, Ogoli, 2003, Paksoy, 2007). Insulative materials are designed to minimise heat transfer through the building envelope. There is a large range of insulations available

commercially with a comprehensive review of types and utilisation presented in Hall 2010. In general, insulation materials have low λ and δ with a large operational temperature range whilst complying with building codes and regulations.

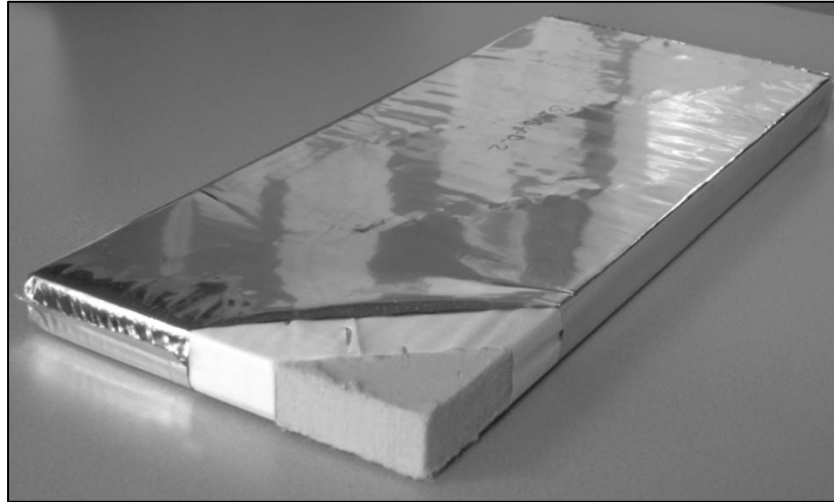


Figure 23 - Photograph of a vacuum insulation panel (Tenpierik and Cauberg, 2006).

Vacuum insulation panels (VIPs) are used as ‘super-insulators’ in the numerical modelling section (see: Section 3.5) of this thesis. Under ideal conditions VIPs can demonstrate very low λ values at reduced material depths (typically 10-40 mm) when compared to other insulation products. A typical VIP panel (see: Figure 23) is constructed from highly porous internal boards, e.g. fumed silica contained within an impermeable foil barrier that has been vacuum evacuated. Penetration of the panels foil layer results in a dramatic reduction in thermal performance and thus VIPs require specialist installation, handling and maintenance (Tenpierik and Cauberg, 2006, Baetens et al., 2009). VIPs are also prone to thermal bridging between the panels (Wang et al., 2007, Fricke et al., 2008) although this can be reduced using multi-layer metallised polymer films as a barrier (Simmler and Brunner, 2005).

2.8 Hygrothermal Investigations

On an increasing scale, hygrothermal research can generally be classified into one of

four categories:

1. Investigations at the material level (*i.e.* characterisation of the hygrothermal properties and pore geometry)
2. Experimental investigations using scaled physical models (*i.e.* laboratory representations of ‘ideal’ conditions)
3. Full scale field testing (*i.e.* monitoring of psychrometric conditions and material behaviour *in situ*)
4. Numerical investigations using transient heat and moisture (HAM) models.

A complete research approach is ideally based across the full scale of material behaviour however, due to time, financial and access limitations this is not always possible. As concluded in Roels et al., 2010 if numerical modelling is to be used to predict future performance, then this must be backed up with a minimum of proper material level investigation to ensure accurate input parameters and to achieve a good level of validation for the numerical model. Without this minimum, there can be little confidence in the numerical results.

2.8.1 Material Level

A range of experimental investigations in the field at a material level have already been presented in Section 2.6. Hall and Allinson presented a thorough analysis of the hygrothermal functional properties and moisture-content-dependent parameters of SRE materials (Hall and Allinson, 2009a, Hall and Allinson, 2009b, Hall and Allinson, 2008). Investigations of the pore geometry (SSA, pore volume and pore size distribution) of materials were presented including sepiolite (Caturla et al., 1999), bentonite (D’Orazio and Quagliarini, 2009), kaolinite (Maeda and Ishida, 2009a), zeolites (Gao et al., 2006, Zalba et al., 2009), silica gel (Ng et al., 2001) and

mesoporous silica (Beck et al., 1992, Inagaki et al., 1996, Jana et al., 2004, Zhao et al., 1998). A study of montmorillonite-quartz mixtures (Villar and Rivas, 1994) used the same techniques as those above to characterise pore geometry:

- N₂ or benzene physisorption to characterise micro and mesopore geometry with:
 - BET theory applied to determine SSA
 - BJH theory applied to determine pore size distribution
 - Pore volume calculated at $p/p_o \rightarrow 1.0$
- Small angle x-ray scattering (SAXRS) and transmission electron microscopy (TEM) to corroborate mesopore size

Moisture vapour dynamic properties have been investigated by many of the same authors listed above (among others) using techniques including:

- Determination of the sorption/ desorption isotherms and ΔRH cycling using:
 - Sealed desiccator jars containing various saturated salt solutions to control partial vapour pressure (*i.e.* RH). (Caturla et al., 1999, D'Orazio and Quagliarini, 2009, Hall and Allinson, 2009a, Ramos et al., 2010, Roels et al., 2010)
 - Specialised dynamic vapour sorption (DVS) equipment (Gao et al., 2005, Inagaki et al., 1996, Ng et al., 2001, Ohashi et al., 1999)
 - Climatic chambers (Cerolini et al., 2009, Delgado et al., 2006, Kalamees and Vinha, 2003, Peuhkuri et al., 2008, Ramos et al., 2010)
- Determination of material vapour permeability using wet/ dry cup tests (Collet et al., 2011, Desta et al., 2011, Roels et al., 2010, Hall and Allinson, 2009a)

- Determination of material water absorption using partial immersion tests (Hall and Allinson, 2009a, Ramos et al., 2010, Koronthalyova, 2011)

From the review of the literature of material level characterisation methods and the theory presented, characterisation techniques were selected for this research with details of the experimental design provided in Sections 3.2 and 3.3.

2.8.2 Physical Models

As reported by Pavlik and Cerny, 2008 semi-scale experiments or physical models can be a logical bridge between full-scale hygrothermal (field) tests and material level experimentation. The same rigorous nature employed at material level in the laboratory is applied to the model which would not be present in a full scale test. Physical models employed for hygrothermal testing can be used to determine the resultant psychrometric conditions observed when utilising hygrothermal materials in a controlled environment (under defined boundary conditions) and are usually undertaken on a comparative basis against other materials or an ‘empty’ scenario. Psychrometric data gathered can then be analysed or used for validation of numerical simulations under the same conditions, allowing predictive modelling to be undertaken. Physical models can vary significantly depending on the nature of the research (*i.e.* material type, parameters to be measured etc.) and consequently require individual case by case experimental design.

In a study of the hygrothermal performance of insulation systems (Pavlík and Cerný, 2008), the authors used a two part climate chamber with the sample wall (450 mm brick/argillite and 70-80 mm mineral wool insulation) being tested placed between the two chambers to simulate exterior and interior conditions. As this study was concerned with changes to material properties, moisture content, relative humidity,

temperature and heat flux within the sample wall were measured. In a similar study (Van Belleghem et al., 2011), the authors constructed a custom built room-sized chamber consisting of inner and outer chambers with an air handling unit. Measurement of T and RH was carried out at various depths within the sample to provide validation data for a 1D numerical heat and moisture (HAM) model. T and RH levels in the inner chamber were monitored when extra hygrothermal 'plates' were introduced to provide a validation data set for a 3D (CFD based) numerical model.

Kalamees and Vinha, 2003 presented a study of heat and moisture transfer within three wall types using a large chamber contained within a freezer unit to simulate Nordic conditions (*i.e.* warm interior and cold exterior). As in the previous investigations, the data for interior T and RH from the physical model was used for validation of numerical HAM models (1D-HAM, MATCH, and WUFI 2D).

A range of investigations using physical models have been undertaken to assess the moisture diffusivity, D_w Moisture Buffer Value (MBV) and Effective Moisture Penetration Depth (EMPD) of many hygrothermal materials. A small climate chamber was used by Ramos et al, 2010 to analyse the MBV of gypsum with four different finish coatings (acrylic and vinyl). Moisture uptake for the sample boards was monitored using a balance over a stepped RH cycle. The MBV of lightweight timber materials was determined using a custom built 8 m³ climate chamber balanced on load cells to measure moisture levels by (Meissner et al., 2010). Whilst there is data presented for the MBV of the samples, it is not clear what materials the timber samples were, allowing no comparison to be undertaken.

A custom built physical model has been presented to test the MBV of spruce plywood similar to the previous study (Osanyintola and Simonson, 2006,

Osanyintola et al., 2006). The authors used desiccator jars and a transient moisture transfer model to investigate the differences in data for MBV obtained with both natural and forced air convection. The data was then used to validate a numerical model to facilitate further investigations of the effect of initial conditions, boundary conditions and sample thickness on the MBV.

Based on this review of physical modelling methods and the theory presented, a physical model was designed for this research with details of the experimental design provided in Section 3.4.

2.8.3 Full Scale Testing

Whilst physical models can range from small scale MBV tests (Rode and Grau, 2008) up to large scale single-room tests (Yoshino et al., 2009, Kunzel et al., 2004) and full house tests (Plathner and Woloszyn, 2002, Salonvaara et al., 2004), it is usually not possible to recreate a complete set of climate conditions or random interaction of occupants and other unknown variables with the model. Alongside ‘*in situ*’ material investigations, full scale or field tests can also be used to analyse occupant acceptance of their environment in terms of comfort and air quality (see: Section 2.3). The majority of the past research into thermal comfort and Indoor air quality (IAQ) in buildings has been undertaken with a view to air conditioning technologies (*i.e.* HVAC) however, the impact of using hygrothermal materials to provide thermal comfort by controlling temperature and humidity has gained ground in recent years.

An investigation of 46 newly built houses with differing wall materials was conducted to determine the effect of both permeable and hygroscopic lightweight structures on thermal comfort in a cold climates (Kurnitski et al., 2007). The results

presented show that the use of hygroscopic materials significantly reduced peak indoor *RH* levels (up to 12%) and thus improved perceived thermal comfort. Similar studies were performed on 25 office buildings in A Coruna, Spain (Orosa and Baaliña, 2009, Orosa and Oliveira, 2009). The use of hygrothermal and permeable materials on the interior side of the wall reduced the percentage of people dissatisfied (PPD) with the thermal environment (reduction in PPD of 15%), significantly in the first few hours, but less so during the trailing hours of occupation.

A long term study was carried out on 170 detached houses to determine the real moisture buffering levels of varying surface finishes used in building envelopes (Kalamees et al., 2009). The authors propose that in cold climates, low outdoor humidity levels, when combined with overheating inside the house, reduce *RH* and IAQ to levels leading to numerous health symptoms. The authors conclude that air infiltration had a greater effect on *RH* levels and IAQ than hygroscopic materials in the envelope and that the current material and physical model methods may not reflect realistic scenarios.

Other research looking into the possibility of improving thermal comfort by utilising hygrothermal materials also consequently research improvement of IAQ. Some of these have already been discussed, such as Simonson et al., 2002 who showed that the PPD with IAQ in all climates can be reduced by 25% in the morning when permeable and hygroscopic structures are applied to the indoor environment. Kurnitski et al., 2007 also found that permeable and hygroscopic structures improved PAQ in the summer season, to an extent where the ventilation rate for a non-hygroscopic environment of 6 l/s/person could be reduced to 4 l/s/person in a hygroscopic environment. Again, Orosa and Baaliña, 2009 and Orosa and Oliveira,

2009 also studied the PAQ alongside the thermal comfort in office buildings and found that there was a comparable improvement in PAQ through the use of hygrothermal materials. Whilst it would be advantageous to use the full range of physical investigation techniques, due to monetary and time limitations, full scale investigations were excluded from this research whilst material level investigations and physical models were included.

2.8.4 Numerical Investigations

Ingress of moisture into the building envelope can affect thermal comfort, IAQ, structural preservation and operational energy efficiency and therefore full understanding and prediction of the behaviour of this moisture can lead to improvements in occupants comfort, energy savings and reduced aging/deterioration of the building fabric. This can be accurately informed by the use of hygrothermal numerical models. A hygrothermal model will take account of heat and moisture storage, latent heat effects, and liquid and convective transport under transient boundary and initial conditions.

The development and significance of building physics modelling has been growing for many years, however, until recently was considered only from the perspective of heat transfer – ignoring any simultaneous mass transfer within the envelope. Two widely accepted models are the ‘Glaser model’ (BSi, 2002a) and the ‘cyclic-response admittance method’ (BSi, 2007b), although numerous other models also exist including the Heat Balance Method (ASHRAE, 2009a) and other computer based models e.g. EnergyPlus (USDE, 2007), TAS (EDSL, 2010) among others (Hall et al., 2012a). Over the past few years there has been a push towards transient heat and moisture (HAM) models. Some of those that have been developed can be seen in

Table 10.

Model	Developer	Published use
1D HAM	Chalmers University, Sweden & MIT, Cambridge, United States	(Kalamees and Vinha, 2003)
BSim	Building Research Institute, Denmark	(Rode et al., 2004)
Clim2000	EDF, France	(Woloszyn et al., 2009)
DELPHIN	Bauklimatik, Dresden University	(Nofal et al., 2001)
HAM-BE	Concordia University, Canada	(Li et al., 2009)
HAM-FitPlus	British Columbia IT, Canada	(Yoshino et al., 2009)
HAM-Tools	IBPT, Sweden & Denmark	(Woloszyn et al., 2009)
IDA-ICE	EQUA, Sweden	(Woloszyn et al., 2009)
LATENITE-VTT	VTT, Finland	(Simonson et al., 2002) (Salonvaara et al., 2004)
MATCH	Technical University of Denmark	(Kalamees and Vinha, 2003)
MATLAB	Mathworks Inc., United States	(van Schijndel, 2008)
MOISTURE-EXPERT	Oak Ridge National Laboratory	(Karagiozis, 2001)
TRANSYS (v16)	University of Wisconsin, United States	(Woloszyn et al., 2009)
WUFI Group (Plus, Pro & 2D)	IBP Fraunhofer, Germany	(Allinson and Hall, 2010) (Charoenvai et al., 2005) (Hall and Allinson, 2010) (Holm and Künzelt, 2002) (Kalamees and Vinha, 2003) (Künzelt and Kiessl, 1996) (Künzelt et al., 2005)
SIMULINK	Mathworks Inc., United States	(van Schijndel, 2008)

Table 10 - Source and application of existing hygrothermal numerical models in published literature (Hall et al., 2012a).

All transient HAM or ‘hygrothermal’ numerical models must include transport and storage phenomena as set out in BS EN 15026: 2007 (BSi, 2007a):

- heat storage in dry building materials and any absorbed water
- heat transport by moisture-dependent thermal conduction
- latent heat transfer by vapour diffusion
- moisture storage by vapour sorption and capillary forces
- moisture transport by vapour diffusion

- moisture transport by liquid transport (surface diffusion and capillary flow)

Numerical models also require inputs such as exterior climate, envelope construction, orientation and initial conditions (see: Figure 24). The WUFI group of hygrothermal models require material properties as outlined in Section 1.2 and use the following differential equations for heat and moisture balances:

$$\frac{dw}{d\varphi} \cdot \frac{\partial \varphi}{\partial t} = \nabla \cdot (D_w \nabla \varphi + \delta_p \nabla (\varphi \cdot p_{sat})) \quad \text{Eq 2.25}$$

$$\frac{dH}{dT} \cdot \frac{\partial T}{\partial t} = \nabla \cdot (\lambda \nabla T) + h_v \nabla \cdot (\delta_p \nabla (\varphi \cdot p_{sat})) \quad \text{Eq 2.26}$$

The left hand side of each equation denotes the storage with enthalpy, H in Eq. 2.26 combining the heat capacity of both the dry material and enthalpy of any absorbed moisture, whilst in Eq. 2.25 the moisture storage is represented by w . The right hand sides of the equations represent the transport functions. In Eq. 2.25, liquid conductivity, D_w is governed by the relative humidity, φ with vapour flow (strongly temperature dependent) governed by the vapour pressure ($\varphi \cdot P_{sat}$) (see: Section 2.4.3.1). In Eq. 2.26 sensible heat flow is governed by the thermal conductivity, λ whilst latent heat is governed by the vapour enthalpy flow, h_v from the absorption and release of latent heat due to moisture vapour evaporation/condensation.

When the model has been executed and convergence reached, the outputs may be categorized into temperature field and heat flux distributions and moisture fields, RH levels and moisture flux distributions with their evolution over the calculation period. WUFI provides output results as numerical data which allows for further input/analysis with the use of statistical or data analysis software, or data can be displayed graphically using the inbuilt analysis tools as a time-dependent simulation of the fluxes and distribution through a building envelope cross section over time

(Hall et al., 2012a). Whilst WUFI Pro v5 performs analysis of a 1D ‘slice’ of a wall envelope whereas WUFI Plus v2.1.1.73 combines the analysis of all walls, floors, ceilings and other envelope components to perform 3D whole building analysis, both use the same governing equations for transient HAM transport and storage. WUFI Plus also provides data on occupant comfort, operational energy in addition to predictive data on the hygrothermal performance of each envelope assembly.

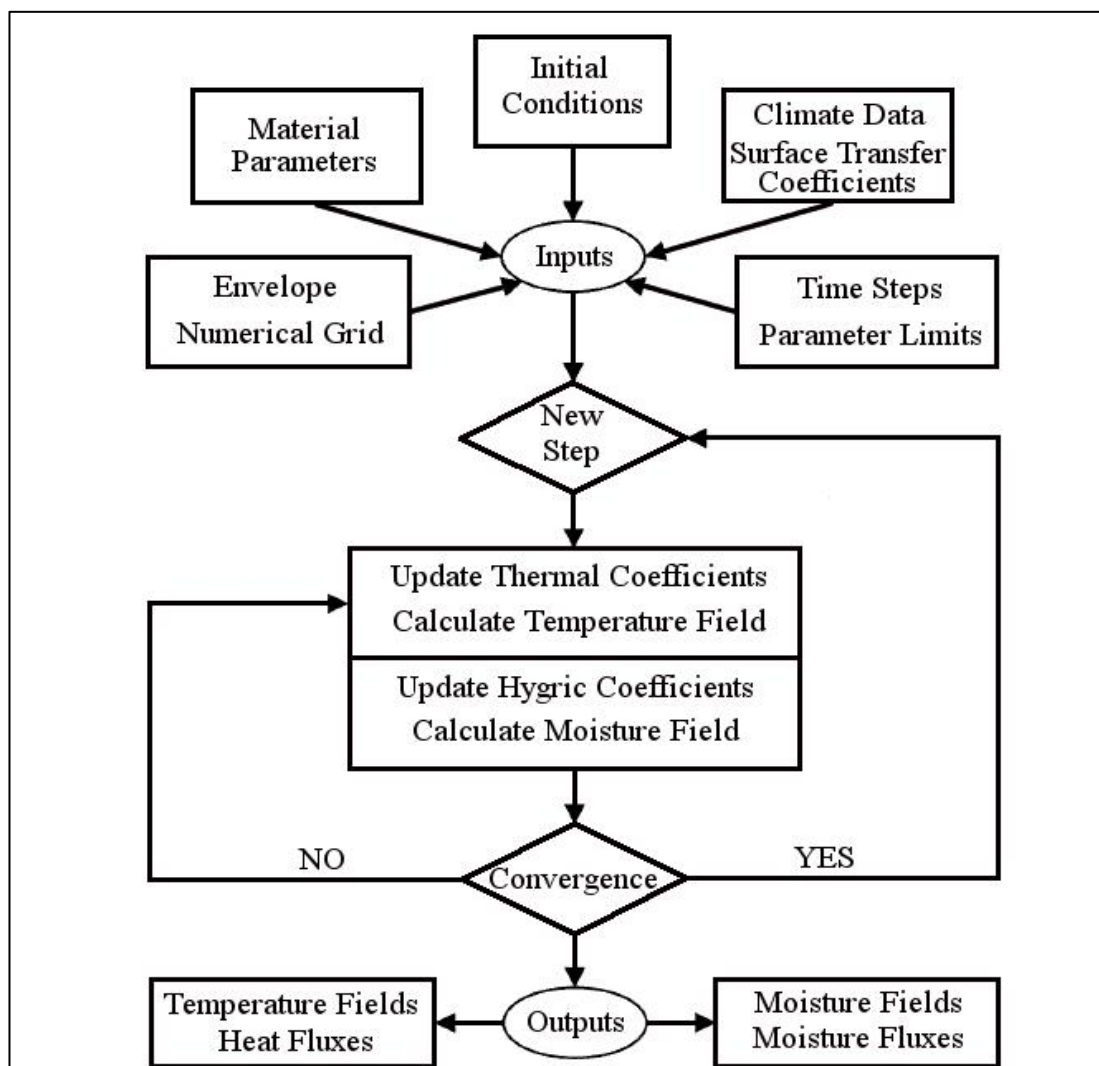


Figure 24 - Flowchart of inputs, calculation technique and outputs for the WUFI group of programs. Adapted from: (Künzel, 1995).

The WUFI group of hygrothermal models have been validated against experimental data and field work in many studies. The 1D version of the software, WUFI Pro has been used for validation of SRE material behaviour by Hall & Allinson, 2010, drying

of an Autoclaved Aerated Concrete (AAC) roof by Holm and Künzle, 2002 and natural stone facades by Künzle and Kiessl, 1996. WUFI 2-D was validated against experimental results for performances of three different wall fabrics with different insulation and vapour barriers by Kalamees and Vinha, 2003. The predicted indoor RH and T simulated by WUFI Plus (3D version) were validated at the Fraunhofer Institute (IBP) using two identical rooms, one lined with aluminium and the other with lime-gypsum plaster with internal moisture loads (Künzel et al., 2003). WUFI Plus has been validated against field results for an unoccupied SRE test room that was monitored for 10 months by Allinson and Hall, 2010. Künzle et al., 2005 validated the model against the humidity buffering performance of wood lined rooms. Testing was performed in custom built-test rooms at the IBP Fraunhofer facility in Germany.

Based on the availability, simple graphical user interface and extensive, peer reviewed validation record both WUFI Pro v5 and WUFI Plus v2.1.1.73 were selected to fulfill objectives 3 and 4 and 5 for this research (see: Section 1.4).

2.9 Summary

This chapter has outlined the underlying theory associated with heat and moisture transfer and storage in the context of building physics. Psychrometrics and occupant comfort have been described to provide background knowledge to the research. A range of materials have been reviewed that display favourable hygrothermal properties for humidity buffering applications. Based on the moisture transfer and storage theory outlined in Section 2.4, Mesoporous Silica was selected as the prime candidate material for this research due to the ability to synthesise the material with fine-tuned pore size distribution, allowing for investigation of the links between

behaviour and pore geometry. Four MS samples with different pore diameters were synthesised by colleagues at the University of Oxford as part of a collaboration with four other desiccants selected for comparative analysis:

- MS 3.3 nm
- MS 4.7 nm
- MMS 4.8 nm
- MS 8.3 nm
- Clinoptilolite (Natural zeolite)
- Molecular Sieves (Synthetic Zeolite) 10 Å
- Silica Gel
- Bentonite (Clay)

From the review of the literature, experimental techniques were selected to accurately characterise the hygrothermal properties and pore networks of the candidate materials (see: Chapter 3). Physical models to determine the hygrothermal behaviour and resultant interior psychrometric conditions within closed environments and validate the numerical models were designed. The numerical models WUFI Pro and WUFI Plus were selected to analyse the predictive hygrothermal behaviour, energetic analysis and resultant internal psychrometric conditions using the candidate materials.

CHAPTER 3: Methodology

3.1 Introduction

This chapter introduces the experimental and numerical techniques that were selected based on the literature review to meet the objectives outlined in Chapter 1. Detailed explanations of the relevant fundamental theory supporting each technique are referenced. A process flow chart (see: Figure 25) shows a summary of the research methodology adopted to meet the objectives as set out in Section 1.4.

The research methodology consisted of three distinct stages;

Stage 1. Material characterisation – The hygrothermal functional properties and the pore network of the materials were characterised and links between material behaviour and pore structure investigated.

Stage 2. 1D Modelling – Physical and validated numerical models were designed to parametrically analyse material behaviour based on the hygrothermal properties from Stage 1. A range of ΔRH_{ie} amplitudes were simulated to provide sensitivity analysis of material behaviour and a comparative study of the desiccant material performance to traditional materials under representative climate conditions and building envelopes. Analysis was carried out to determine the applicability of using the numerical model as a material selection tool by ‘tuning’ material properties and linking with the porous characteristics from Stage 1.

Stage 3. 3D Modelling - Physical and validated numerical models were designed to parametrically analyse changes to internal climate conditions and occupant comfort resulting from the presence of the hygrothermal materials

under representative moisture generation schedules. The analysis was expanded by altering envelope assemblies, materials, occupancy levels and air infiltration to the interior environment. Energetic modelling was also conducted to determine potential energy savings.

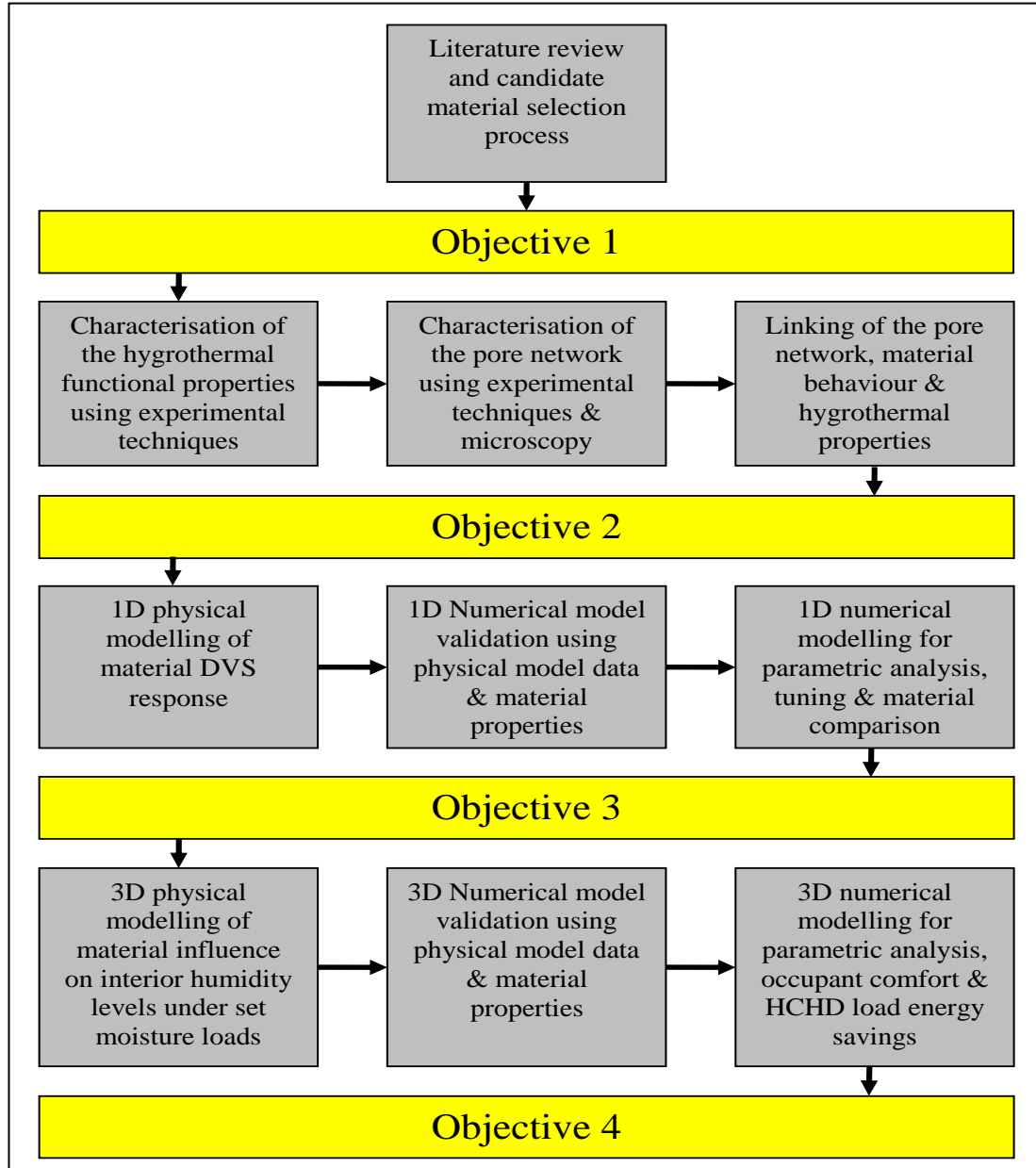


Figure 25 – Process flow chart outlining the research approach.

3.1.1 Mesoporous Silica Synthesis

As stated in Section 2.9, four mesoporous silica (MS) samples with different pore

diameters were synthesised by Prof. Edman Tsang at the Wolfson Catalysis Centre, Department of Chemistry, University of Oxford as part of a collaboration. The description of MS synthesis provided here is taken from Hall et al., 2012b. All chemicals used for MS synthesis were as supplied:

1. tetraethyl orthosilicate (TEOS) $\geq 98.0\%$ supplied by Sigma–Aldrich–Fluka,
2. hexadecyltrimethylammonium bromide (CTAB) supplied by Sigma–Aldrich
3. trimethyl benzene (TMB) $\geq 99.0\%$ supplied by Sigma–Aldrich
4. sodium hydroxide (NaOH) $\geq 99.0\%$ supplied by BDH/ Analar
5. methanol (CH_3OH) $\geq 99.0\%$ supplied by Fisher Scientific

Changing the length of the surface directing agents and introducing organic auxiliary chemicals are both effective techniques in controlling the pore diameter of MS during synthesis. For MS synthesis in this research alkyltrimethylammonium ($\text{C}_n\text{H}_{2n+1}(\text{CH}_3)_3\text{N}^+$, $n = 16$ and $(\text{C}_n\text{H}_{2n+1}(\text{C}_2\text{H}_5)_3\text{N}^+$, $n = 12, 16$) with a large head group surfactant was used to tune the pore size. If a surfactant with a larger head group and greater number of carbon chains was used, it was observed that this produced an MS material with a greater pore diameter. In solution, cationic surfactants arrange themselves such that the cationic heads point outwards and the anionic hydrophobic chains point inwards to minimize their water contact and maximize the inter-organic chemical interactions. This results in micelles and predominantly coulombic interactions between the charged head groups. The final product is then determined by the micellar shape or packing of the surfactant (*i.e.* surfactant control).

Generally, MS with a worm-like pore network was produced by firstly mixing the quaternary ammonium surfactant in water with NaOH, resulting in a clear solution. After a period ($t = 30$ min) of stirring, 0.03 g TEOS was added producing a white

solution, indicating hydrolysis of the TEOS. Next, 0.0218 g of CTAB was dissolved in a mixture of 35 ml of water and 0.02 g of NaOH in a round bottom flask with constant stirring at 700 rpm at $T = 30\text{ }^{\circ}\text{C}$, whilst maintaining the pH of the resulting solution between 9 and 12. The mixture was then continually stirred at $T = 23\text{ }^{\circ}\text{C}$ for a period $t = 4\text{ h}$ to allow the sol–gel reaction to continue to completion, followed by vacuum exposure at $T = 65\text{ }^{\circ}\text{C}$ to remove the ethanol formed during hydrolysis. Gelation was accomplished by keeping the flask open at $T = 60\text{ }^{\circ}\text{C}$ for $t = 48\text{ h}$.

After gelation was complete, the solid product was recovered and dried at $T = 23\text{ }^{\circ}\text{C}$ before being calcined at $T = 550\text{ }^{\circ}\text{C}$ for $t = 6\text{ h}$. Silica with larger pore diameters was obtained by introducing 0.0483g of TMB, which is hydrophobic and enters the micelle, causing expansion and increased pore size of the resulting MS material. In the case of mono-dispersed MMS, 0.88 g of CTAB and 2.28 ml of 1M NaOH was dissolved in a 400g mixture of methanol/water (50:50) with constant stirring at $T = 25\text{ }^{\circ}\text{C}$. After $t = 30\text{ min}$, 1.231 g of TEOS was added turning the solution white. The reaction was allowed to continue for $t = 6\text{ h}$ and then aged overnight. The product obtained ($\approx 1\text{ g}$) was then filtered, washed with distilled water and dried at $T = 50\text{ }^{\circ}\text{C}$ for $t = 24\text{ h}$, followed by heating at $T = 550\text{ }^{\circ}\text{C}$ to remove the surfactant.

3.2 Characterisation of the Pore Network and Microstructure

Table 11 contains a summary of the techniques used to characterise the candidate materials microstructure and pore network. Due to the small quantities ($< 1\text{ g}$ for some materials) and powder form, some of the standardised test methods were modified. All the techniques are explained in detail in the following sections starting with characterisation of the bulk properties followed by the macro and meso scale

properties.

Property	Characterisation Technique
Bulk density, ρ_{bulk}	Gravimetric Method
Solid density, ρ_s	Gas Pycnometry
Mesopore volume, V_m	N ₂ Physisorption
Mean pore diameter, ϕ_m	N ₂ Physisorption (BJH), SAXRS, TEM
Specific surface area, SSA	N ₂ Physisorption (BET model)

Table 11 - Summary of the pore network characterisation techniques.

3.2.1 Porosity and Density

3.2.1.1 Gas Pycnometry

Gas pycnometry is a gas displacement technique used to calculate the solid volume V_s of a porous material. If the mass of the sample is known, then calculation of the solid density ρ_s is possible. It must be noted that the ρ_s accounts for only ‘open’ pores that are accessible to the gas, ‘closed’ pores are not accounted for.

Samples were first prepared by vacuum desiccation for a period $t > 24$ h to ensure all moisture and volatiles were removed from the pores *i.e.* $w = w_0$. A Micrometrics Accupyc 1330 gas pycnometer with helium as the inert gas was used to determine ρ_s in accordance with BS ISO 21687 (BSi, 2007c). Five test runs were carried out for each of the eight candidate materials allowing a mean value of ρ_s to be calculated. In addition, both granular and powder forms of each material were tested.

A sample of known mass (*i.e.* $m_s \approx 1$ g), but unknown solid volume, V_s was placed into a sample cell of known volume, V_c which was then sealed (see: Figure 26). The pressure of the sample cell was recorded as P_s . The reference cell of known volume V_r was pressurised and recorded as P_r . An isolating valve was then opened, allowing the two cells to equilibrate at a pressure, P_q . The sample volume, V_x was then

calculated using Eq. 3.1:

$$V_s = \frac{(P_q \cdot V_c + P_q \cdot V_r - P_s \cdot V_s - P_r \cdot V_r)}{P_q - P_s} \quad \text{Eq 3.1}$$

Solid density was then calculated using Eq. 3.2;

$$\rho_s = \frac{m_s}{V_s} \quad \text{Eq 3.2}$$

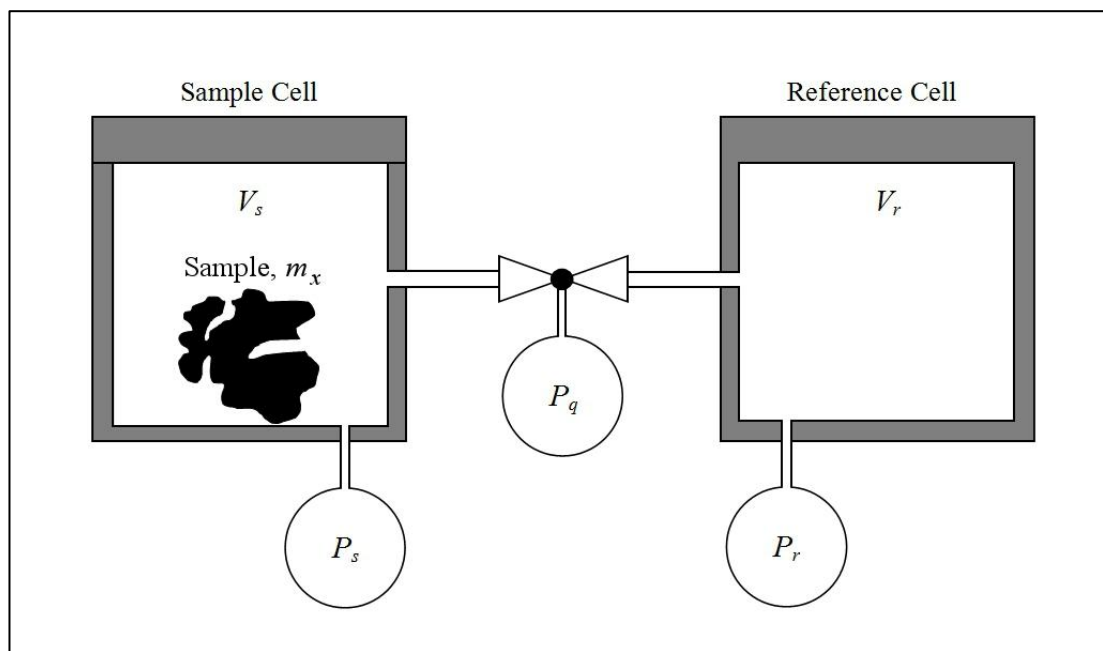


Figure 26 - Schematic diagram of Gas Pycnometry technique.

3.2.1.2 Gravimetric Testing

Bulk density ρ_{bulk} can be considered as the mass per unit volume of a solid, including all void spaces in a 'bulk' sample of a material. This has been illustrated in Figure 27. Uncompacted bulk density ρ_{bulk} was determined using the gravimetric measurement method in accordance with BS 1097-3 (BSi, 1998).

Measurement of ρ_{bulk} was carried out using an identical graduated cylinder to the experimental setup used for liquid water absorption (see: Figure 39). The cylinder was *tared* on the balance and the loose powder sample carefully emptied into it. Care

was taken to leave the cylinder undisturbed as any disturbance would cause the sample to compact, producing a ‘tapped’ density measurement. The volume V_{bulk} and mass m were recorded and ρ_{bulk} calculated. Each test was repeated 3 times for each candidate material allowing the mean value of ρ_{bulk} to be calculated. Due to the minimal quantities of sample available ($m_s \approx 1$ g), accuracy in both volume and mass measurements were essential. To achieve this, an air-shielded VIBRA HT Series tuning fork analytical balance (VIBRA, 2011), accurate to ± 0.1 mg was used for mass measurement.

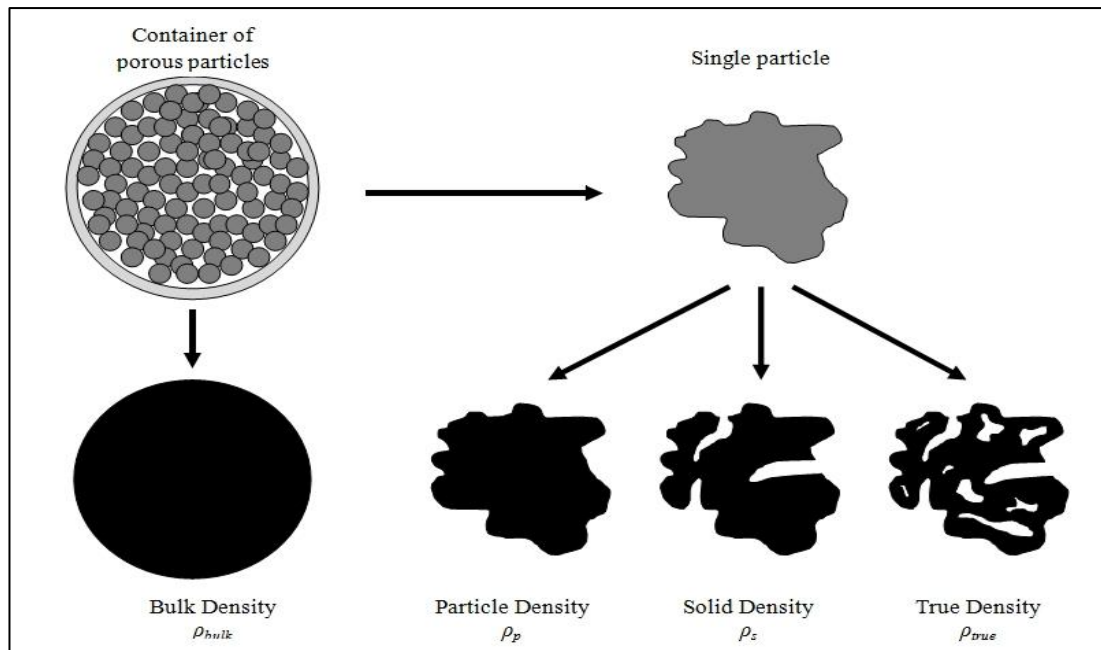


Figure 27 - Classification of density types for porous particles. Adapted from: (Webb, 2001)

3.2.2 The Macropore Network

Scanning electron microscopy (SEM) was used to characterise the materials surface morphology, confirm the silica elemental composition and also to indicate macropore distribution.

3.2.2.1 Scanning Electron Microscopy

SEM is a technique that allows high resolution, high depth-of-field magnified images of objects. Figure 28 provides a schematic diagram of a typical SEM. The microscope consists of an electron column (1), which uses an electron gun (2) at the top to create a stable electron beam (3). The diverged beam is accelerated down the column, through a series of magnetic lenses, apertures and deflector coils to focus it (4, 5, 6). The beam then interacts with the prepared sample surface (7) in the sample chamber (8). Different detectors can be used to monitor the beam-sample interaction phenomena, such as generation of secondary electrons (SE) (9) and back-scattered electrons (BS) (10). All detection is usually conducted under high vacuum (11) conditions to remove contaminating air borne particles. The signal detected is then output as a digital image to a connected computer (12).

There is a ‘interaction volume’ where the beam electrons interact with the sample (see: Figure 29). When the primary beam enters the sample and interacts with another electron it can change its trajectory or ‘scatter’. Secondary electrons having low energy ≤ 50 eV, are generated within the near surface of the reaction volume through collisions with the sample electrons. Topographical contrast is achieved due to many interrelated factors including:

- Local absorption
- The number and trajectories of back scattered BS versus the number of SE electrons
- The angle of incidence between the beam and the sample surface (*i.e.* larger reaction volume surface area)
- The inclination of the specimen

- The placement and type of detector used

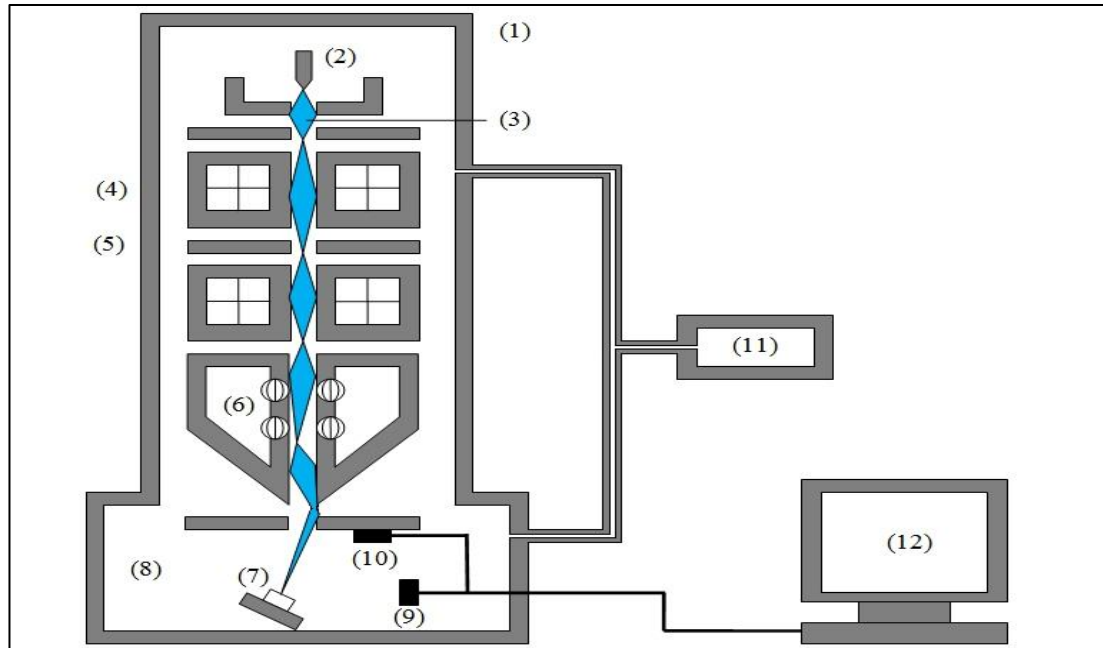


Figure 28 - Schematic diagram of a scanning electron microscope where (1) electron column, (2) electron gun, (3) electron beam, (4) lenses, (5) apertures, (6) deflector coils, (7) sample, (8) sample chamber, (9, 10) SE and BSE detectors, (11) vacuum unit and (12) computer.

SE micrographs are primarily used to study sample topography where peaks appear bright and valleys dark. SE micrographs provide very close similarity to that of a visual image. Back scatter electrons (BSE) are the original beam electrons that escape back out of the sample and thus have greater energy, typically from 50 eV up to the accelerating voltage. They interact with a slightly greater volume of the sample which reduces image resolution (see: Figure 29). Image contrast is formed by the point to point differences in the locally averaged atomic number of the sample with higher atomic number nuclei scattering greater numbers of electrons back in the direction of incident electrons *i.e.* a brighter image. BSE images are primarily used to investigate composition of samples, displaying the different relative atomic densities of the sample as lighter or darker regions in the micrograph.

Energy dispersive characteristic X-Rays are emitted when the primary beam

dislodges a photoelectron from specific orbits of an atom in the specimen. An electron from an outer orbiting shell moves into this core vacancy, and emits energy in the form of an X-ray photon. As the X-rays generated have a wavelength and energy characteristic of the elemental atom (atomic number) from which they originate, elemental information can be obtained about the sample. The relationship between atomic number and energy for a given X-ray is given by Moseley's Law (Khare and Swarup, 2010):

$$\sqrt{E} = C_1(Z - C_2) \quad \text{Eq 3.3}$$

Where E is the energy of the emission line for a given X-ray series (*e.g.* $K\alpha$, $K\beta$, $L\alpha$, $M\alpha$, *etc.*), Z is the atomic number and C_1 , C_2 are constants.

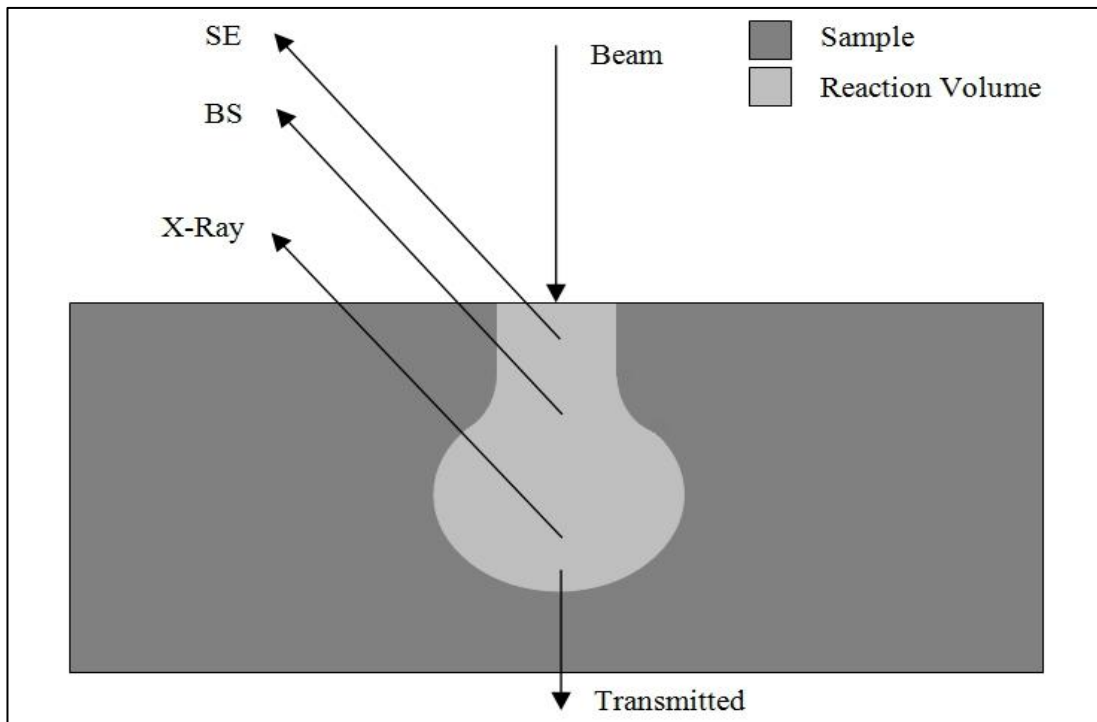


Figure 29 - Schematic representation of the sample/ beam interaction for an SEM.

SEM analysis was conducted using a Philips XL30 Environmental scanning electron microscope with a field emission gun equipped with an Oxford Instruments Inca model spectrometer for energy dispersive X-ray (EDS) analysis. Elemental mapping

was performed using EDX spectral analysis, which can achieve 133 eV resolution of the Mn K_{α} peak at full width half maximum (see: Figure 30). Samples were prepared by vacuum desiccation for $t = 24$ h to remove any residual moisture and volatiles from the pores. Approximately 5 mg of dried powder was deposited onto an adhesive carbon tab fastened to an aluminium stub. Any surplus material was removed using a compressed air jet. A Pt sputter coating was then applied to the powder at a rate of ~ 7 nm/min for a period $t = 90$ s. SEM micrographs were recorded using an Everhart–Thornley type secondary electron detector and a backscattered electron detector (supplied by K.E. Developments). SEM was conducted on the four MS materials only.

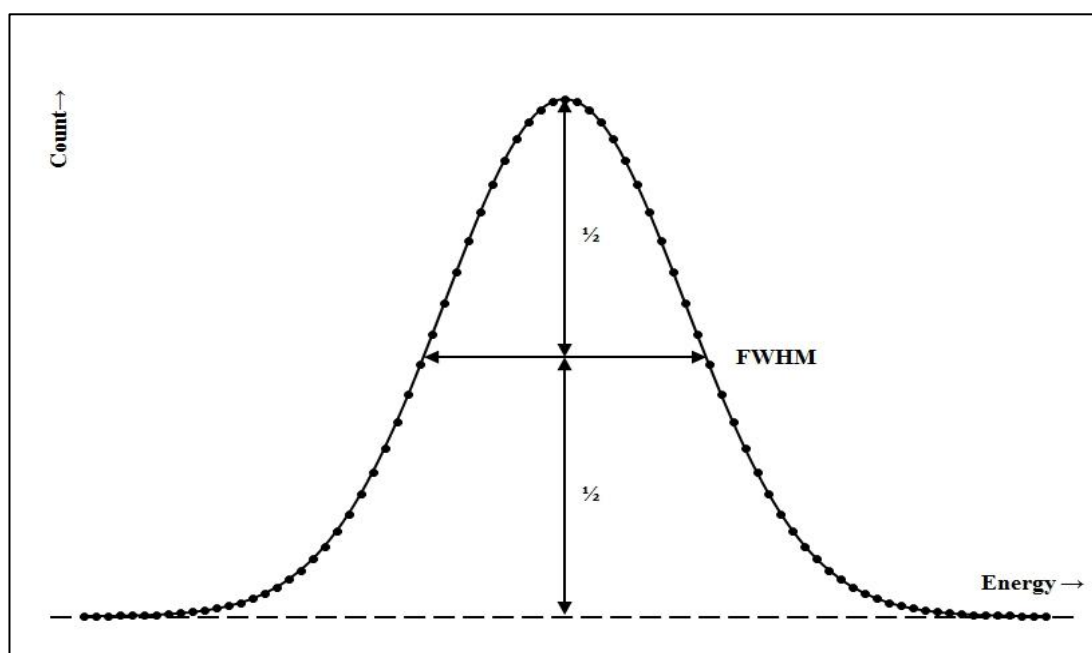


Figure 30 - Graphical representation of 'full width half maximum' for EDS.

3.2.3 The Mesopore Network

Linking the pore geometry and the hygrothermal behaviour of materials is part of the aim for this research therefore, it was important that the pore geometry be characterised as accurately as possible. To achieve this, the approach was to use

multiple techniques to characterise the pore geometry of the materials using primarily N_2 physisorption to determine specific surface area, mean pore diameter and pore volume, with Small Angle X-ray Scattering (SAXRS) and Transmission Electron Microscopy (TEM) to corroborate the physisorption results.

3.2.3.1 N_2 Physisorption

Physisorption is the interaction of incompletely bound atoms on the surface of a solid with gas, vapour and liquids due to van der Waals forces. Analysis was performed on the MS materials by the Prof. Edman Tsang at the Wolfson Catalysis Centre, Department of Chemistry, University of Oxford using a Sorptomatic 1990 with CE Instruments analytical software with analysis of the four conventional materials (i.e. Silica Gel, Mol Sieves, Bentonite and Clinoptilolite) conducted at Nottingham using a Quantachrome Autosorb instrument in accordance with BS 4359-1. A schematic of the process can be seen in Figure 31

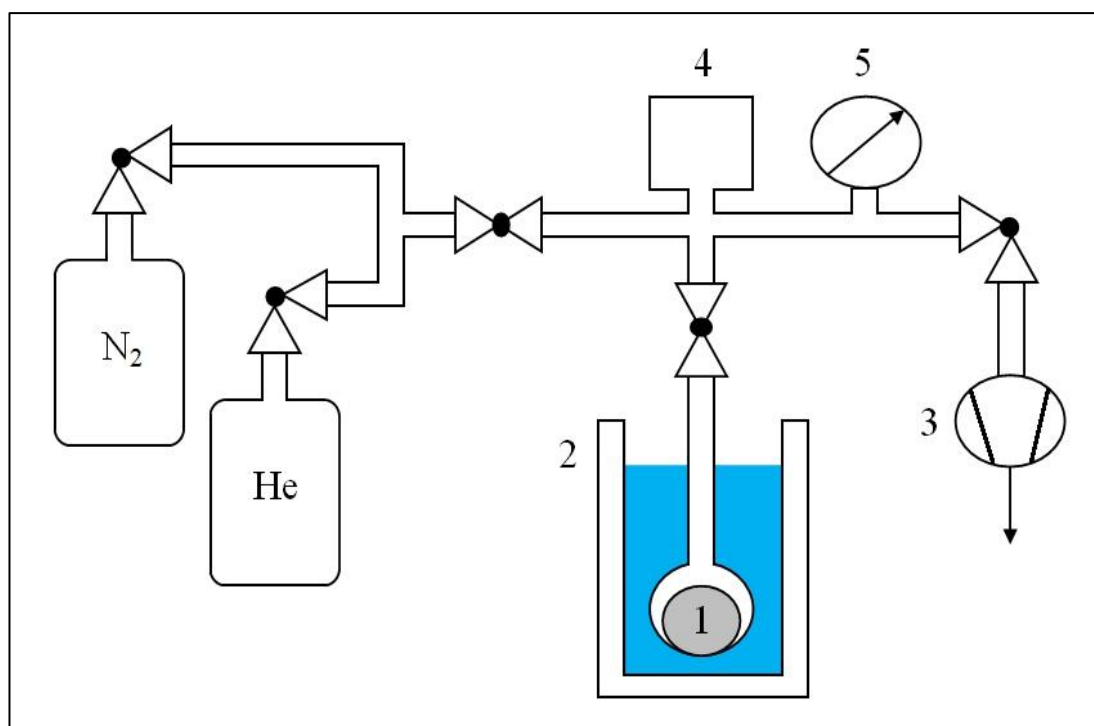


Figure 31 - Schematic of N_2 physisorption process where (1) sample, (2) Dewar vessel containing liquid Nitrogen, (3) vacuum generation pump, (4) calibrated

volume and (5) manometer. Adapted from: (BSi, 1996)

Samples of mass $m \approx 0.25$ g were initially vacuum desiccated for a period $t = 24$ h to achieve the condition $w = w_0$. They were then placed in a sample vial on the test rig and prepared by outgassing under elevated temperature $T \geq 120$ °C and vacuum conditions for a period of time $t = 6$ h to ensure the pores were adequately evacuated of moisture and volatiles prior to testing. The sample vial was then transferred to the testing station and immersed in liquid nitrogen at $T = -196$ °C. Using the volumetric measurement method, a dose of adsorptive gas (N_2) was admitted to the degassed solid under controlled temperature conditions at set increments of relative pressure (p/p_0) and allowed to equilibrate for a period $t = 2$ mins before the next dose was added automatically. A minimum of 25 increments each was used for the adsorption branch of the isotherm and the same procedure repeated with decreasing p/p_0 providing the desorption branch of the isotherm. The pressure at each increment was recorded and the amount of gas adsorbed calculated. When plotted, the resulting pressure against mass absorbed provided an N_2 sorption/ desorption isotherm (see: Section 2.4.2).

As discussed in Section 2.4.2, for materials with pores in the mesoporous range with a tightly controlled mean pore diameter, a type IV isotherm would be expected. Specific surface area, mesopore volume and pore size distribution can be calculated using different models applied to the isotherm generated. These are outlined in the following sections. Testing was conducted on all eight candidate materials with three test runs performed for each sample to ensure repeatability of the results.

3.2.3.1.1 Specific Surface Area

Specific Surface Area (SSA) is calculated volumetrically from the formation of a

single monolayer of adsorptive. It is derived using the Brunauer, Emmett and Teller (BET) model applied to the adsorption isotherm, in the pressure range $p/p_0 \approx 0.05 \rightarrow 0.3$ as indicated by (A) in Figure 6. The SSA (m^2/g) can be calculated from:

$$SSA = n_m \cdot a_m \cdot L_A \quad \text{Eq 3.4}$$

Where n_m is the specific monolayer capacity of adsorbate, a_m is the molecular cross-sectional area occupied by an adsorbed molecule in a complete monolayer (0.162 nm^2 for N_2 @ 77.2 K) and L_A is the Avogadro constant ($6,022 \times 10^{23} \text{ mol}^{-1}$).

3.2.3.1.2 Mesopore Volume and Mean Pore Diameter

As the relative pressure increases and monolayer formation completes ($p/p_0 > 0.3$) as indicated by (B) in Figure 6, multilayer formation and capillary condensation begin. Condensation occurs in the smallest diameter pores first and continues until saturation of all pores is reached where the isotherm flattens out *i.e.* no more gas can be adsorbed. The adsorptive gas pressure is then reduced in increments allowing evaporation of adsorbate from the pores to occur. Typically, there will be hysteresis evident between the adsorption and desorption branches of the isotherm as discussed in Section 2.4.2.

The Barrett Joyner Halenda (BJH) model was used to calculate mesopore size distribution and mean pore diameter ϕ_m . The BJH model (see: Eq. 3.5) is a modified Kelvin equation and is typically applied to the multi-molecular region of the desorption branch of the N_2 isotherm in the pressure range $p/p_0 \approx 0.2 \rightarrow 0.99$.

$$d = \frac{2 \cdot \gamma \cdot V_L}{R \cdot T \cdot \ln\left(\frac{p}{p_0}\right)} + 2t \quad \text{Eq 3.5}$$

Where γ is the surface tension, and V_L is the molar liquid volume. Certain

assumptions are used for the BJH model including:

- Pore shape is cylindrical
- Pores do not intersect each other
- Menisci are hemispherical with zero contact angle

Mesopore volume was calculated from the volume of adsorbate at saturation pressure $p/p_0 \approx 0.99$, which assumes complete saturation of the sample.

3.2.3.2 Small Angle X-Ray Scattering

X-ray diffraction (XRD) is a technique where the spatial distribution and intensity of x-rays scattered from shell electrons provide information on the arrangement of atoms within a sample. The X-rays used in XRD are a form of energetic electromagnetic radiation of comparable size to the spacing of atoms within a solid (wavelength $\approx 10^{-10} \rightarrow 10^{-11}$ m). Depending on the Bravais lattice of the crystal in the solid and the X-ray wavelength, constructive interference (*i.e.* in phase) of the scattered wavelets occurs in set directions. The positions of the resultant maxima in scattering intensity can then be used to determine the plane spacings within the crystal structure of the solid (Koughia et al., 2006). The Bragg equation (Eq. 3.6) is used to describe the scattering angles corresponding to these maxima:

$$n\lambda = 2d \sin\theta \quad \text{Eq 3.6}$$

Where d is the plane spacing, λ is the X-ray wavelength and θ is the angle of diffraction (see: Figure 32).

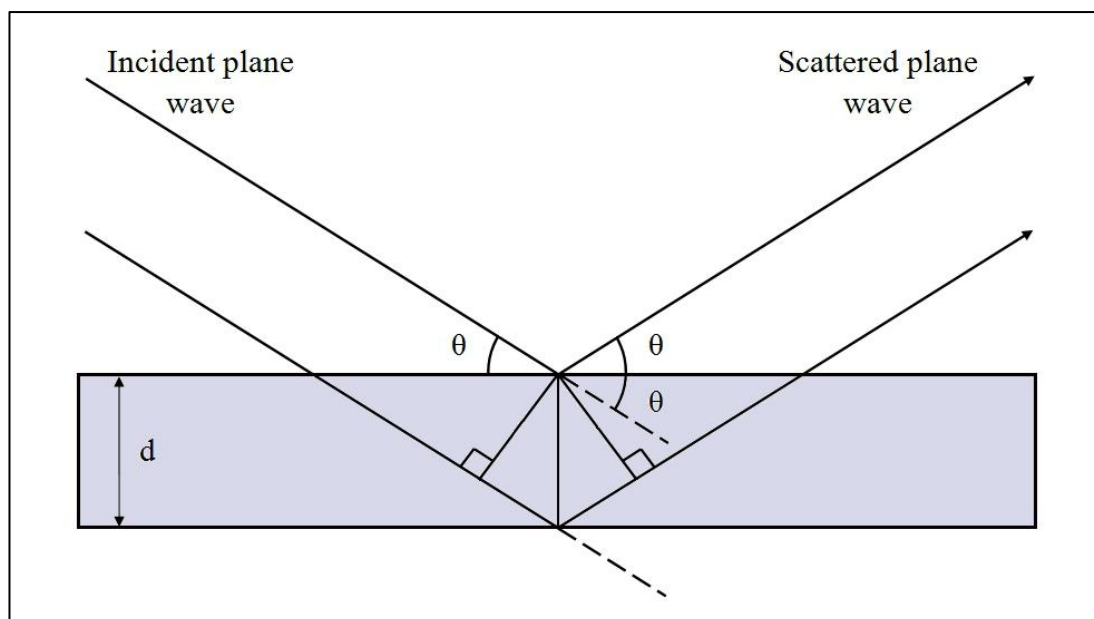


Figure 32 - Graphical representation of Bragg diffraction. Adapted from (Koughia et al., 2006).

In an amorphous powder such as the MS materials used in this research there is no crystalline structure and thus no d -spacings. Lower 2θ ranges (typically $0.5^\circ \rightarrow 5^\circ$) where the incidence angle of the x-ray beam is close to the critical angle of total external reflection of a thin film, can be utilised to measure pores in the mesopore range by using the constructive interference from the pore walls through scattering as opposed to diffraction. This technique is called small-angle X-ray scattering (SAXRS).

SAXRS was carried out by Prof. Edman Tsang at the Wolfson Catalysis Centre, Department of Chemistry, University of Oxford as part of a collaboration. Patterns for each of the four MS samples were measured on a Phillips PW1729 diffractometer, operating in Bragg–Brentano focusing geometry and using Cu K_α radiation ($\lambda = 1.5418 \text{ \AA}$) from a generator operating at 40 kV and 30 mA. The diffractograms were recorded in a 2θ range from 0.6° to 5° , with a 2θ step size of 0.01 and a step time $t = 1 \text{ s}$. Due to availability limitations, a single run of tests could only be conducted on the four MS materials.

3.2.3.3 Transmission Electron Microscopy

Transmission electron microscopy (TEM) was utilised to help corroborate the N₂ physisorption and SAXRS results for mesopore size and distribution. TEM is a technique similar in basic principles to SEM, however images are formed from the transmission and/or diffraction of electrons through the sample, rather than near surface interaction and scattering. Samples are required to be very thin (typically ≤ 100 nm) to be electron transparent. Figure 33 provides a schematic diagram of a typical TEM. Like SEM an electron beam (1) is generated using an electron gun (2) at the top of the beam column (3). A series of condensing, objective and projection electromagnetic lenses (4) and apertures (5) are used to focus the beam.

Unlike SEM, the beam passes through the sample within the beam column. Depending on the density of the material present, a portion of the electrons in the beam are scattered at the sample stage (6) and others transmitted through the sample. Transmitted electrons collide at the bottom of the microscope with a fluorescent screen (7), and provide a shadow image of the sample. In bright field imaging, areas of the sample are displayed in varied darkness according to their density. The region surrounding the electron gun (2) is usually under high vacuum ($\approx 10^{-9}$ mbar) (8) conditions to remove contaminating air borne particles whilst less vacuum can be tolerated further down the column ($\approx 10^{-2}$ mbar). TEM images are then output as a photographic image to connected printer (9).

Images in TEM can be formed using directly transmitted or scattered electrons. Images formed using the transmitted beam are called bright field (BF) images whilst dark field (DF) images are formed by aligning a diffracted beam down the optic axis of the microscope. There are three modes of contrast formation (Almeida, 2010):

1. In amorphous samples, thicker regions of the sample and areas with a higher atomic number appear dark, due to mass-thickness contrast.
2. Low index crystalline orientations of crystalline samples that satisfy Bragg diffraction also appear dark, termed diffraction contrast.
3. If the objective aperture is removed, images with contrast arising from constructive and destructive interference of the electron waves, termed phase contrast, can reveal lattice with atomic resolution, known as HRTEM.

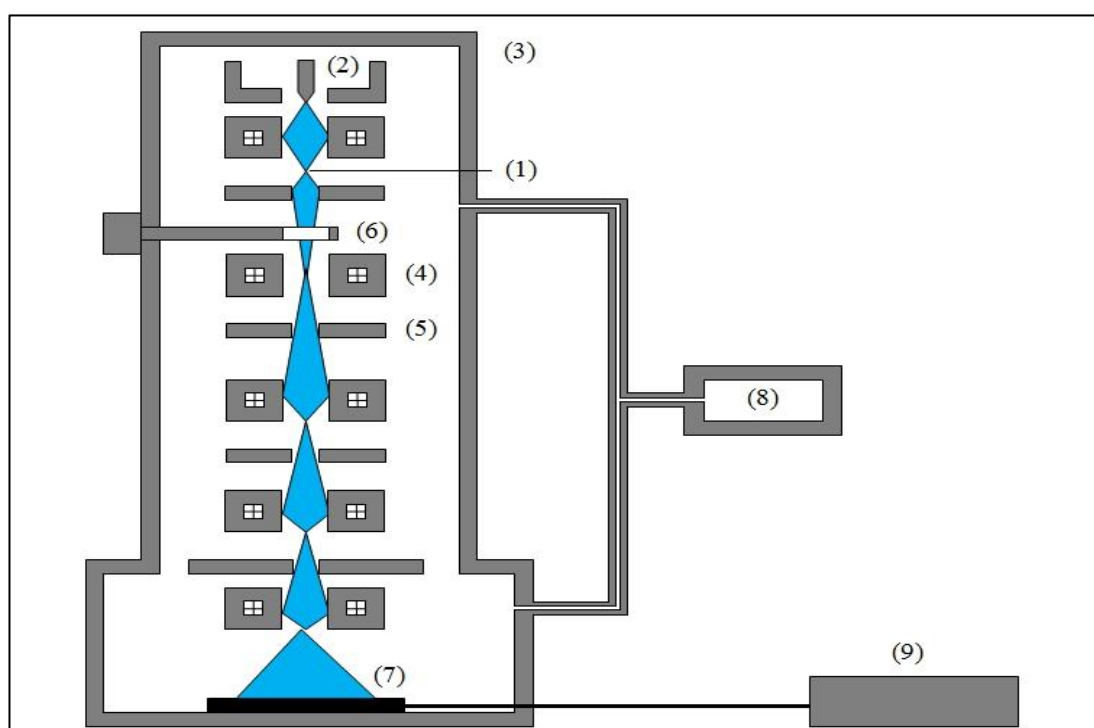


Figure 33 - Schematic diagram of a transmission electron microscope where (1) electron beam, (2) electron gun, (3) beam column, (4) condensing, objective and projection electromagnetic lenses (5) apertures, (6) sample stage, (7) fluorescent screen, (8) vacuum unit and (9) printer.

TEM analysis was conducted by the Prof. Edman Tsang at the Wolfson Catalysis Centre, Department of Chemistry, University of Oxford using a Jeol 2000FX transmission electron microscope operating at a 200 kV accelerating voltage. Samples were prepared by vacuum desiccation for $t = 24$ h to remove any residual moisture and volatiles from the pores. The powder was then dispersed as slurry using ethanol in a glass vial and sonicated for $t = 10$ min. The slurry was then deposited on

a perforated carbon film on a Cu grid and the ethanol allowed evaporate before testing commenced. Analysis was conducted on the four MS samples only.

3.3 Characterisation of Hygrothermal Functional Properties

As discussed in Section 1.2, it is the hygrothermal functional properties of a material that determine its hygrothermal behaviour. To establish a link between material behaviour under set psychrometric conditions and the material's pore network geometry, characterisation of the properties was necessary. The functional properties also form part of the input for hygrothermal numerical modelling (see: Section 2.8.4). The range of techniques that were used for characterisation is detailed in the following sections and a summary is shown in Table 12.

Property	Characterisation Technique
Thermal conductivity, λ	Modified Transient Plane Source (MTPS)
Specific heat capacity, c_p	Differential Scanning Calorimetry (DSC)
Moisture storage function, ζ	Dynamic Vapour Sorption (DVS)
Vapour permeability, W	Wet Cup Method
Liquid absorption, A_w	Partial Immersion Method

Table 12 - Summary of material properties and characterisation techniques.

3.3.1 Dynamic Vapour Sorption

Dynamic vapour sorption (DVS) was used as a technique to provide information on the moisture storage capacity *i.e.* equilibrium moisture content (EMC) and the rate of moisture uptake of the material *i.e.* the time taken to reach EMC (t_{emc}). For this research, two methods of measuring the moisture vapour isotherms were used.

3.3.1.1 Desiccators

A simple and cost effective method to determine the sorption isotherm of a material

was to use the desiccator jar method. Desiccator analysis was performed using a series of eleven ‘Kilner’ jars with compression sealed, airtight lids (see: Figure 34) in accordance with BS ISO 12571 (BSi, 2000b). Ten jars were used for sample testing whilst one control jar contained a Tinytag Ultra 2 sensor (Tinytag, 2012) which was used to monitor internal *RH*. Temperature and *RH* data were recorded at intervals $t = 30\text{s}$ and downloaded upon completion of the test using the SWCD-0040 Tinytag Explorer software. Low voltage, slow rotation circulation fans were attached to the underside of each lid to prevent stagnation of the air above the sample being tested.

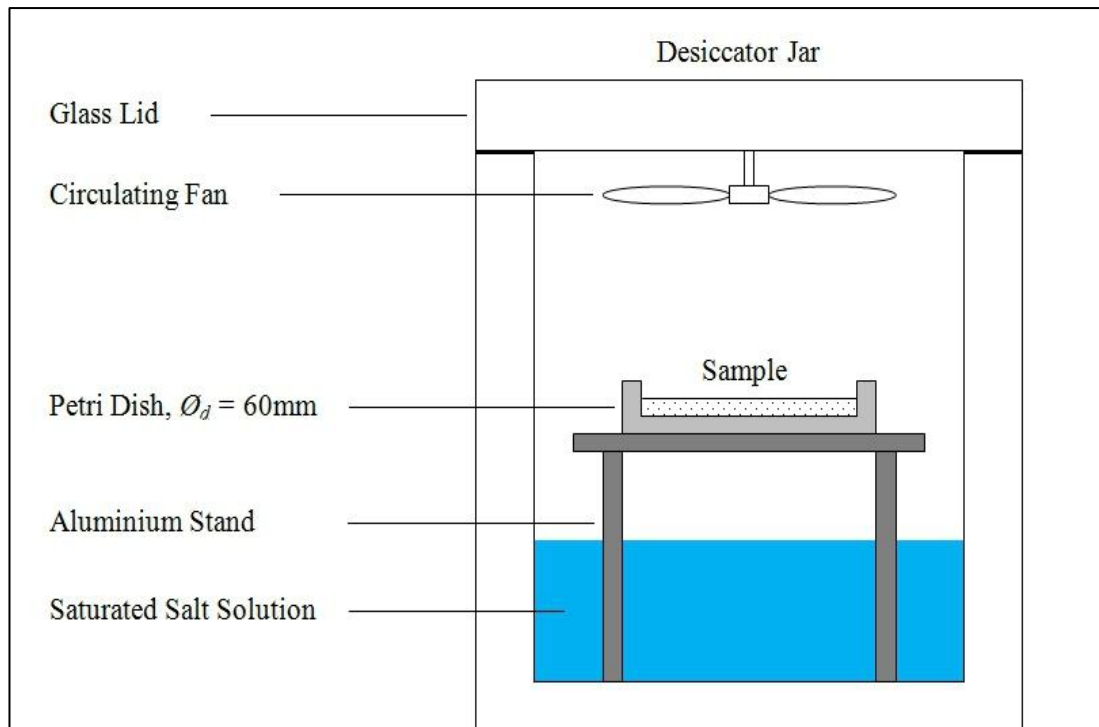


Figure 34 - Schematic of experimental setup using a desiccator jar for sorption/desorption moisture vapour isotherm tests.

Samples were first dried in an oven at $T = 105\text{ }^{\circ}\text{C}$ in accordance BS EN ISO 12570 (BSi, 2000a) for a period $t = 24\text{ h}$ to achieve the condition $w = w_0$. The dry samples were then placed in glass petri dishes of known mass, the sample mass recorded using the air-shielded VIBRA HT analytical balance and the dish with sample placed on a perforated aluminium stand above a saturated salt solution. Sample mass was

recorded at periodic time intervals of

$$t_1 = 0 \text{ h}, t_2 = 2 \text{ h}, t_3 = 6 \text{ h}, t_4 = 24 \text{ h}, t_5 = 48 \text{ h}, t_6 = 72 \text{ h}, \text{ etc.}$$

To perform the periodic mass recordings, it was necessary to remove the sample dish from the desiccator. Every effort was taken to minimise the time taken for mass recording, to ensure minimal disturbance to both sample mass and internal RH . To monitor RH , the control jar was opened for a similar period. EMC for a set internal RH was achieved when change in mass uptake was below 0.5% for a period $t = 24 \text{ h}$ *i.e.* $\Delta m < \pm 0.5\%$.

Testing was repeated using four saturated salt solutions (see: Table 13) to achieve a range of relative humidities at 23°C ($33\% < RH < 94\%$) and with deionised water to achieve the condition where $RH \rightarrow 100\%$ RH . EMCs for each material at each set point of RH were then collated and plotted as an adsorption isotherm.

Saturated Salt Solution	RH (%) at 23°C
Magnesium chloride	32.90 ± 0.17
Sodium bromide	58.20 ± 0.42
Sodium chloride	75.36 ± 0.13
Potassium nitrate	94.00 ± 0.60

Table 13 - Relative humidity above saturated salt solutions prepared in accordance with BS ISO 12571.

Desiccator tests were performed on the MS 3.3, MS 4.7, molecular sieve 10A, silica gel, bentonite and clinoptilolite materials. There were a range of disadvantages to using desiccator jars:

- Necessary human interaction in the experimental procedure
- Uncontrolled external environment (T & RH)
- Limited dynamic data collected *i.e.* rate of moisture uptake over the range of RH .

This undoubtedly led to inaccuracy in the resulting isotherms for the samples. To overcome this it was decided to use a climate chamber to repeat the isotherm experiments (see: Section 3.3.1.2).

3.3.1.2 Climate Chamber

Use of a climate chamber to determine a materials sorption isotherm would eliminate the need to intervene during the experiment and allow for complete control of the internal environment, with the balance placed within the chamber and dynamic mass data logged to a connected computer.

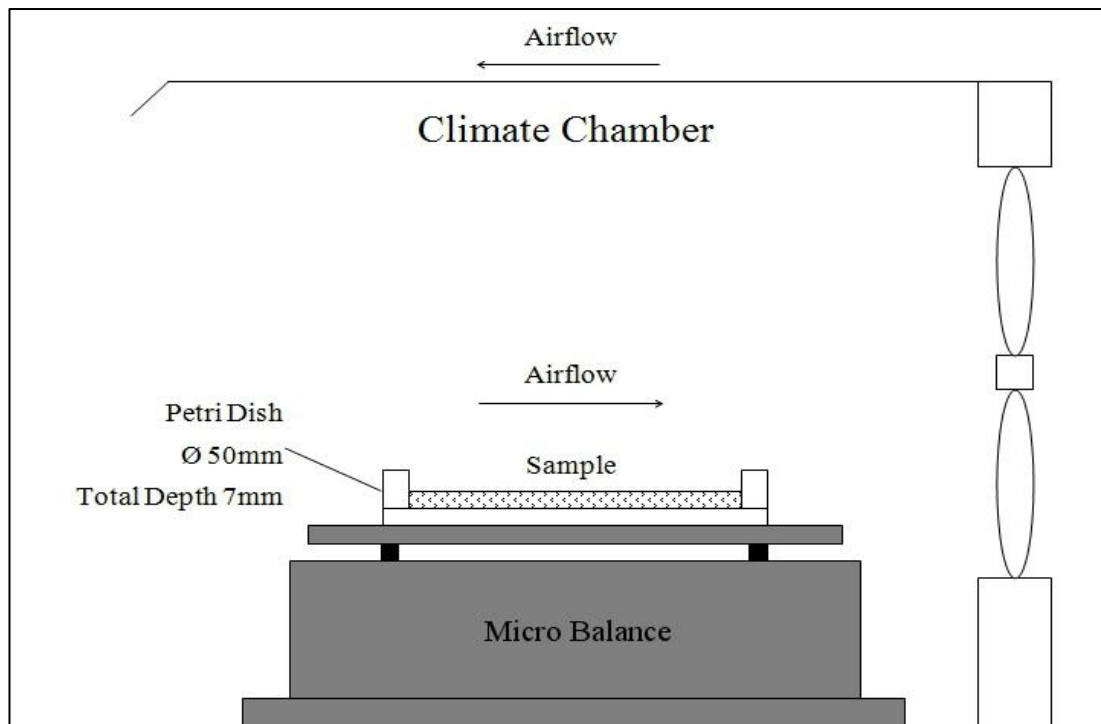


Figure 35 - Schematic of experimental setup using the climate chamber for sorption/desorption moisture vapour isotherm tests.

The sorption isotherms were again determined in accordance with BS EN ISO 12571. A Series 3 LTCL – 600 Climatic Chamber (TAS, 2008) manufactured by Temperature Applied Sciences Ltd., West Sussex, UK was used to independently control T_{db} and RH to an accuracy of ± 1 K and $\pm 3\%$, respectively (see: Figure 35). Climatic data from the chamber was logged using a Silver Series Plus HMI and the

data converted using the Easy - Converter software package.

The samples were first vacuum desiccated for a period $t > 24$ h prior to achieve $w = w_0$. The dry samples were then placed in a glass Petri dish on the balance. The depth of sample in the dish was $d \approx 2$ mm. The climatic chamber was programmed to increase RH in steps from $20\% \rightarrow 50\% \rightarrow 80\% \rightarrow 95\%$ successively. Mass change, Δm of the samples was recorded using the VIBRA HT balance via an RS232 connection to a PC using Eltima RS232 data logging software at intervals of $t = 30$ s. Isotherms for all eight candidate materials were generated with each test repeated to ensure integrity.

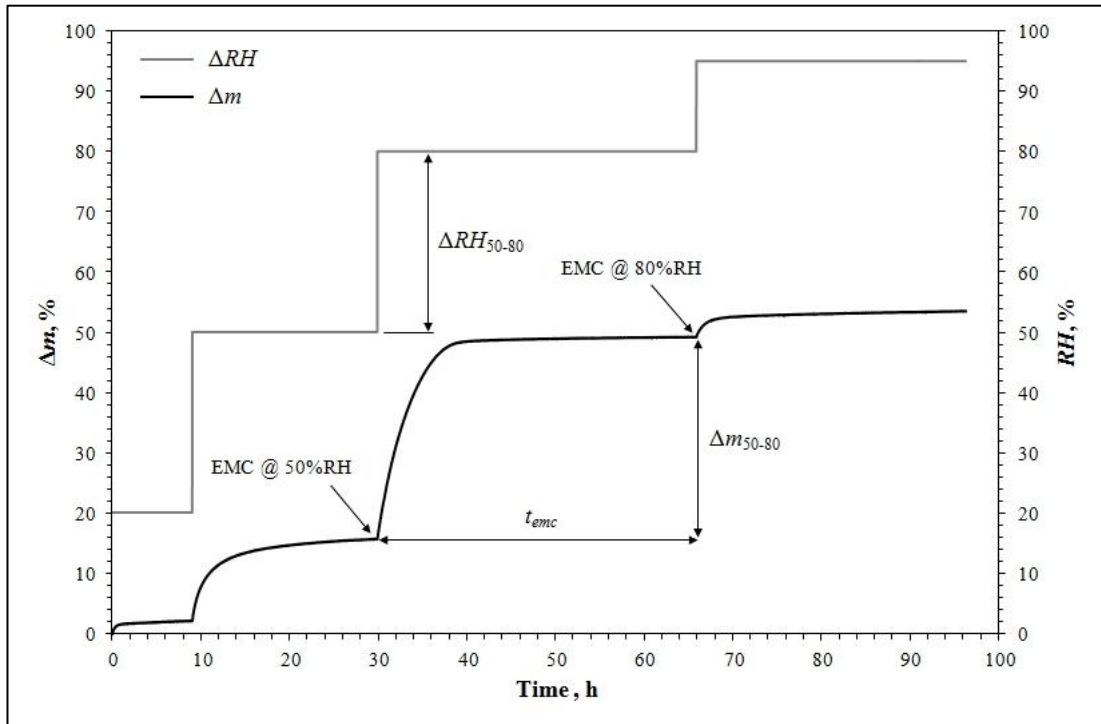


Figure 36 - Characteristic dynamic moisture uptake result graph showing change in mass against time.

As in the desiccator test, EMC was deemed to be reached when change in mass was below 0.5% for a period $t = 24$ h *i.e.* $\Delta m < \pm 0.5\%$. EMC data for $RH \rightarrow 100\%$ was reused from the previous desiccator tests. Data from the climate chamber DVS tests was used to provide sorption isotherms for the samples. Dynamic data for the rate of

moisture uptake (t_{emc}) was also obtained due to the continuous recording of mass change during the test (see: Figure 36).

3.3.2 Vapour Permeability

Vapour permeability, δ is the moisture transport that occurs within a material via Fickian diffusion due to a pressure gradient across the material (see: Section 2.4.3.1) and can be determined using either the wet cup or dry cup test. In a dry cup test (at constant T) the interior environment of the cup is maintained at $RH = 0 \pm 3\%$ using a desiccant (*i.e.* silica gel) and the exterior maintained at $RH = 50 \pm 3\%$ using the climate chamber, inducing a flow from exterior to interior. Dry cup tests provide information about material performance in the lower humidity range, where moisture transfer is dominated by vapour diffusion.

In a wet cup test (at constant T) the interior environment of the cup is maintained at $RH = 94 \pm 0.6\%$ using a saturated salt solution of potassium nitrate, KNO_3 (see: Table 13) and the exterior maintained at $RH = 50 \pm 3\%$, inducing a flow from interior to exterior. Wet cup tests provide information about material performance in the higher humidity range, where moisture transfer by vapour diffusion can be reduced due to increased capillary transport resulting from filling of the materials pores.

Vapour permeability for all samples was determined using a modified wet cup test (see: Figure 37) in accordance with BS EN ISO 12572 (BSi, 2001b). Samples of ~ 1 g were prepared by packing into an aluminium sealed sample holder with PTFE tape applied to the bottom of the tube to retain the sample. The samples were preconditioned at $RH = 50\%$ for $t = 24$ h to achieve the condition $w = w_{50}$. After conditioning, the holder was fitted into an aluminium lined modified wet cup

assembly with a silicone sealant applied to ensure vapour tightness. The entire cup assembly was then placed on the VIBRA HT balance in the climate chamber at $T = 23\text{ }^{\circ}\text{C}$ and $RH = 50 \pm 3\%$. Change in mass, Δm (of the entire assembly) was assumed to be due to vapour diffusion through the sample, and was logged at intervals of $t = 30\text{ s}$ using the same setup described in Section 3.3.1.2. All eight candidate materials were tested twice with the mean value for δ calculated. The water vapour flow rate, G was calculated as the slope of the linear portion of Δm against t , assuming a steady state of mass loss had been achieved. W , δ and μ were then calculated as described in Section 2.4.3.1.

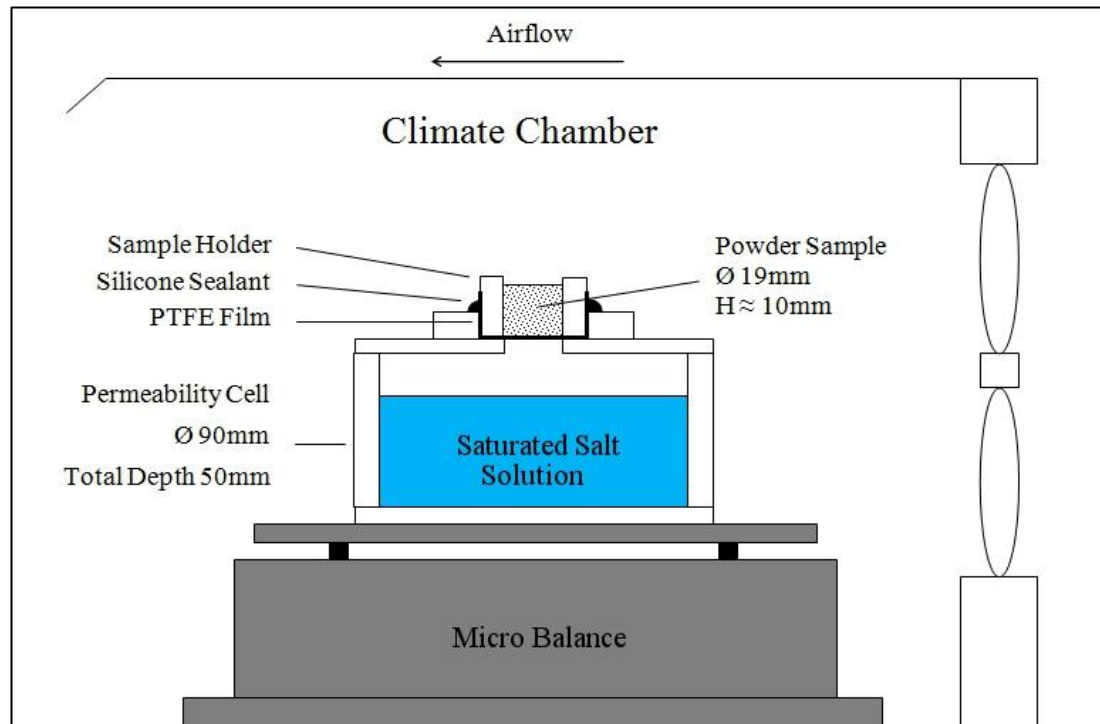


Figure 37 - Schematic of experimental setup for vapour permeability tests.

3.3.3 Liquid Water Absorption

Liquid water absorption, A_w can be defined as the mass of water absorbed by a sample per exposed surface area and per square root of time ($\text{kg}/\text{m}^2\text{s}^{0.5}$). The partial immersion test for A_w is used to indicate a material's water absorption due to

exposure to constant wetting (*i.e.* driving rain or partial immersion of a sample in water). To calculate A_w it is necessary to plot the change in mass per exposed surface area, Δm_t against the square root of time, \sqrt{t} . The resulting plot will show either a Type 1 or Type 2 curve as illustrated in Figure 38.

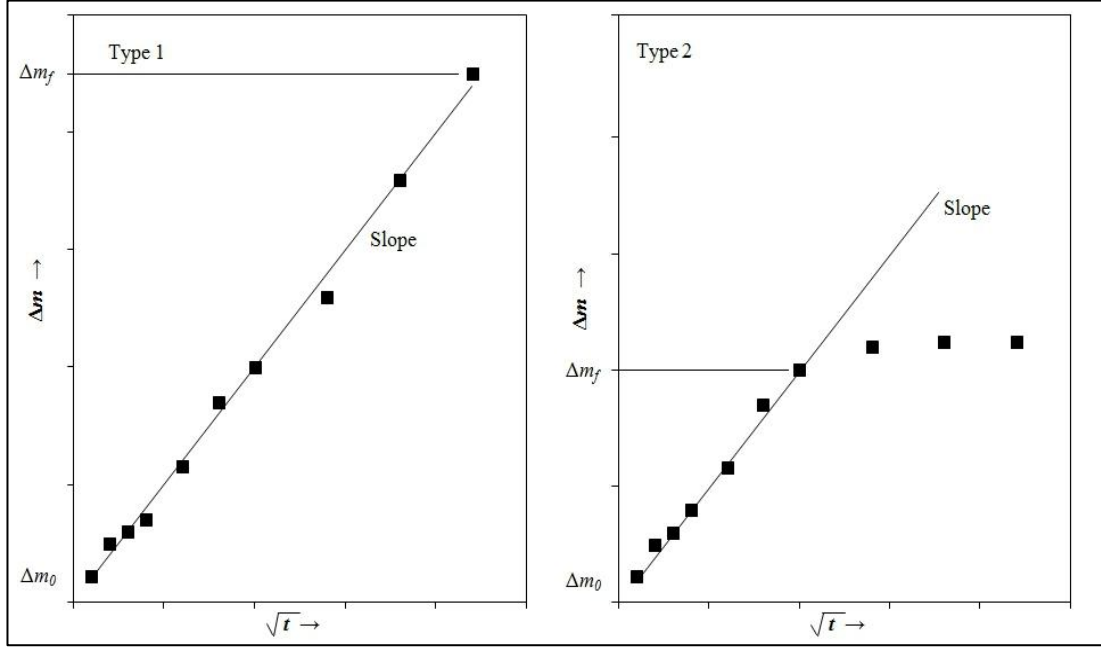


Figure 38 - Figure showing Type 1 and Type 2 water absorption plots.

For the Type 1 curve, A_w can be calculated from the slope of the entire test data, whilst the Type 2 curve, where surface wetting has occurred, should be calculated from only the linear portion of the data. Eq. 3.7 can be used to calculate A_w :

$$A_w = \frac{\Delta m_{tf} - \Delta m_0}{\sqrt{t}} \quad \text{Eq 3.7}$$

where Δm_t is calculated as the difference in mass per exposed surface area as:

$$\Delta m_t = \frac{\Delta m}{A} \quad \text{Eq 3.8}$$

The absorption coefficient for all samples was determined using a modified partial immersion test (see: Figure 39) in accordance with BS EN ISO 15148 (BSi, 2002b).

Samples of ~1 g were prepared by loose filling a Perspex graduated cylinder ($\varnothing_{int} = 5\text{mm}$) with PTFE film applied to the bottom of the cylinder to retain the sample. The samples were preconditioned at $RH = 50\%$ for $t = 24\text{ h}$ in the climate chamber to achieve the condition $w = w_{50}$. After conditioning, the cylinder was placed onto the cylinder supports in the deionised water filled aluminium dish, submerging ~5mm of the cylinder. Change in sample mass, Δm was recorded by removing the cylinder from the dish, blotting excess water from the bottom of the PTFE film using filter paper and weighing using the VIBRA HT balance. Recordings of Δm were taken at periodic time intervals as shown in Table 14. All eight candidate materials were tested twice with the mean value for A_w calculated.

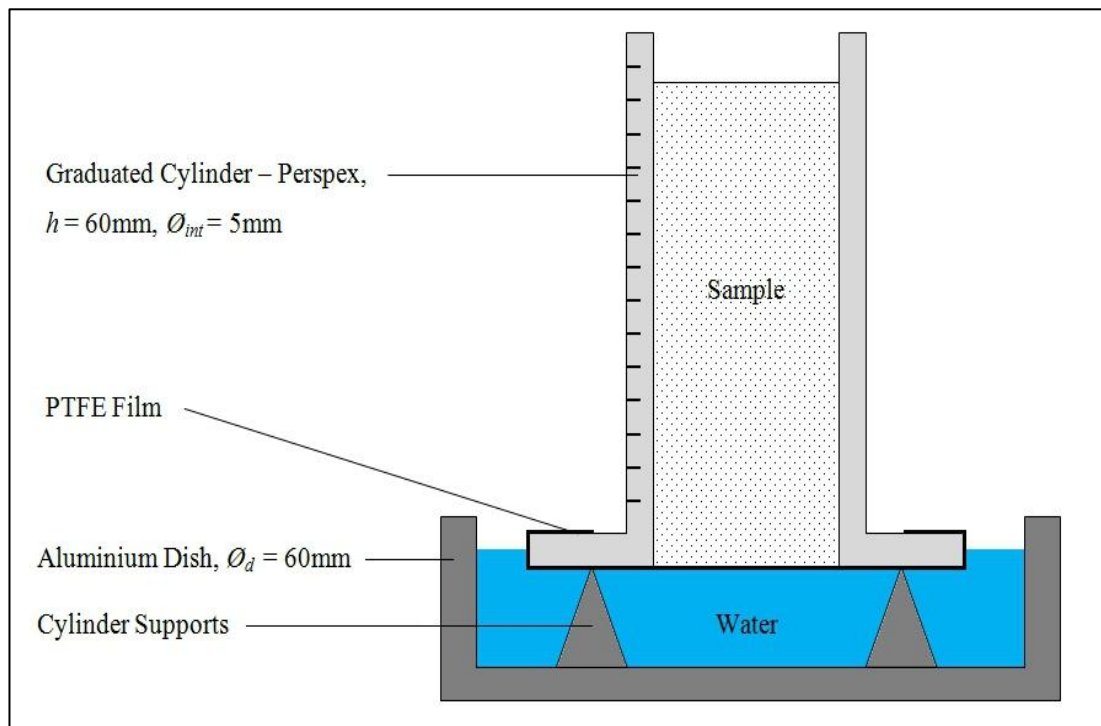


Figure 39 - Schematic of experimental setup for water absorption tests.

Period	t_1	t_2	t_3	t_4	t_5	t_6	t_7	t_8	t_9	t_{10}	t_{11}	t_{12}
Time, s	0	10	30	90	210	330	450	570	690	990	1590	2190

Table 14 - Time periods for Δm recording of for water absorption testing.

The test was terminated when either condition A or B was achieved:

- A. Water was observed on the top surface of the sample, indicating capillary saturation (*i.e.* $\Psi = 0$)
- B. Changes in mass, Δm was less than or equal to 0.5% for a period $t = 600$ s (*i.e.* $\Delta m < \pm 0.5\%$ with $\Psi \rightarrow 0$)

3.3.4 Specific Heat Capacity

For this research the differential scanning calorimetry (DSC) method for determining c_p was used (see: Figure 40). Testing was carried out in accordance with BS EN ISO 11357-4 (BSi, 2005b) using a TA Instruments Q10 differential scanning calorimeter (TA, 2012). The DSC uses two aluminium pans (2), one containing the sample material (1). The pans are placed in an insulated crucible (3) with a removable insulated lid (4). The pans are located on elements that can apply a structured heating load to the pans. An RCS90 refrigeration system with a cooling head is fitted around the crucible to provide a cooling load (not shown). One element is used for the sample (5) and the other as a baseline reference (6). To raise the temperature of the elements, an electrical signal to the elements is controlled using the TA Instruments Operating Software via a connection (7) to a computer (8).

The DSC operates on the principle that, using the same increasing temperature profile, the rate of flow of heat, F (*i.e.* $\Delta Q/\Delta T$) into the pan containing the sample will differ from the rate into the reference (empty) pan. The difference in flow can be attributed to the heat capacity of the sample, providing all other conditions are identical. For a continuous scanning test, three runs, using the same temperature profile are carried out to determine c_p (see: Figure 41):

1. A baseline run of two empty pans
2. A calibration run using one empty reference pan and one pan with a sample of known c_p *i.e.* sapphire
3. A sample run again using one empty reference pan and one pan with a sample of unknown c_p

The c_p of the sample can be calculated using the heat flow rates from the baseline (F_{base}), sample (F_{sp}), and reference (F_{ref}) runs along with the mass of the sample (m_{sp}) and reference (m_{ref}) using Eq. 3.9:

$$c_{p,sp} = c_{p,ref} \cdot \frac{m_{ref}(F_{sp} - F_{base})}{m_{sp}(F_{ref} - F_{base})} \quad \text{Eq 3.9}$$

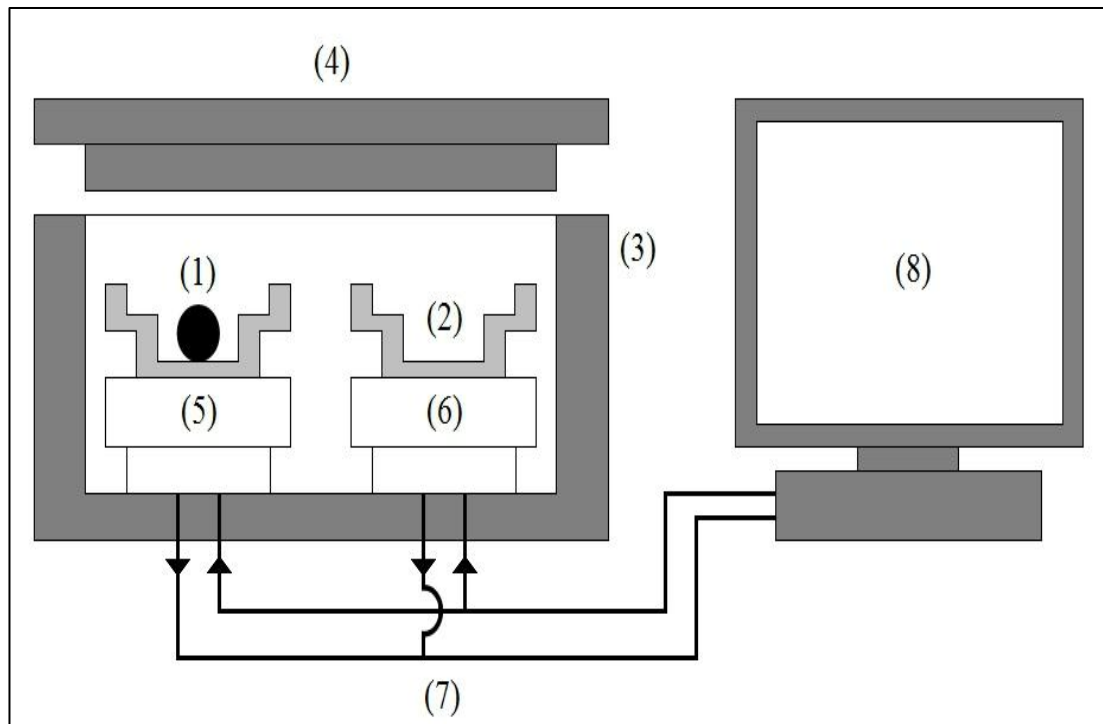


Figure 40 - Schematic diagram of a differential scanning calorimeter where (1) sample, (2) empty pan, (3) crucible, (4) lid, (5 & 6) heating elements (7) connecting cables and (8) computer.

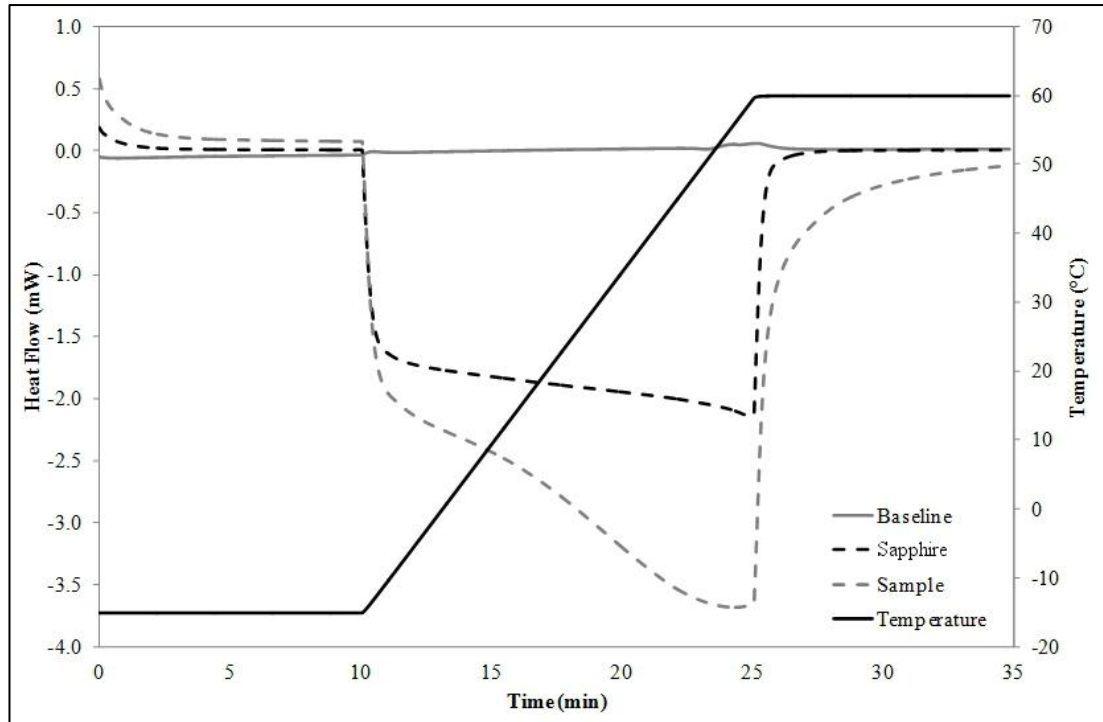


Figure 41 - Example heat flow curves and temperature profile from a DSC test.

Samples were first vacuum desiccated for a period $t = 24$ h prior to achieve $w = w_0$. Testing was carried out by initially recording a baseline using the two empty aluminium pans. A calibration run was then recorded using certified sapphire as a calibration standard. Finally a mass, ~ 5 mg of material was used for the sample run. The baseline, calibration and sample scans were carried out over a temperature range of $258 < T < 333$ K at a ramp rate of 5 K min^{-1} . Samples were held isothermal at the lower and upper temperatures limits for a period $t = 10$ min at the beginning and end of each test run. Three test runs for each of the eight candidate materials were performed and the mean value of c_p calculated.

3.3.5 Thermal Conductivity

Whilst there are many methods for determining thermal conductivity, λ , (*i.e.* Heat Flow Meter, Hot Wire etc.) the minimal quantities of sample available and their powder form necessitated use of a new technique - Modified Transient Plane Source (MTPS). Testing was carried out in accordance with BS EN ISO 22007-2 (BSi,

2012) using a Setaram TCi MTPS device (Setaram, 2012). In the MTPS technique a sample of powder (1) is placed within the locating ring (2) on the top of a one-sided, interfacial, heat reflectance sensor of negligible heat capacity (3) (see: Figure 42). A compacting mass (4) is placed on the sample to ensure good contact with the sensor. The sensor is connected to a computer (5) through the systems control unit (6). During testing the control unit applies a known, momentary current to the sensor's heating element resulting in a constant heat source at the sample/ sensor interface of $\Delta T \approx 2$ K and generating a dynamic temperature field within the sample. This induces a change in the voltage drop of the sensor element.

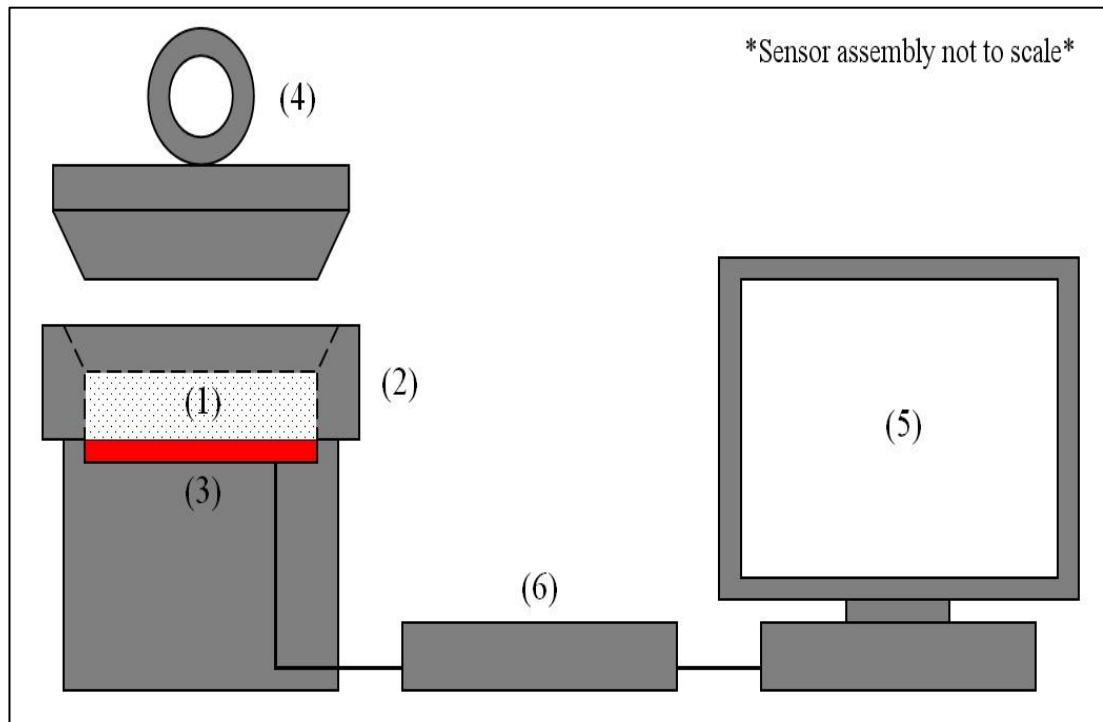


Figure 42 - Schematic diagram of a modified transient plane source test kit where (1) powder sample, (2) locating ring, (3) sensor, (4) compacting mass, (5) computer and (6) control unit.

By measuring the rate of increase in the sensor voltage it is possible to determine the thermo-physical properties (*i.e.* thermal conductivity and thermal effusivity) of the sample, at constant temperature and pressure when c_p and ρ_{bulk} are also known. The thermo-physical properties of the sample material are inversely proportional to the

rate of increase in the sensor voltage.

As discussed in Section 2.5.1 moisture dependent thermal conductivity, λ^* is an important property in thermal transfer of building envelopes due to the increased λ corresponding to increased w however, as the expected thickness of interior material coatings is minimal (2 mm) coupled with already significant insulation levels (see: Section 3.5), this effect can be somewhat neglected. In practice RH levels rarely drop to low levels with some level of moisture present in the coating at all times. To account for absorbed moisture a total of five tests runs were carried out at $RH = 50\%$ to achieve the condition $w = w_{50}$ for each candidate material and the average values for λ^* calculated.

3.4 Physical Modelling

In addition to the hygrothermal functional properties as detailed previously, it is necessary to understand the interaction of the materials and their surrounding environmental conditions. The behaviour of the materials under varying psychrometric conditions allows for understanding of how the materials can alter those conditions whilst also providing data sets for validation of the numerical modelling in the next section. To provide experimental measures of moisture uptake in the candidate materials, a series of 1D physical models were designed whilst a series of 3D physical models were used to measure resultant RH_{ie} levels in a controlled volume with and without the presence of hygrothermal materials. Details of these models are contained in the following sections.

3.4.1 1D Physical Modelling

The physical models outlined in the following sections were designed to study the

response of the sample materials to changes in the surrounding psychrometric conditions. 1D moisture transfer to and from the materials was controlled by exposing a single surface area to the test environment. Two tests were carried out;

1. An ASHRAE comfort range step test to study the moisture kinetics of the materials solely within the ASHRAE comfort range (*i.e.* $40\% \leq RH_{ie} \leq 70\%$ and $T_{ie} = 23^{\circ}\text{C}$).
2. A sinusoidal cyclic response test to study the materials moisture sorption/desorption over a range of RH_{ie} amplitudes and to provide a validation data set for the 1D numerical model.

3.4.1.1 ASHRAE Comfort Range Step Test

Knowledge of the moisture kinetics of a sorption/ desorption isotherm is vital for buffering applications since, due to domestic occupancy time scales, a buffering material rarely reaches saturation; however, it is required to respond as rapidly as possible to RH_{ie} changes. A series of dynamic vapour sorption tests were carried out to determine 1D sample mass uptake response to step changes in RH_{ie} amplitude between 40 and 70%. This test was designed to analyse the moisture kinetics of the materials in the ASHRAE comfort range (ASHRAE, 2009a).

To determine an appropriate time period, $t_{40-70-40}$ for each step, the change in mass between 40% and 70% (Δm_{40-70}) and the corresponding time to reach EMC (t_{emc}) was determined from the vapour sorption isotherms (see: Section 3.3.1.2). As hygric materials rarely reach full equilibrium in humidity buffering applications, an arbitrary EMC interval, $m_{75\%}$ was chosen which represented 75% of the EMC, but gave an equal or greater reduction of t_{emc} . A corresponding time interval, $t_{75\%}$ was then interpolated from $m_{75\%}$, as illustrated in Figure 43. The step time period, $t_{40-70-40}$

was then calculated as $2t_{75\%}$.

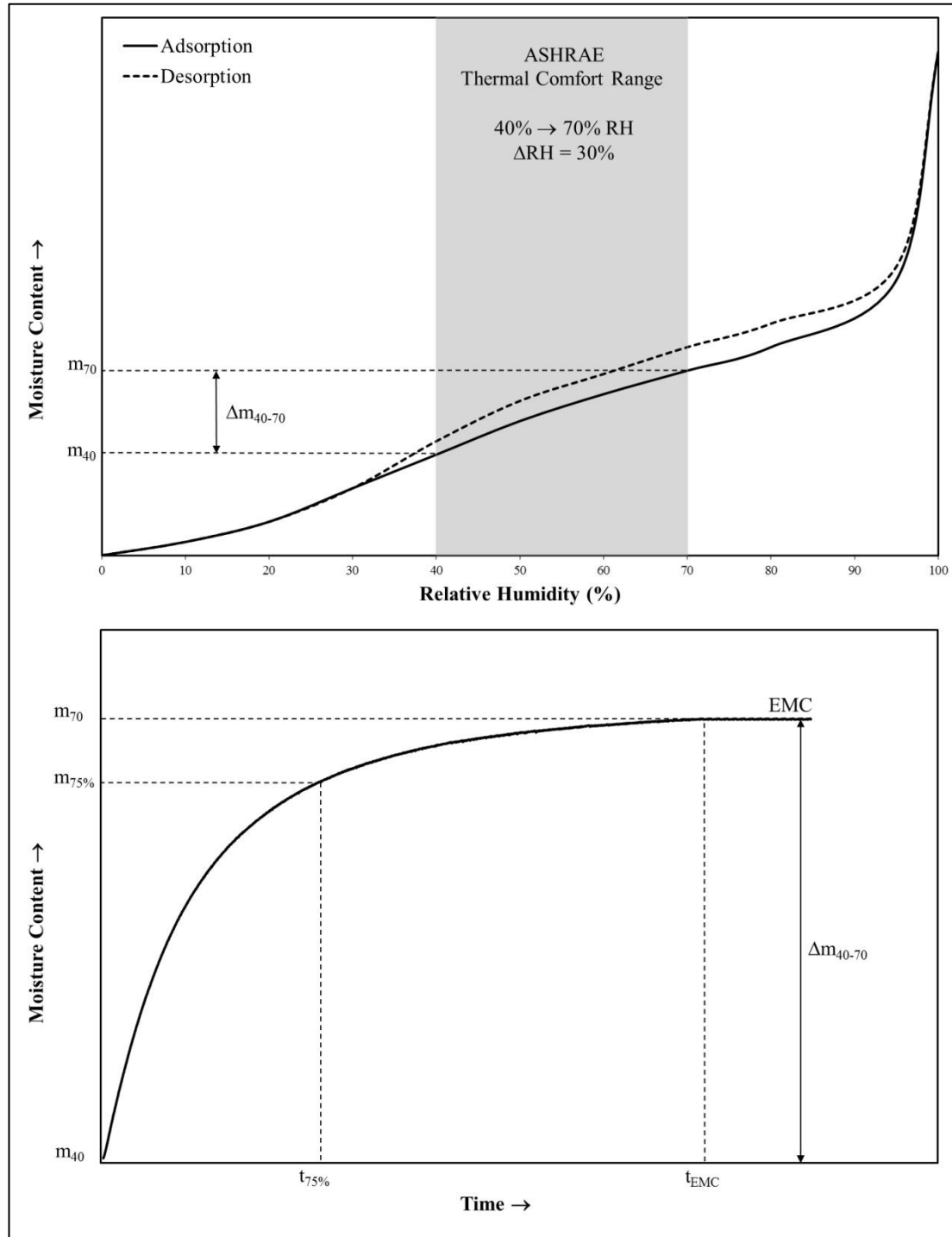


Figure 43 - Methodology for determining $t_{75\%}$ for thermal comfort range step testing (Hall et al., 2012b).

Testing was carried out using the same experimental setup as that outlined for determination of the materials sorption isotherms (see: Section 3.3.1.2). Samples were vacuum desiccated for a period $t = 24$ h prior to testing to achieve the condition

$w = w_0$. The dry sample mass was recorded and the sample was then conditioned in the climate chamber at $RH_{ie} = 40\%$ for $t = 24\text{h}$ prior to testing to achieve the condition $w = w_{40}$. RH_{ie} was stepped from 40 to 70% (*i.e.* $\Delta RH_{ie} = 30\%$) for a period $t_{40-70-40} = 2t_{75\%}$ and repeated for six cycles (see: Figure 44). Testing was performed on all eight candidate materials and repeated once to ensure integrity of the results.

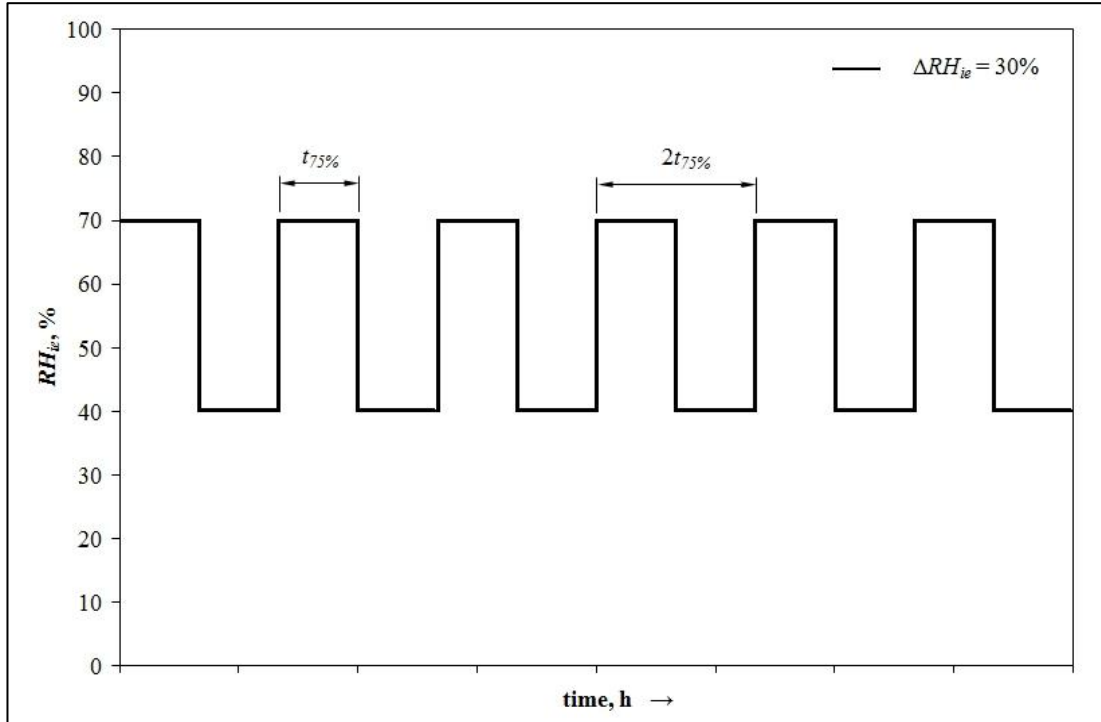


Figure 44 – Step variation of RH_{ie} for thermal comfort range step testing.

3.4.1.2 Sinusoidal Cyclic Response Test

A series of sinusoidal tests were required to determine the materials 1D mass uptake response to sinusoidal amplitude changes in RH_{ie} . Data acquired from these tests was used as the validation data set for the 1D numerical models (*i.e.* WUFI Pro). Testing was carried out using the same experimental setup as that outlined for determination of the materials sorption isotherms (see: Section 3.3.1.2).

All samples were vacuum desiccated for a period $t = 24\text{ h}$ prior to testing to achieve the condition $w_{coat} = w_0$. The dry sample mass was recorded and the sample was then

conditioned in the climate chamber at $RH_{ie} = 50\%$ for $t = 24$ h prior to testing to achieve the condition $w_{coat} = w_{50}$. During the experiment, RH_{ie} was sinusoidally fluctuated about a median ($RH_{ie} = 50\%$) for a single peak to peak cycle period $t_t = 24$ h using two different amplitudes;

- $RH_{ie} 35\% \rightarrow 65\% \rightarrow 35\%$ giving a $\Delta RH_{ie} = 30\%$ and
- $RH_{ie} 15\% \rightarrow 85\% \rightarrow 15\%$ giving a $\Delta RH_{ie} = 70\%$.

The RH_{ie} sine waves for each of the two amplitudes, ΔRH_{ie} were generated for each time period ($t = 0.1$ h) using Eq. 3.10:

$$RH = \frac{\Delta RH}{2} \cdot \sin(cf \cdot t) + 50 \quad \text{Eq 3.10}$$

Where cf is the cyclic frequency (radians/s) and is given by:

$$cf = 2 \pi \frac{1}{t_t} \quad \text{Eq 3.11}$$

The cycle was repeated twice to complete the test (see: Figure 45). Mass change, Δm (%) was recorded at intervals, $t = 30$ s throughout the test and w_{coat} was calculated from mass change using Eq. 3.12. Testing was performed on the MS 3.3, MS 4.7 and MS 8.3 samples only and repeated once to ensure data integrity.

$$w_{coat} = \frac{m \cdot \rho_{bulk}}{100} \quad \text{Eq 3.12}$$

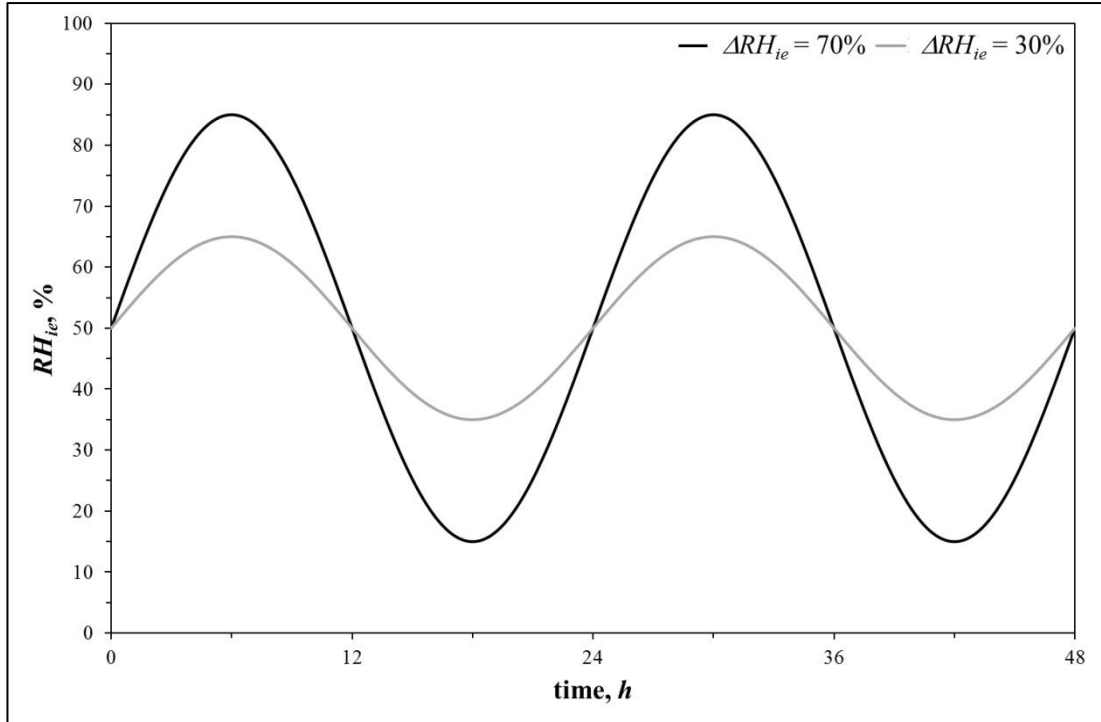


Figure 45 - Sinusoidal variation of RH_{ie} for cyclic response testing (Casey et al., 2012).

3.4.1.3 Moisture Buffer Value

To compare the candidate materials in terms of potential application to other published traditional building envelope materials, the Effective Moisture Penetration Depth (EMPD) and Moisture Buffer Value (MBV) were determined. The EMPD is defined as the distance between the surface and the point in the material where the amplitude of the vapour variation equals 1% of the variation at the materials' surface (Arfvidsson, 1999) and gives an indication of how much material may be required to provide vapour storage. To calculate EMPD, moisture diffusivity, D_w (m^2/s) was first calculated as a function of moisture storage, ξ_u , vapour permeability, δ , bulk density, ρ_{bulk} and the saturation pressure, p_s at 23 °C:

$$D_w = \frac{\delta \cdot p_s}{\rho \cdot \xi_u} \quad \text{Eq 3.13}$$

EMPD was then calculated using Eq. 3.14 (Rode et al., 2005):

$$d_{p,1\%} \approx 4.61 \sqrt{\frac{D_w \times t}{\pi}} \quad \text{Eq 3.14}$$

The practical Moisture Buffer Value $MBV_{\text{practical}}$ of any material can be defined as the amount of water that is transported in or out of a material per open surface area, during a certain period of time, when it is subjected to variations in relative humidity of the surrounding air (Rode et al., 2005). Using MBV has the advantage of allowing materials to be classified (see: Figure 46) and thus compared using a single value however, as all tests are isothermal the MBV is not an ideal measure.

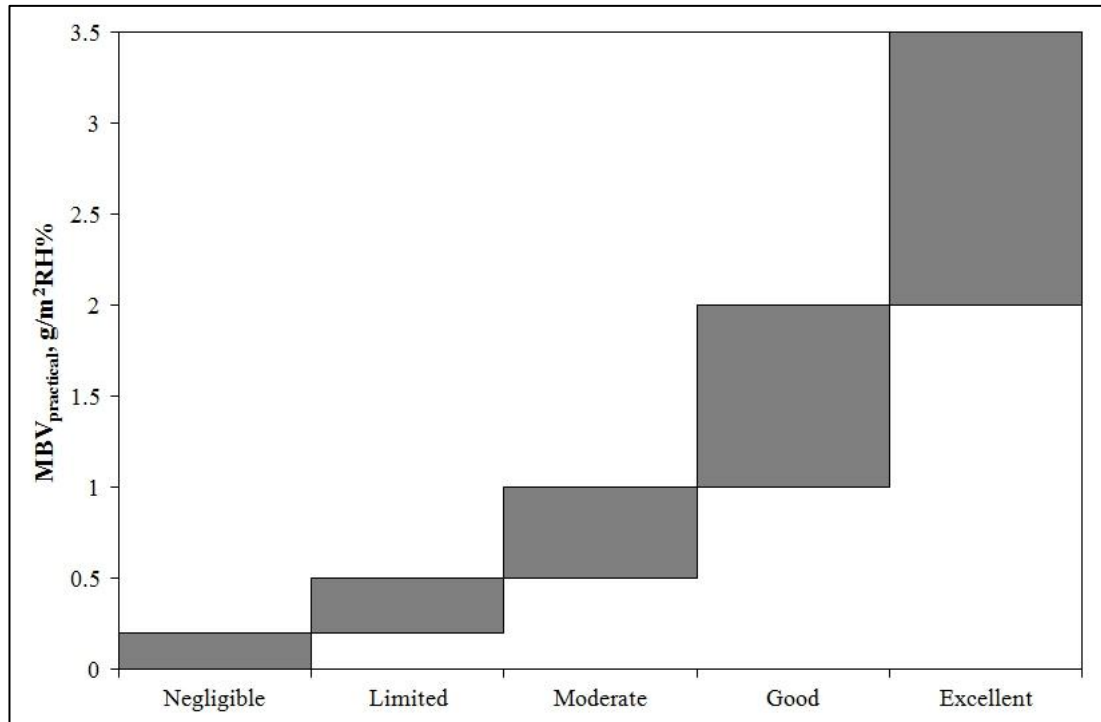


Figure 46 - Graph showing the MBV classification system for materials. Adapted from (Rode et al., 2005).

$MBV_{\text{practical}}$ was calculated using Δm values calculated for the sorption isotherms (see: Section 3.3.1.2) assuming $t_{40-70-40}$ to be constant and the absorbed mass to be variable. Apparent surface area was calculated from the diameter of the petri dish ($A_s = 0.001257 \text{ m}^2$). Eq. 3.15 was then used to calculate $MBV_{\text{practical}}$ (Meissner et al., 2010) with the results presented in Section 4.3.5:

$$MBV_{\text{practical}} = \frac{\Delta m}{A_s \cdot \Delta RH} \quad \text{Eq 3.15}$$

3.4.2 3D Physical Modelling

The physical models outlined in the following sections were designed to study the changes in the environmental conditions surrounding the desiccant materials resulting from the presence of the hygrothermal materials. Although the interior environment was a 3D volume, moisture transfer to and from the material itself was still 1D and controlled by exposing a single surface area to the test environment. Testing was carried out using a custom made isolated test box which represented a closed environment *i.e.* an interior volume that was hygrially and thermally isolated from the exterior environment. Details of the isolated box can be seen in the following sections. The 3D physical modelling consisted of two stages:

1. A series of moisture generation rates experiments to quantify the levels of moisture introduced into the isolated box volume.
2. A series of moisture buffering tests to determine the levels of reduction in RH_{ie} with the presence of the hygrothermal materials in the isolated box. This data was used as the validation data set for the 1D numerical models.

3.4.2.1 Moisture Generation Rates

Size limitations exist within both the physical and numerical model. The internal dimensions of the climate chamber allow for a maximum internal volume of 0.0072m^3 for the isolated box, allowing for adequate space around the exterior of the box for insulation, manipulation, instrumentation and air flow. In the numerical model a minimum internal volume of 1m^3 is permissible due to the software limits. It was necessary to scale the standardised moisture generation rates shown in Table 15,

to the corresponding volumes of the physical and numerical models.

	Moisture Load (g/h)	Thermal Conductive (W)	Thermal Radiant (W)	CO ₂ Load (g/h)
Toddler (3 – 6 years)	90	20	12	32
Teenager (14 – 16 Years)	50	60	30	33.8
Adult - Sedentary	43	65	36	30.3
Adult – Desk Work	59	80	41	36.3
Adult - Active	123	158	47	60.5
Cooking (Gas)	125 ^a	---	---	---
Showering	2400 ^a	---	---	---

Table 15 - Occupant loads obtained from WUFI Plus v2.1.1.73 (IBP, 2012a) and ^aBS 5250 (BSi, 2011).

3.4.2.1.1 Scaling factor for the physical model volume

Standard room, V_{sr}	4m x 4m x 2.4m	=	38.4m ³
Isolated Box, V_{ib}	0.2m x 0.2m x 0.18m	=	0.0072m ³
Scaling Factor, S_f	V_{sr} / V_{ib}	=	5333.33

The volume adjusted generated rates (assuming linearity) are shown in Table 16:

	Moisture Load (g/h)	Thermal Conductive (W)	Thermal Radiant (W)	CO ₂ Load (g/h)
Toddler (3 – 6 years)	0.017	0.0038	0.0023	0.017
Teenager (14 – 16 Years)	0.009	0.0113	0.0056	0.009
Adult - Sedentary	0.008	0.0122	0.0068	0.008
Adult – Desk Work	0.011	0.0150	0.0077	0.011
Adult - Active	0.023	0.0296	0.0088	0.023
Cooking (Gas)	0.023	---	---	---
Showering	0.450	---	---	---

Table 16 - Volume adjusted loads for the physical model calculated from Table 15.

3.4.2.1.2 Scaling factor for the 1m³ numerical model volume

Standard room, V_{sr}	4m x 4m x 2.4m	=	38.4m ³
Isolated Box, V_{ib}	1m x 1m x 1m	=	1m ³

$$\text{Scaling Factor, } S_f \quad V_{sr} / V_{ib} \quad = \quad 38.4$$

	Moisture Load (g/h)	Thermal Conductive (W)	Thermal Radiant (W)	CO ₂ Load (g/h)
Toddler (3 – 6 years)	2.344	0.521	0.313	0.833
Teenager (14 – 16 Years)	1.302	1.563	0.781	0.880
Adult - Sedentary	1.120	1.693	0.938	0.789
Adult – Desk Work	1.536	2.083	1.068	0.945
Adult - Active	3.203	4.115	1.224	1.576
Cooking (Gas)	3.255	---	---	---
Showering	62.50	---	---	---

Table 17 - Volume adjusted occupant loads for the 1m³ numerical model calculated from Table 15.

3.4.2.2 Evaporation rates

Due to the scaling of moisture generation rates outlined previously (see: Section 3.4.2.1), it was necessary to devise a method of introducing the required moisture into the isolated box volume. A series of four experiments were conducted using dishes of deionised water with increasing diameters *i.e.* $\varnothing_d = 30, 45, 60$ and 75 mm respectively with each test repeated twice and the mean value calculated.

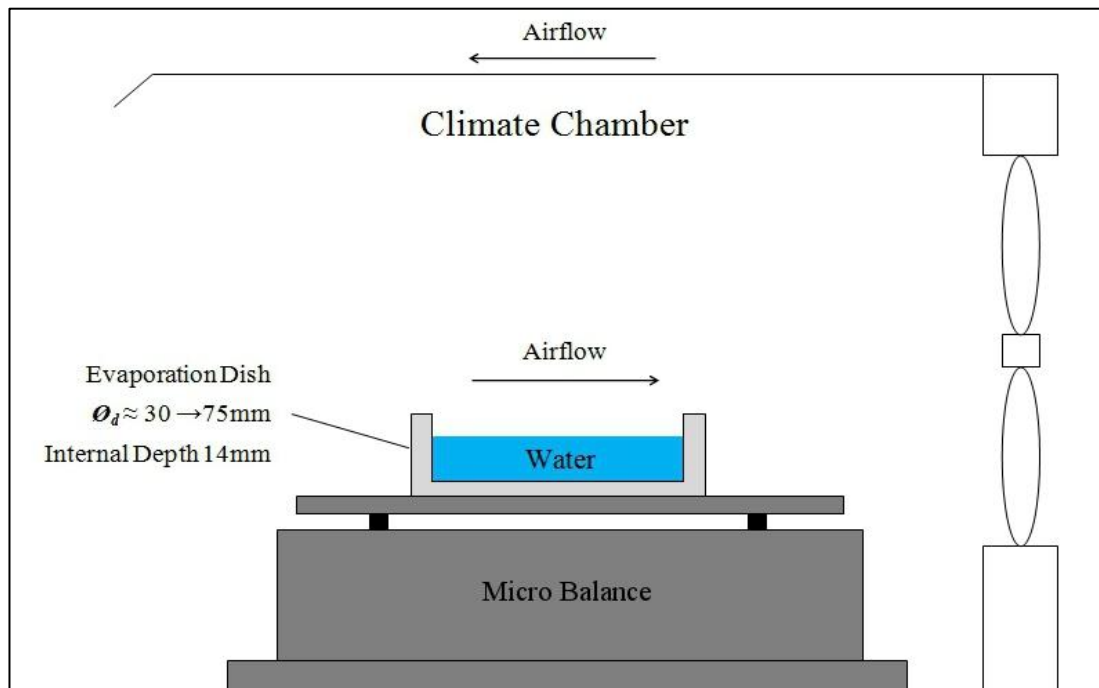


Figure 47 - Schematic of experimental setup for water evaporation tests.

Mass loss, Δm due to moisture evaporation, g_g was recorded at intervals $t = 30$ s by placing the dish with ≈ 20 g deionised water on the air-shielded VIBRA HT analytical balance inside the climate chamber (see: Figure 47). Each test was carried out under identical psychrometric conditions ($RH_{ie} = 50\%$ and $T = 23^\circ\text{C}$) for a period $t = 24$ h. The evaporation rate test was designed to establish a link between ϕ_d and Δm and allow for an appropriate dish diameter to be selected to generate any desired moisture generation rate for the physical model in the isolated box.

3.4.2.3 Humidity Buffering Experiments

A series of humidity buffering tests were carried out on both the MS materials and conventional building materials to determine the changes in the internal environmental conditions resulting from the presence of the hygrothermal materials under controlled moisture loading using a physical isolated box model (see: Figure 48).

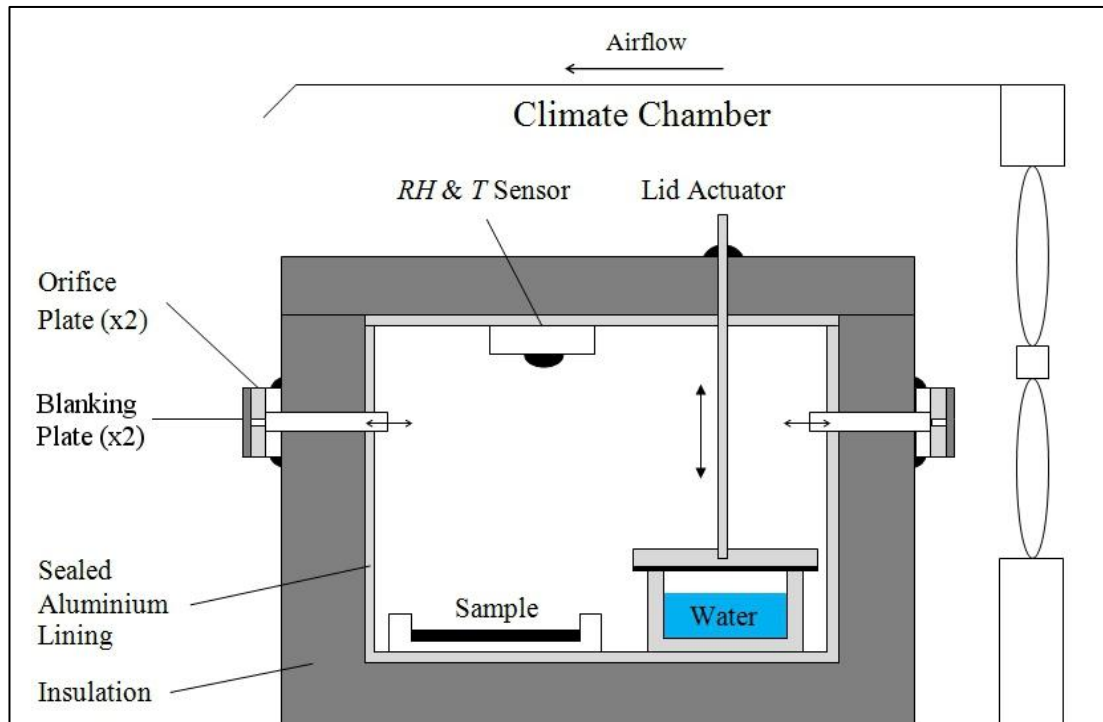


Figure 48 - Schematic of experimental setup for RH_{ie} buffering tests.

The internal structure of the box was constructed using 18mm spruce plywood with an internal facing phenolic moisture barrier (UPM, 2009). A double layer of aluminium foil was then applied to the interior and exterior of the box and stepped lid with all internal edges sealed using silicone sealant. The box was then ‘wrapped’ in 100 mm polyisocyanurate (PIR) foil lined rigid insulation ($\lambda = 0.022 \text{ W/(mK)}$) (Kingspan, 2011). The exterior of the insulation was sealed using generic parcel tape to reduce dust contamination and provide a level of robustness to the assembly. Two holes ($\varnothing = 32 \text{ mm}$) were drilled into opposing faces from the exterior through to the interior to facilitate a ventilation assembly for possible future research.

The ventilation assembly (see: Figure 49) was constructed using a length of Perspex tubing (1) with external and internal diameters of 32 mm and 24 mm, respectively. The tubing was attached to a backing plate (2) which had a central hole pre-drilled ($\varnothing = 32 \text{ mm}$). Silicone sealant (3) was applied to the intersection of the pipe and plate to eliminate air leakage. Four M6 bolts (4) were fixed through countersunk holes in the backing plate and sealed again using silicone. These bolts allow an aluminium orifice plate (5) with a desired pre-drilled ventilation hole (6) to be attached and secured using M6 nuts (7). In addition, silicone grease was applied between the faces of the backing and orifice plates to ensure airflow only through the orifice hole. For the airtight tests an aluminium blanking plate (no ventilation hole) was fitted to the assembly.

All tests were carried out under identical psychrometric conditions with the climate chamber RH (*i.e.* RH_{oe}) sinusoidally fluctuated about a median ($RH_{oe} = 50\%$) for a single peak to peak cycle period $t = 24\text{h}$ with an amplitude;

$RH_{oe} 15\% \rightarrow 85\% \rightarrow 15\%$ giving a $\Delta RH_{oe} = 70\%$.

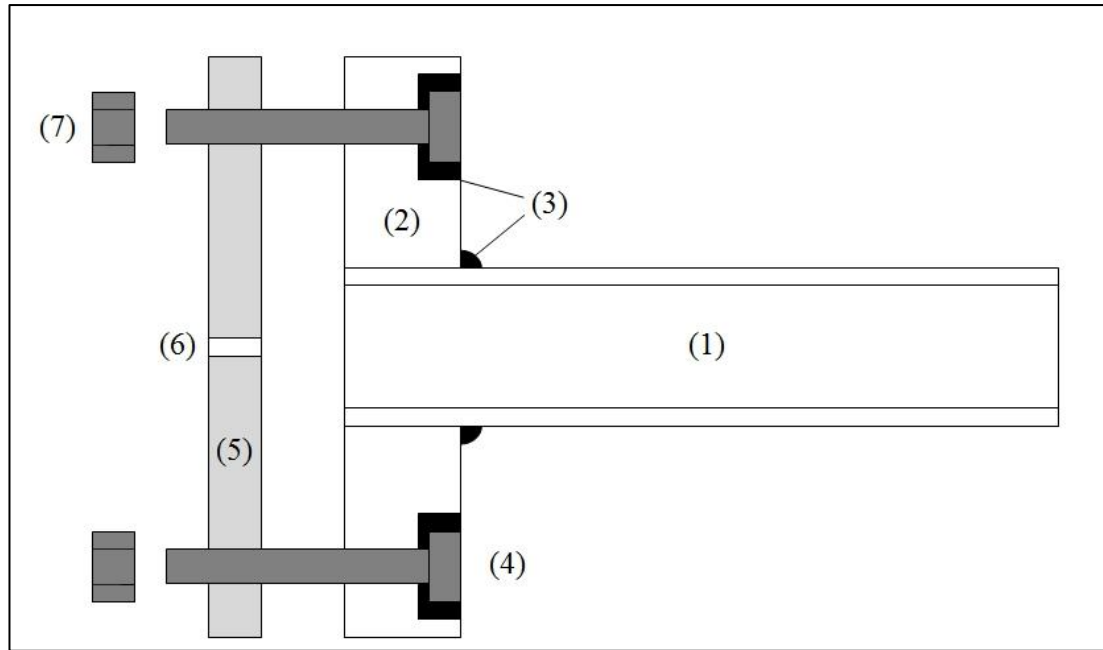


Figure 49 - Schematic diagram of the ventilation assembly for the isolated box where (1) Perspex tube, (2) backing plate, (3) sealant, (4) M6 bolts, (5) orifice plate, (6) ventilation hole and (7) M6 nuts.

The isolated box interior T_{ie} and RH_{ie} were monitored using two Tinytag Ultra 2 sensors at an accuracy of ± 3 %RH and $\pm 0.5^\circ$ C at 25° C. Data was recorded over a test period $t = 48$ h with RH_{ie} and T monitored at intervals $t = 30$ s and downloaded upon completion using the SWCD-0040 Tinytag Explorer software. Data acquired from these tests was used as the validation data set for the 3D numerical models (*i.e.* WUFI Plus).

A water evaporation dish with $\varnothing = 16.8$ mm (see: Section 3.4.2.2) was placed in the interior of the box to represent occupant moisture loading:

Standard box @ 86 g/h = WUFI 1m³ box @ 2.22 g/h = Isolated Box @ 0.016 g/h

Control of evaporation time was provided using an actuator attached to a lid with a rubber gasket fixed to the underside to ensure a good seal was achieved. At the intersection of the actuator and the stepped lid, lithium grease was used to ensure the box remained airtight.

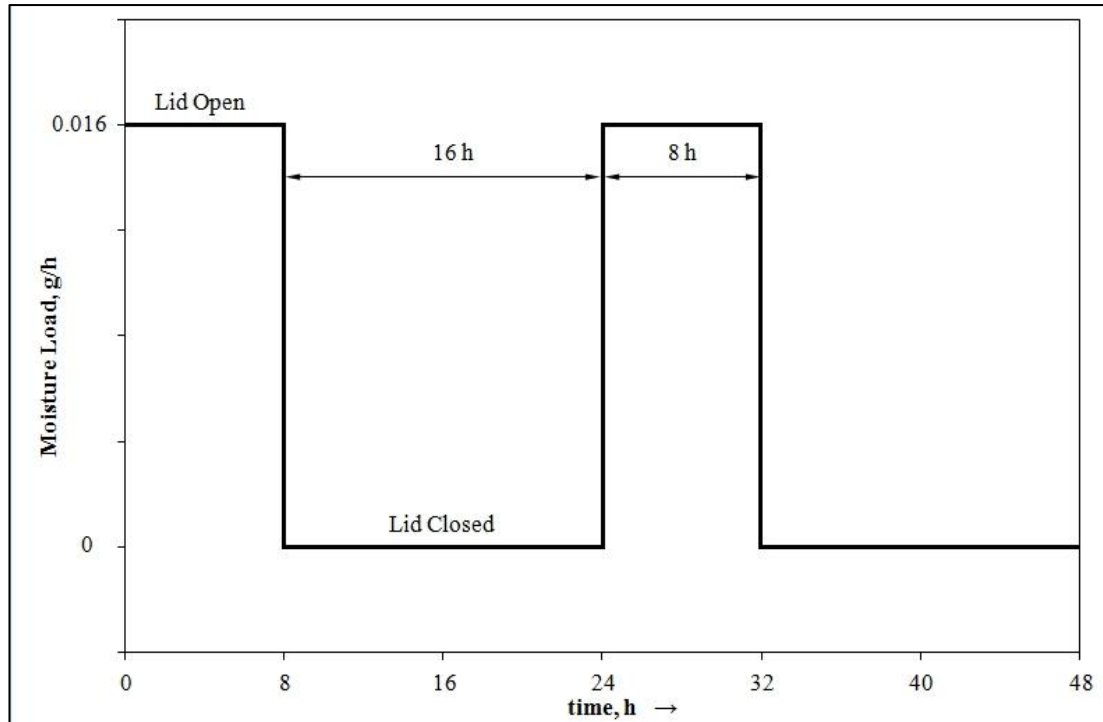


Figure 50 - Moisture generation schedule for humidity buffering testing.

The moisture evaporation schedule to the box was controlled by opening the lid for a fixed period of 8 h and closing for 16 h to simulate the moisture load from two adult occupants at rest overnight in a standard bedroom (See: Figure 50). All samples were conditioned in the climate chamber at $RH_{ie} = 50\%$ for $t = 48$ h prior to testing to achieve the condition $w_{coat} = w_{50}$. A total of six tests were performed twice for data integrity:

- Test 1. No material present
- Test 2. MS 3.3nm – 2mm layer in Petri Dish ($\varnothing = 50\text{mm}$)
- Test 3. MS 4.8nm – 2mm layer in Petri Dish ($\varnothing = 50\text{mm}$)
- Test 4. MS 8.3nm – 2mm layer in Petri Dish ($\varnothing = 50\text{mm}$)
- Test 5. Spruce timber core – ($d = 15\text{mm}$, $\varnothing = 50\text{mm}$) Epoxy resin and foil lining applied to side and bottom surfaces to ensure 1D moisture transfer
- Test 6. Gypsum core – ($d = 15\text{mm}$, $\varnothing = 50\text{mm}$) Painted top surface. Epoxy

resin and foil lining applied to side and bottom surfaces to ensure 1D moisture transfer

3.5 Numerical Modelling

Using the same experimental design and the material properties from the physical models, 1D and 3D numerical models of the materials predicted response were simulated and model validation carried out. For the 1D modelling the WUFI Pro v5.1 hygrothermal simulation model was used whilst for the whole building (3D) modelling the WUFI Plus 2.1.1.73 hygrothermal simulation model was used (IBP, 2012a, IBP, 2012b). Details of the model setup (*i.e.* envelope assemblies, climate conditions, input parameters etc.,) are contained in the following sections.

3.5.1 1D Numerical Models

The 1D numerical models were designed to replicate the testing carried out in the 1D physical modelling sections (see: Section 3.4.1). The 1D model was used to simulate material response to changes in interior and exterior psychrometric conditions. Once validated against the physical model, the numerical model was then utilised to perform a comparative study by simulating representative interior and exterior psychrometric conditions, different envelope assemblies, air-tightness levels etc. Further modelling was also undertaken to perform parametric analysis of material behaviour resulting from adjustment of the hygrothermal functional properties and to investigate the potential for material selection by using the model as a ‘tuning’ tool. All model numerics were set to have increased accuracy and adaptive convergence with grid spacing set to ‘medium’.

3.5.1.1 Sorption Isotherm Model

The sorption isotherm numerical model was designed to assess that the MS materials moisture uptake from the sorption isotherm tests could be easily replicated. The time period, t_{RH} for each RH step in the climate file was based on the t_{emc} data from the physical isotherm tests for each material (see: Figure 51). To represent the same conditions used in the physical model, the component assembly used in WUFI Pro v5.1 was designed to hygrically isolate the materials such that 1D moisture flow was achieved. A 2mm glass barrier ($\mu = 10000$) was placed on the exterior side of the assembly to represent a petri dish with the sample material placed on the interior side in a 2mm layer (see: Figure 52). All model parameters can be seen in Table 18.

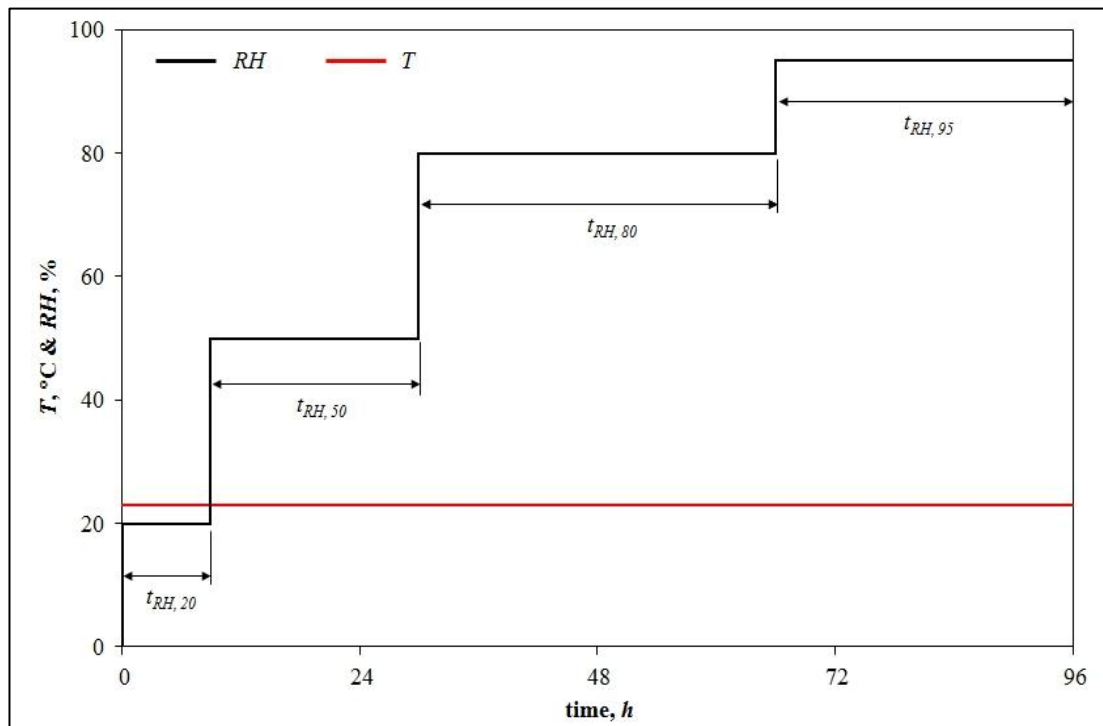


Figure 51 - Variation of RH for sorption isotherm numerical modelling.

Parameter	Value	Parameter	Value
Calculation Period	3 days	Heat Resistance (Ext.)	0.0588 m ² K/W
Time Step	0.05 h	Heat Resistance (Int.)	0.125 m ² K/W
Inclination	0°	Initial RH / T	0% / 23 °C
Exterior RH / T	Step / 23 °C	Interior RH / T	Step / 23 °C

Table 18 - Input parameters for the numerical sorption isotherm model.

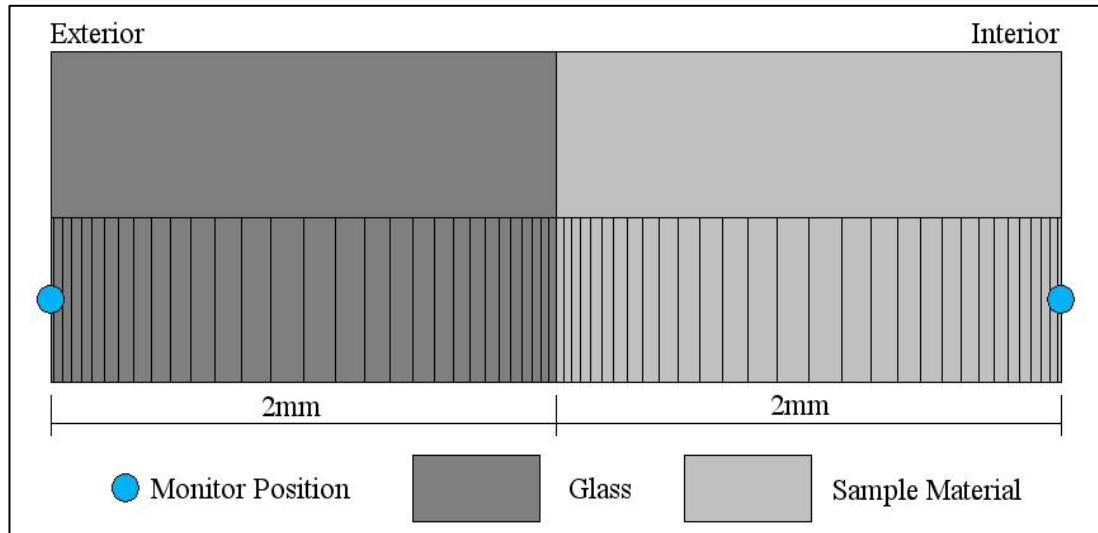


Figure 52 - Component assembly for the numerical sorption isotherm model showing monitor positions and grid spacing.

3.5.1.2 Vapour Permeability Model

The vapour permeability numerical model was designed to assess the accuracy of the models simulation of moisture fluxes through the MS materials. The component assembly used in WUFI Pro v5.1 was designed such that a unidirectional 1D moisture flow was achieved through the material from the exterior to the interior. This was achieved by a sample of depth, d_δ (equal to the materials corresponding depth in the physical model) left open to both the exterior and interior climates (see: Figure 53). The MS materials were simulated and all parameters used in the models can be seen in Table 19.

Parameter	Value	Parameter	Value
Calculation Period	24 h	Heat Resistance (Ext.)	0
Time Step	1 h	S_d -Value (Ext.)	0
Material Layers	1	Heat Resistance (Int.)	0
Orientation	----	S_d -Value (Int.)	0
Inclination	0°	Initial RH / T	50% / 23 °C
Exterior RH / T	94% / 23 °C	Interior RH / T	50% / 23 °C

Table 19 - Input parameters for the numerical vapour permeability model.

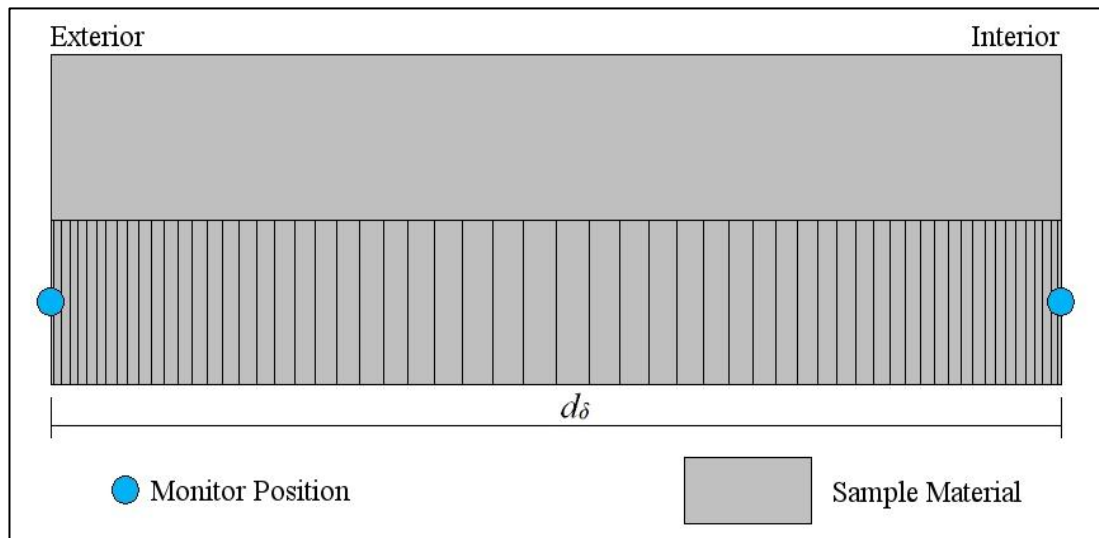


Figure 53- Component assembly for the numerical vapour permeability model showing monitor positions and grid spacing.

3.5.1.3 Sinusoidal Cyclic Response Model

The sinusoidal cyclic response model, using the same low (30%) and high (70%) ΔRH_{ie} amplitudes as the physical model (see: Section 3.4.1.2) was used to validate the WUFI Pro v5.1 numerical model. To recreate the physical model, the component assembly was designed to thermally and hygrically isolate the indoor environment from the outdoor environment (see: Figure 54). This was achieved by placing a 1mm vapour barrier ($S_d = 1500m$) to either side of a 100mm ‘Super Insulator’ ($\lambda = 0.005$ W/(m K)), with the MS sample material layer ($d = 2mm$) placed on the interior surface. The MS materials were simulated and all parameters used in the model can be seen in Table 20.

Parameter	Value	Parameter	Value
Calculation Period	48 h	Heat Resistance (Ext.)	0.0588 m ² K/W
Time Step	1 h	S _d -Value (Ext.)	1500 m
Material Layers	4	Heat Resistance (Int.)	0.125 m ² K/W
Orientation	----	S _d -Value (Int.)	0
Inclination	0°	Initial RH / T	50% / 23 °C
Exterior RH / T	Sine / 23 °C	Interior RH / T	Sine / 23 °C

Table 20 - Input parameters for the numerical sinusoidal cyclic response model.

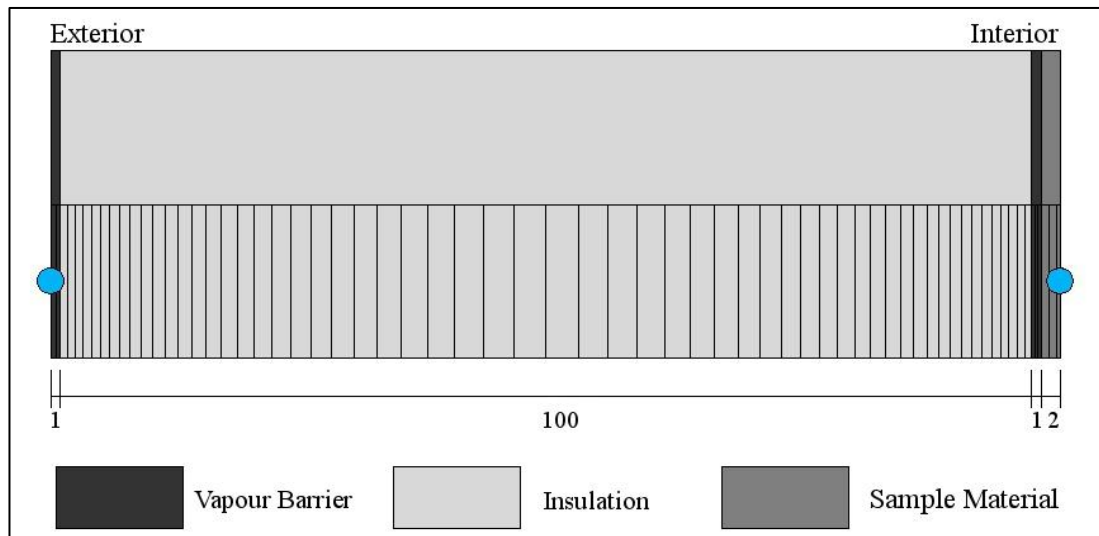


Figure 54 - Component assembly for the numerical sinusoidal cyclic response model showing monitor positions and grid spacing.

In order to assess the level of confidence in the WUFI model, the statistical variance between the numerically predicted data and the physical data was analysed. The mean difference between the coating's water content in the physical model, $w_{coat, p}$ and the numerical model, $w_{coat, n}$ was calculated as the mean variance, var_{mean} . The mean variance was then applied as a lower limit, $var_{(lower)}$ and upper limit, $var_{(upper)}$ for the numerical value $w_{coat, n}$, (see: Figure 55) where $var_{(lower)} \leftarrow w_{coat, n} \rightarrow var_{(upper)}$. This allowed a statistical level of confidence to be applied to the numerical model variance by determining the percentage of occurrence of the physical data $w_{coat, p}$ either inside or outside of the variance limits using Eq. 3.16.

$$\text{IF}[w_{coat,p} \geq var_{(lower)}]\text{AND}[w_{coat,p} \leq var_{(upper)}],$$

$$\text{TRUE} = \text{"Inside"}, \quad \text{FALSE} = \text{"Outside"} \quad \text{Eq 3.16}$$

Using Eq. 3.15, the variance of each material was extrapolated both above and below the calculated value of var_{mean} , to generate a map of variance against occurrence within limits (*i.e.* model confidence) (see: Figure 56). As the plot approaches the maximum y-axis value ($y = 100\%$) as indicated in the diagram, occurrence within limits increases and variance reduces. This implies that a material plot approaching this region shows increased accuracy in the numerical model for that material.

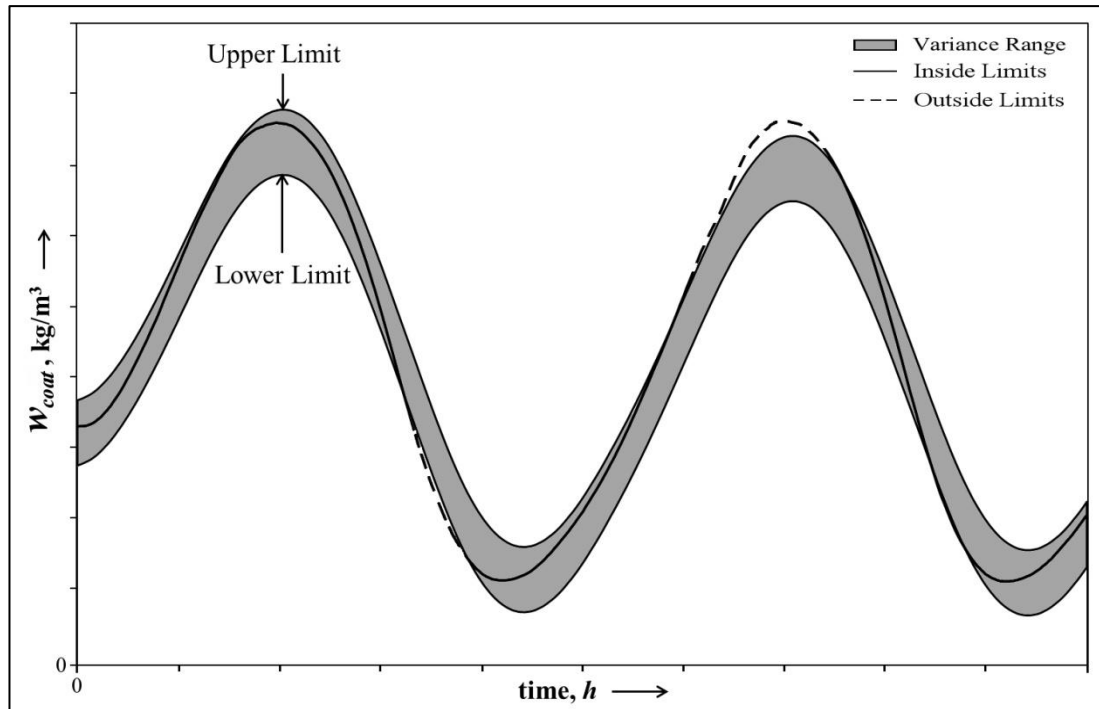


Figure 55 - Methodology for calculating variance occurrence inside and outside limits (Casey et al., 2012b).

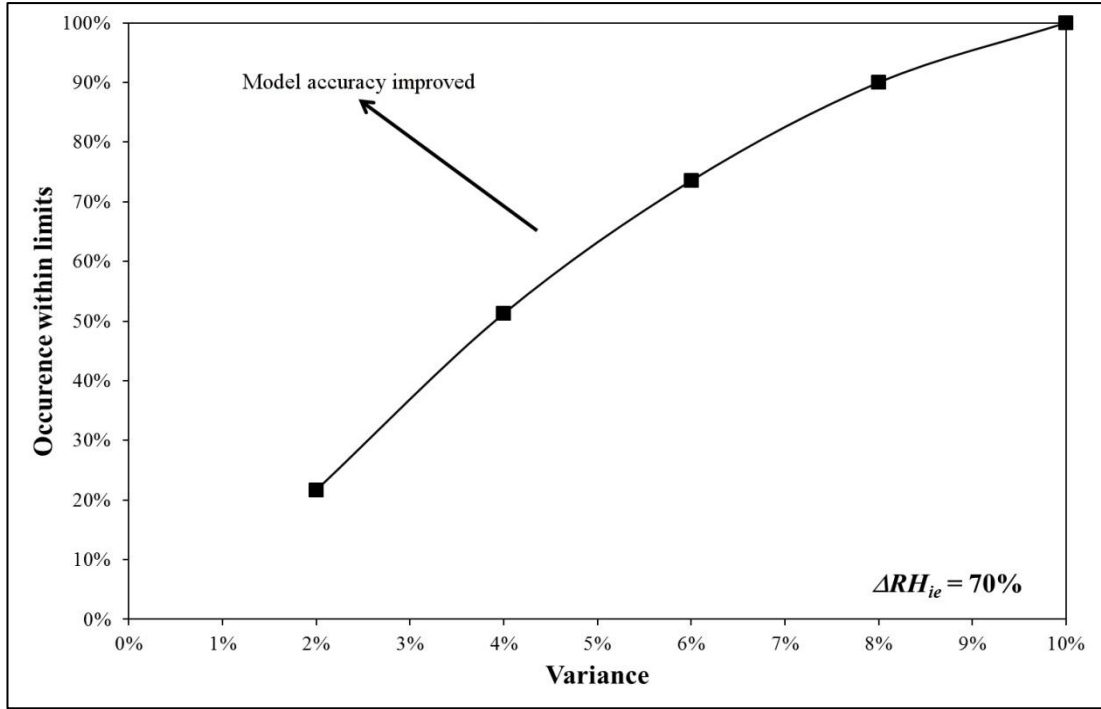


Figure 56 - Methodology for determining variance range and model confidence (Casey et al., 2012b).

3.5.1.4 ΔRH_{ie} Sensitivity Analysis Model

The next stage of the 1D modelling was to determine the sensitivity of RH_{coat} and w_{coat} to changes in RH_{ie} for the MS materials within the model. To achieve this, the sinusoidal cyclic response simulations were expanded, whilst maintaining identical parameters, to cover an increased ΔRH_{ie} range (see: Figure 57):

$\Delta RH_{ie} = 10\%, 30\%, 50\%, 70\%$ and 90% .

As in the previous model, all amplitudes were fluctuated sinusoidally about a RH_{ie} mean of 50% across a period $t = 24$ h for two full cycles. The total change in moisture content, Δw_{coat} and relative humidity, ΔRH_{coat} were then calculated using the simulated maximum and minimum values, respectively and plotted against the corresponding ΔRH_{ie} to assess material response over the RH_{ie} range. For the sensitivity of ΔRH_{ie} , only MS 3.3 MS 4.7 and MS 8.3 were simulated.

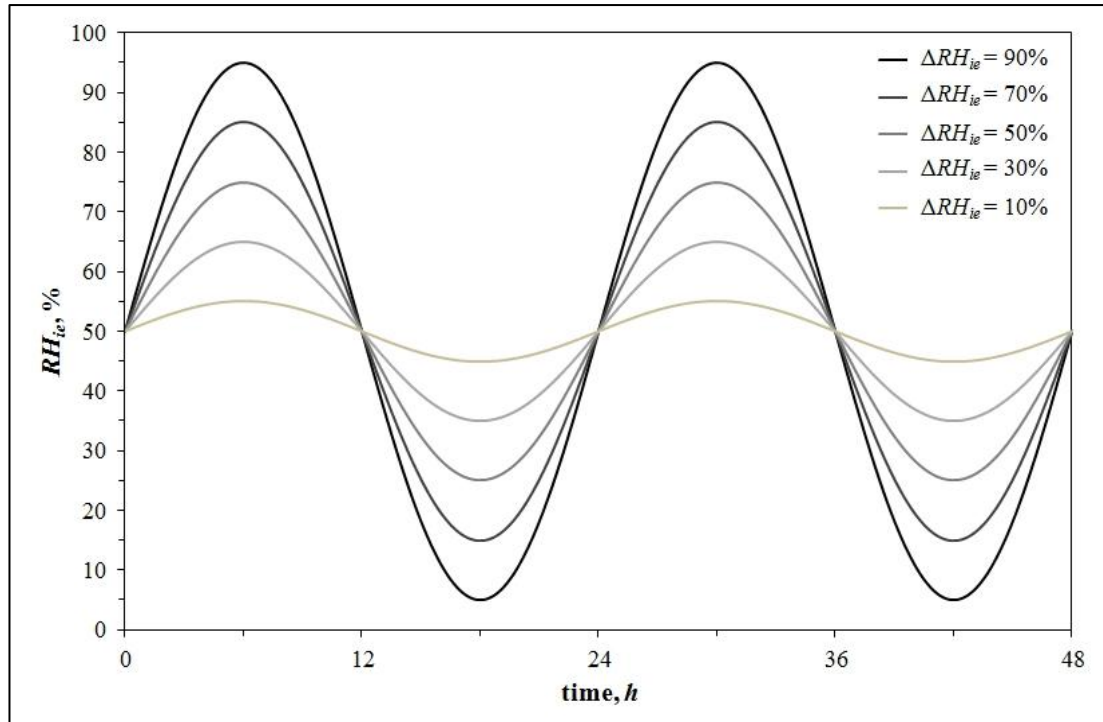


Figure 57 - Sinusoidal variation of RH_{ie} for sensitivity analysis model.

3.5.1.5 Material Tuning Model

The next stage of sensitivity analysis was to focus on utilising WUFI Pro v5.1 as a numerical tool to allow MS materials to be tuned for any specific application, *i.e.* a given set of psychrometric conditions. To test this hypothesis, it was necessary to determine to what extent each of the hygrothermal functional properties contribute to the behaviour of the MS coatings in the software. A series of three models were designed, each one tuning the behaviour of one MS material to match that of another:

MS 3.3 \rightarrow MS 8.3, MS 4.7 \rightarrow MS 3.3 and MS 4.7 \rightarrow MS 8.3

The procedure in each case was carried out as follows:

1. Adjust the sorption isotherm values ($w_{20} \rightarrow w_{50} \rightarrow w_{80} \rightarrow w_f$) to match the new material values
2. Adjust the water vapour diffusion resistance factor, μ to match the new

material

3. Adjust the water absorption coefficient, A_w to match the new material

Considering the difference in ΔRH_{coat} and Δw_{coat} values between the old and new material to represent 100%, the percentage changes in response to each adjustment were then quantified relative to this where a case of identical behaviour between old and new materials gave a percentage match approaching zero. All three models were simulated using an identical setup as that outlined for the sinusoidal cyclic response model (see: Section 3.5.1.3) and again run under the same ΔRH_{ie} range used in the previous test (10%, 30%, 50%, 70% and 90%) with average values of ΔRH_{coat} and Δw_{coat} used.

3.5.1.6 1D Building Retrofit Model

The final stage of the 1D numerical modelling was to perform a comparative study by analysing the performance of the three MS materials under representative external climate conditions and compare the results with those of traditional construction materials. To achieve this, four test cases were designed (see: Figures 58 - 61):

- Case 1. Standard wall. A solid brick wall with 15mm dense gypsum plaster having a painted interior surface finish.
- Case 2. Retrofitted gypsum wall. A solid brick wall with dense gypsum plaster. Retrofitted internally with a vapour barrier, vacuum insulation panel and dense gypsum plaster panelling with painted surface finish.
- Case 3. Retrofitted spruce wall. A solid brick wall with dense gypsum plaster. Retrofitted internally with a vapour barrier, vacuum insulation panel and unfinished spruce cladding.
- Case 4. Retrofitted MS wall. A solid brick wall with dense gypsum plaster.

Retrofitted internally with a vapour barrier, vacuum insulation panel and a thin MS material coating.

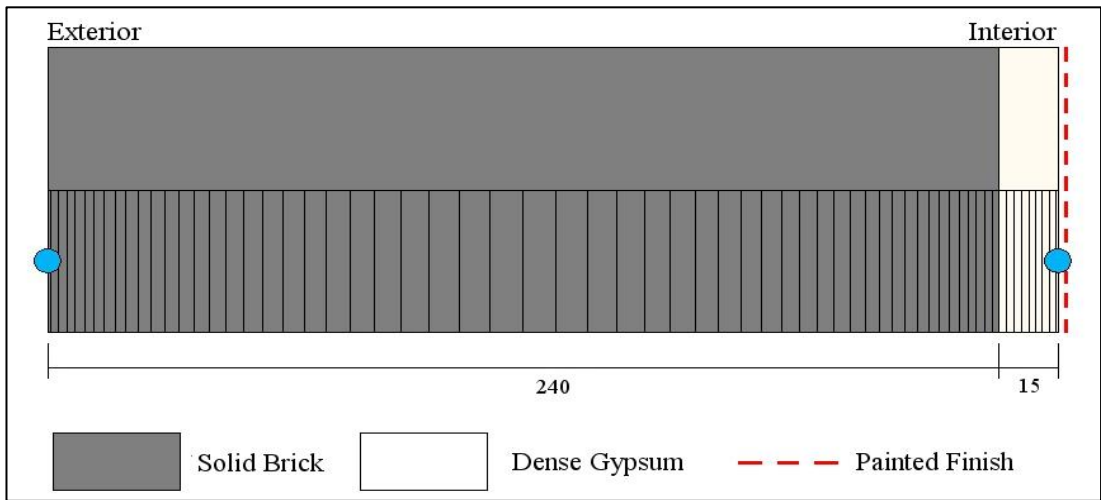


Figure 58 – Case 1 assembly for the numerical building retrofit model showing monitor positions and grid spacing.

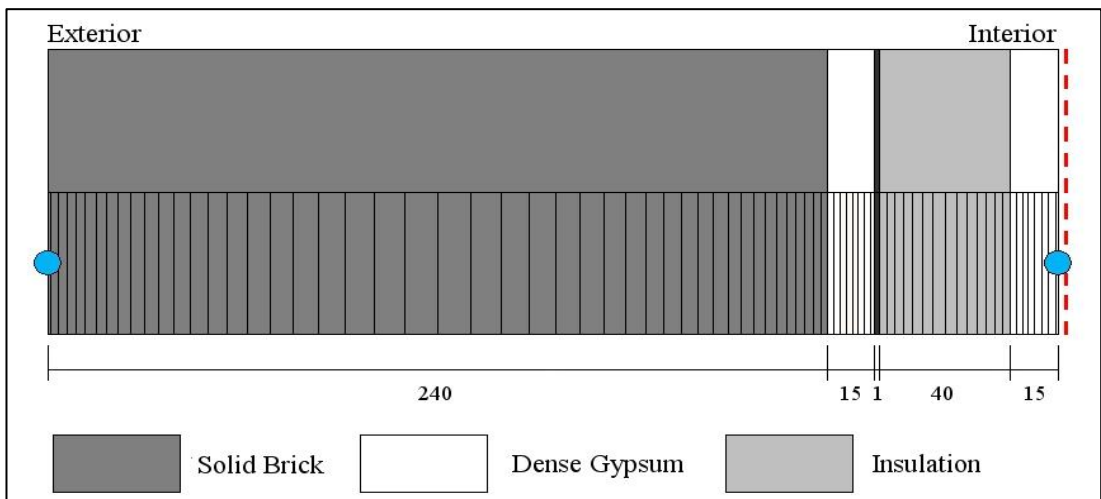


Figure 59 - Case 2 assembly for the numerical building retrofit model showing monitor positions and grid spacing.

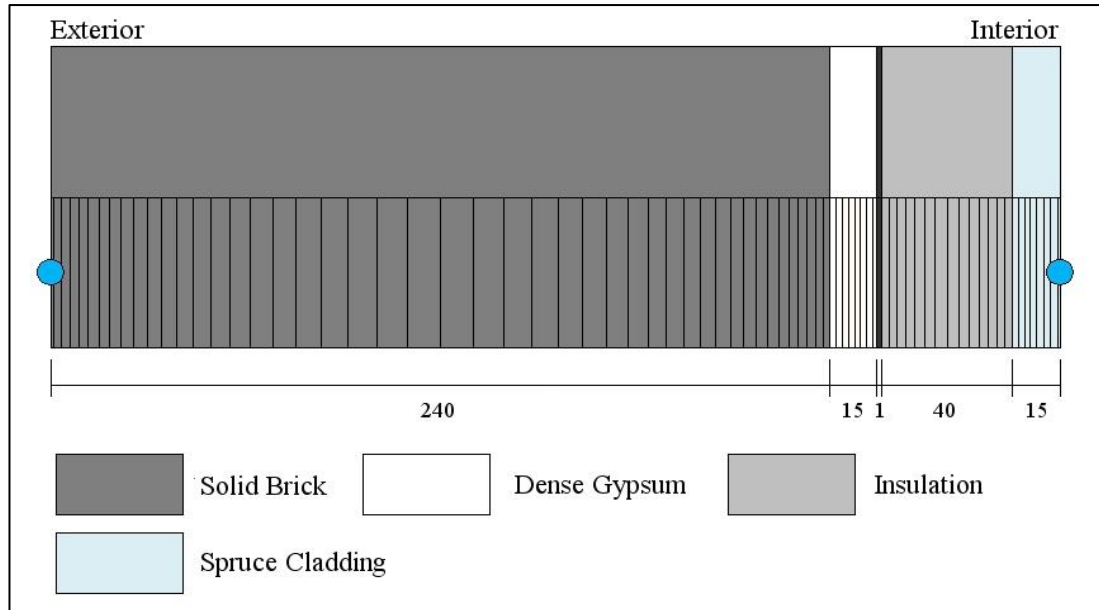


Figure 60 - Case 3 assembly for the numerical building retrofit model showing monitor positions and grid spacing.

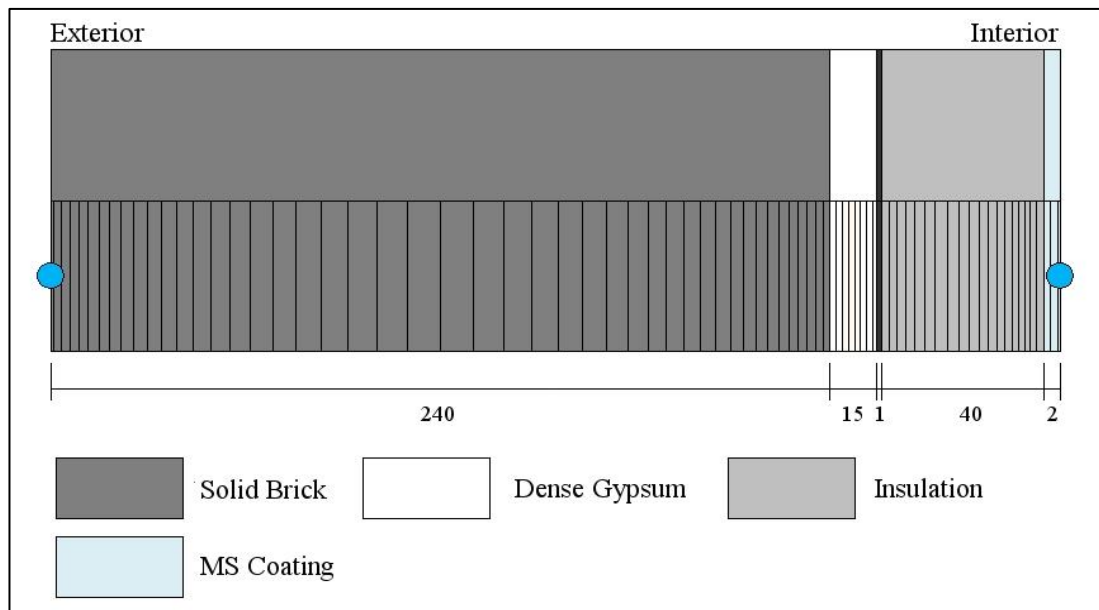


Figure 61 - Case 4 assembly for the numerical building retrofit model showing monitor positions and grid spacing.

To simulate a typical building scenario, the building volume was set to 500m^3 with a user defined air exchange rate of 0.5 ACH for Case 1 (*i.e.* pre retrofitting) and 0.1 ACH for Cases 2 - 4 (*i.e.* post retrofitting). Short-wave absorptivity, α was assumed to be 0.68 for red brick and a long-wave emissivity, ε of 0.7. Internal vapour resistances were set according to material type except for Case 1 and 2 where an S_d -

Value of 0.5 m was selected to represent increased vapour resistance from the paint finish on the gypsum.

The exterior climate file used (see: Figure 62) for the model was generated from the CIBSE test reference year (TRY) file for Nottingham (CIBSE, 2008), using WUFI's 'create climate file' software tool. The calculation period was for one year from 1st October 2011 to 1st October 2012. The interior climate file was generated from the exterior file using WUFI's built in calculator. This is an iterative calculation method based on ASHRAE 160 standard (ASHRAE, 2009b) that is used to determine indoor design conditions. 'Heating Only' was selected for the air conditioning method with a floating indoor temperature shift of 6°C and a set point for heating of 23°C. Moisture generation was set at 9×10^{-5} kg/s for all cases. Other parameters used in the model can be seen in Table 21.

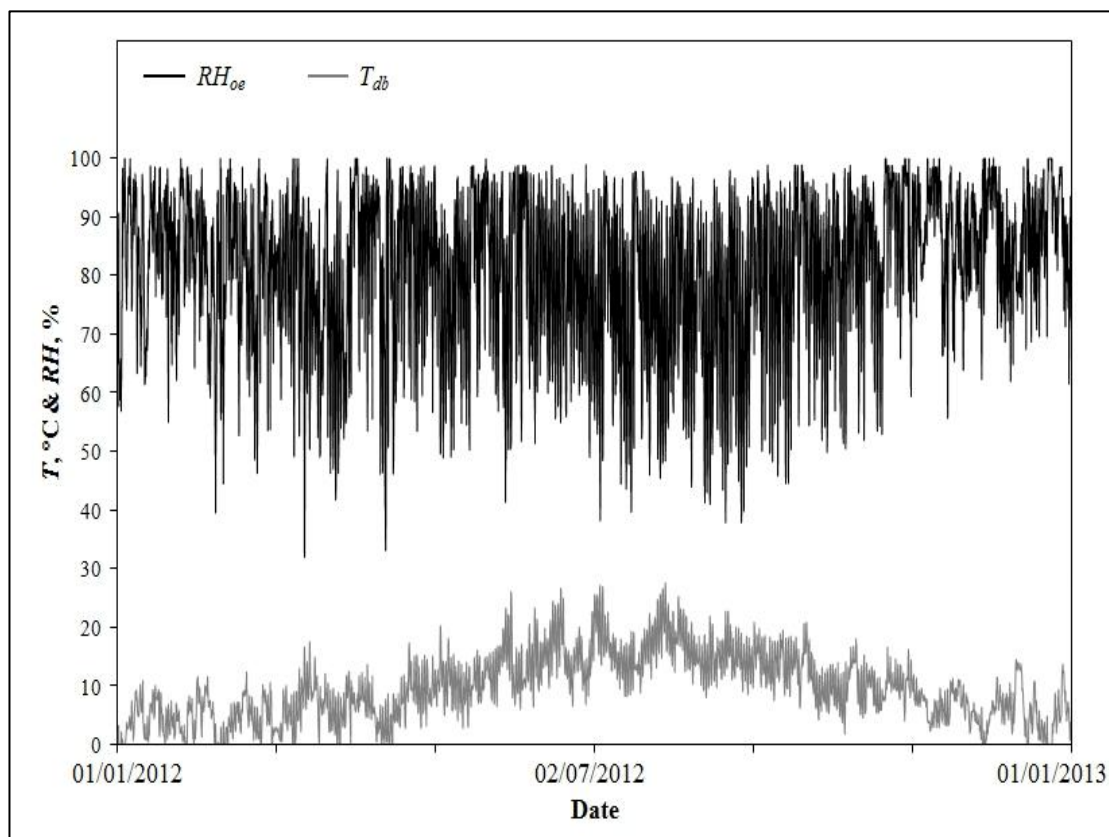


Figure 62 - External climate for the 3D building retrofit model generated from the Nottingham CIBSE TRY file.

Parameter	Value	Parameter	Value
Calculation Period	1 year	Heat Resistance (Ext.)	0.0588 m ² K/W
Time Step	1 h	S_a -Value (Ext.)	0
Orientation	West	Heat Resistance (Int.)	0.125 m ² K/W
Inclination	90°	Initial RH / T	80% / 20 °C
Exterior RH / T	CIBSE TRY	Interior RH / T	ASHRAE 160

Table 21 - Input parameters for the numerical building retrofit model.

3.5.2 3D Numerical Models

The whole building (3D) numerical models were designed to replicate the testing carried out in the 3D physical modelling section (see: Section 3.4.2). The 3D models were used to perform parametric analysis of the material's influence on interior humidity levels by altering envelope assemblies, materials, occupancy levels and ventilation and/or air infiltration to the interior environment.

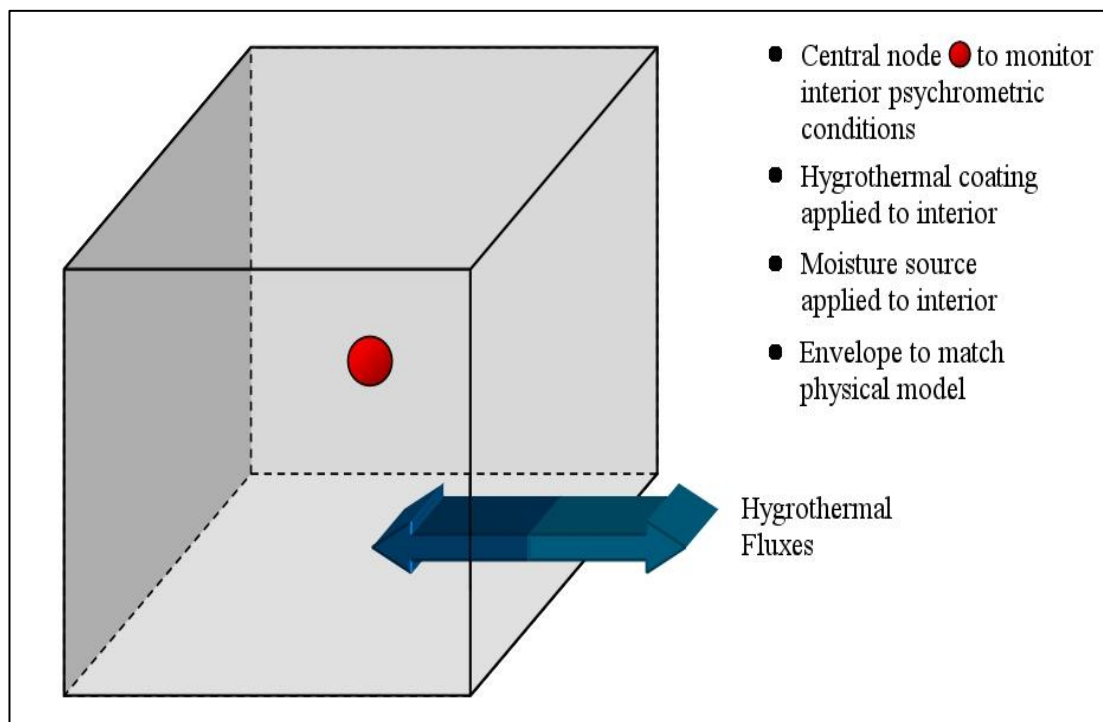


Figure 63 - Schematic representation of the 3D numerical model volume showing a central monitoring node and the hygrothermal fluxes.

Unlike the 1D model, the 3D model allows monitoring of the changes to interior

psychrometric conditions using a central monitoring node based on the changes listed above (see: Figure 63). Once validated against the physical model, the numerical model was then utilised to perform a comparative study of humidity buffering performance by using representative exterior psychrometric conditions with different envelope assemblies. Further energetic 3D modelling was used to determine potential operational energy savings by utilising oversized HCHD plant (see: Section 3.5.2.6).

All 3D models were scaled as discussed in Section 3.4.2.1 and have certain parameters that remain the same through the various modelling phases and are listed in Table 22. The volumes were constructed using the WUFI building wizard to have a rectangular main facade with $d1 = 1$ m and $d2 = 1$ m. The storey height was set at 1 m for 1 storey only. The roof was selected as an unheated space with dimensions $h1 = 0.5$ m. The bottom of the volume was selected as ‘On ground’. In all cases the roof space was designated as an ‘unheated space’ and set to the outer climate. As in the 1D simulations, all model numerics were set to have increased accuracy and adaptive convergence with grid spacing set to ‘medium’.

Parameter	Value	Parameter	Value
Time Step	1 h	Optional Climate	50% / 23 °C
Net Volume	1 m ³	Inner Climate	Calculated
Main Orientation	South	Initial <i>RH</i> / <i>T</i>	50% / 23 °C
Initial CO₂	1000 ppmv	Calculation Accuracy	0.5% / 0.5 °C

Table 22 - Unchanged input parameters for all 3D numerical models.

3.5.2.1 Material Humidity Buffering Model

The material humidity buffering model was designed to validate the numerical model using the same conditions as the humidity buffering experiments (see: Section

3.4.2.3). Once validated, the numerical model was then used to perform a range of expansive simulations as described in the following sections. The parameters used in the material humidity buffering model can be found in Table 23.

The envelope was designed to thermally and hygrically isolate the indoor environment from the outdoor. (see: Figure 64). This was achieved by placing a 2mm vapour barrier ($S_d = 1500$ m) to the exterior and interior of a 240 mm ‘super-insulator’ ($\lambda = 0.003$ W/(m K)). The same assembly was used for walls, floor and ceiling. A moisture profile was applied to the model using the ‘Inner Loads/Occupancy’ tool with a scaled up generation rate of 2.24 g/h being added between 0:00 and 8:00 to match the physical model (see: Section 3.4.2.1). A steady state external climate file was used for all simulations ($T = 23$ °C, $RH_{oe} = 50\%$) with no air infiltration.

Parameter	Value	Parameter	Value
Calculation Period	7 Days	HVAC	None
S_d -Value (Int.)	1500 m	S_d -Value (Ext.)	1500 m
R_{si} (Wall)	0.13 m ² K/W	R_{se} (Wall)	0.04 m ² K/W
R_{si} (Roof)	0.1 m ² K/W	R_{se} (Roof)	0.1 m ² K/W
R_{si} (Ground)	0.17 m ² K/W	R_{se} (Ground)	0.04 m ² K/W
Absorption Coefficient	0	Emission Coefficient	0
Envelope U-Value	0.004 W/m ² K	Envelope R-Value	240 m ² K/W

Table 23 - Input parameters for the material humidity buffering model.

To match the physical model, a total of six simulations were performed. As the ratio of hygrothermal material (exposed surface area) to interior wall surface area in the physical model was approximately 3%, it was necessary to maintain this ratio in the numerical model also. To achieve this, a ‘Non-Visualised Component’ with a proportional surface area ($A = 0.12$ m²) was added to the model and attached to the

building interior (Zone 1: Heated Space). The assembly of the component consisted of an oversized vapour barrier ($S_d = 1500 \text{ m}$) to ensure moisture transfer to the test materials placed on the interior was 1D only. Material depth was selected to match that of the physical model (See: Section 3.4.2.3).

In order to assess the level of confidence in the WUFI Plus model, the statistical variance between the numerically predicted data and the physical data was analysed using the same procedure as discussed in Section 3.5.1.3.

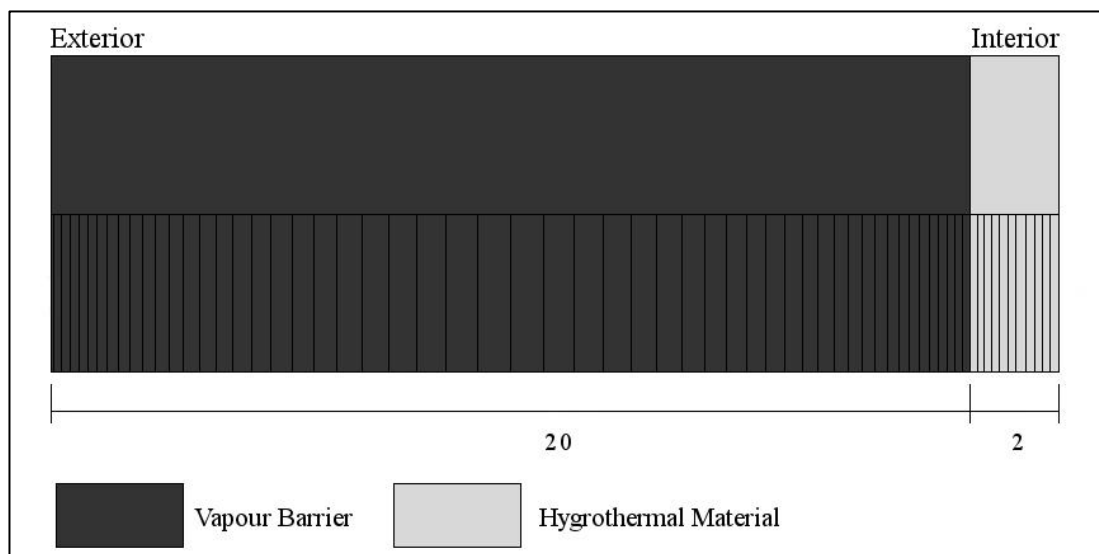


Figure 64 - Envelope assembly for the 'non-visualised attachment' in the humidity buffering model.

3.5.2.2 Increased Hygrothermal Area/ Volume Ratio Model

The increased hygrothermal area/ volume model expanded on the previous model by sequentially increasing the ratio of hygrothermal material surface area to the internal wall surface area. This allowed analysis of the effectiveness of the materials to be determined *i.e.* what quantity of material is required to produce the desired humidity buffering within ASHRAE limits. The steps were:

0% → 5% → 10% → 20% → 40% → 60% → 80% → 100%

For the six hygrothermal materials, the envelope and 'non-visualised component'

constructions remained the same as those used in the previous model. An external climate file was generated using the ‘Create Climate File’ software to sinusoidally fluctuate RH_{oe} about a median ($RH_{oe} = 50\%$) at constant temperature ($T = 23\text{ }^{\circ}\text{C}$) for a single peak to peak cycle period $t = 24\text{ h}$ with an amplitude:

$RH_{oe} 15\% \rightarrow 85\% \rightarrow 15\%$ giving a $\Delta RH_{oe} = 70\%$ (see: Figure 57).

The model was then further expanded by running the same set of proportional area simulations under four different air exchange rates, with and without the moisture generation schedule from Section 3.4.2.1 to assess the impact of air infiltration on material effectiveness. The steps were:

0.1 ACH \rightarrow 0.2 ACH \rightarrow 0.5 ACH \rightarrow 1.0 ACH.

3.5.2.3 Cyclic Response Testing Model

The cyclic response testing model was designed to assess the effects of the hygrothermal materials (at 100% surface area ratio) on RH_{ie} under differing ΔRH_{oe} amplitude variations. Similarly to the 1D sensitivity analysis model (see: Section 3.5.1.4), this allowed sensitivity analysis to be undertaken over an extended humidity range testing model linearity. An external climate file was generated to sinusoidally fluctuate RH_{oe} about a median ($RH_{oe} = 50\%$) at constant temperature ($T = 23\text{ }^{\circ}\text{C}$) for a single peak to peak cycle period $t = 24\text{ h}$ for 4 different climates (see: Figure 57 for illustrative example):

Climate 1. $RH_{oe} 15\% \rightarrow 85\% \rightarrow 15\%$ giving a $\Delta RH_{oe} = 70\%$

Climate 2. $RH_{oe} 25\% \rightarrow 75\% \rightarrow 25\%$ giving a $\Delta RH_{oe} = 50\%$

Climate 3. $RH_{oe} 35\% \rightarrow 65\% \rightarrow 35\%$ giving a $\Delta RH_{oe} = 30\%$

Climate 4. $RH_{oe} 45\% \rightarrow 55\% \rightarrow 45\%$ giving a $\Delta RH_{oe} = 10\%$

In total, 6 building scenarios were designed to represent the retrofitting of a typical building. To have continuity across the research the cases reflected those in the 1D building retrofit models (see: Section 3.5.1.6). All material properties and dimensions were identical. However there were no monitor positions in the constructions. (see: Figures 58 - 61).

An identical envelope assembly (for each case) was used for all walls, floors and ceilings. Common parameters across all cases are contained in Table 24, whilst all other parameters applicable for each case can be seen in Tables 25 – 28. As in the previous section, the model was again further expanded by running the same set of simulations under four different air exchange rates to assess the impact of air infiltration on ΔRH_{ie} sensitivity (see: Section 3.5.2.1).

Parameter	Value	Parameter	Value
Calculation Period	7 Days	HVAC	None
Rsi (Wall)	0.13 m ² K/W	Rse (Wall)	0.04 m ² K/W
Rsi (Roof)	0.1 m ² K/W	Rse (Roof)	0.1 m ² K/W
Rsi (Ground)	0.17 m ² K/W	Rse (Ground)	0.04 m ² K/W
Absorption Coefficient	0.68	Emission Coefficient	0.9

Table 24 - Common input parameters for all cyclic response 3D numerical models.

Parameter	Value	Parameter	Value
S_d -Value (Int.)	0.5 m	S_d -Value (Ext.)	0 m
Envelope U-Value	1.55 W/m ² K	Envelope R-Value	0.475 m ² K/W

Table 25 - Input parameters for the cyclic response model - Case 1: Standard Wall.

Parameter	Value	Parameter	Value
S_d -Value (Int.)	0.5 m	S_d -Value (Ext.)	0 m
Envelope U-Value	0.02 W/m ² K	Envelope R-Value	40.55 m ² K/W

Table 26 - Input parameters for the cyclic response model - Case 2: Retrofitted Wall.

Parameter	Value	Parameter	Value
S_d -Value (Int.)	0 m	S_d -Value (Ext.)	0 m
Envelope U-Value	0.02 W/m ² K	Envelope R-Value	40.642 m ² K/W

Table 27 - Input parameters for the cyclic response model - Case 3: Spruce Cladding.

Parameter	Value	Parameter	Value
S_d -Value (Int.)	0 m	S_d -Value (Ext.)	0 m
Envelope U-Value	0.02 W/m ² K	Envelope R-Value	40.515 m ² K/W

Table 28 - Input parameters for the cyclic response model - Case 4: MS Coating.

3.5.2.4 Increased Moisture Load Model

The increased moisture load model was designed to assess the effects of the hygrothermal materials on the indoor conditions under a moisture ‘over-loading’ scenario. An example of this would be a large gathering of people in a house or use of excessive moisture generating equipment (*i.e.* steam cleaner). The external climate file was generated to sinusoidally fluctuate RH_{oe} about a median ($RH_{oe} = 50\%$) at constant temperature ($T = 23\text{ }^{\circ}\text{C}$) for a single peak to peak cycle period $t = 24\text{h}$:

$$RH_{oe} 15\% \rightarrow 85\% \rightarrow 15\% \text{ giving a } \Delta RH_{oe} = 70\%$$

As in the previous model, a total of six building scenarios were simulated to represent the retrofitting of a typical building with identical material properties, parameters and dimensions. The envelope assemblies used for all walls, floors and ceilings (for each case) remained the same. Two sets of increased moisture profiles were applied to the model in order to represent 16 ‘Active Adults’ present in either the morning or evening for a period $t = 4\text{ h}$. Table 29 contains the profiles of times and moisture loads, g_g . As in the previous section, the model was again further expanded by running the same set of simulations under four different air exchange

rates to assess the impact of air infiltration on ΔRH_{oe} sensitivity (see: Section 3.5.2.1).

Morning Occupancy		Evening Occupancy	
Time (h)	g_g (g/h)	Time (h)	g_g (g/h)
0 to 8	0	0 to 18	0
8 to 12	51.25	18 to 22	51.25
12 to 24	0	22 to 24	0

Table 29 - Morning and evening moisture profiles for the increased occupancy numerical model.

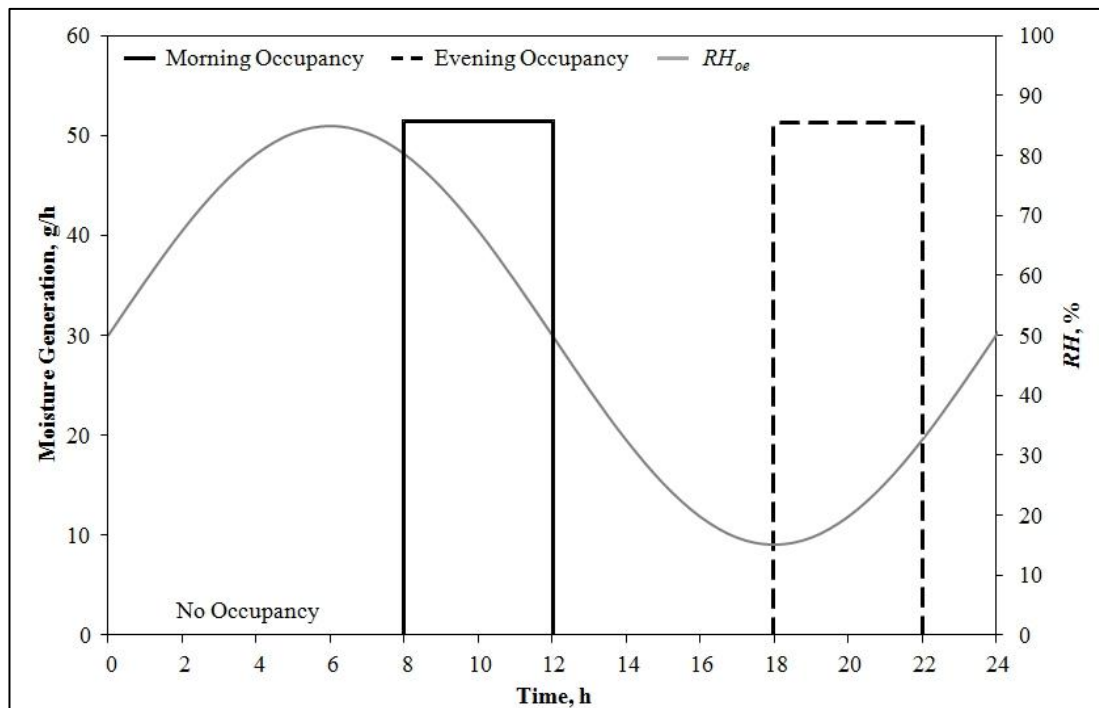


Figure 65 - Graph showing 'over-loading' occupancy schedules and sinusoidal variation of RH_{oe} for the increased moisture load model.

3.5.2.5 Increased Air Exchange Rate Model

The increased air exchange rate model was designed to assess the effectiveness of the hygrothermal materials under a sudden increase in ventilation. A typical example of this scenario would be opening numerous windows in a house. The external climate file used was the same as the previous model ($\Delta RH_{oe} = 70\%$ at 23 °C). The same six building scenarios were simulated with identical material properties,

parameters and dimensions (see: Section 3.5.2.4). The envelope assemblies used for all walls, floors and ceilings (for each case) remained the same. Two sets of increased ventilation profiles were applied to the model using the ‘Ventilation’ tab in the ‘Design Conditions’ tool. A profile was input to simulate opening a number of windows, either in the morning or evening, for a period $t = 8$ h. Table 30 contains the profiles of times and ventilation, ACH. The model was expanded by simulating under 5 increased ventilation rates:

1 ACH \rightarrow 2 ACH \rightarrow 3 ACH \rightarrow 5 ACH \rightarrow 10 ACH.

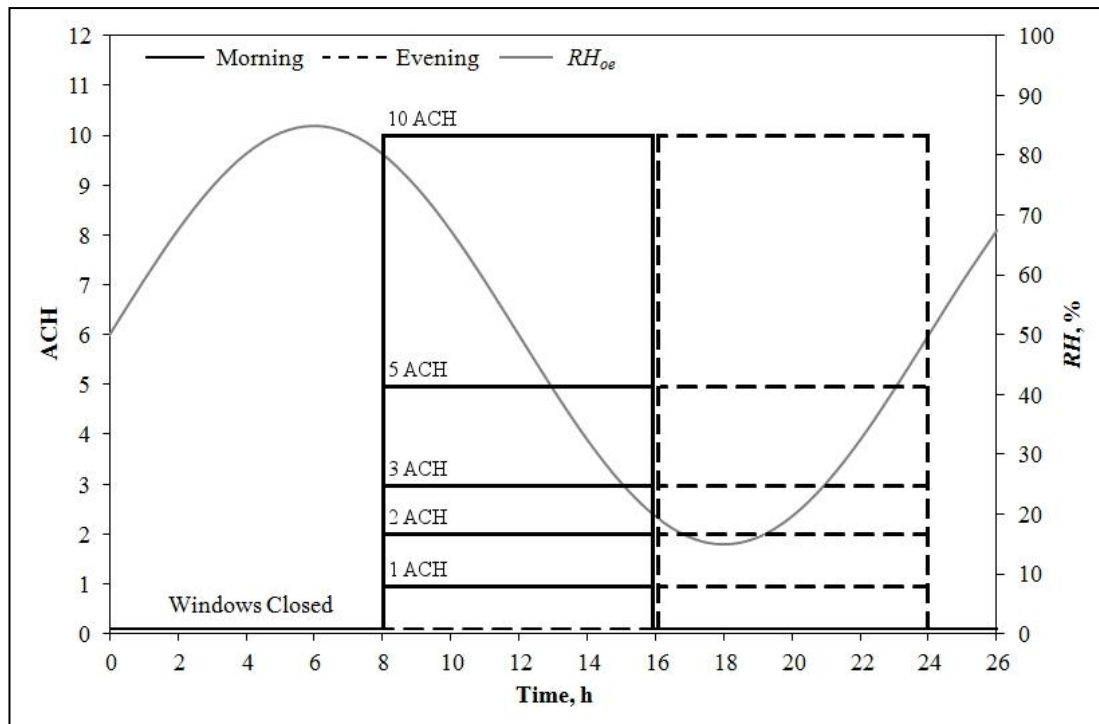


Figure 66 - Graph showing window opening schedules and sinusoidal variation of RH_{oe} for the increased air exchange rate model.

Morning Occupancy		Evening Occupancy	
Time (h)	ACH	Time (h)	ACH
0 to 8	0.1	0 to 16	0.1
8 to 16	1, 2, 3, 5, 10	16 to 24	1, 2, 3, 5, 10
16 to 24	0.1		

Table 30 - Morning and evening ACH profiles for the increased air exchange numerical model.

3.5.2.6 3D Representative Climate Model

The final stage of the 3D numerical modelling was to perform a comparative study of the three MS materials and the traditional construction materials using the same exterior climate file used in Section 3.5.1.6, generated from the CIBSE test reference year (TRY) file for Nottingham (see: Figure 62).

In addition WUFI Plus was used to perform analysis of any potential operational energy savings gained from using the MS materials to buffer RH_{ie} by monitoring the HCHD plant energy load required for control when the humidity moved outside of preset limits. To achieve this and to perform comparative analysis, the same six test cases were again used with identical parameters as used previously for four modelling stages:

- Stage 1. Simulation of a 2 year period to investigate the influence of increasing depths of the material coatings (2 mm, 4 mm, 8 mm and 12 mm)
- Stage 2. Repeat of stage 1 at a selected material depth with and without occupation to perform further comparative analysis
- Stage 3. Repeat of stage 2 (occupied only) with a HCHD plant specified to control the interior climate at $21\text{ }^{\circ}\text{C} < T < 25\text{ }^{\circ}\text{C}$ and $45\% < RH_{ie} < 65\%$ complete HCHD control for $t = 24\text{ h}$
- Stage 4. Repeat of stage 3 with partial HCHD control for $t = 8\text{ h}$
- Stage 5. Repeat of stage 4 with the HCHD plant limits set at $T = 23\text{ }^{\circ}\text{C}$ and $40\% < RH_{ie} < 70\%$ to represent the ASHRAE comfort conditions

The oversized HCHD plant (1 GW) was specified so that any equipment limitations would not be a factor in the analysis. This allowed for instantaneous and complete control of T_{ie} and RH_{ie} when outside the limits set out above. In the complete control

scenario the HCHD plant was operated constantly, whilst for the partial control scenario the HCHD control was set to operate only for the period where typical building occupation would occur, from 00:00 to 08:00 ($t = 8$ h).

The calculation period for all simulations was for two years from 01/01/12 to 01/01/14. It is important to note however that the climate file used is not an actual representation of these years. Results presented in Section 6.8 are for the second year only to allow for one full year of pre-simulation and correct convergence within the model. In general, this resulted in slightly higher RH_{ie} levels than would have been otherwise presented for the first year only and so was deemed to be a better representation of moisture loading.

3.6 Experimental Error

3.6.1 Pore Network Characterisation

For the physisorption results (see: Section 4.2.1) errors are shown in the results where applicable. Mean pore diameter, pore volume and monolayer volume results have no error shown as the data is interpreted from the adsorption isotherm results (see: Figures 68 and 69). The solid density results obtained using the helium pycnometer are accurate to within $\pm 0.09\%$ when the sample volume, cell volume and sample mass errors are considered (see: Section 4.2.4). Where the average value is represented, the cumulative accuracy across the five tests is calculated and shown in Table 32.

For the bulk density results measured gravimetrically the mass measurements taken using the Vibra HT balance were accurate to ± 0.1 mg ($\approx 0.01\%$ for a 1 g sample) and are negligible. Volume measurements were accurate only to 5% using the graduated cylinder. Where the bulk density average value is represented, the cumulative accuracy across the three tests is calculated and shown in Table 33 with

the corresponding porosity error shown in Table 34.

3.6.2 Hygrothermal Characterisation

The sorption isotherm, vapour permeability, water absorption and MBV tests (see: Section 4.3.1 – 4.3.5) were carried out using the same Vibra HT balance (accuracy $\pm 0.01\%$) and therefore any errors are negligible.

The thermal conductivity testing performed using the Seteram MTPS technique was accurate to $\pm 5\%$. Where the average value is represented, the cumulative accuracy across the five tests is calculated and shown in Table 41. The specific heat capacity measurements performed using differential scanning calorimetry was accurate to $\pm 2\%$ with the cumulative accuracy across the five tests is calculated and shown in Table 42.

3.6.3 Physical Modelling

The 1D physical modelling was undertaken using the Vibra HT balance to measure mass uptake (accuracy $\pm 0.01\%$) and therefore any errors are negligible and are not shown. In the 3D model, however relative humidity is measured using the Tinytag Ultra sensors which have accuracy of $\pm 3\%$ RH at $23\text{ }^{\circ}\text{C}$. This error is represented graphically in Section 6.3.1, Figure 98 with the results from the physical model shown as a grey shaded area.

3.7 Summary

This chapter outlined the methodology that was designed to meet the objectives outlined in Section 1.4. The research methodology consisted of three distinct stages:

- To establish a link between material behaviour under set psychrometric conditions and the material's pore network geometry, experimental analysis

to characterise the hygrothermal functional properties and the pore network of the materials using a range of techniques as outlined in Sections 3.2 and 3.3 were carried out.

- In Sections 3.4.1 and 3.5.1 the 1D physical and validated numerical models were designed to parametrically analyse material behaviour based on the hygrothermal properties obtained during Section 3.3. The range of ΔRH_{ie} amplitudes simulated allowed sensitivity analysis of material behaviour. A comparative study of the desiccant material performance against that of traditional materials under representative climate conditions and building envelopes was also designed. This enabled analysis to be carried out to determine the applicability of using the numerical model as a material selection tool by ‘tuning’ material properties and linking with the pore network characteristics.
- In Sections 3.4.2 and 3.5.2 the 3D physical and validated numerical models were designed to parametrically analyse changes to internal climate conditions, occupant comfort and potential energy savings resulting from the presence of the hygrothermal materials under representative moisture generation schedules and external climates. The analysis was expanded by altering envelope assemblies, materials, occupancy levels and air infiltration to the interior environment.

CHAPTER 4: Material Characterisation Results

4.1 Introduction

This chapter presents the results obtained from the characterisation of the pore network and hygrothermal functional properties as discussed in Section 1.4 to meet Objective 2.

4.2 Characterisation of the Porous Network Results

4.2.1 N₂ Physisorption

N₂ Physisorption results were obtained based on the techniques and theory presented in Sections 2.4 and 4.2.1. As discussed, powder samples of mass $m \approx 0.25$ g were initially vacuum desiccated for a period $t = 24$ h before being placed in a sample vial on the test rig and prepared by outgassing under elevated temperature $T \geq 120$ °C and vacuum conditions for a period of time $t = 6$ h. The specific surface area (SSA), pore volume and monolayer adsorption for the eight candidate materials; MS3.3, MMS4.8, MS4.7, MS8.3, Bentonite, Mol Sieve 10Å, Silica Gel and Clinoptilolite were determined using multipoint Brunauer-Emmett-Teller (BET) analysis and the data is presented in Table 31.

For MS 4.7, MS 8.3 and MMS 4.8 the SSA was significantly higher than the conventional desiccants whilst MS 3.3 and silica gel appear to have similar SSA's. Both bentonite and clinoptilolite have comparatively low SSA's of 29 m²/g. There was a positive relationship between mesopore diameter and pore volume in the MS/MMS samples, but not to SSA which may suggest that the mesopores have varying degrees of corrugation contributing to an increased SSA for the MMS 4.8

and MS 4.7 samples. All data for the non MS samples compared favourably with previously published data (Gao et al., 2006, Wang et al., 2009, ASHRAE, 2009a, Zalba et al., 2009).

	BET Surface Area (m ² /g)	Monolayer Volume (cm ³ /g)	Pore Volume (cm ³ /g)	Mean pore Diameter (nm)
MS 3.3*	748 ± 5.24	163.31	0.65	3.3
MMS 4.8*	1574 ± 22.27	361.78	0.72	4.7
MS 4.7*	1114 ± 17.65	256.10	1.14	4.7
MS 8.3*	1084 ± 8.62	249.11	1.32	8.3
Mol Sieve 10Å	538 ± 10.67	123.63	0.35	1.2
Silica Gel	701 ± 2.06	161.09	0.42	2.6
Clinoptilolite	29 ± 0.13	6.66	0.14	≈30
Bentonite	29 ± 0.04	6.68	0.18	≈14

*Results obtained by Prof. Edman Tsang at the University of Oxford

Table 31 - Results of N₂ physisorption measurements of the candidate materials (Hall et al., 2012).

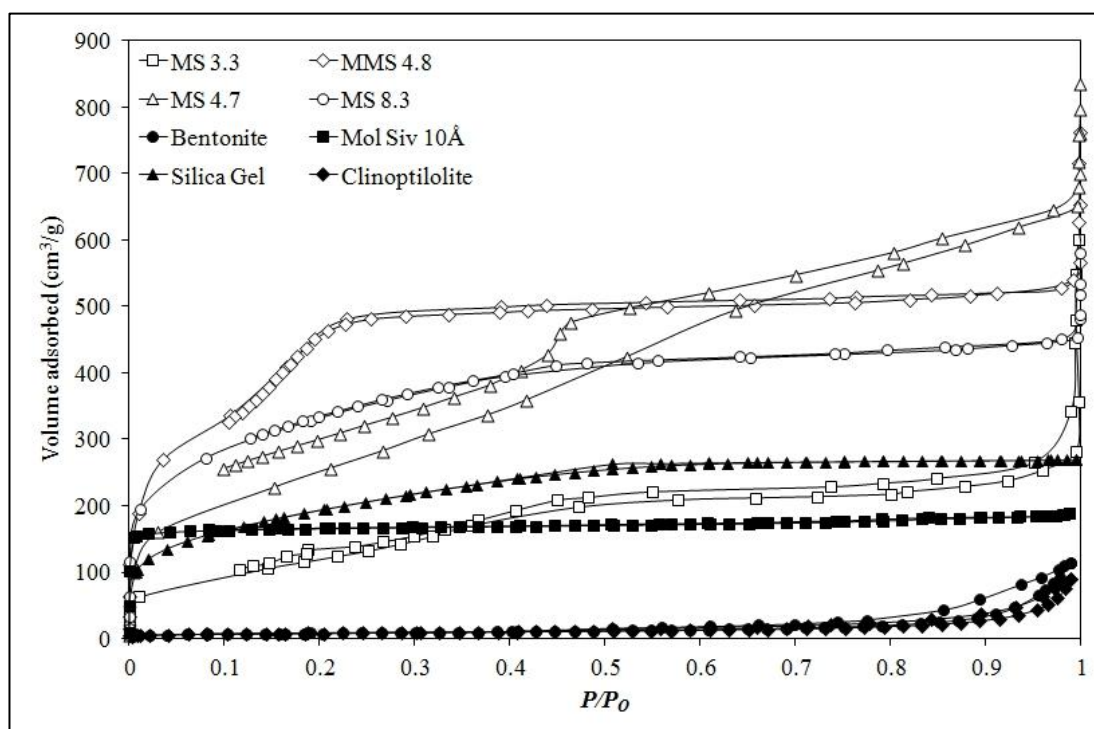


Figure 67 – N₂ adsorption/desorption isotherms of all candidate materials.

The N₂ isotherms for the candidate materials are shown in Figure 67. The MS

materials showed increased N_2 monolayer capacities over the conventional desiccants with the exception of MS 3.3 having less capacity than the silica gel sample. The MS materials were all variants of Type IV isotherms indicating a mesoporous network with MS 4.7 displaying pronounced hysteresis suggestive of type 'b' pores with narrow openings leading to the 'ink bottle' effect (see: Section 2.4.1). The 10\AA molecular sieve showed typical Type I isotherm behaviour associated with microporous materials with significant initial uptake but no N_2 adsorption in the mesopore range. Clinoptilolite and bentonite showed minimal adsorption across the entire pore range.

Figures 68 and 69 show the mesopore diameter volumetric distribution, determined by the Barrett–Joyner–Halenda (BJH) method, for the candidate materials. Clinoptilolite and bentonite displayed wide ranging mesopore distributions approaching the macropore range. There was evident bimodal pore distribution for the MMS 4.8 sample again suggesting some corrugation within the pore network leading to misinterpretation of the N_2 desorption isotherm by the BJH algorithm.

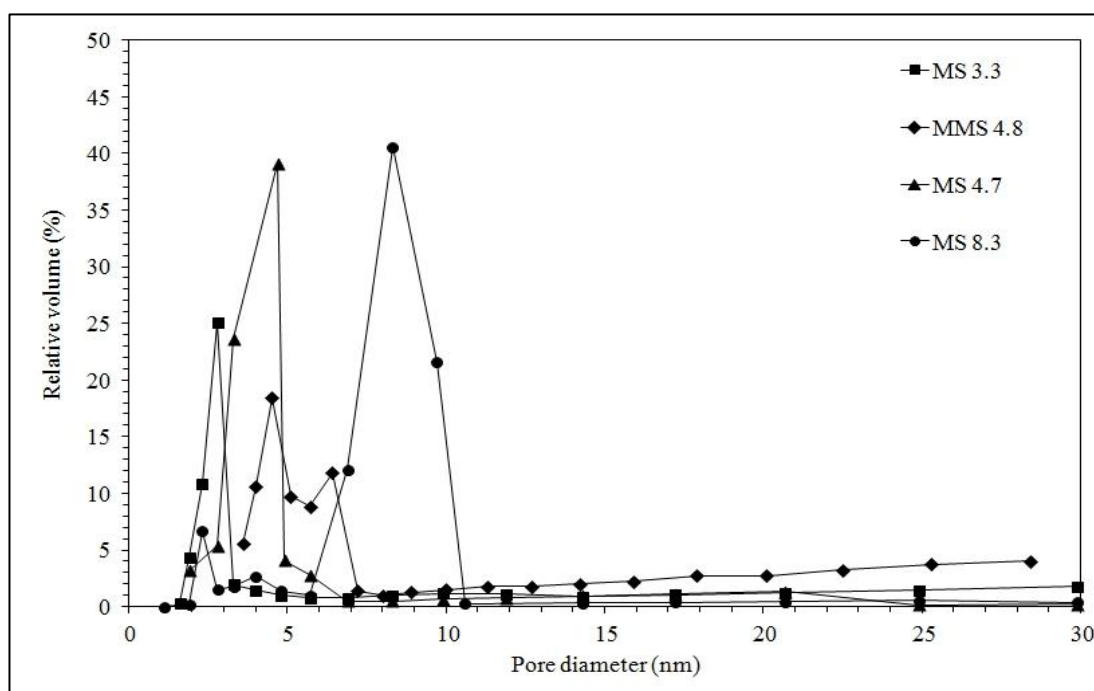


Figure 68 - BJH pore size distribution of the MS samples (Hall et al., 2012b).

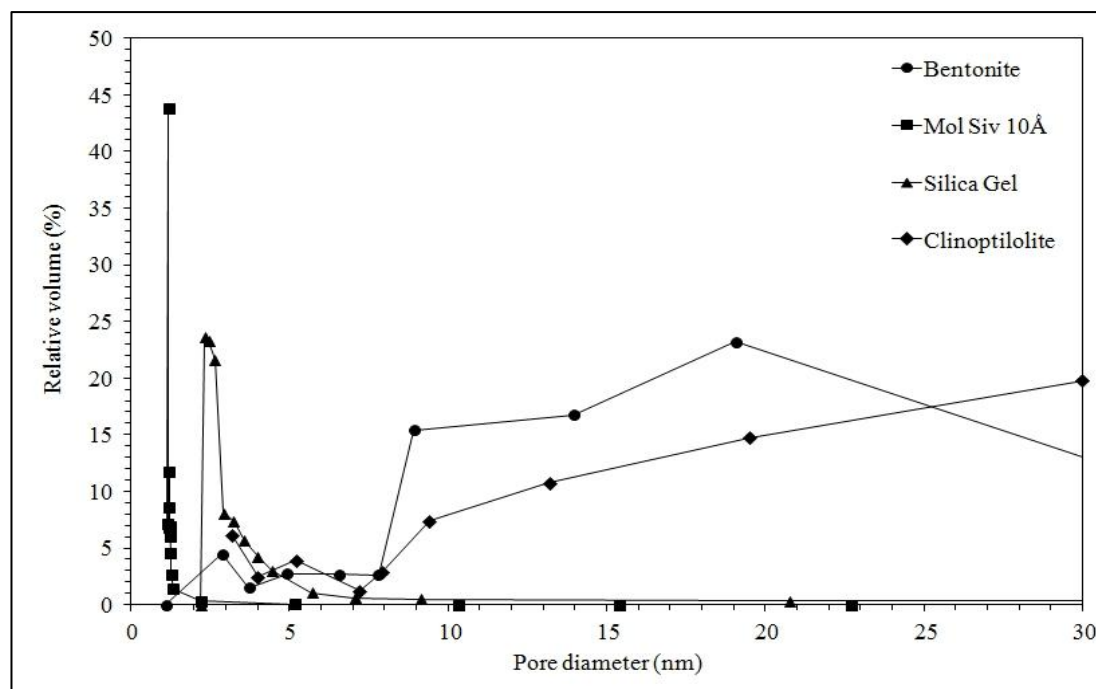


Figure 69 - BJH ($C = 90$) pore size distribution of the four non-MS samples.

4.2.2 Corroboration of N_2 Physisorption Results

Due to the lack of certainty obtained from the N_2 physisorption results for the MS samples it was deemed necessary to corroborate the data using supporting evidence from additional pore characterisation techniques.

4.2.2.1 Small Angle X-Ray Scattering

Powder Small Angle X-Ray Scattering (SAXRS) results were obtained and interpreted by colleagues at the University of Oxford based on the techniques and theory presented in Section 3.2.3.2. In general the d spacings shown in Figure 70 correspond to the mean mesopore diameters as determined by N_2 physisorption previously. There was no evidence of a double spacing for the MMS 4.8 material that appeared from the BJH analysis with single peak equivalent pore size diameters for all MS materials, supporting the theory that corrugation may occur within the pores of the MMS 4.8 material.

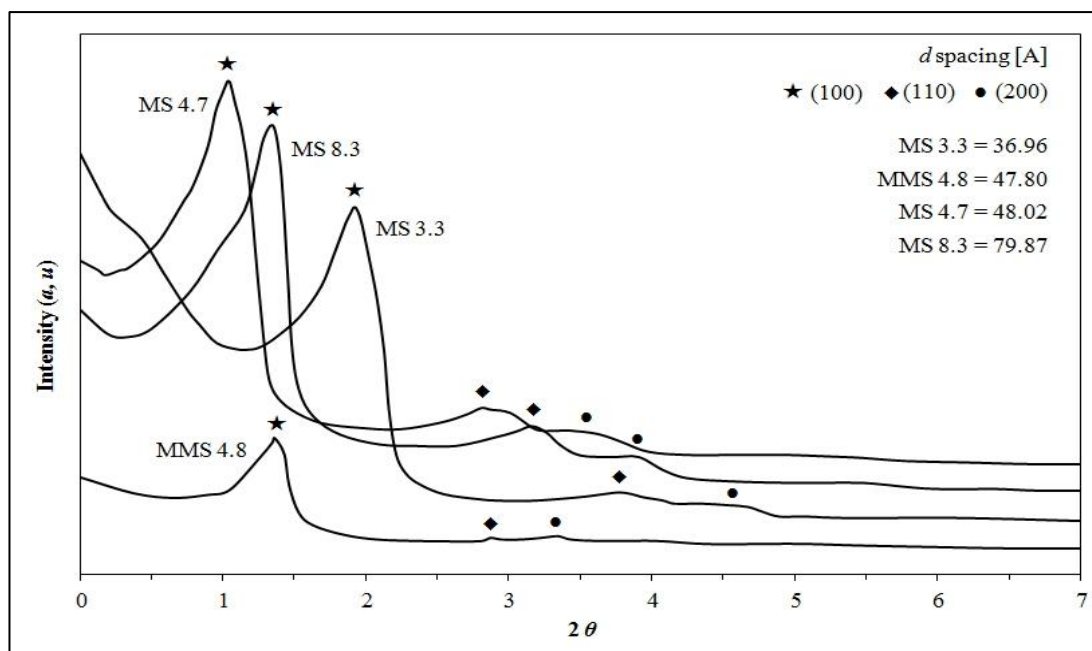


Figure 70 - SAXRS diffractograms of the MS samples obtained by Prof. Edman Tsang at the Wolfson Catalysis Centre, Department of Chemistry, University of Oxford (Hall et al., 2012b).

4.2.2.2 Transmission Electron Microscopy

To finalise the corroboration of MS pore size distribution Transmission Electron Microscopy (TEM) was conducted by colleagues at the University of Oxford based on the techniques and theory presented in Section 3.2.3.3. Figure 71 shows the TEM bright-field-contrasted micrographs for (A) MS 3.3, (B) MMS 4.8, (C) MS 4.7 and (D) MS 8.3.

There was evidence of the mesoporous structure observed in images A, C and D whilst image B showed the spherical form of the MMS 4.8 material with an average particle diameter of $\approx 500\text{nm}$. Thresholding analysis of A, C and D using the graphical software Image J was carried out to measure pore size by bracketing the contrast/ brightness in the micrographs with a series of width measurements taken using calibrated line measurements of the thresholded pore spaces. The results showed good corroboration of the results from both BJH and SAXRS methods used

previously.

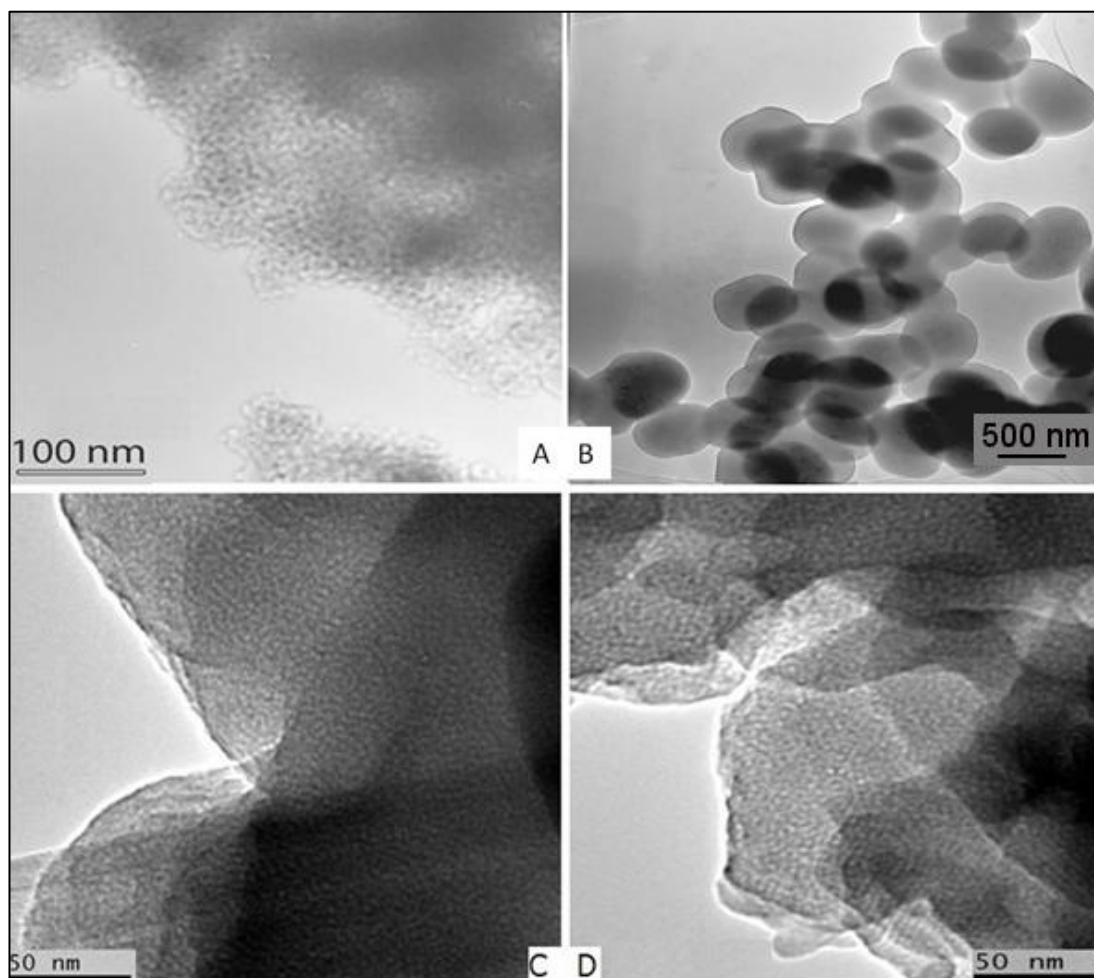


Figure 71 - TEM bright field micrographs of the MS samples obtained by Prof. Edman Tsang at the Wolfson Catalysis Centre, Department of Chemistry, University of Oxford (Hall et al., 2012b).

4.2.3 Scanning Electron Microscopy

As presented in Section 3.2.2, Scanning Electron Microscopy (SEM) was conducted based on the outlined techniques and theory to characterise the MS materials surface morphology, investigate any impurities, confirm the silica elemental composition and also to indicate macropore distribution. Figure 72 shows micrographs for the four MS materials with MS 3.3 (A), MMS 4.8 (B), MS 4.7 (C) and MS 8.3 (D). To provide an indication of macropore size distribution a scaled set of pore sizes (25 nm → 250 nm) were superimposed onto the micrographs.

It was evident that the MMS 4.8 (B) sample showed the same mono-dispersed spherical nature observed from the TEM analysis (see: Section 4.2.2) with corroboration of particle size distribution (>500 nm). The MS materials (A,B and C) appeared to be formed from clusters of individual particles which had sintered together to form agglomerations forming meso and macro-pore networks between the clusters. Sintering of the particles (D) was evident with resultant damage (F) after separation. This can be seen in greater detail in the multi-scale set of images contained in Figure 73. The Pt sputter coating (E) obscured any imaging of individual mesopores whilst macropores were clearly visible.

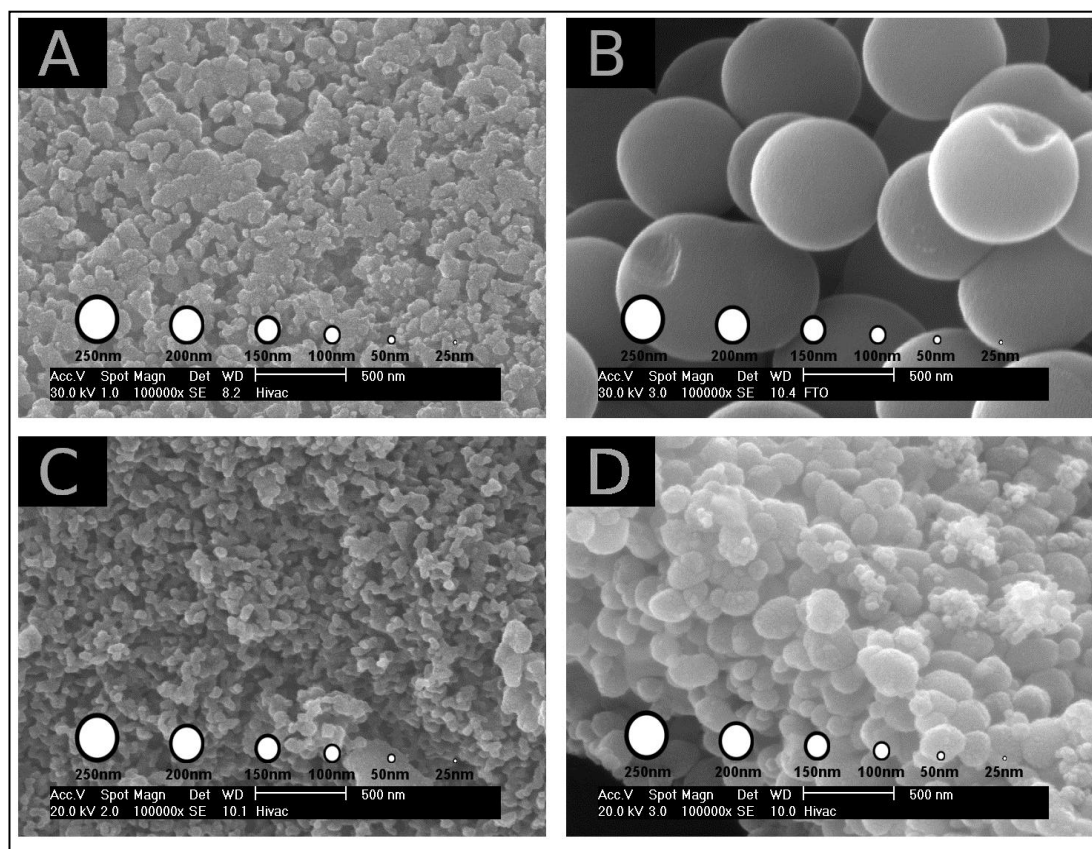


Figure 72 - SEM micrographs of the four MS samples (Hall et al., 2012b).

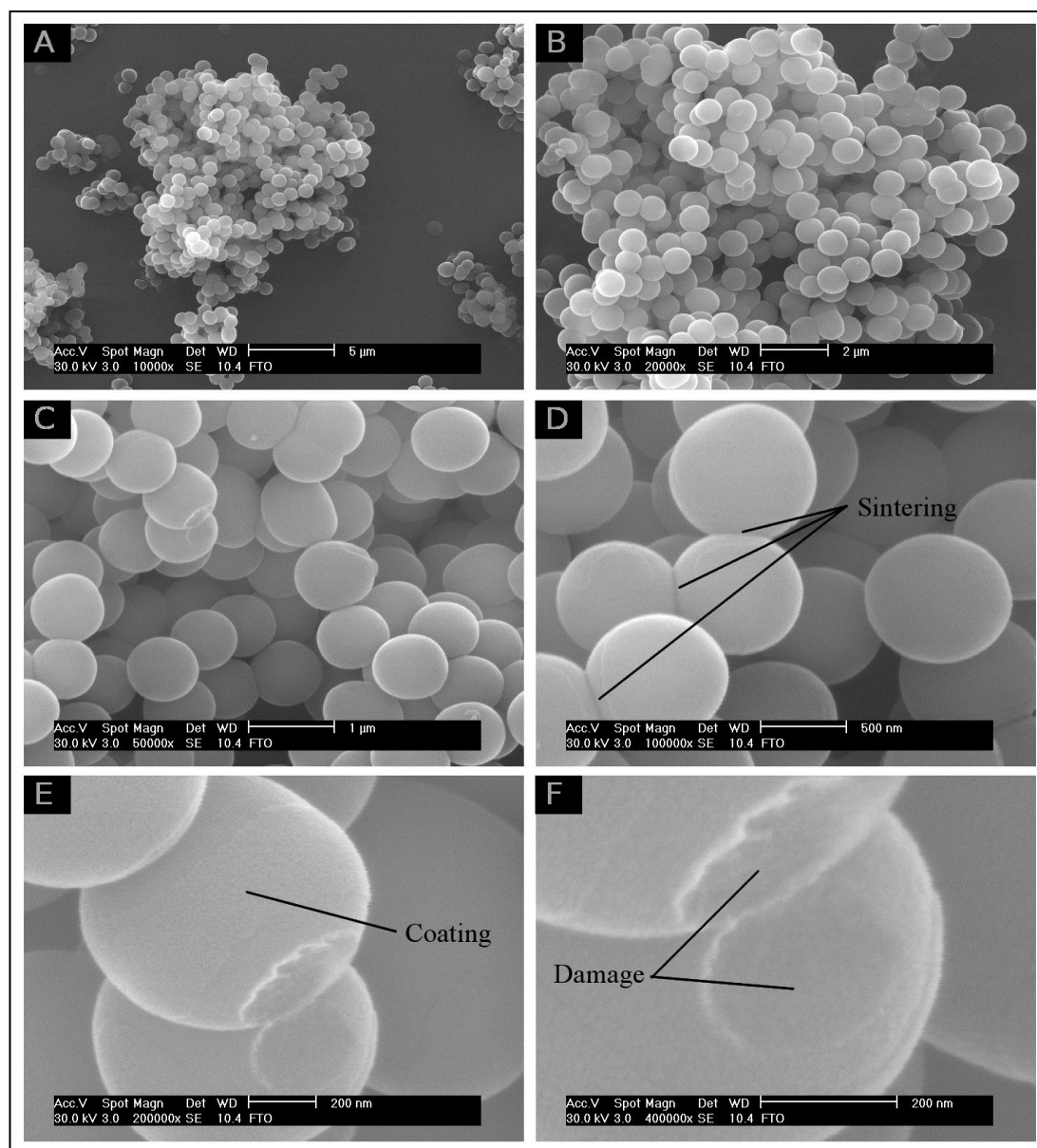


Figure 73 - Multi-scale SEM micrographs of MMS 4.8.

Spectral analysis using EDX was conducted on all MS samples with Figures 74 - 76 showing the EDX results. Whilst all samples were generally free from contamination and, as expected were composed of silica, the spectral analysis of MS 8.3 showed traces of Sodium (Na) and Bromine (Br) suggesting the possible presence of Sodium Bromide (NaBr) residues due to incomplete washing during the MS synthesis (see: Section 3.1.1).

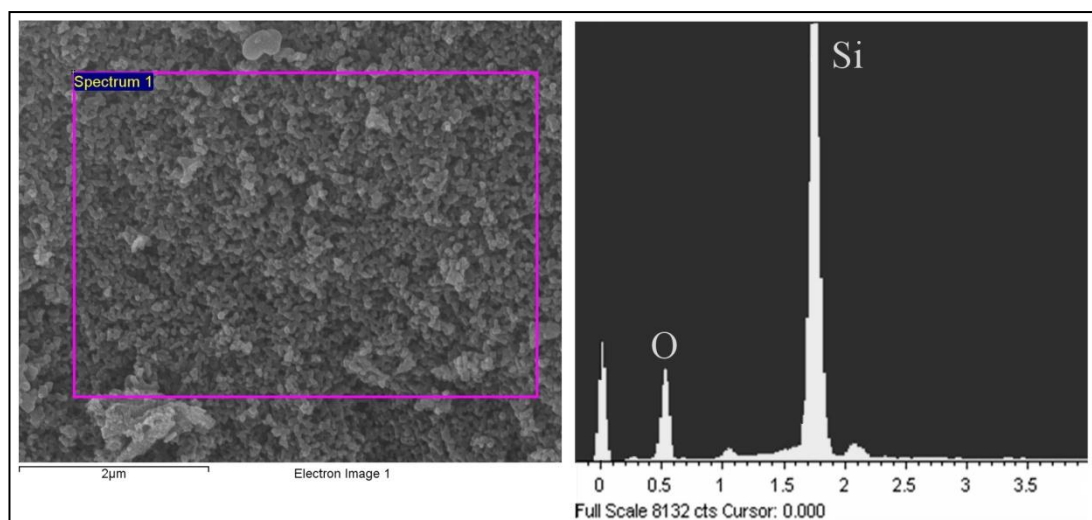


Figure 74 - EDX spectral analysis of MS 4.7.

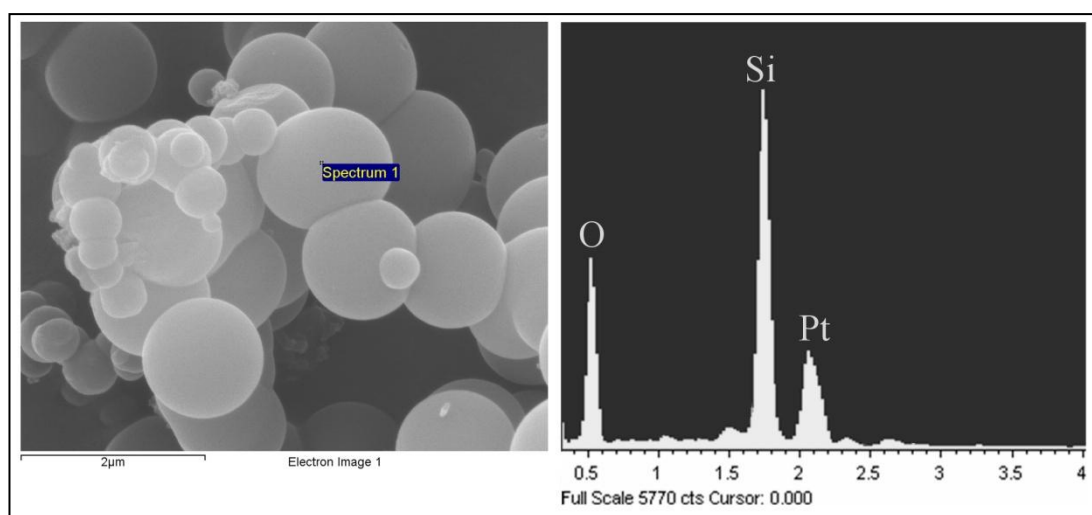


Figure 75 - EDX spectral analysis of MMS 4.8.

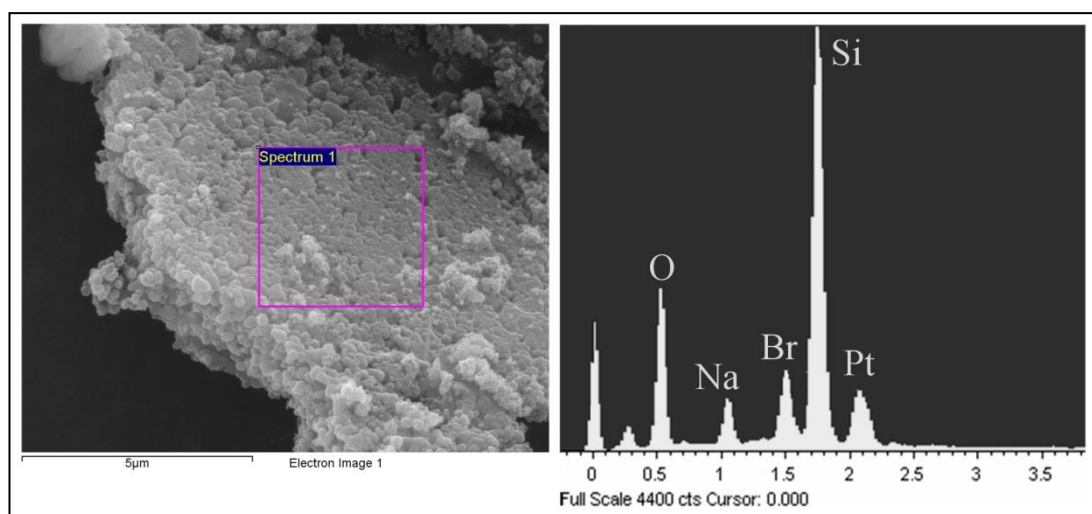


Figure 76 - EDX spectral analysis of MS 8.3.

4.2.4 Density and Porosity

Solid density was determined by helium pycnometry using the Micrometrics Accupyc 1330 gas pycnometer as described in Section 3.2.1.1. Sample masses ($m \approx 0.5$ g) of each MS/MMS and conventional desiccant material were analysed with the results for ρ_{solid} presented in Table 32. MS 8.3 had a slightly elevated density ($\rho_{solid} = 2.65$ g/cm³) compared to the other three MS samples ($\rho_{solid} \approx 2.14$ g/cm³) which is in agreement with the SEM spectral analysis that found the possible presence of residual NaBr (having a higher solid density, $\rho_{solid} = 3.21$ g/cm³).

	Solid Density (g/cm ³)					
	ρ_1	ρ_2	ρ_3	ρ_4	ρ_5	$\rho_{average}$
MS 3.3	2.13	2.09	2.07	2.09	2.08	2.09 ± 0.024
MMS 4.8	2.23	2.16	2.15	2.15	2.13	2.16 ± 0.034
MS 4.7	2.23	2.18	2.19	2.17	2.14	2.18 ± 0.054
MS 8.3	2.65	2.65	2.65	2.65	2.65	2.65 ± 0.005
Mol Siv 10Å	2.57	2.42	2.34	2.28	2.25	2.37 ± 0.174
Silica Gel	2.20	2.15	2.13	2.12	2.11	2.14 ± 0.044
Clinoptilolite	2.31	2.28	2.27	2.26	2.25	2.27 ± 0.034
Bentonite	2.61	2.62	2.62	2.61	2.63	2.62 ± 0.025

Table 32 - Solid density for the eight candidate materials.

Bulk density, ρ_{bulk} for the eight candidate materials was determined gravimetrically as described in Section 3.2.1.2 with the results presented in Table 33. Using data for solid and bulk density, combined with data from the BET analysis, calculation of the relative proportion of mesopore volume, V_{Meso} and macropore volume V_{Macro} to total pore volume, V_{total} was carried out (see: Table 34). V_{total} was calculated as the reciprocal of ρ_{bulk} . The proportion of V_{Meso} was determined as the percentage of V_{Meso} to V_{total} .

	Mass (g)	Volume (cm ³)			Density (g/cm ³)			
	m_1	V_1	V_2	V_3	ρ_1	ρ_2	ρ_3	$\rho_{average}$
MS 3.3	1.14	2.18	2.27	2.36	0.52	0.50	0.48	0.50 ± 0.06
MMS 4.8	1.28	1.98	2.13	1.86	0.64	0.60	0.69	0.64 ± 0.12
MS 4.7	0.86	2.69	2.42	2.55	0.32	0.35	0.34	0.34 ± 0.04
MS 8.3	1.23	2.13	1.98	1.86	0.58	0.62	0.66	0.62 ± 0.11
Mol Siv 10Å	2.57	3.12	3.74	3.40	0.83	0.69	0.76	0.76 ± 0.17
Silica Gel	2.69	3.54	3.40	3.27	0.76	0.79	0.82	0.79 ± 0.09
Clinoptilolite	2.54	3.69	3.55	3.83	0.69	0.72	0.66	0.69 ± 0.09
Bentonite	2.30	3.26	3.24	3.69	0.70	0.54	0.62	0.62 ± 0.11

Table 33 - Bulk density for the eight candidate materials.

	ρ_{solid} g/cm ³	ρ_{bulk} g/cm ³	V_{Total} cm ³ /g	V_{Meso} cm ³ /g	V_{Macro} %	V_{Meso} %	Porosity %
MS 3.3nm	2.09	0.50	1.99	0.65	67.37	32.63	76.02 ± 12
MMS 4.8nm	2.16	0.64	1.56	0.72	53.49	46.51	70.26 ± 18
MS 4.7nm	2.18	0.34	2.97	1.14	61.83	38.17	84.59 ± 14
MS 8.3nm	2.65	0.62	1.62	1.32	18.61	81.39	76.70 ± 18
Mol Siv 10Å	2.37	0.76	1.32	0.35	73.59	26.41	68.10 ± 22
Silica Gel	2.14	0.79	1.26	0.42	67.07	32.93	63.01 ± 12
Clinoptilolite	2.27	0.69	1.45	0.14	90.48	9.52	69.61 ± 12
Bentonite	2.62	0.62	1.61	0.18	89.10	10.90	76.23 ± 18

Table 34 - Summary of the porous network properties for the eight candidate materials.

Figure 77 shows the relative proportion of mesopore and macropore volume to total volume for each candidate material. In general, as the pore diameter increased for the MS materials, V_{Meso} increased correspondingly whilst V_{total} and V_{Macro} decreased. This suggests that the pore wall thickness reduces as the mesopore diameter is increased during MS material synthesis. MS 4.7 in particular has a large ratio of macro/meso pores when compared to the other MS materials.

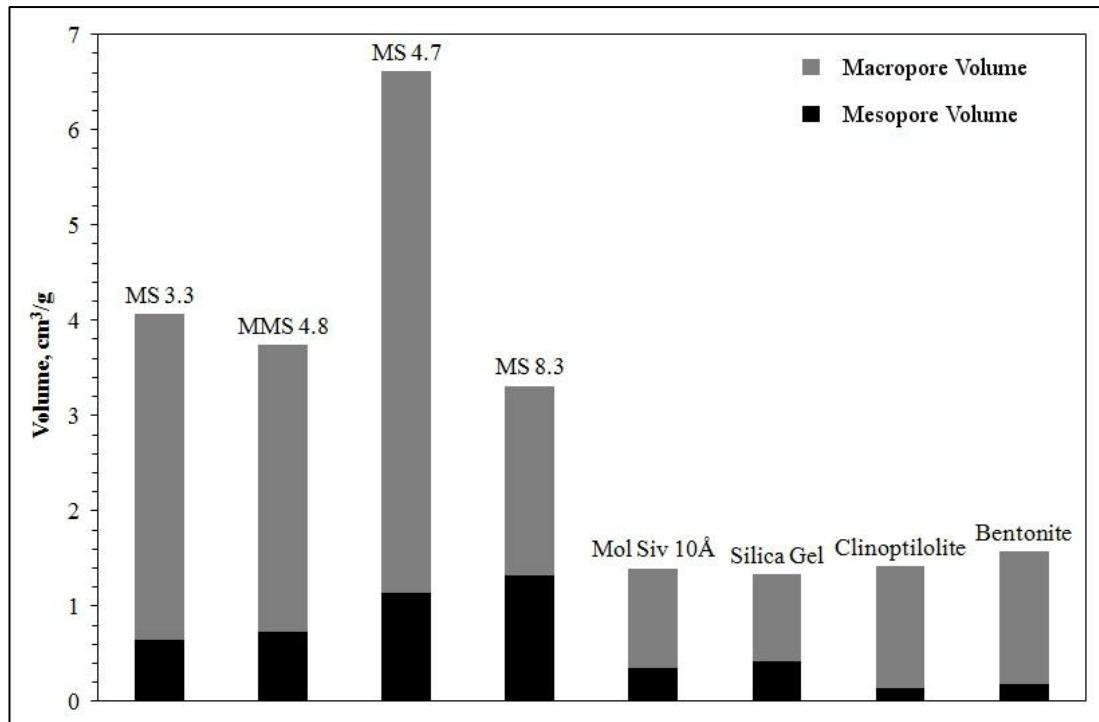


Figure 77 - Graph showing the relative proportion of mesopore and macropore volume to total pore volume for the eight candidate materials (Hall et al., 2012b).

4.3 Characterisation of Hygric Functional Properties Results

4.3.1 Sorption Isotherms

4.3.1.1 Desiccator Jars

The initial set of vapour sorption isotherm tests was carried out using the desiccator jar method as described in Section 3.3.1.1. From Figure 78 it can be seen that the EMC levels in the hygroscopic range for the two MS materials were very low when compared to the other desiccants and not as expected (see: Section 2.6.4). The molecular sieve (Mol Siv 10Å) displayed a typical microporous (Type I) isotherm with the majority of moisture adsorbed below 20%RH and limited uptake in the hygroscopic region. Silica gel, bentonite and clinoptilolite all showed Type IV isotherms as expected.

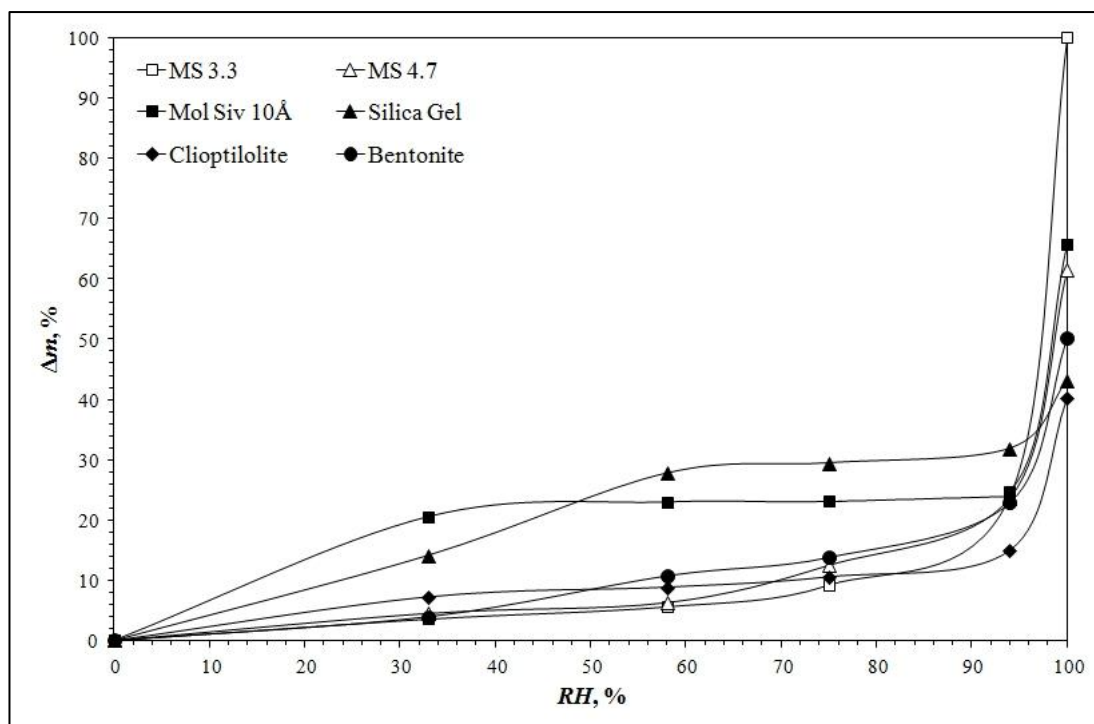


Figure 78 - Graph showing the moisture vapour sorption isotherms determined using the desiccator jar method for six candidate materials.

Further tests were performed on the two MS materials to investigate the poor EMC performance within the hygroscopic region. A series of six tests were carried out by exposing the samples at $RH = 75\%$ for $t = 48\text{h}$ followed by regeneration (*i.e.* oven drying for $t = 24\text{h}$ at $T = 105\text{ }^{\circ}\text{C}$). The results (see: Figure 79) showed a large degradation in EMC between the first and third tests followed by a gradual levelling off in uptake levels on subsequent cycles for both materials. This suggests that damage may have occurred within the mesopore network during the drying process in the oven with possible pore wall collapse or cracking due to the expanding forces of the drying liquid exceeding the pore wall strength (Sakka, 2005).

Pore wall collapse could lead to formation of larger pores with sizes in the macropore range which is evidenced by the still elevated EMC levels as $RH \rightarrow 100\%$ (see: Figure 78). Based on these initial results further regeneration of the MS materials was only carried out by vacuum desiccation.

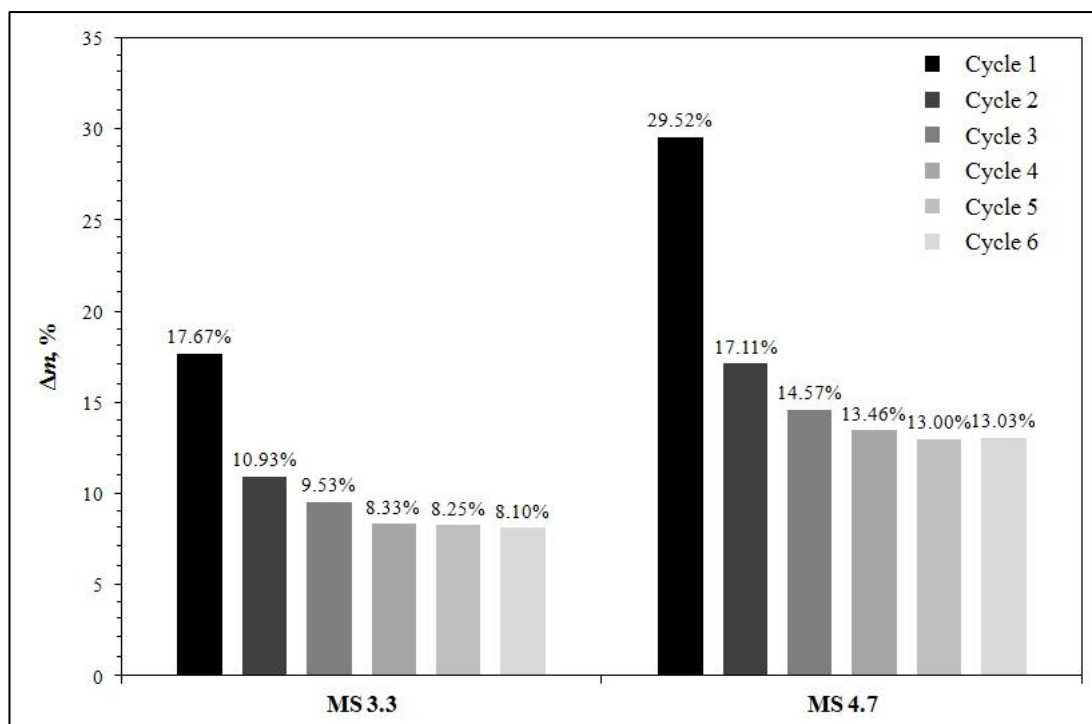


Figure 79 - Graph showing the cycle to cycle degradation in EMC for the two MS materials.

4.3.1.2 Climatic Chamber

A second set of water vapour sorption isotherms for all candidate materials were determined using gravimetric dynamic vapour sorption (DVS) in the climate chamber as outlined in Section 3.3.1.2. The sorption isotherms for all candidate materials can be seen in Figure 80. When compared to the desiccator tests the molecular sieve, silica gel and bentonite displayed near identical shape and EMC levels, as can be seen in Table 35. In the lower range ($RH = 20\%$) Mol Siv 10\AA had the highest EMC levels again indicating minimal sorption after completion of the monolayer (*i.e.* microporous). As in the desiccator tests all other materials had type IV isotherms with multilayer filling evidenced by increased uptake in the hygroscopic region. Between the RH levels of 20% and 50%, MMS 4.8 and silica gel showed the highest rate of increase and EMC (at 50%RH) and had closely matched isotherms, indicating similarity in their pore structure. At higher relative humidity

ranges ($RH > 80\%$) MS 3.3, MS 4.7 and MS 8.3 showed considerably higher EMC levels over the conventional desiccants, with EMC's of 69%, 108% and 246%, respectively as $RH \rightarrow 100\%$.

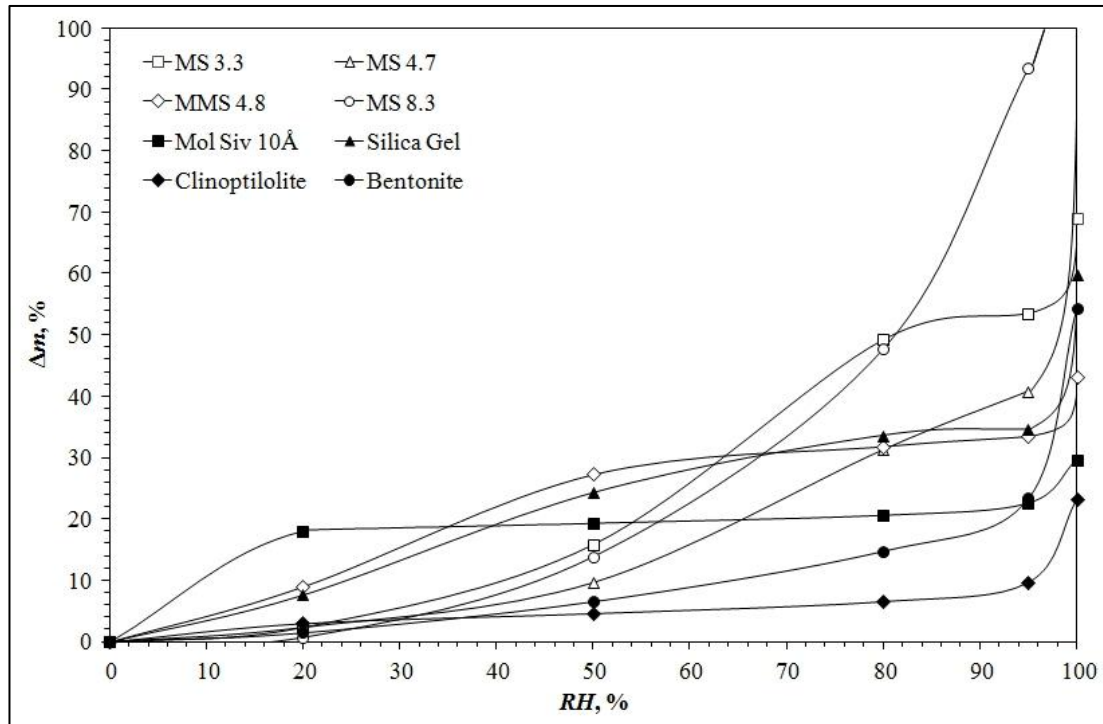


Figure 80 - Graph showing the moisture vapour sorption isotherms determined using the climate chamber for all candidate materials (Hall et al., 2012b).

		EMC, %					
	$RH, \%$	0	20	50	80	95	100
Mol Siv 10Å	DVS	0	18	19	21	23	30
	DJ	0	15	23	23	24	66
Silica Gel	DVS	0	8	24	34	35	60
	DJ	0	9	23	30	32	46
Clinoptilolite	DVS	0	3	5	7	10	23
	DJ	0	4	9	10	14	40
Bentonite	DVS	0	2	7	15	23	54
	DJ	0	2	11	14	23	51

Table 35 - Comparison of dynamic vapour sorption (DVS) and desiccator (DJ) EMC levels.

As stated in Section 3.3.1, use of continuous mass recording allowed for analysis of the moisture kinetics associated with each RH step. Table 36 shows the change in mass, Δm and associated response time, t_{emc} for each RH step. The moisture storage

function, ζ_u for each material is also provided which gives an indication of the sorption performance of the material in the hygroscopic range. MS 3.3 and MS 8.3 displayed the best ζ_u values at ≈ 0.78 kg/kg, almost double that of the next closest desiccant. MS 4.7 and silica gel again had similar storage functions of 0.381 and 0.433 kg/kg, respectively. Further analysis of t_{emc} is contained in Section 4.3.6.

	0 \rightarrow 20%		20 \rightarrow 50%		50 \rightarrow 80%		80 \rightarrow 95%		ζ_u (kg/kg)
	Δm	t_{emc}	Δm	t_{emc}	Δm	t_{emc}	Δm	t_{emc}	
	(%)	(h)	(%)	(h)	(%)	(h)	(%)	(h)	
MS 3.3	1.8	1.7	13.0	14.8	33.0	13.1	3.8	12.8	0.782
MMS 4.8	8.5	3.4	17.8	4.5	4.6	18.7	1.2	5.1	0.381
MS 4.7	1.9	0.4	6.9	15.0	21.6	17.0	9.1	13.5	0.481
MS 8.3	0.7	0.6	12.7	9.6	33.8	23.6	52.1	59.9	0.783
Mol Siv 10Å	17.5	11.5	0.8	0.7	13.9	1.3	1.6	7.9	0.043
Silica Gel	7.2	10.9	16.1	20.2	9.3	19.1	0.5	0.8	0.433
Clinoptilolite	2.5	1.5	1.2	0.8	2.0	12.0	2.6	7.6	0.221
Bentonite	1.0	1.0	4.7	6.5	7.9	21.7	8.1	24.7	0.060

Table 36 - Summary of changes in mass with corresponding response times and moisture storage functions for all candidate materials.

4.3.2 Vapour Permeability

Vapour permeability, δ measurements were carried out using a modified ‘wet-cup’ method as described in Section 3.3.2. Linear mass loss was achieved for all sample materials as shown in Figure 81. These results are an estimation only and it should be noted that they may not be accurate for uses other than those contained in this work. An inverse relationship was found between vapour permeability and mean mesopore diameter for the MS materials which suggests that vapour transfer into the MS materials may be dominated by the macropore geometry. This suggests that bulk vapour response rates may be limited for the MS materials at significantly increased

thicknesses. As it was not possible to investigate this effect experimentally due to the minimal quantity of MS materials available, sensitivity analysis of increasing MS material thickness was carried out using numerical simulation (see: Section 6.8.1).

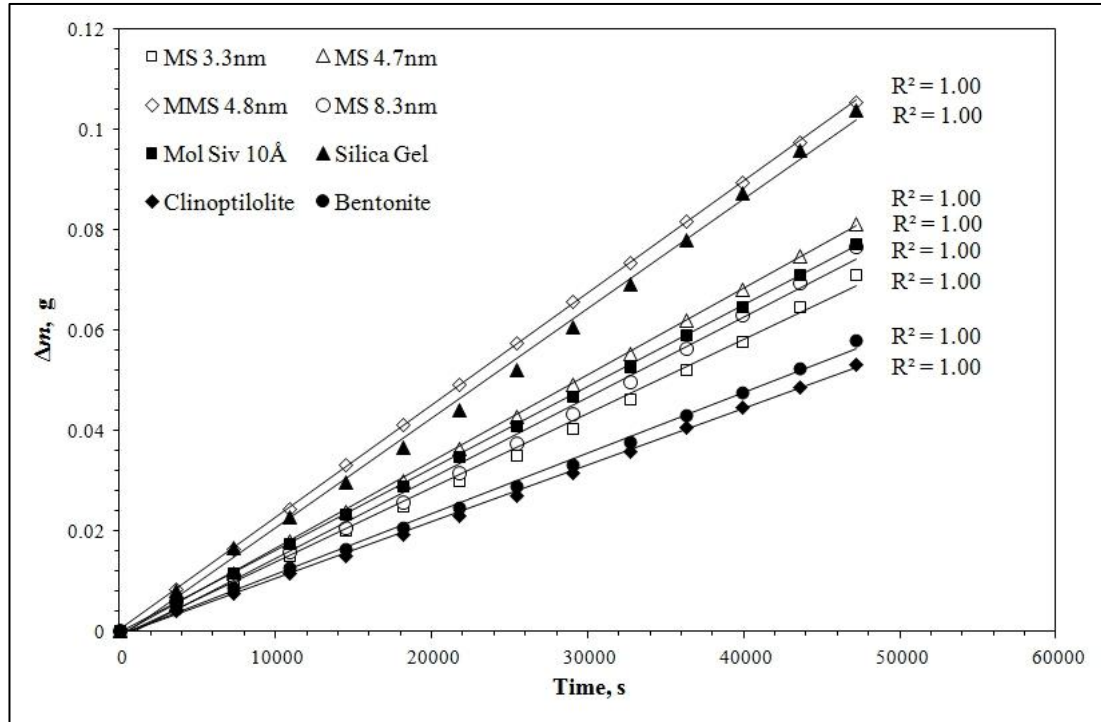


Figure 81 - Graph showing the linear mass loss from the wet- cup assembly in the vapour permeability tests (Hall et al., 2012b).

	d	G	W	δ	μ
	mm	kg/s	kg/m ² s Pa	kg/m s Pa	----
MS 3.3	11	$1.37 \cdot 10^{-9}$	$3.91 \cdot 10^{-9}$	$4.30 \cdot 10^{-11}$	4.54
MMS 4.8	10	$2.07 \cdot 10^{-9}$	$2.95 \cdot 10^{-9}$	$2.95 \cdot 10^{-11}$	6.61
MS 4.7	12	$1.60 \cdot 10^{-9}$	$2.28 \cdot 10^{-9}$	$2.74 \cdot 10^{-11}$	7.13
MS 8.3	9	$1.44 \cdot 10^{-9}$	$2.06 \cdot 10^{-9}$	$1.86 \cdot 10^{-11}$	10.52
Mol Siv 10Å	12	$1.51 \cdot 10^{-9}$	$2.16 \cdot 10^{-9}$	$2.59 \cdot 10^{-11}$	7.55
Silica Gel	12	$2.04 \cdot 10^{-9}$	$2.92 \cdot 10^{-9}$	$3.50 \cdot 10^{-11}$	5.58
Clinoptilolite	13	$1.04 \cdot 10^{-9}$	$2.98 \cdot 10^{-9}$	$3.88 \cdot 10^{-11}$	5.03
Bentonite	13	$1.11 \cdot 10^{-9}$	$3.19 \cdot 10^{-9}$	$4.14 \cdot 10^{-11}$	4.72

Table 37 - Water vapour transmission properties for all candidate materials.

4.3.3 Liquid Water Absorption

Liquid water absorption, A_w was determined using the partial immersion test (see: Section 3.3.3). As with the vapour permeability results in the previous section, these results are an estimation only and it should be noted that they may not be accurate for uses other than those contained in this work. Bentonite was the only material that had a Type 2 plot where no surface wetting occurred during the test. The bentonite also showed very minimal liquid transfer potential indicative of its high swelling potential described earlier (see: Section 2.6.1.3). All other materials showed Type 1 curves with MS 4.7, MS 8.3 and in particular MS 3.3 displaying very rapid water absorption (see: Table 38).

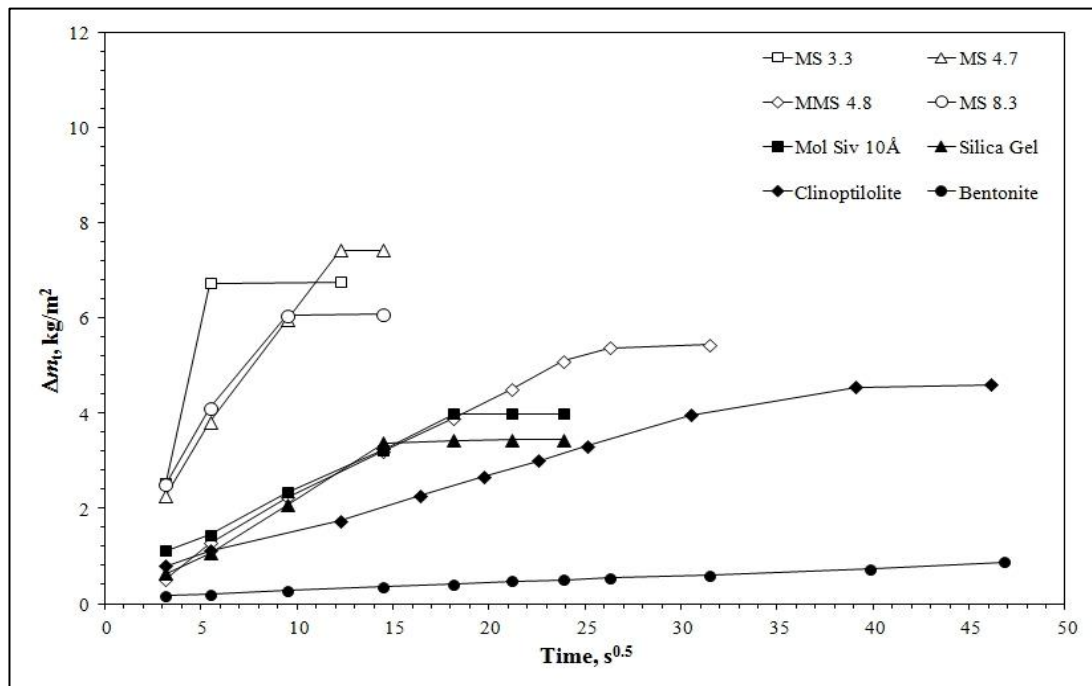


Figure 82 - Graph showing the liquid water absorbed per exposed surface area against square root of time.

	Δm kg	\sqrt{t} $s^{0.5}$	Δm_t kg/m^2	A_w $kg/m^2 s^{0.5}$
MS 3.3	3.06	12.25	6.76	2.112
MMS 4.8	2.46	31.46	5.44	0.204
MS 4.7	3.37	14.49	7.44	0.561
MS 8.3	2.75	14.49	6.08	0.550
Mol Siv 10Å	1.81	23.87	3.99	0.193
Silica Gel	1.56	23.87	3.45	0.246
Clinoptilolite	2.08	46.15	4.60	0.115
Bentonite	0.39	46.80	0.87	0.016

Table 38 - Liquid water absorption properties for all candidate materials.

4.3.4 Vapour Sorption Response

As outlined in Section 3.3.1 knowledge of the moisture kinetics for sorption/desorption is vital for buffering applications since the EMC of a buffering material is rarely reached but it is required to respond as rapidly as possible to ΔRH amplitude changes. Figure 83 shows the kinetic Δm curves between 40% and 70%RH for all candidate materials which were determined from the sorption isotherms (see: Section 4.3.1.2). Table 39 shows the actual Δm measurements taken from the isotherms with corresponding values for $t_{75\%}$ and $t_{40-70-40}$ calculated as $2t_{75\%}$. There was a marked reduction from t_{emc} to $t_{75\%}$ in all materials with an average reduction of 80%, corresponding to only 25% reduction from EMC to $m_{75\%}$.

	Δm_{40-70} %	t_{emc} h	$m_{75\%}$ %	$t_{75\%}$ h	$t_{40-70-40}$ h
MS 3.3	33.0	13.1	24.7	4.6	9.2
MMS 4.8	4.6	18.7	3.5	1.0	2.0
MS 4.7	21.6	17.0	16.2	2.4	4.8
MS 8.3	33.8	23.6	25.4	8.0	16.0
Mol Siv 10Å	1.3	13.9	1.0	2.1	4.1
Silica Gel	9.3	19.1	7.0	3.1	6.2
Clinoptilolite	2.0	12.0	1.5	1.6	3.2
Bentonite	7.9	21.7	5.9	6.0	12.0

Table 39 - Kinetic moisture data for calculation of $t_{75\%}$ and $t_{40-70-40}$.

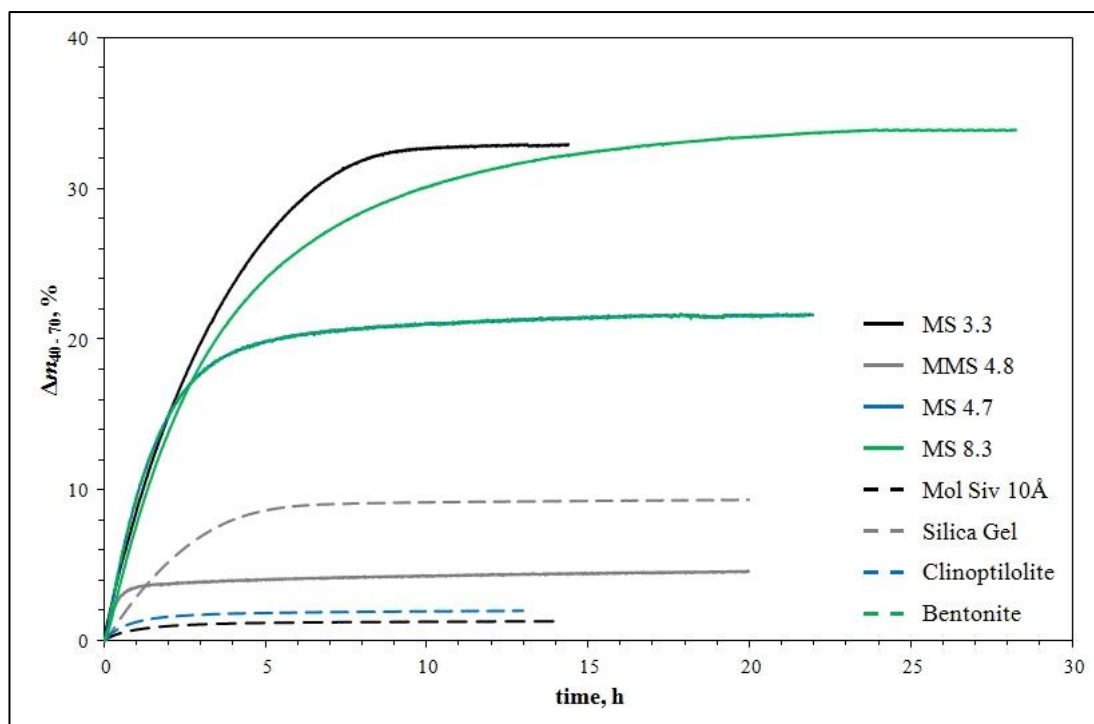


Figure 83 - Graph showing the kinetic moisture uptake curves between 40% and 70% RH used to determine $t_{75\%}$.

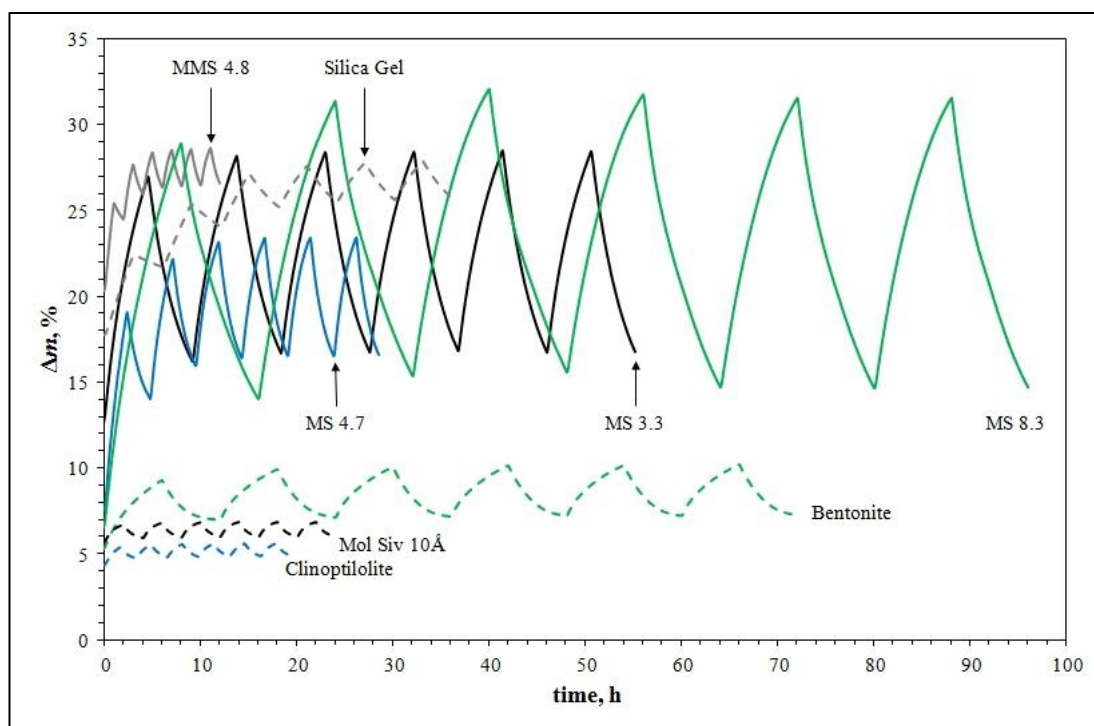


Figure 84 - Vapour sorption response for all candidate materials measured between 40% and 70% RH at 23 °C (Hall et al., 2012b).

Results from the vapour sorption response tests with cycle times determined above are shown in Figure 84. All the MS materials displayed rapid, near linear steep sorption/desorption curves over the six cycles ($\Delta m = f(t)$) whilst the other candidates showed high rates of decay evidenced by the shallow slopes on both sorption and desorption curves. This suggests that the non-MS materials approach their peak capacity much more rapidly than the MS materials whose maximum capacity appears to be significantly beyond that required for buffering within the $t_{75\%}$ time period.

Figure 85 shows the cyclic response including mean and range of Δm for all candidate materials over a normalised time period for comparative analysis. MS 3.3, MS 4.7 and particularly MS 8.3 showed superior performance in terms of sorption/desorption capacity (shaded area), whilst the MMS 4.8 and silica gel again showed very similar capacity and mean Δm levels as discussed previously (see: Section 4.3.1.2). Hysteresis between the sorption and desorption curves was observed in all candidate materials, as can be seen by the increase in mean moisture content in the initial cycles and is more pronounced in the MS samples. This may be indicative of their higher sorption rate and larger uptake range compared to the other materials coupled with initial pore wall wetting and incomplete desorption. This occurred in the first three cycles only, after which all the candidate materials appeared to reach a steady state of sorption/ desorption and hysteresis disappeared.

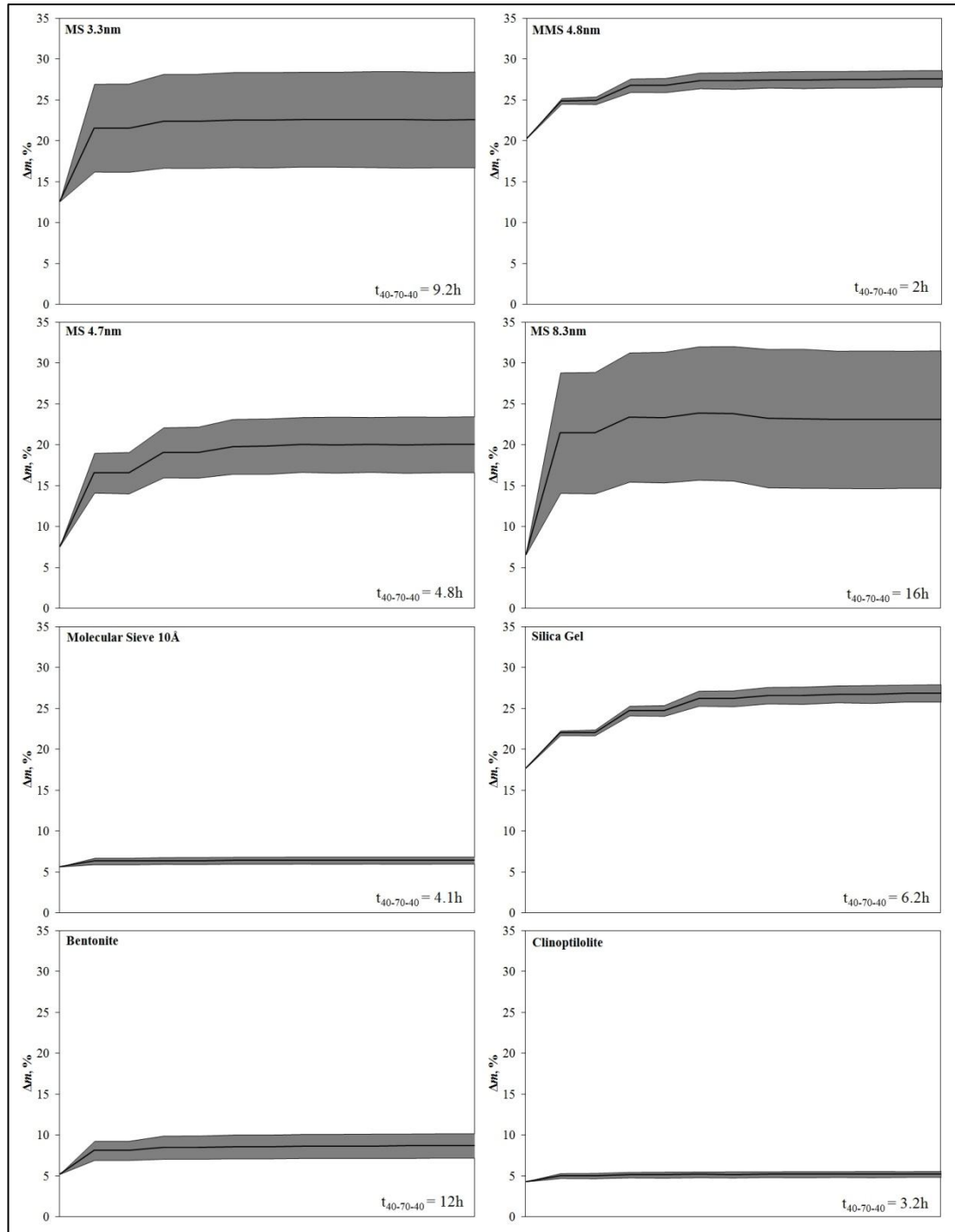


Figure 85 - Mean and total range of moisture uptake in the thermal comfort range with normalized time scale for all materials at 23 °C (Hall et al., 2012b).

4.3.5 Moisture Buffer Value

Moisture diffusivity, D_w , effective moisture penetration depth (EMPD) and the practical moisture buffer value ($MBV_{\text{practical}}$) were calculated based on the theory outlined in Section 3.4.1.3. As expected from the vapour permeability calculations

(see: Section 4.3.2), a positive linear relationship was observed for the MS materials between D_w and mean mesopore diameter. EMPD, $d_{p, 1\%}$ is shown in Table 40 for all materials and indicates that for the MS and other desiccants $d_{p, 1\%}$ was larger than the sample thickness used in both physical and numerical modelling. As all materials were hygrically isolated from the envelope wall by means of a vapour barrier (see: Section 5.7) humidity buffering was deemed to occur throughout the entire depth of all material coatings.

As stated in Section 3.4.1.3, calculation of $MBV_{\text{practical}}$ has the advantage of allowing materials to be compared by classification using a single value. The MBV values for all the candidate materials are presented in Figure 86 and compared with traditional materials commonly used for some levels of moisture buffering in buildings (see: Table 40).

	Δm g	ΔRH %	A_s m ²	D_w m ² /s	$d_{p, 1\%}$ mm	MBV g/m ² %RH
MS 3.3	0.33	30	$1.26 \cdot 10^{-03}$	$2.57 \cdot 10^{-10}$	12	8.87
MMS 4.8	0.18	30	$1.26 \cdot 10^{-03}$	$2.83 \cdot 10^{-10}$	13	4.85
MS 4.7	0.22	30	$1.26 \cdot 10^{-03}$	$3.97 \cdot 10^{-10}$	15	5.72
MS 8.3	0.34	30	$1.26 \cdot 10^{-03}$	$8.99 \cdot 10^{-11}$	7	8.98
Mol Siv 10Å	0.01	30	$1.26 \cdot 10^{-03}$	$1.87 \cdot 10^{-09}$	33	0.34
Silica Gel	0.09	30	$1.26 \cdot 10^{-03}$	$2.39 \cdot 10^{-10}$	12	2.47
Clinoptilolite	0.02	30	$1.26 \cdot 10^{-03}$	$2.43 \cdot 10^{-09}$	38	0.52
Bentonite	0.08	30	$1.26 \cdot 10^{-03}$	$6.35 \cdot 10^{-10}$	19	2.18
Wood (Spruce) ^A	----	42	$7.20 \cdot 10^{-02}$	$4.05 \cdot 10^{-10}$	15	1.16
Gypsum ^A	----	42	$4.70 \cdot 10^{-02}$	$2.22 \cdot 10^{-09}$	36	0.64
Brick ^A	----	42	$1.40 \cdot 10^{-02}$	$1.54 \cdot 10^{-08}$	95	0.48
Concrete ^A	----	42	$1.90 \cdot 10^{-02}$	$5.47 \cdot 10^{-11}$	6	0.38

Table 40 - MBV, liquid diffusivity and EMPD for candidate and traditional materials. ^A Values adapted from (Rode et al., 2005).

MS 3.3 and MS 8.3 had $MBV_{\text{practical}}$ values of ≈ 8.9 g/m²%RH which were more than

one order of magnitude greater than the capacity of the traditional building envelope materials (gypsum plaster, brick and concrete), whilst Mol Siv 10Å and clinoptilolite had more than three times higher capacity over the other candidate materials (bentonite and silica gel). The $MBV_{\text{practical}}$ of all MS materials was significantly higher than the maximum “excellent” rating of 2.0 as presented by Rode et al., (see: Figure 46), and corresponded to a $\approx 800\%$ increase over uncoated gypsum plaster, a very common interior envelope material previously recognized as a good indoor humidity buffering material.

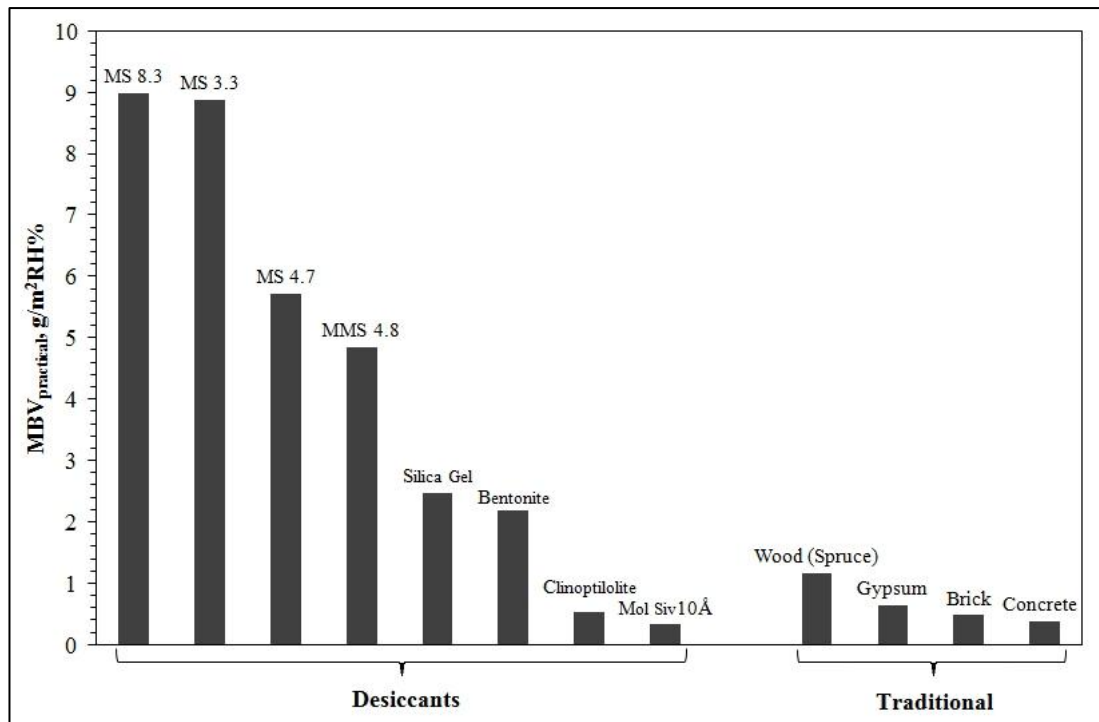


Figure 86 - Graph showing $MBV_{\text{practical}}$ levels of the candidate and traditional materials (Hall et al., 2012b).

4.3.6 Mean Pore Diameter & Response Time Relationship

As discussed in Section 1.3, an integral element in meeting Objective 2 for this research was determination of structure-property relationships between pore (meso and macro) network geometry and material behaviour through characterisation of the hygrothermal functional properties. Section 2.6.1.2 outlines the principle that it is

rarely the moisture capacity of a material that governs its hygric performance but its response time or moisture kinetics, specifically within the ASHRAE comfort range ($40\% \leq RH \leq 70\%$). From Figure 87 it can be seen that there is evidence of a positive logarithmic correlation between t_{emc} and the mean mesopore diameter in the MS materials with better correlation achieved when the mono-dispersed MMS 4.8 was excluded (Hall et al., 2012b). This suggests that MS materials with wider mean mesopore diameters require longer to fill across the ASHRAE comfort range, in terms of both completion of multi-molecular layer adsorption and capillary condensation, and thus have a slower equilibrium DVS response time, t_{emc} . As mesopore diameter was also directly linked with pore volume (see: Section 4.2.1) this suggests that MS mesopore geometry may be tuned in order to give a desired dynamic vapour sorption/ desorption response rate (t_{emc}) and storage capacity (EMC) to suit a given set of ambient psychrometric operating conditions (Hall et al., 2012b).

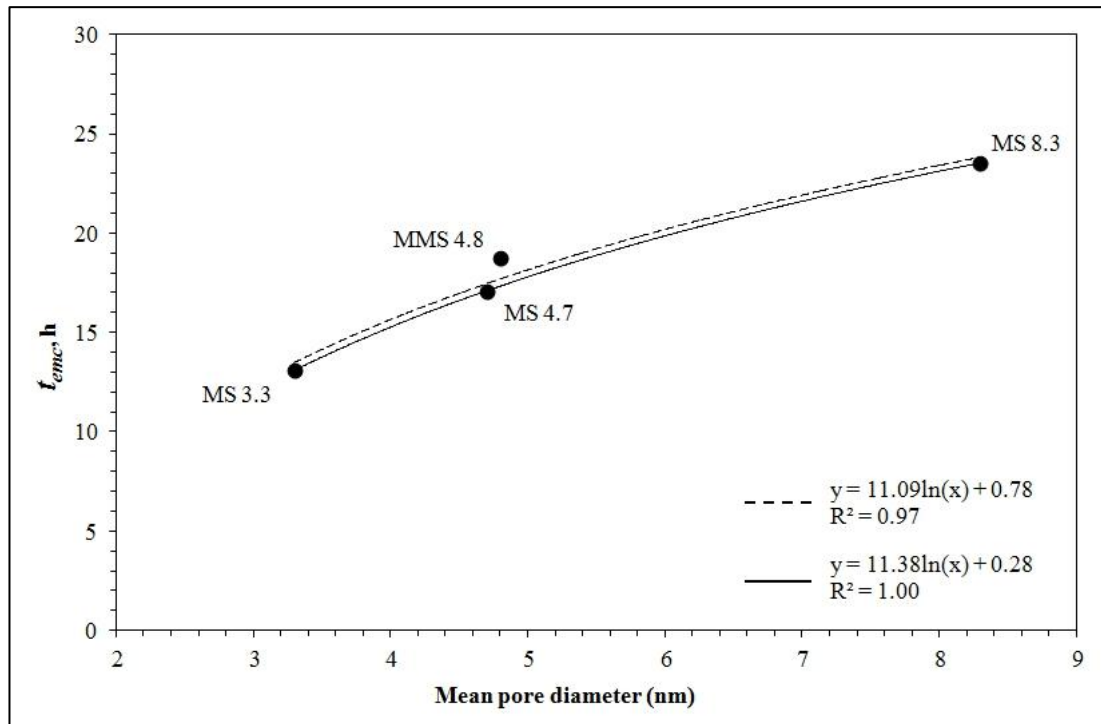


Figure 87 - Graph showing the logarithmic relationship between mean pores diameter and t_{emc} (Hall et al., 2012b).

4.4 Characterisation of Thermal Functional Properties Results

4.4.1 Thermal Conductivity

Moisture-dependent thermal conductivity, λ^* was determined using the modified transient plane source (MTPS) technique as described in Section 3.3.5. The results from MTPS analysis at $RH = 50\%$ are given in Table 41. As expected, the presence of moisture within the meso and macro pore network and void spaces of the MS materials had the effect of increasing λ^* over dry state values ($\lambda \approx 0.05$ W/mK) presented previously (Hall et al., 2012) whilst λ^* values for the other candidate materials compared well with the literature (Ozaydin et al., 2006, Murashov and White, 2002, Gurgel and Klüppel, 1996).

	λ^* , w/mK @ 50%RH					Mean
	Run 1	Run 2	Run 3	Run 4	Run 5	
MS 3.3	0.073	0.073	0.073	0.072	0.072	0.073 ± 0.008
MMS 4.8	0.071	0.072	0.072	0.072	0.072	0.072 ± 0.007
MS 4.7	0.067	0.068	0.068	0.068	0.068	0.068 ± 0.007
MS 8.3	0.081	0.081	0.081	0.081	0.081	0.081 ± 0.008
Mol Siv 10Å	0.129	0.115	0.115	0.115	0.115	0.118 ± 0.026
Silica Gel	0.115	0.115	0.115	0.114	0.114	0.115 ± 0.012
Clinoptilolite	0.193	0.124	0.123	0.123	0.123	0.137 ± 0.086
Bentonite	0.115	0.105	0.103	0.102	0.102	0.105 ± 0.024

Table 41 - Thermal conductivity of candidate materials measured at 50%RH.

4.4.2 Specific Heat Capacity

The dry state specific heat capacity, c_p of the candidate materials was tested using differential scanning calorimetry (DSC) as described in Section 3.3.4. The results shown in Table 42 show an increase for all materials as temperature increases. Values for all candidate materials compared favourably with those previously

published in the literature (Gurgel and Klüppel, 1996, Hemmingway and Robie, 1984, Qiu et al., 2000, Wilson et al., 2011).

	c_p , J/kg·K					
	263 K	273 K	283 K	293 K	303 K	Mean @ 296 K
MS 3.3	793	949	1031	1101	1169	1126 ± 203
MMS 4.8	1204	1428	1825	2561	3531	2862 ± 372
MS 4.7	1451	1591	1742	1866	2050	1931 ± 309
MS 8.3	1065	1313	1522	1691	1731	1734 ± 225
Mol Siv 10Å	1234	1379	1579	1929	2415	2086 ± 313
Silica Gel	995	1116	1265	1500	1832	1609 ± 177
Clinoptilolite	949	1177	1438	1856	2374	2017 ± 343
Bentonite	1060	1331	1602	1941	2456	2119 ± 212

Table 42 - Dry-state specific heat capacity of the eight candidate materials (Hall et al., 2012b).

4.5 Summary

The main conclusions from Chapter 4 are:

1. The MS/MMS materials displayed type IV N_2 physisorption isotherms and had significantly higher mesopore volume and SSA when compared to the other conventional candidate materials
2. There is a positive relationship between mesopore diameter and mesopore volume in the MS/MMS samples, but not to SSA suggesting corrugation within the pores
3. MS/MMS pore size distribution results obtained using N_2 physisorption were corroborated using SAXRS and TEM analysis
4. MS/MMS V_{meso} increased as pore diameter increased whilst V_{total} and V_{Macro} decreased suggesting that pore wall thickness reduces as the mesopore diameter is increased during synthesis

5. The MS/MMS materials displayed Type IV moisture vapour sorption isotherms with significantly increased EMC levels and moisture storage functions in the hygroscopic range
6. There was an inverse relationship between permeability and mesopore diameter for the MS materials suggesting that vapour transfer is dominated by macropore geometry
7. MS 3.3, MS 4.7 and particularly MS 8.3 showed rapid, near linear steep sorption/desorption curves and superior capacity over the conventional desiccants during cyclic response testing
8. The $MBV_{\text{practical}}$ of all MS materials was significantly higher than the maximum “excellent” rating with up to $\approx 800\%$ increase over uncoated gypsum plaster
9. There is positive logarithmic correlation between t_{emc} and mean mesopore diameter in the MS materials

To summarise, the MS materials have significantly higher EMC and faster response rates when compared to the conventional desiccant. Vapour transfer to/from an MS desiccant substrate appears to be dominated by the macropore geometry and this may dominate bulk vapour sorption/desorption response rates at greater material depths. The DVS response time, t_{emc} has significant and positive logarithmic relationships with both the mesopore diameter and the mesopore volume implying that mesopore geometry can be tuned in order to give the desired dynamic vapour sorption/desorption response rate and storage capacity to suit a given set of interior psychrometric conditions.

CHAPTER 5: Results of 1D Hygrothermal Modelling

5.1 Introduction

This chapter presents the results from the 1D numerical investigations using the building performance simulation software WUFI Pro v5.1 to meet Objective 3 (see: Section 1.4). Due to the poor vapour sorption response of MMS 4.8, silica gel, molecular sieve, bentonite and clinoptilolite (see: Section 4.3.4), it was decided that no further comparative analysis using these materials would be undertaken. MS 3.3, MS 4.7 and MS 8.3 were selected for further research with gypsum and spruce selected as traditional humidity buffering materials for comparative simulation.

5.2 Sorption Isotherm Model

Figure 88 directly compares the physical and numerical kinetic moisture uptake plots for the three MS materials determined as outlined in Sections 3.3.1.2 and 3.5.1.1. Moisture content values (Δm , %) were converted to specific moisture contents (w , kg/m³) using the materials bulk density (ρ_{bulk} , kg/m³). Moisture contents, w were identical in most cases except for MS 8.3 where there was a pronounced under prediction of the final EMC for the corresponding t_{RH} (t_{emc}) for $RH = 95\%$ when simulated using the numerical model WUFI Pro v.5.1. This was a surprising result as all other predicted EMC values correspond to the input values used when creating the materials for the WUFI database. A possible suggestion is that due to the highly increased EMC level the model may assume a much larger t_{emc} interval than was observed in the sorption experiments. This may result in the EMC being reached over an extended period however repeated simulations of this were not successful.

The initial rates of sorption were stronger in the physical model for all cases as

evidenced by the steeper gradients in Figure 88. This suggests that whilst WUFI predicts final EMC values accurately (in most cases), there may be some level of variance between measured and predicted levels of w for RH fluctuations with shorter time periods (*i.e.* $t < t_{\text{emc}}$) coupled with some under prediction when w levels approach those shown for MS 8.3.

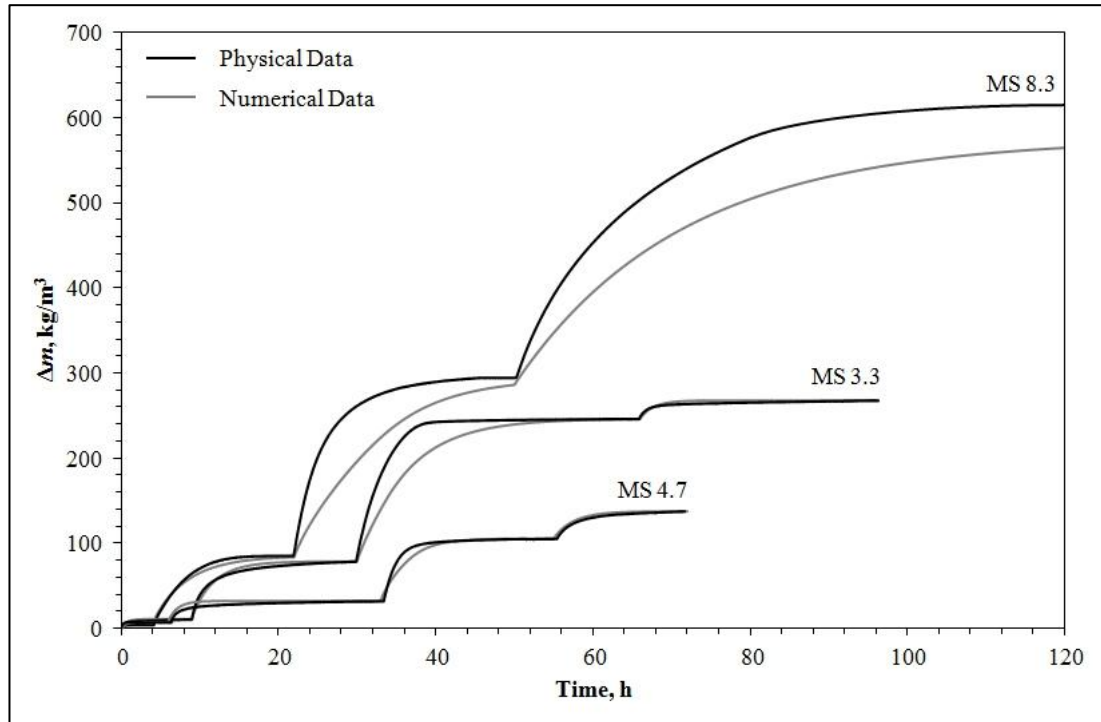


Figure 88 - Graph showing physical and numerical kinetic moisture uptake results for the three MS materials.

5.3 Vapour Permeability Model

Numerical modelling of 1D moisture transfer through the three MS materials was carried out in accordance with the methods outlined in Section 3.5.1.2 and compared against the physical modelling results (see: Section 4.3.2). Moisture flux, g_g ($\text{kg/s}\cdot\text{m}^2$) in the physical vapour permeability model was calculated as the moisture flow rate, G (kg/s) per exposed surface area, A (m^2). All three MS materials achieved a predicted steady state of moisture vapour transfer after 1.5 h (see: Figure 89) with negligible difference between numerical and physical results for g_g in the MS 3.3 and

MS 8.3 materials ($< 0.5\%$). MS 4.7 shows a greater difference at 9.33% (see: Table 43) however, all results were deemed acceptable due to the minimal proposed depth to be used in the WUFI model coatings ($d \approx 2\text{mm}$).

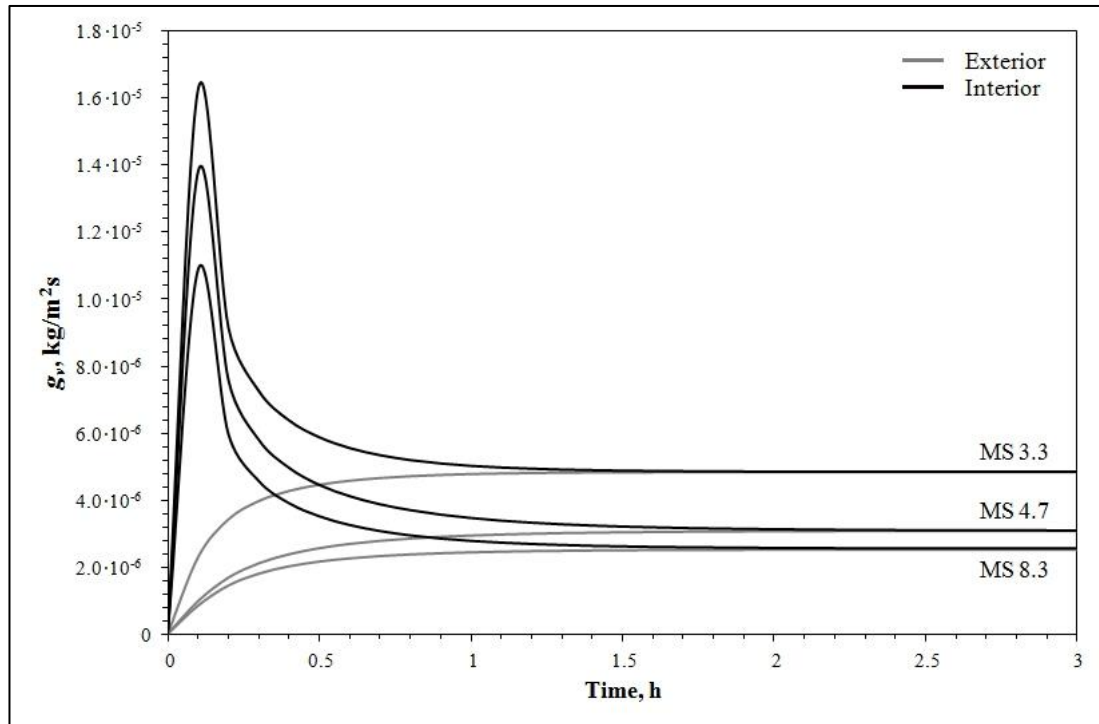


Figure 89 - Graph showing numerically predicted interior and exterior vapour fluxes for the three MS materials.

	Vapour Flux, g_v ($\text{kg/m}^2\text{s}$)		
	Numerical	Physical	Difference
MS 3.3	$4.837 \cdot 10^{-6}$	$4.818 \cdot 10^{-6}$	0.39%
MS 4.7	$3.080 \cdot 10^{-6}$	$2.817 \cdot 10^{-6}$	9.33%
MS 8.3	$2.552 \cdot 10^{-6}$	$2.546 \cdot 10^{-6}$	0.22%

Table 43 - Comparison of the numerically predicted and experimentally calculated vapour fluxes for the three MS materials.

5.4 Cyclic Response Experiments

A series of physical and numerical cyclic DVS response models using the three MS materials were conducted to establish the accuracy of the 1D numerical software (WUFI Pro v5.1) under two RH_{ie} amplitudes as outlined in Sections 3.4.1.2 and 3.5.1.3. The following two sections present the results of the validation and variance

testing of the numerical model.

5.4.1 1D Numerical Model Validation

The results from the physical and numerical models are shown in Figure 90 with good agreement evident for most cases.

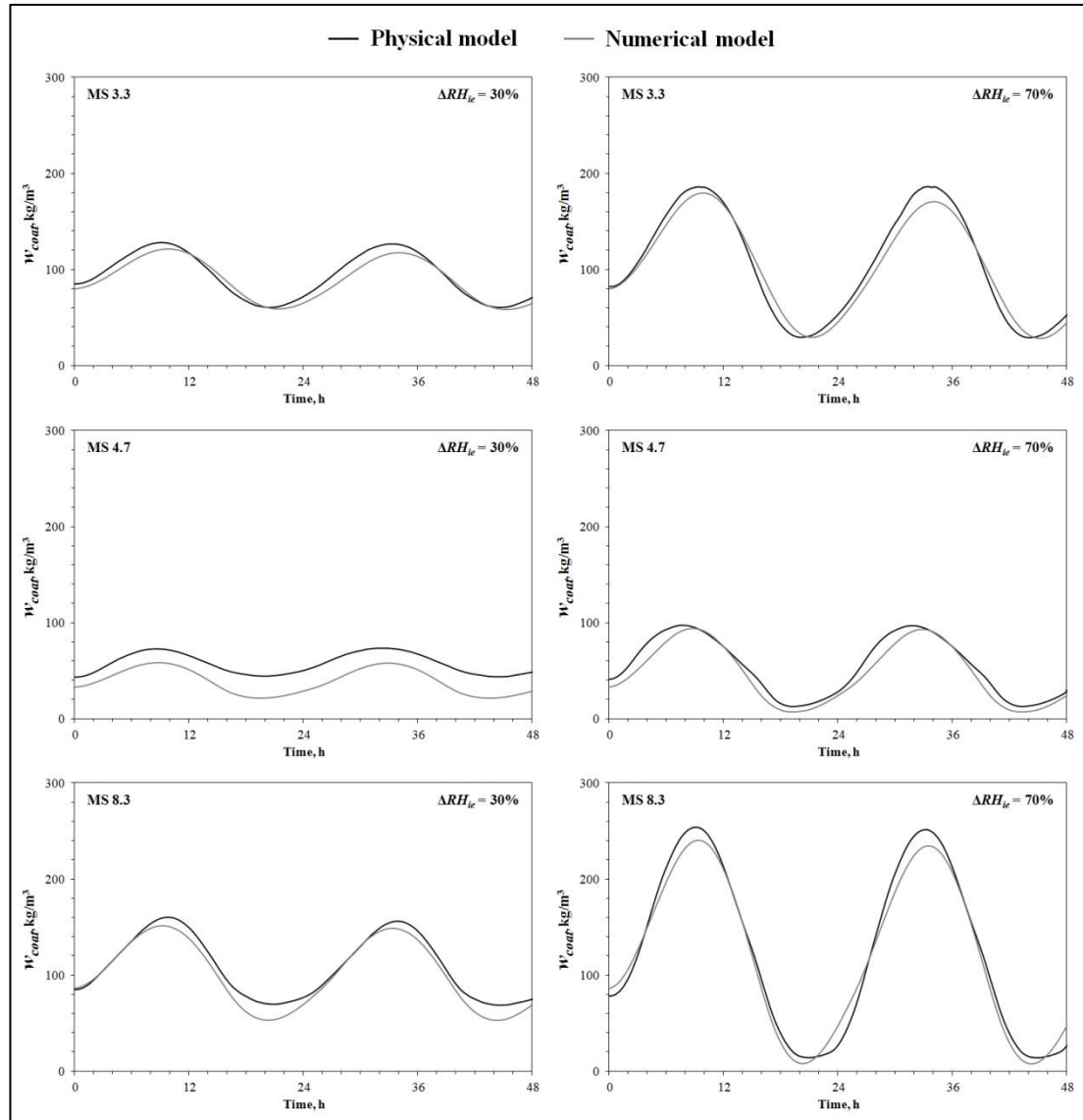


Figure 90 - Graph showing the physical and numerical cyclic response results (Casey et al., 2012).

Whilst the plots for both appear initially very similar there was a slight decline in maximum water content, $w_{\text{coat, max}}$ in the numerically predicted results on the second cycle for all cases, with no evidence of similar decline in the physical model. The

errors in the numerical prediction resulted in underestimation of both response rate and $w_{coat, max}$ in all cases, the most pronounced disagreement being MS 4.7 for the lower humidity amplitude ($\Delta RH_{ie} = 30\%$). WUFI, as with other numerical hygrothermal models, does not allow for coupling of dynamic response data (t_{emc}) to EMC levels, which could account for this discrepancy. Also as discussed in Section 5.2 there may be some level of variance between measured and predicted levels of w for RH_{ie} fluctuations with time periods shorter than those needed to reach EMC (*i.e.* $t < t_{emc}$). In addition, as all three MS materials have very rapid initial sorption rates and high SSA it is possible that the enthalpy (heat) of sorption (not currently considered in WUFI) has a small but significant effect, since the sorption/desorption hysteresis has previously been found to be minimal (see: Section 4.3.4).

5.4.2 Variance Testing

The statistical variance of the numerically predicted values from the physical model data was analysed in order to assess the level of confidence in the numerical model as outlined in Section 3.5.1.3. The variance plots for the three MS materials at both high and low RH amplitudes ($\Delta RH_{ie} = 30\%$ and 70%) are shown in Figure 91. There was a large difference between the numerical and physical results for MS 4.7 at $\Delta RH_{ie} = 30\%$ with 100% occurrence within limits only achieved at a variance of 36% (see: Table 44). MS 4.7 is therefore not shown on the graph due to axis scale limitations. At the higher amplitude ($\Delta RH_{ie} = 70\%$) MS 4.7 achieved 100% occurrence at 18% variance. Both MS 3.3 and MS 8.3 show the best fit between variance and confidence with 100% occurrence achieved at a variance level of $\approx 10\%$ for both materials at $\Delta RH_{ie} = 70\%$, and 12% variance (MS 8.3) at $\Delta RH_{ie} = 30\%$. The correlation of variance against occurrence within limits was deemed acceptable

and allowed further 1D numerical models to be simulated within these statistical confidence limits.

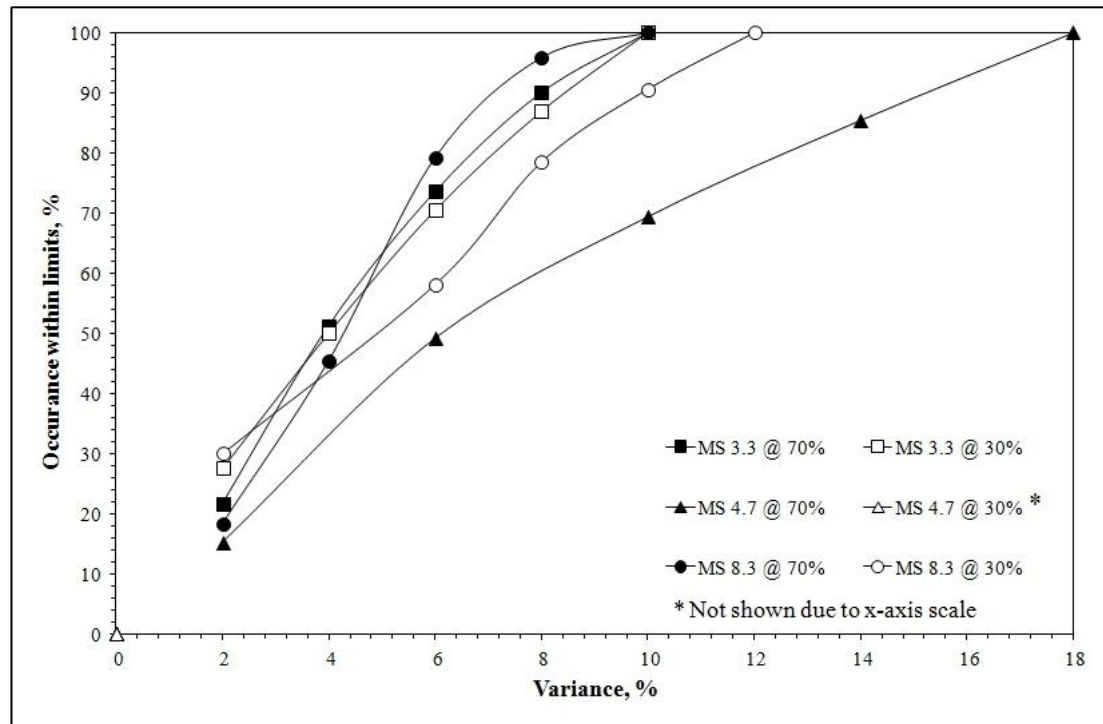


Figure 91 - Graph showing variance and occurrence within limits for the three MS materials (Casey et al., 2012).

$\Delta RH_{ie} = 70\%$						$\Delta RH_{ie} = 30\%$					
MS 3.3		MS 4.7		MS 8.3		MS 3.3		MS 4.7		MS 8.3	
V	O	V	O	V	O	V	O	V	O	V	O
2%	22%	2%	15%	2%	18%	2%	28%	12%	0%	2%	30%
4%	51%	6%	49%	4%	45%	4%	50%	18%	8%	6%	58%
6%	74%	10%	69%	6%	79%	6%	70%	24%	41%	8%	79%
8%	90%	14%	85%	8%	96%	8%	87%	30%	75%	10%	91%
10%	100%	18%	100%	10%	100%	10%	100%	36%	100%	12%	100%

V = variance O = occurrence

Table 44 - Variance and occurrence within limits for all three MS materials at 30% and 70% RH amplitudes.

5.5 Sensitivity Analysis for Variation of ΔRH_{ie}

As outlined in Section 3.5.1.4 the first stage of 1D numerical model testing was to determine the sensitivity of RH_{coat} and w_{coat} to changes in RH_{ie} for the three MS materials within the model using expanded sinusoidal cyclic response simulations to

cover an increased ΔRH_{ie} range from 10% to 90%. The total change in moisture content, Δw_{coat} and relative humidity, ΔRH_{coat} were plotted against the corresponding ΔRH_{ie} amplitude with the results shown in Figure 92.

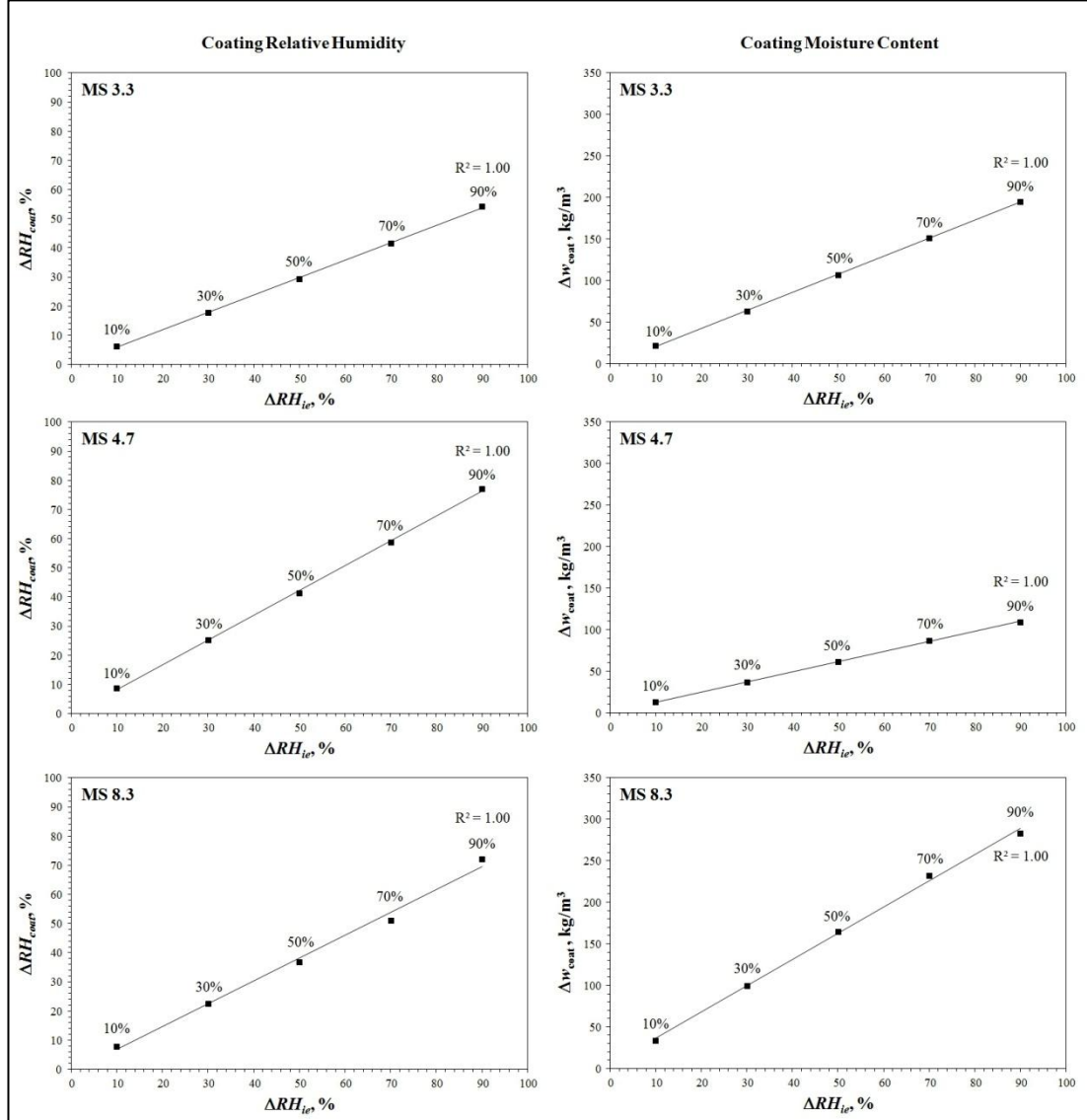


Figure 92 - Graph showing 1D model sensitivity of RH_{coat} and w_{coat} to increasing ΔRH_{ie} amplitudes (Casey et al., 2012).

There was a positive linear relationship between ΔRH_{ie} and ΔRH_{coat} and also between ΔRH_{ie} and Δw_{coat} ($R^2 = 1.00$) for all three MS coating cases suggesting good linearity across the range of ΔRH_{ie} within the WUFI model. Both MS 3.3 and MS 8.3 showed approximate equal distribution between ΔRH_{coat} and Δw_{coat} , with MS 8.3

displaying the highest levels of both measures. MS 4.7 showed an imbalance between the measures with considerably higher change in levels of ΔRH_{coat} than Δw_{coat} . This could be due to MS 4.7 having significantly higher bulk porosity, n combined with much lower w_{50} and w_{80} values when compared to MS 3.3 and MS 8.3 (see: Table 35). This is consistent with the higher macro/meso pore ratio for MS 4.7 discussed previously (see: Figure 77) when compared to both MS 3.3 and MS 8.3.

5.6 Sensitivity Analysis for Material tuning

Sensitivity analysis to investigate using WUFI Pro v5.1 as a numerical design tool to allow the MS materials to be tuned for any specific set of psychrometric conditions was undertaken as outlined in Section 3.5.1.5. Figure 93 and Table 45 display the contributing factor for each hygrothermal property altered in the models.

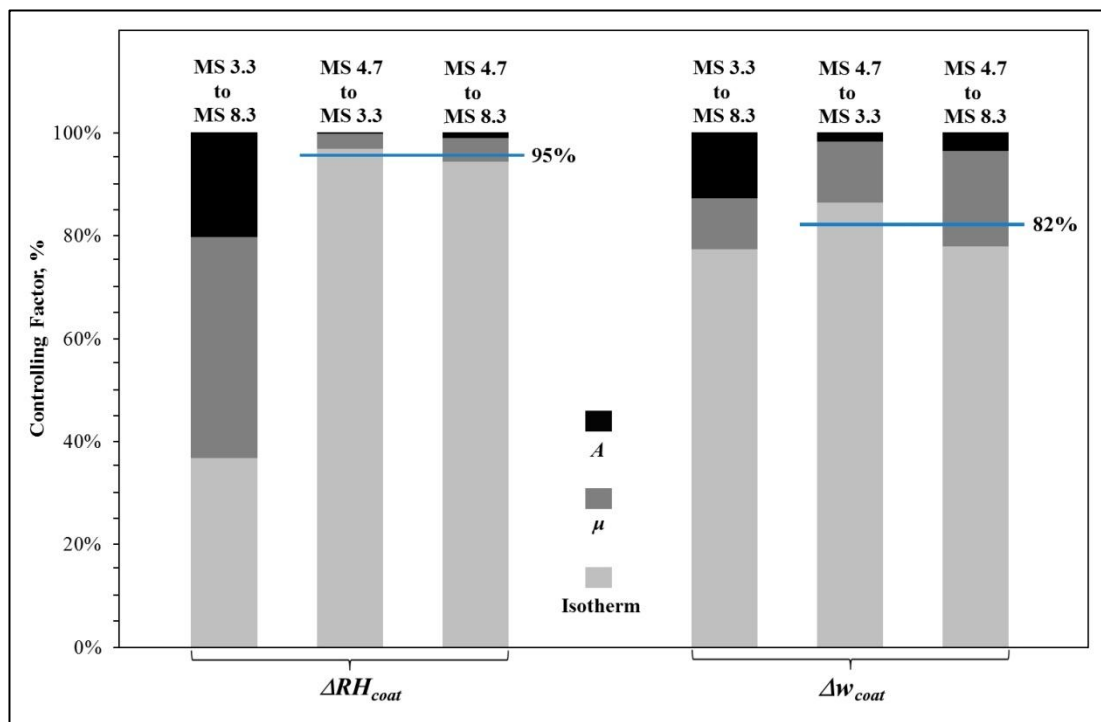


Figure 93 - Graph showing the controlling factor of hygrothermal material properties using WUFI for material tuning (Casey et al., 2012).

For the MS 3.3 \rightarrow MS 8.3 case, it can be seen that adjustment of the complete isotherm had a large contributing factor in respect of Δw_{coat} (77%) however there was a distinct difference in isotherm contribution to ΔRH_{coat} when compared to the other cases. Reverting to the isotherm results (see: Table 35) shows that MS 3.3 and MS 8.3 already have very similar EMC levels and therefore it is the adjustment of μ and A_w that were proportionally more sensitive. It is evident that for the MS 4.7 \rightarrow MS 3.3 and MS 4.7 \rightarrow MS 8.3 cases where there is a large difference in the hygrothermal properties the main contributing factor was the adjustment of the sorption isotherm, particularly with respect to adjustment of the $w_{50} - w_{80}$ values. This resulted in a mean contributing factor of 95% for ΔRH_{coat} and 82% for Δw_{coat} . As discussed in Hall et al., 2012 it is the dynamics of vapour sorption that appears to dominate the behaviour of the MS materials, and adjustment of EMC values and t_{emc} through material design should therefore allow tuning of these materials to suit any given set of psychrometric variables.

	MS 3.3 \rightarrow MS 8.3		MS 4.7 \rightarrow MS 3.3		MS 4.7 \rightarrow MS 8.3	
	ΔRH_{coat}	Δw_{coat}	ΔRH_{coat}	Δw_{coat}	ΔRH_{coat}	Δw_{coat}
w_{20}	16%	19%	6%	2%	4%	22%
w_{50}	30%	38%	10%	4%	9%	39%
w_{80}	32%	70%	96%	86%	94%	78%
w_{95}	37%	77%	97%	86%	94%	78%
μ	80%	87%	100%	98%	99%	96%
A_w	100%	100%	100%	100%	100%	100%

Table 45 - Controlling factors for material tuning using WUFI.

5.7 1D Building Retrofit Model

The final stage of 1D numerical simulation using WUFI Pro v5.1 was to undertake a

comparative study by analysing the performance of the three MS materials under representative external climate conditions and to compare the results with those of traditional construction materials as described in Section 3.5.1.6.

From Figure 94 it can be seen that for the solid and retrofitted walls (Cases A and B) the results showed very little water vapour sorption/desorption capacity in the interior gypsum coating, w_{coat} . As the gypsum had a painted interior surface which creates a vapour retarding effect ($S_d = 0.5\text{m}$) combined with a low sorption isotherm, this was somewhat expected. The spruce cladding and MS 4.7 displayed similar mean values for w_{coat} , however MS 4.7 had a higher range, Δw_{coat} compared to the spruce (see: Table 46). MS 4.7 also appeared to track the profile changes in RH_{ie} whereas the spruce does not, with a flattened profile which is indicative of the significantly greater initial response rate in MS 4.7.

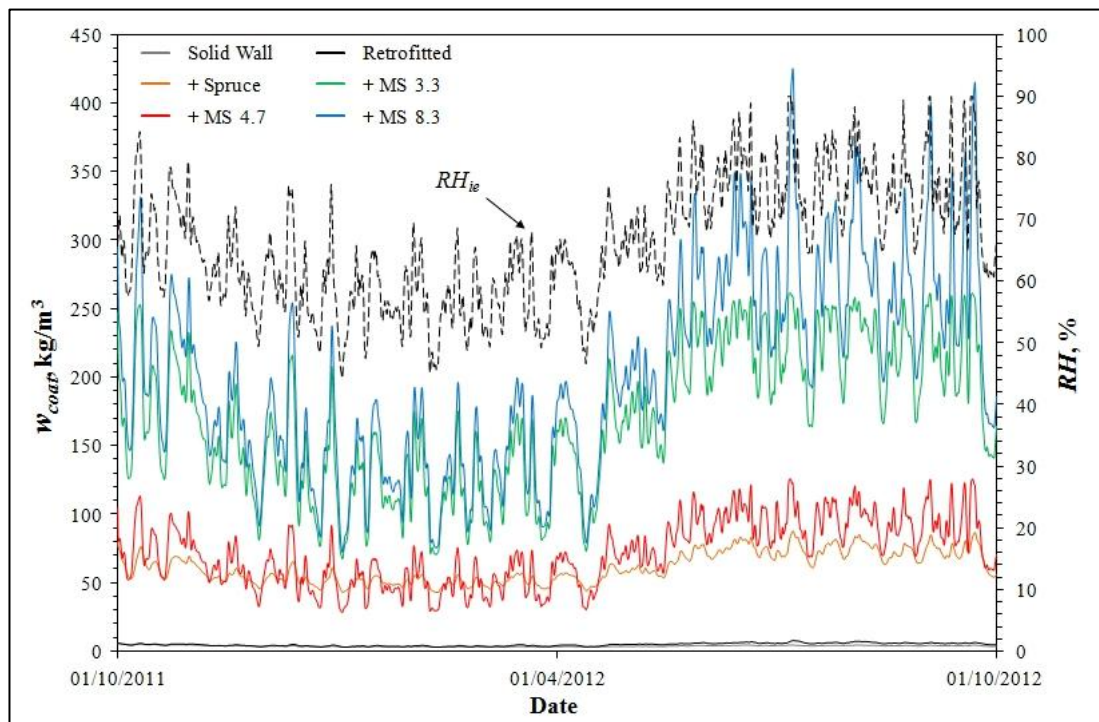


Figure 94 – Graph showing simulated yearly w_{coat} levels for all interior coating materials (Casey et al., 2012).

MS 3.3 and MS 8.3 displayed substantially higher predicted mean levels of w_{coat} ,

with lower w_{min} and higher w_{max} consistent with their higher sorption isotherms compared to other materials, whilst also showing closer tracking of RH_{ie} due to their significantly faster initial response rates. Table 46 shows that all three MS materials, and in particular MS 3.3 and MS 8.3, had significantly larger ranges of sorption/desorption, Δw_{coat} compared to the traditional material coatings which provides a good indication of humidity buffering potential.

	$w_{coat}, \text{kg/m}^3$			
	Min	Mean	Max	Δw_{coat}
Solid Wall	3.08	4.07	6.30	3.22
Retrofitted Wall	3.12	4.99	7.85	4.72
+ Spruce	43.09	61.35	88.14	45.05
+ MS 3.3	67.17	168.75	260.91	193.74
+ MS 4.7	28.03	71.78	126.05	98.03
+ MS 8.3	71.90	201.50	425.45	353.55

Table 46 - Summary of w_{coat} levels for all interior coating materials.

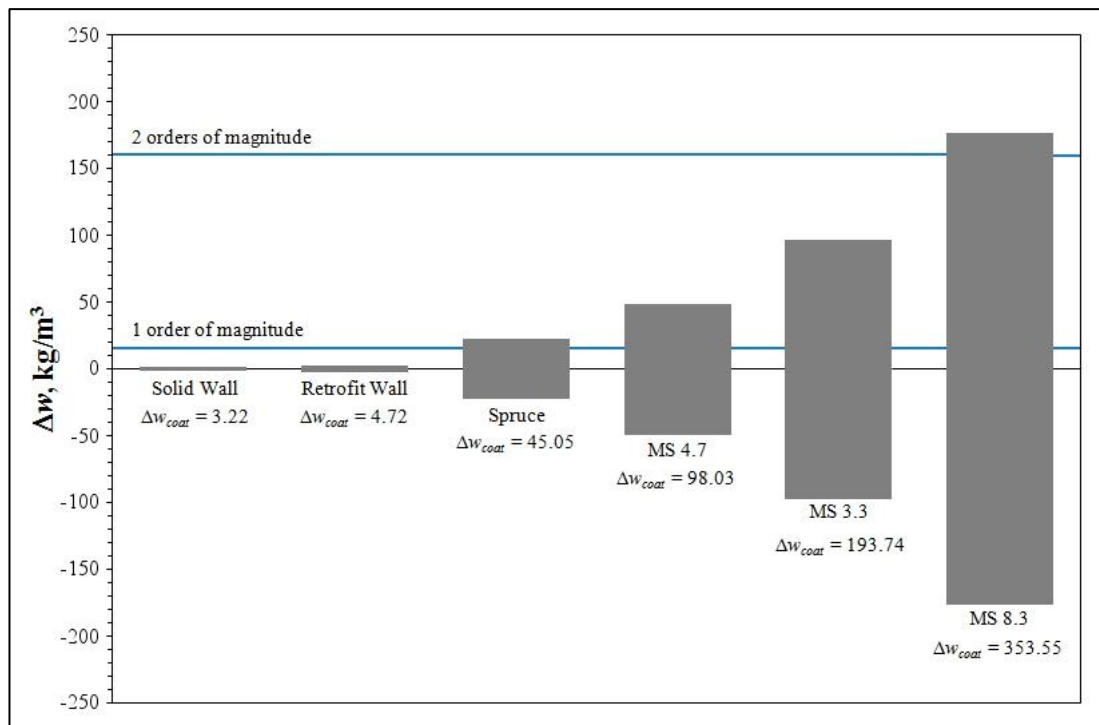


Figure 95 - Graph showing normalised yearly range of w_{coat} for all interior coating materials (Casey et al., 2012).

Figure 95 provides a graphical representation of Δw_{coat} normalised to zero for comparative reasons for each envelope coating case over the complete test period. Whilst the spruce cladding had a buffering capacity over one order of magnitude greater than that of both painted gypsum cases, the increased capacity for sorption/desorption of MS materials is immediately apparent with MS 8.3 displaying a buffering capacity at least two orders of magnitude greater. For humidity buffering applications, the tracking of RH_{ie} by w_{coat} is perhaps the most important factor when considering materials.

5.8 Summary

The main conclusions from Chapter 5 are:

1. WUFI predicted final isotherm EMC values accurately (in most cases) with under prediction of w_{coat} levels for RH fluctuations with time periods shorter than the EMC response time, t_{emc} .
2. There was a minimal and acceptable difference between numerical and physical results for vapour transfer rates, g_g .
3. Errors in cyclic numerical prediction resulted in underestimation of both initial response rate and $w_{coat, max}$ in all cases, the most pronounced disagreement being MS 4.7 for the lower humidity amplitude possibly due to Point 1 above.
4. The correlation of variance against occurrence within limits was deemed acceptable and allowed further 1D numerical models to be simulated within these statistical confidence limits.
5. A positive linear relationship between ΔRH_{ie} and ΔRH_{coat} and also between ΔRH_{ie} and Δw_{coat} ($R^2 = 1.00$) was found for all cases suggesting good

linearity within the WUFI model across the range of ΔRH_{ie} .

6. MS materials displayed DVS sorption/desorption, Δw_{coat} levels up to at least two orders of magnitude greater than traditional materials.

The increased performance, Δw_{coat} coupled with the tracking of RH_{ie} by w_{coat} suggests that the MS materials are able to provide rapid response humidity buffering more than two orders of magnitude greater than that of traditional interior building materials. The sorption isotherm, and in particular adjustment of the $w_{50} - w_{80}$ gradient of the absorption branch isotherm, is by far the most sensitive parameter when using WUFI as a design tool for material functional properties. Variance between physical data and numerically predicted results may be reduced by coupling t_{emc} and EMC data within the model. As discussed in Section 4.3.6, there is a positive logarithmic relationship between MS mesopore diameter and t_{emc} . Using WUFI Pro it is therefore possible to tune an MS material to suit a particular set of psychrometric conditions, e.g. a humidity buffering building physics application.

CHAPTER 6: Results of Energetic 3D Hygrothermal Modelling

6.1 Introduction

This chapter presents the results obtained using the whole-building energetic hygrothermal simulation software WUFI Plus v2.1.1.73 to meet Objective 4 and 5 (see: Section 1.4).

6.2 Moisture Generation Rates Experiment

Four separate experiments were carried out to establish the correlation between evaporation rate/moisture generation rate, g_g and exposed surface area of water, A_s or dish diameter, \varnothing_d . As outlined in Section 3.4.2.2, decreasing mass, Δm due to water evaporation was recorded for four dish diameters ($\varnothing_d = 30, 45, 60$ and 75 mm) and the results are presented in Figure 96.

The results show increasing linear mass loss for each dish diameter. The slope of each dataset was calculated to provide the water evaporation rate. These results were correlated and a positive linear relationship between exposed water surface area and the evaporation rate, g_g was plotted (see: Figure 97). This allows for calculation of the necessary dish diameter and, if required, exposed surface area to give a desired moisture generation rate using Eq. 6.1.

$$\varnothing_d = \frac{g_g + 0.0547}{0.0042} \quad \text{Eq 6.1}$$

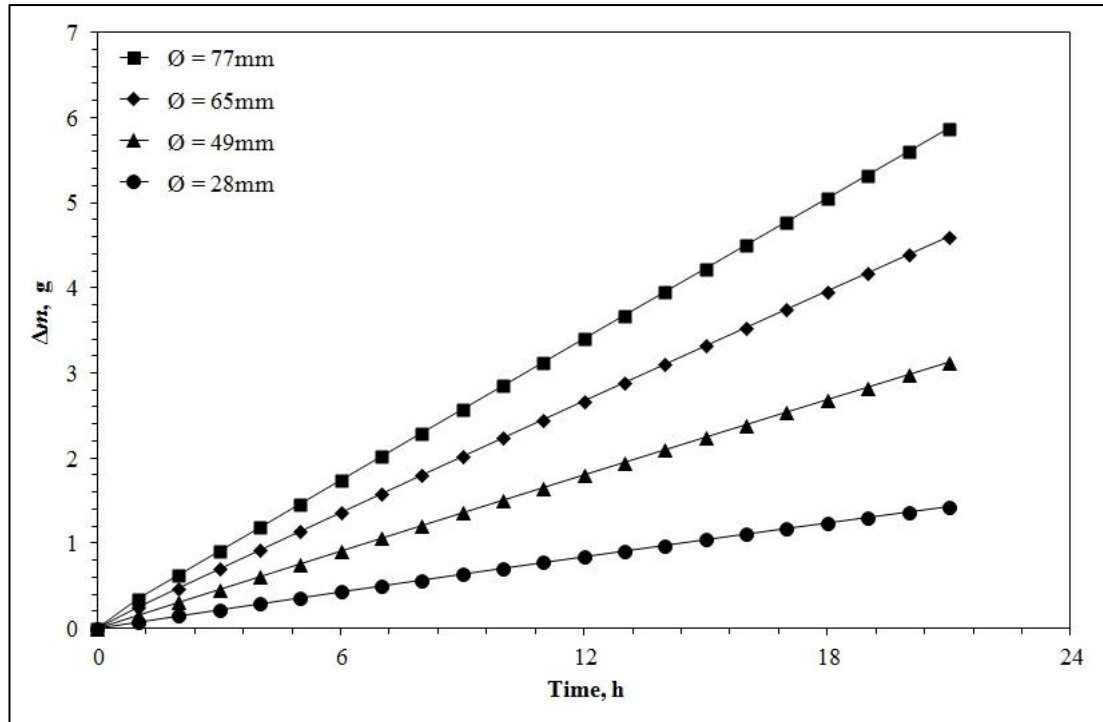


Figure 96 – Graph showing change in mass (loss) from evaporation for dish $\phi_d = 28$, 49, 65 and 77mm.

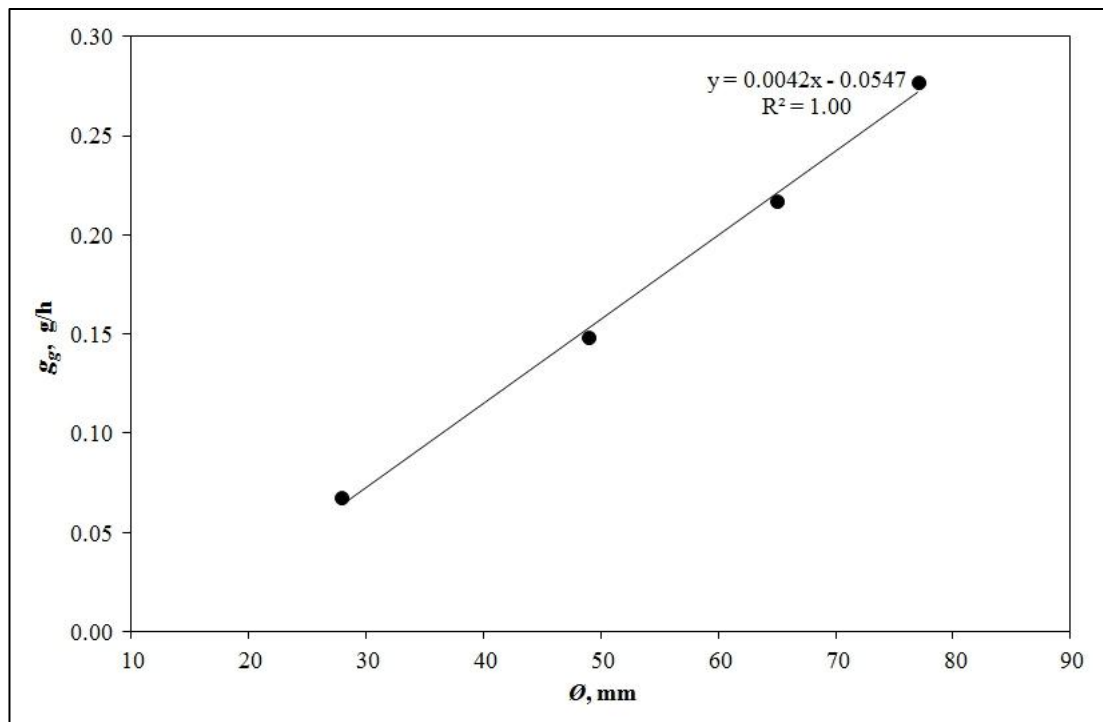


Figure 97 – Graph showing water evaporation rate plotted against dish diameter.

	\varnothing mm	A_s mm ²	m_i g	m_f g	g_g g/h
Test 1	77	$4.66 \cdot 10^{-03}$	0.344	5.87	0.277
Test 2	65	$3.32 \cdot 10^{-03}$	0.249	4.60	0.218
Test 3	49	$1.89 \cdot 10^{-03}$	0.153	3.12	0.148
Test 4	28	$6.16 \cdot 10^{-04}$	0.072	1.43	0.068

Table 47 - Water evaporation rate calculation data.

6.3 Material Humidity Buffering Model

A series of six physical and numerical material humidity buffering models using the three MS materials, gypsum, spruce and aluminium foil were conducted to establish the accuracy of the 3D numerical software (WUFI Plus) under internal moisture loads as outlined in Sections 3.4.2.3 and 3.5.2.1. The following two sections present the results of the validation and variance testing of the numerical model where the numerically-predicted are represented by the black line and the physical modelling results by the shaded grey area representing the $\pm 3\%$ error about the measured results.

6.3.1 3D Numerical Model Validation

From Figure 98 it can be seen that there was some divergence between the numerically-predicted and physical modelling results for the spruce which may be indicative of small differences between the values in the WUFI material properties database and those of the actual sample of timber tested. For the MS 4.7 sample, the model appeared to underestimate the buffering potential of the material for reducing RH_{ie} levels. As stated previously (see: Section 5.4) the coupling of dynamic response data (t_{emc}) to EMC levels combined with the variance between measured and predicted levels of w_{coat} for RH fluctuations with time periods shorter than those needed to reach EMC (*i.e.* $t < t_{emc}$) could account for this underestimation.

In general, the results for the aluminium foil, gypsum, MS 3.3 and MS 8.3 showed better agreement with the physical model with excellent matching of both day 1 and 2 RH_{ie} levels. In all cases the physical results showed lower peak RH_{ie} levels when compared to the numerically predicted results, however final RH_{ie} levels (day 2) appeared very similar.

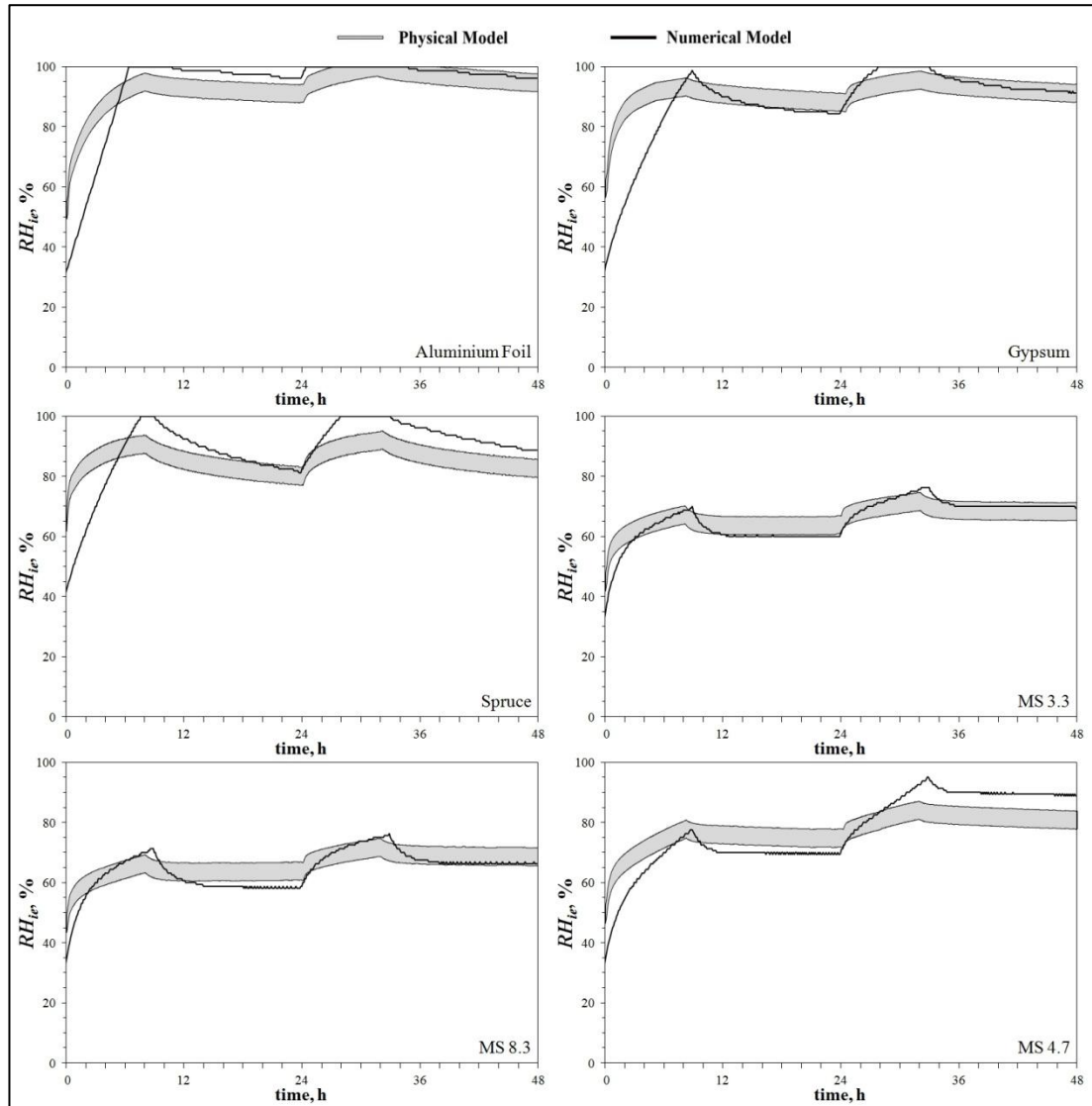


Figure 98 - Graph showing the physical and numerical material humidity buffering results.

6.3.2 Variance Testing

The statistical variance of the numerically predicted values from the physical model data was analysed in order to assess the level of confidence in the numerical model. The variance plots for the six samples are shown in Figure 99. As discussed in Section 3.5.1.3, as the plot approaches the maximum value on the Y axis, data variance is reduced and confidence is increased and thus numerical model accuracy increased. MS 3.3 and MS 8.3 showed the best fit between variance and confidence with >93% occurrence achieved at a relatively low model variance of 8%. The gypsum variance showed good accuracy in part due to there being very little differences between manufacturing techniques of gypsum boards and thus a good match between the functional properties of the sample material and the WUFI material data. As expected from the discussion in Section 6.3.1, both MS 4.7 and spruce showed less accuracy with >90% confidence only achieved at $\approx 15\%$ variance in both cases (see: Table 48).

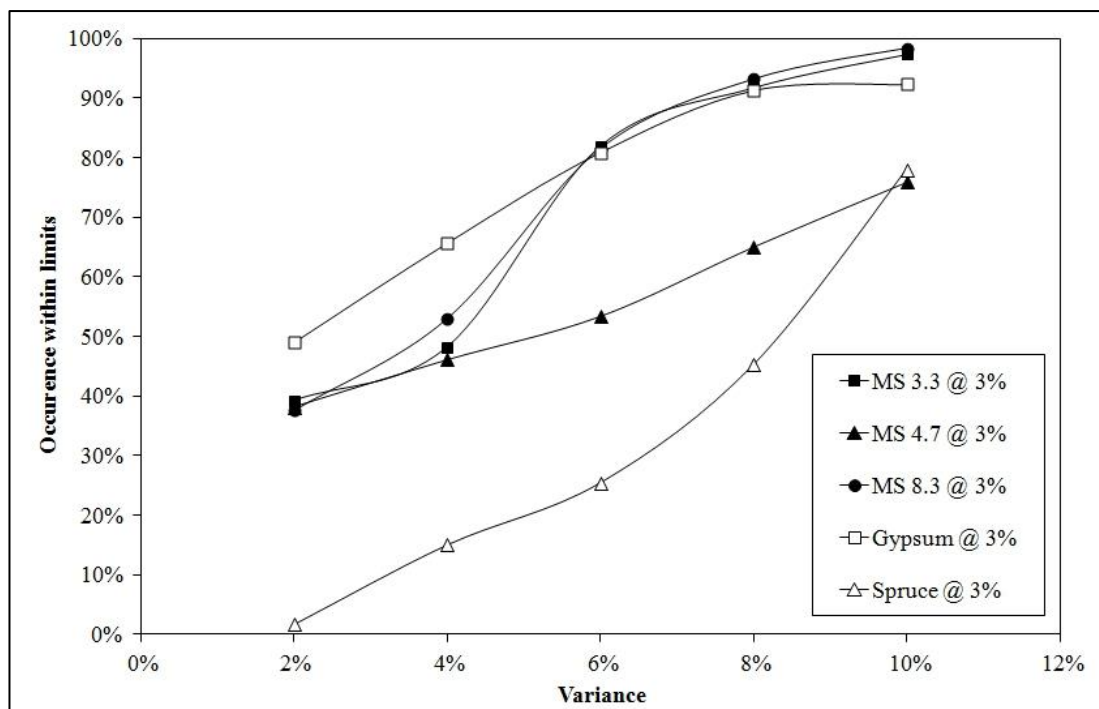


Figure 99 - Graph showing the variance and occurrence within limits for all interior coating materials.

Variance	Occurrence					
	Alu. Foil	MS 3.3	MS 4.7	MS 8.3	Gypsum	Spruce
2%	37%	21%	7%	14%	38%	5%
4%	48%	58%	14%	54%	63%	18%
6%	72%	92%	26%	70%	84%	29%
8%	90%	95%	55%	93%	87%	50%
10%	91%	97%	87%	97%	88%	79%
15%	92%	98%	91%	98%	90%	90%

Table 48 - Variance and occurrence for all interior coating materials.

6.4 Increased Hygrothermal Area/ Volume Ratio Model

As outlined in Section 3.5.2.2, the initial stage of analysis using WUFI Plus was to test the sensitivity of predicted RH_{ie} levels to increasing ratios of exposed surface areas of hygrothermal materials to internal wall area (from 0% → 100%) with the simulation results presented in the following two sections.

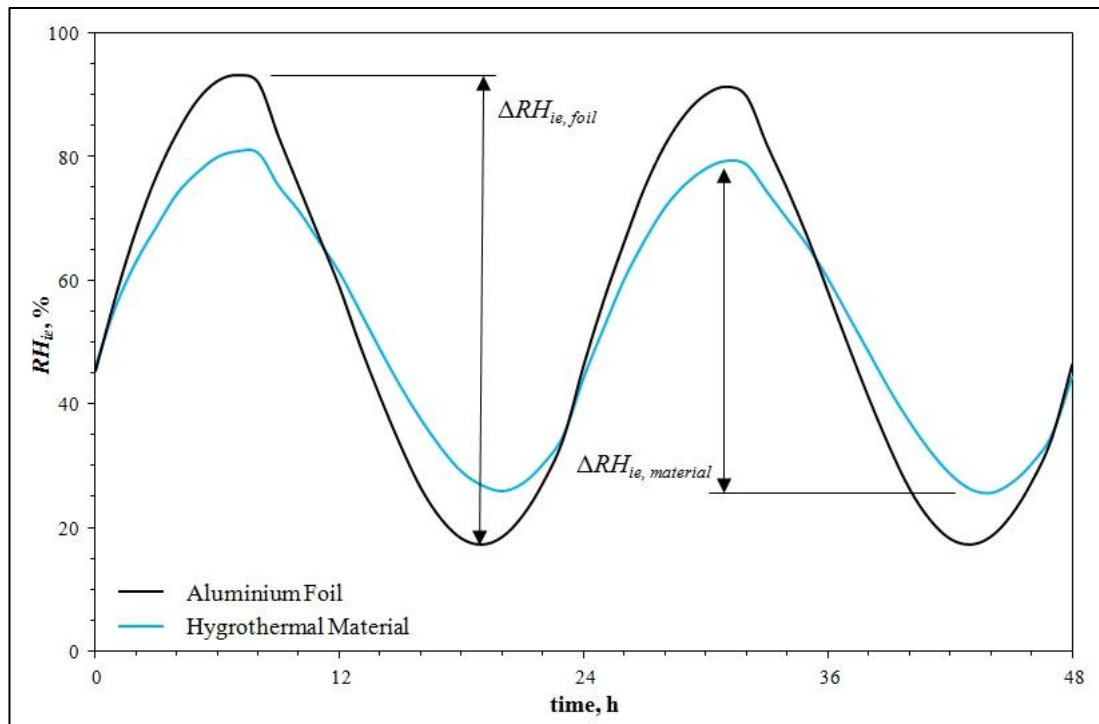


Figure 100 - Model system plot showing methodology for calculating ΔRH_{ie} reduction.

For both simulations, ΔRH_{ie} was calculated from the maximum and minimum values of RH_{ie} predicted over the 48h period. ΔRH_{ie} reduction ($\% \Delta RH_{ie,red}$) was calculated

from ΔRH_{ie} where a hygrothermal buffering material was present, then subtracted from ΔRH_{ie} assuming no buffering material was present (*i.e.* Aluminium foil):

$$\Delta RH_{ie,red} = (\Delta RH_{ie,material} - \Delta RH_{ie,foil}) - 1 \times 100 (\%) \quad \text{Eq 6.2}$$

The maximum area of hygrothermal material needed to successfully reduce RH_{ie} levels such that minimum and maximum RH_{ie} levels did not exceed the ASHRAE comfort levels ($40\% < RH_{ie} < 70\%$) was calculated using Eq. 6.3 where the occurrence, t/t_{yr} of the predicted RH_{ie} within limits is given as a dwell time count, t of the complete time ($t_{yr} = 48$) and presented as a percentage of the total:

$$\text{COUNTIF}(RH_{ie}, ">= 40\%") - \text{COUNTIF}(RH_{ie}, ">= 70\%") \quad \text{Eq 6.3}$$

6.4.1 No Internal Moisture Load

For the first simulations no moisture load was added to the isolated box and thus indoor RH_{ie} is dependent only on moisture transferred via infiltration. The results (see: Figure 101) showed that there is a steady increase in the $\% \Delta RH_{ie,red}$ as the ratio of material increases for all cases and is evidently greater in the MS materials over the traditional materials. At an air exchange rate of 0.1ACH, with an ‘empty’ (Aluminium foil only) ΔRH_{ie} of 28.1% MS 3.3 and MS 8.3 showed a reduction of $> 70\%$ at only 3% area/ volume ratio, increasing to $> 90\%$ at a ratio of 10%. In comparison, the gypsum and spruce achieved a maximum reduction of $\approx 70\%$ and $\approx 90\%$ at a ratio of 100%. In all cases, $\% \Delta RH_{ie,red}$ was less effective as the air exchange rate increased, with ‘empty’ ΔRH_{ie} levels approaching exterior levels. The three MS materials still achieved a $\% \Delta RH_{ie,red}$ of $> 85\%$ at a 40% area/ volume ratio.

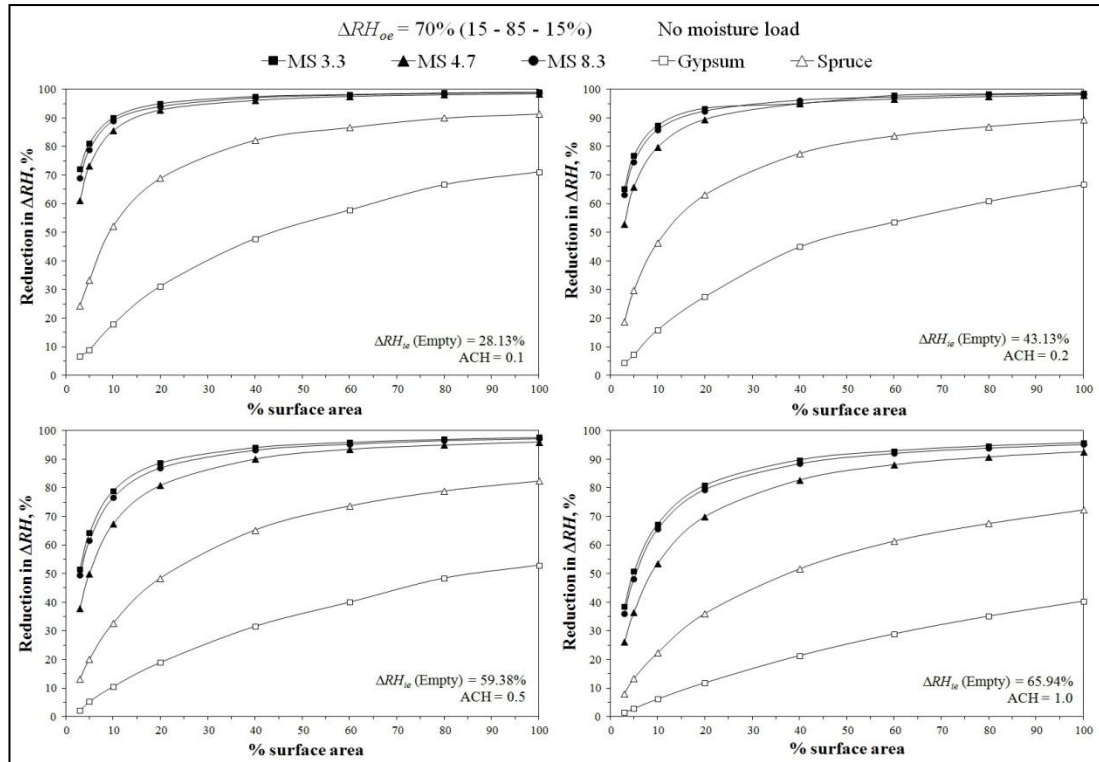


Figure 101 - Graph showing ΔRH_{ie} reduction for increasing hygrothermal material ratio under four air exchange rates without moisture loading.

The results for RH_{ie} dwell time within the ASHRAE limits are presented in Figure 102. All materials showed full occurrence ($t/t_{yr} = 100\%$) of RH_{ie} within ASHRAE comfort limits at the lowest air exchange rate (0.1ACH) due to the empty box levels of ΔRH_{ie} being fully within limits already. Across all cases there were fewer occurrences within ASHRAE limits as air exchange increased. All three MS materials still achieved $t/t_{yr} = 100\%$ at an area/ volume ratio of 20% at an ACH = 1.0, whilst the gypsum can reach only a maximum occurrence of $t/t_{yr} = 64\%$ even at 100% area/ volume ratio.

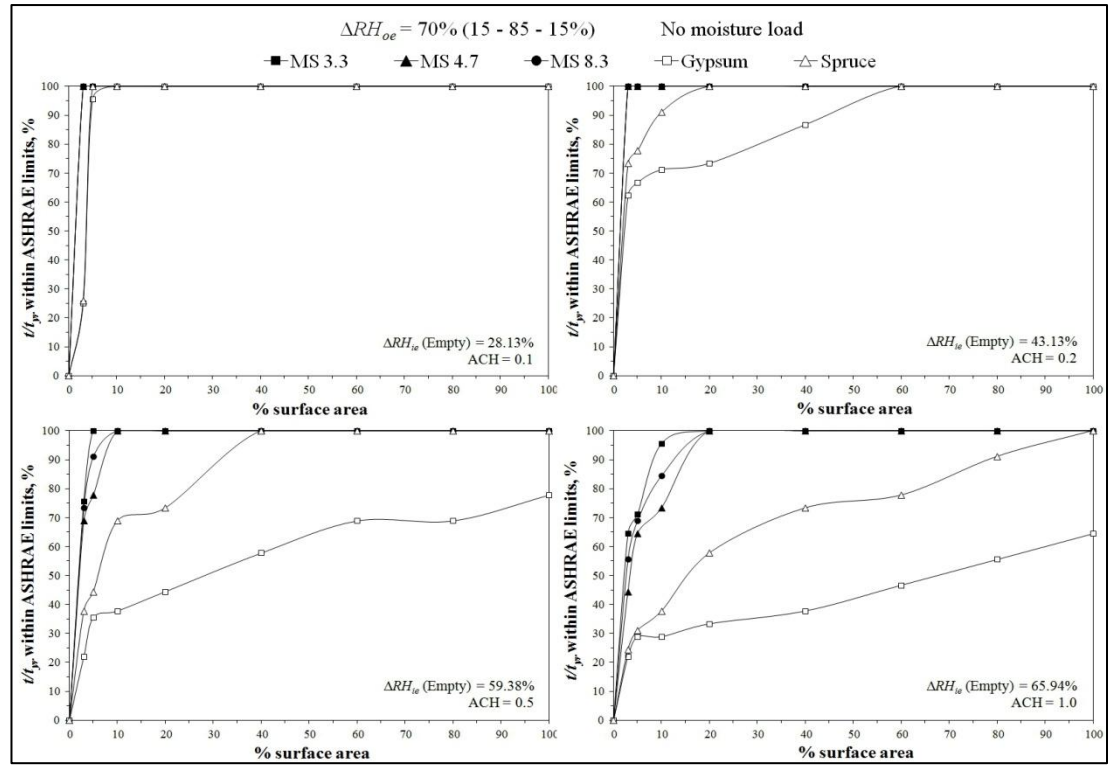


Figure 102 - Graph showing RH_{ie} dwell time for increasing hygrothermal material ratio under four air exchange rates without moisture loading.

6.4.2 With Internal Moisture Load

Moisture loads were added to the isolated box for the second set of simulations as outlined in Section 3.5.2.2 with the results for ΔRH_{ie} reduction shown in Figure 103. When internal moisture loads are added $\% \Delta RH_{ie, red}$ appeared similar to the levels presented without moisture in the previous section, due to the levels of ΔRH_{ie} for the ‘empty’ case significantly increasing. The dwell time of ΔRH_{ie} within the ASHRAE comfort limits decreased across all ACH cases when compared to the previous results and is particularly evident for the gypsum at lower air exchange rates (see: Figure 104). With the additional moisture loads at ACH = 0.1, gypsum dwell time decreased from $t/t_{yr} = 100\%$ (no moisture load) to $t/t_{yr} = 46\%$, at a 10% area/ volume ratio, and only achieved $t/t_{yr} = 100\%$ at a 100% ratio, *i.e.* entire internal wall surface area. All three MS materials performed exceptionally achieving $t/t_{yr} = 100\%$ at \leq

20% area ratio across all air exchange rates.

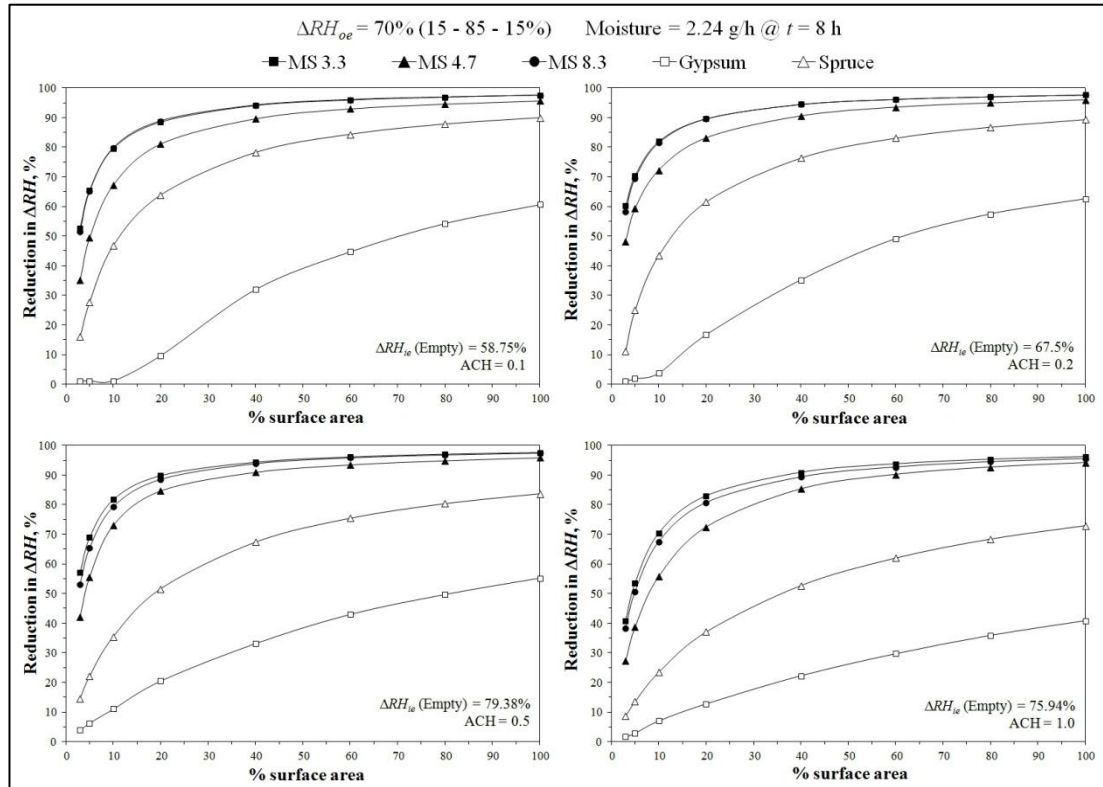


Figure 103 - Graph showing ΔRH_{ie} reduction for increasing hygrothermal material ratio under four air exchange rates with moisture loading.

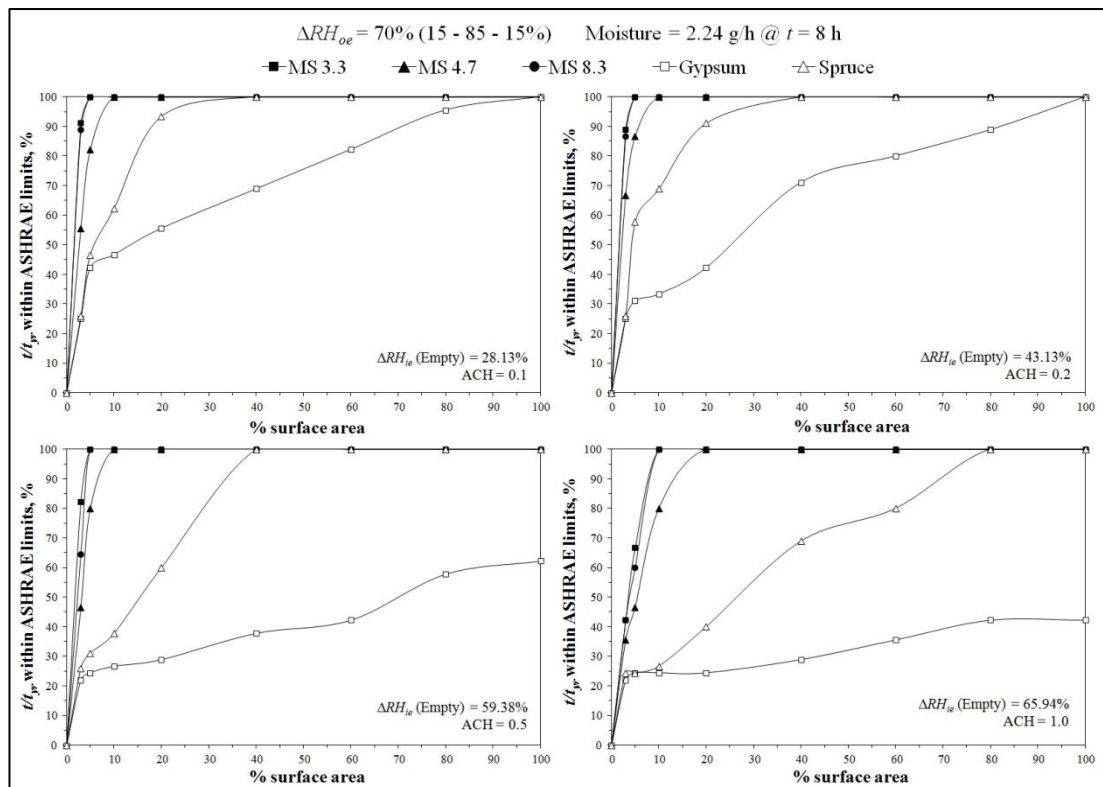


Figure 104 - Graph showing RH_{ie} dwell time for increasing hygrothermal material ratio under four air exchange rates with moisture loading.

6.5 Cyclic Response Model

As outlined in Section 3.5.2.3, the second stage of the 3D numerical model analysis was test the sensitivity of the predicted RH_{ie} levels over a full amplitude range of ΔRH_{oe} (10% \rightarrow 70%) and air exchange rates (ACH = 0.1 \rightarrow 1.0) to investigate the accuracy of the WUFI Plus model. Figure 105 presents the results of the six test cases simulated.

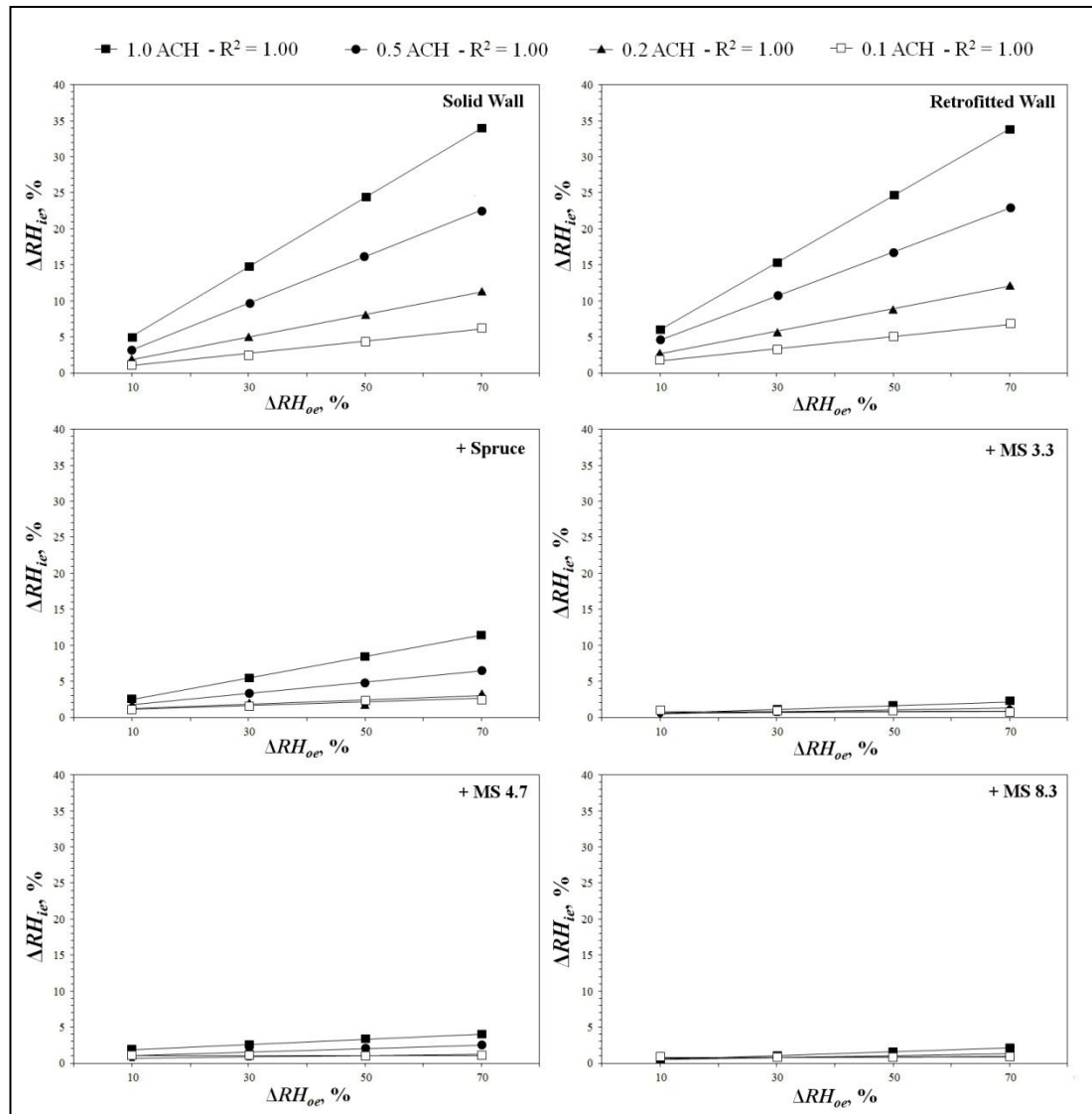


Figure 105 - Graph showing sensitivity of ΔRH_{ie} to varying amplitudes of ΔRH_{oe} under four air exchange rates.

For all pre and post retrofitting cases, ΔRH_{oe} amplitude variation and air exchange

rates there was a positive linear relationship between ΔRH_{ie} and ΔRH_{oe} suggesting extensive linearity across the full range of ΔRH_{oe} and air exchange rates within WUFI Plus. As would be expected when compared to the MS materials and spruce, cases A and B (gypsum) showed significantly increased levels of ΔRH_{ie} for all air exchange rates. All cases showed an increase in ΔRH_{ie} levels as air exchange rate increases, with cases A and B again having more pronounced increases indicating their poor RH_{ie} buffering potential. The MS materials and particularly MS 3.3 and MS 8.3 showed insignificant changes in ΔRH_{ie} levels up to and including 1.0ACH, which indicates considerable humidity buffering potential.

6.6 Increased Moisture Loads Model

A series of increased moisture load simulations, designed to assess ΔRH_{ie} levels under a moisture ‘over-loading’ scenario were simulated using WUFI Plus as described in Section 3.5.2.4. The range and scale of RH_{ie} for both morning and evening schedules were plotted for an airtight scenario and a series of different ACH levels (see: Figure 106).

The results showed a general reduction of minimum RH_{ie} levels for the three non-MS cases (spruce and gypsum), indicating the greater influence of the exterior RH_{oe} as the air exchange rate increases (see: Figure 65). Both the solid and retrofitted walls (gypsum) displayed predicted maximum ΔRH_{ie} levels up to 67% (ACH = 1.0) with mean RH_{ie} values exceeding the upper ASHRAE limit (>70%) across all ACH levels. In addition, upper RH_{ie} levels for both gypsum cases reached 100% for both schedules across all air exchange rates. The spruce cladding performed better with a maximum ΔRH_{ie} of 22% fluctuating about a mean RH_{ie} of 63% (ACH = 1.0) but with upper RH_{ie} levels outside the 40-70% ASHRAE comfort limits across all ACH

levels. In contrast, in the three MS material cases, and again MS 3.3 and 8.3 in particular, RH_{ie} levels remained within the ASHRAE limits under both morning and evening overloading schedules and across the full range of air exchange. MS 8.3 performed better than MS 3.3 and MS 4.7 with a maximum ΔRH_{ie} of 7.5% fluctuating about a mean RH_{ie} of 53% (ACH = 1.0). These simulations demonstrate the ability of the MS materials to continually buffer RH_{ie} fluctuations even when subjected to repeated moisture overloading scenarios.

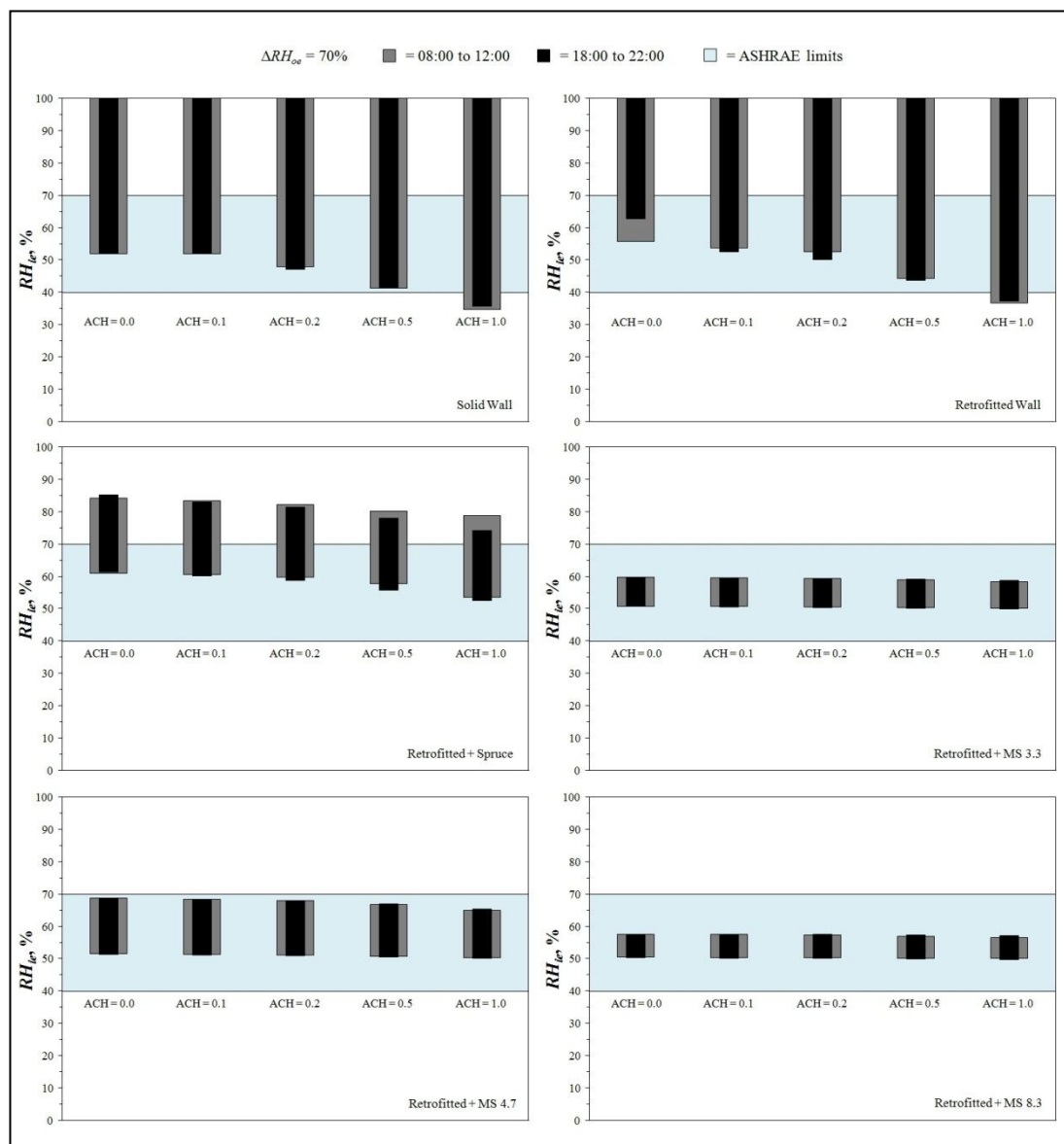


Figure 106 - Graph showing variation of RH_{ie} for increased occupancy moisture loads under five air exchange rates.

6.7 Increased Air Exchange Rate Model

A series of models were simulated to assess the effects of the hygrothermal materials on RH_{ie} levels under both morning and evening increased ventilation scenarios as outlined in Section 3.5.2.5. From the results (see: Figure 107) it can be seen there was a common trend for all cases with decreasing minimum RH_{ie} levels for the later ventilation schedule as air exchange rate (ACH) increased due to the increasing influence of the lower exterior RH_{oe} for the evening schedule (see: Figure 66). For both gypsum cases (*i.e.* solid and retrofitted walls) RH_{ie} levels exceeded the upper and lower ASHRAE comfort limits for both schedules and across all air exchange rates.

Although MS 4.7 displayed better buffering (reduced ΔRH_{ie}) compared to the spruce for the later ventilation schedule, they both showed similar RH_{ie} levels remaining within the limits during the early schedule for all exchange rates, but exceeding the lower limit at ACH's > 1.0 during the later schedule. Both the MS 3.3 and MS 8.3 cases remained within the ASHRAE limits during the early schedule, but dropped below the lower limit during the later ventilation schedule for air exchange rates greater than 2.0 (*i.e.* windows and doors fully open). The MS materials, particularly MS 3.3 and MS 8.3, displayed a marked reduction in ΔRH_{ie} and thus humidity buffering across all ACH levels and both morning and evening ventilation schedules when compared to the traditional envelope materials.

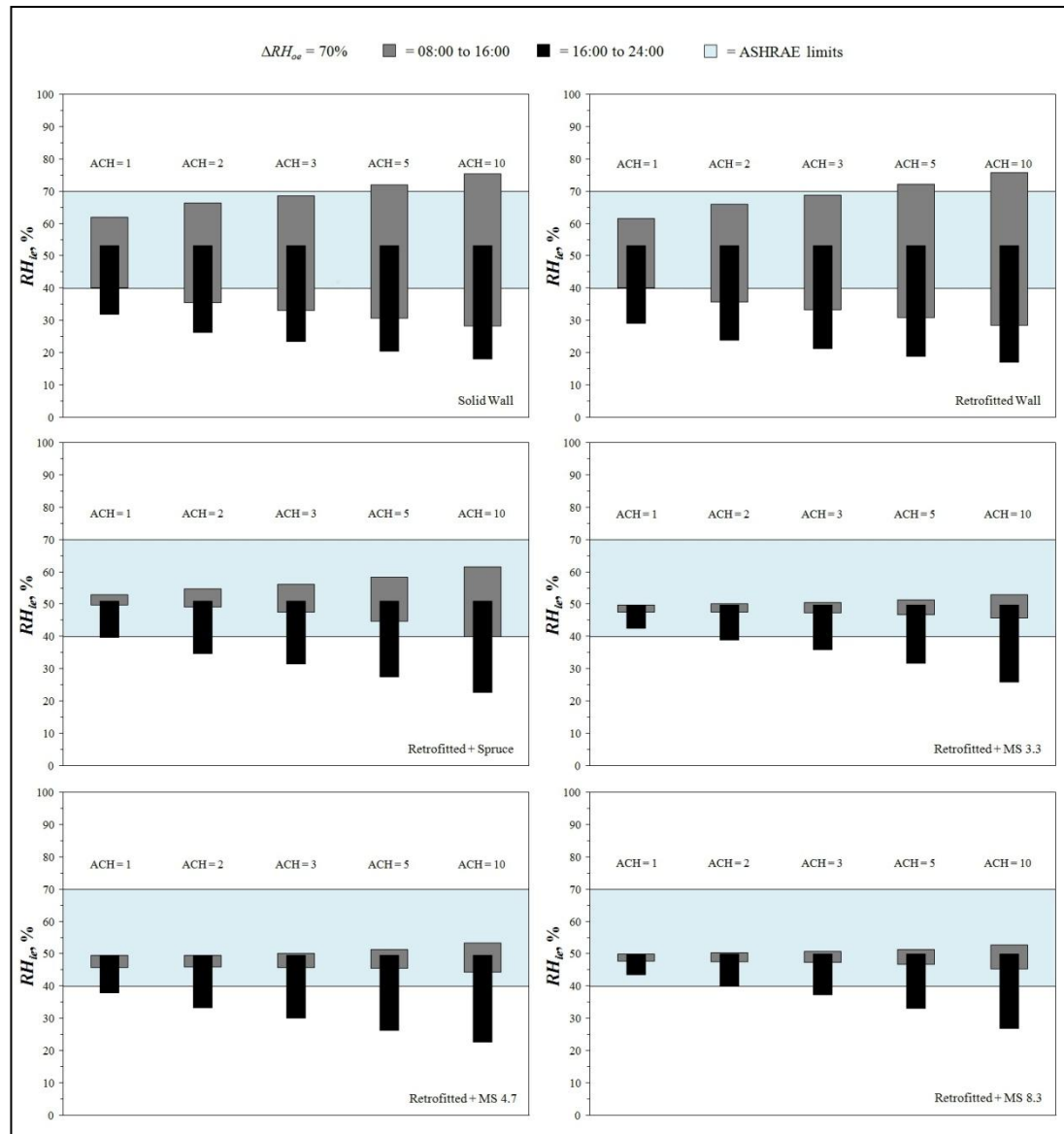


Figure 107 - Graph showing variation of RH_{ie} under increasing air exchange rates.

6.8 Representative Climate Modelling

A series of comparative hygrothermal and energetic simulations were run using WUFI Plus to establish the resultant RH_{ie} levels and performance of the materials under representative (as opposed to parametrically-varied) exterior and interior conditions, using an exterior climate generated from the CIBSE TRY file for Nottingham (UK) as outlined in Section 3.5.2.6. As stated, the results presented in the following sections are for the second year only which allowed for one full year of

pre-simulation.

6.8.1 Material Depth Analysis

The initial analysis (Stage 1) using the representative climate to investigate the influence of coating depth on RH_{ie} levels was undertaken as outlined in Section 3.5.2.6. In practice it might not be practical to envisage a material coating depth less than 15mm for the non-MS cases (Gypsum and spruce) however, these were also simulated for comparative reasons. Figure 108 shows the predicted numerical results obtained from the simulations. For reasons of clarity, only the range and scale of RH_{ie} are displayed as interpretation of the complete plots for each material at each depth would be difficult. ΔRH_{ie} was calculated from the minimum and maximum levels of RH_{ie} over the 2nd year of simulation only.

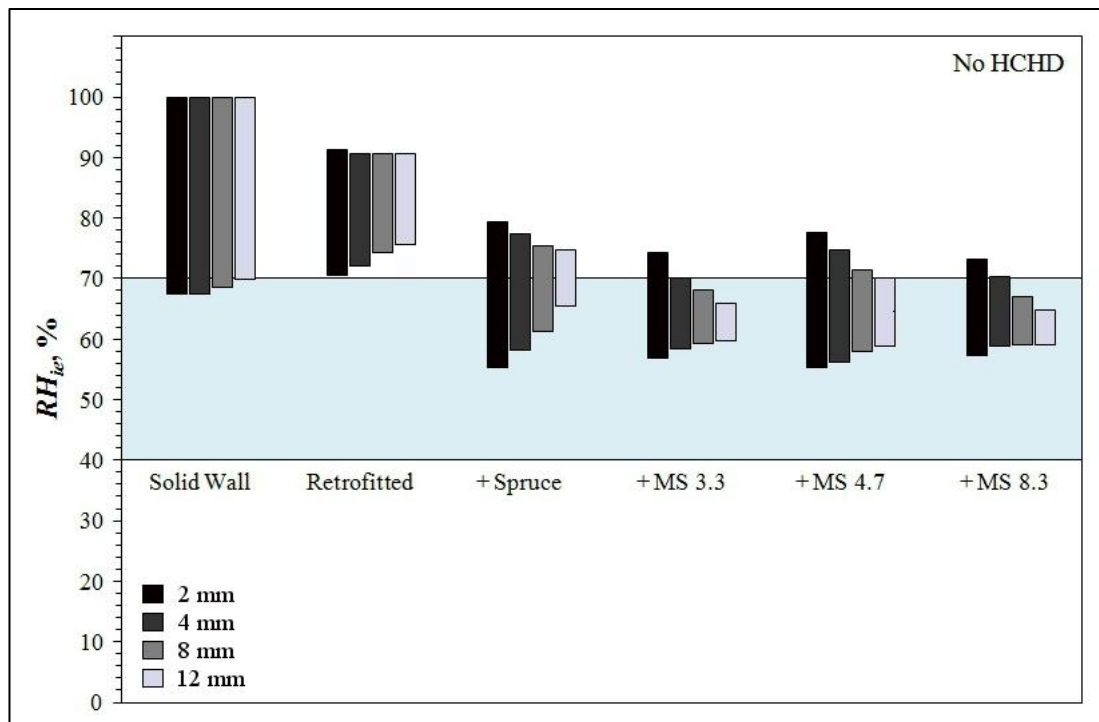


Figure 108 - Graph showing variation of ΔRH_{ie} and ASHRAE comfort zone for the six test cases at four material depths with no HCHD control.

As expected, levels of ΔRH_{ie} decreased across all cases as material depth increased with the exception of the solid wall where the air exchange rate was set at ACH =

0.5. This allowed the exterior climate (T_{oe} and RH_{oe}) to exert a greater influence on RH_{ie} levels than the buffering potential of the gypsum. For the retrofitted case (gypsum) the minimum levels of RH_{ie} never fell below the maximum advisable ASHRAE limit (70%) resulting in an uncomfortable humid environment for occupants. MS 4.7 and spruce again displayed similar ΔRH_{ie} initially at $d = 2$ mm, however the faster DVS response rate of MS 4.7 was evident as the depth increased, with a mean RH_{ie} level of 65% compared with 70% for the spruce at $d = 12$ mm. MS 3.3 and MS 8.3 showed excellent buffering capability at depths > 4 mm, remaining within the ASHRAE limits across the full two year period.

6.8.2 Full HCHD Control

As discussed in Section 3.5.2.6, the representative climate models were also used to perform analysis of predicted interior climate conditions under HCHD control within defined T_{ie} and RH_{ie} limits. The first simulation (Stage 3) was run under continuous HCHD control with control limits set points at $45\% \leq RH_{ie} \leq 65\%$ and $21\text{ }^{\circ}\text{C} \leq T_{ie} \leq 25\text{ }^{\circ}\text{C}$. Figure 109 shows the 2nd year RH_{ie} plots for each test case. The level of humidification and dehumidification in each case was calculated using Equations 6.4 and 6.5 where the occurrence of the predicted RH_{ie} at the lower limit, t_{lower}/t_{yr} and upper limit, t_{upper}/t_{yr} is given as a dwell time count of the complete time ($t_{yr} = 8762$ h) and presented as a ratio of the total:

$$t_{lower}/t_{yr} = \text{COUNTIF}(RH_{ie}, "<= 45\%") \quad \text{Eq 6.4}$$

$$t_{upper}/t_{yr} = \text{COUNTIF}(RH_{ie}, ">= 65\%") \quad \text{Eq 6.5}$$

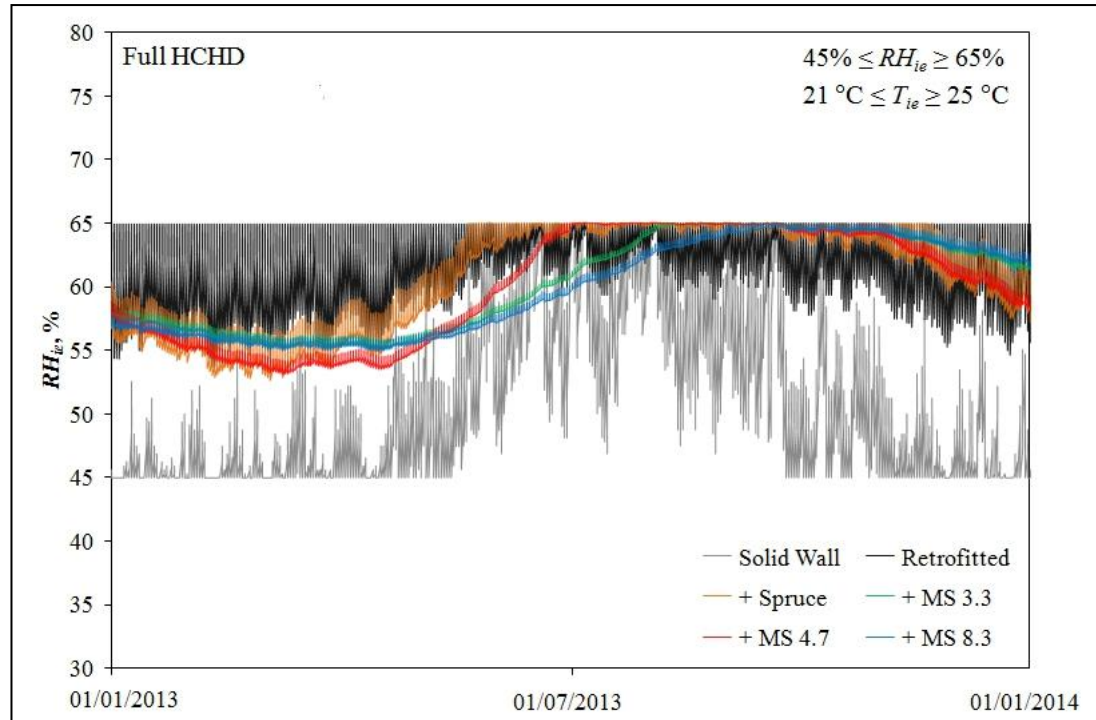


Figure 109 - Graph showing 2nd year RH_{ie} profiles for the six test cases with constant HCHD control at $45\% \leq RH_{ie} \leq 65\%$ and $21\text{ }^{\circ}\text{C} \leq T_{ie} \leq 25\text{ }^{\circ}\text{C}$.

As expected, the results show no RH_{ie} levels outside of the limits due to the continuous HCHD control (see: Figures 109 and 110). Due to the higher air exchange rate set for the solid wall ($ACH = 0.5$), it was the only case that required any humidification (see: Figure 109) throughout the entire year ($t_{lower}/t_{yr} = 0.37$), mostly during the early and late seasons however, little dehumidification ($t_{upper}/t_{yr} = 0.05$) was required during the peak summer period. In contrast, the retrofitted wall required 31% dehumidification ($t_{upper}/t_{yr} = 0.31$) and as can be seen in Figure 109, reached the 65%RH upper limit daily due to increased moisture loads from the occupants and higher air-tightness ($ACH = 0.1$). The spruce performed well where $t_{upper}/t_{yr} = 0.19$ during the summer and autumn, and MS 4.7 had similar predicted results ($t_{upper}/t_{yr} = 0.19$) but with reduced daily RH_{ie} fluctuations compared to the spruce. MS 3.3 and MS 8.3 displayed the best performances where t_{upper}/t_{yr} equalled 0.09 and 0.03, respectively over the entire year.

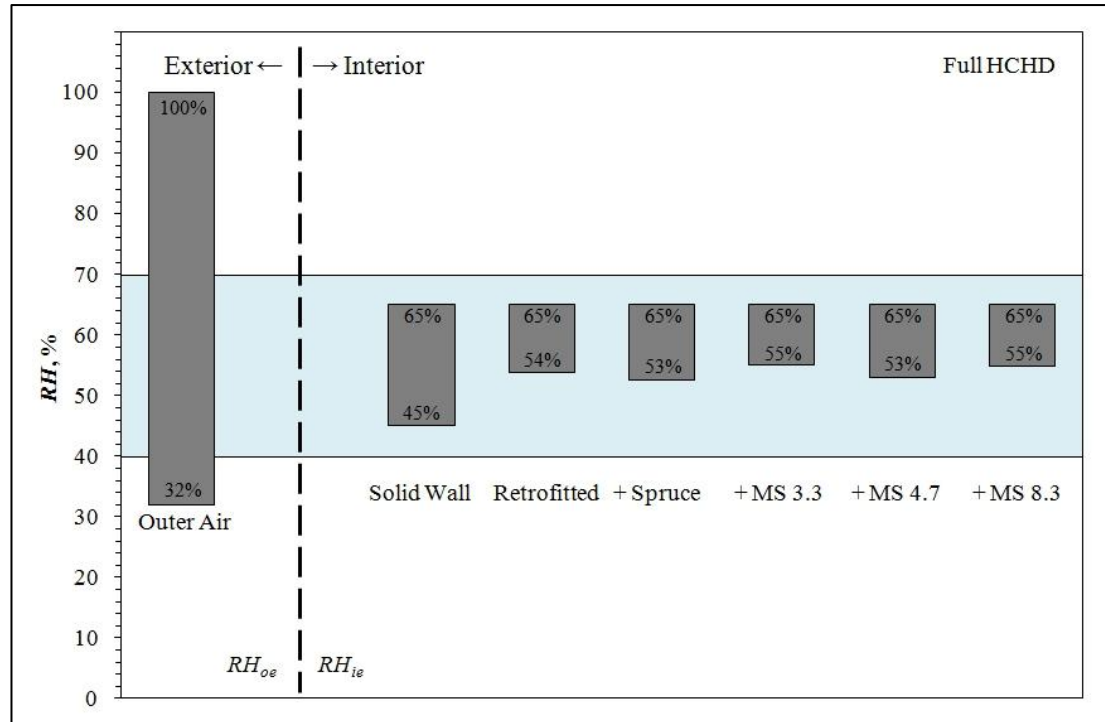


Figure 110 - Graph showing variation of ΔRH_{ie} for the six test cases with constant HCHD control at $45\% \leq RH_{ie} \leq 65\%$ and $21\text{ }^{\circ}\text{C} \leq T_{ie} \leq 25\text{ }^{\circ}\text{C}$.

Figure 111 shows the distribution of dwell time (t/t_{yr}) for the six cases in stepped RH_{ie} bands for the full HCHD control. For each case t/t_{yr} was calculated using the example shown in Eq. 6.6 which was used to calculate t/t_{yr} within the band $40\% \leq RH_{ie} \leq 45\%$:

$$\text{COUNTIF}(RH_{ie}, " \geq 40\%") - \text{COUNTIF}(RH_{ie}, " > 45\%") \quad \text{Eq 6.6}$$

Unexpectedly the solid wall showed predominant dwell time within the 40 – 55% RH_{ie} band ($t/t_{yr} = 0.38$) however, as there is full HCHD control with the lower limit set at $RH_{ie} = 45\%$ this can be considered as dwell time at the lower limit only which is corroborated by the full plot (see: Figure 109). For the retrofitted, spruce and MS 4.7 cases dwell time was spread across three bands from 50 to 65%RH with maximum dwell time ratios within the 60 to 65% band of $t/t_{yr} = 0.64, 0.61$ and 0.54 respectively. MS 3.3 and MS 8.3 remained within the 55 to 60% and 60 to 65% bands with approximately equal distributions of $t/t_{yr} = 0.5$.

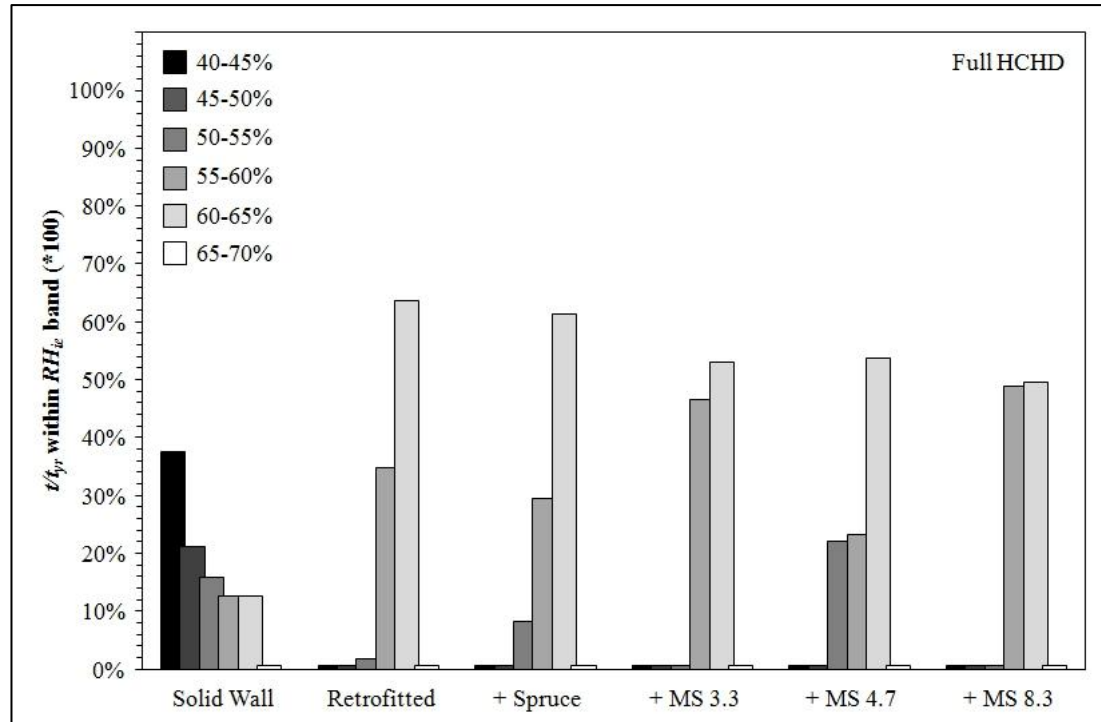


Figure 111 - Graph showing RH_{ie} dwell time for the six test cases with constant HCHD control at $45\% \leq RH_{ie} \leq 65\%$ and $21\text{ }^{\circ}\text{C} \leq T_{ie} \leq 25\text{ }^{\circ}\text{C}$.

6.8.3 Partial HCHD Control

Stage 4 of the representative analysis using WUFI Plus repeated the HCHD control limits set out in Section 3.5.2.6, however as HCHD systems are rarely required to provide 24h continual control, partial HCHD control timed to operate only during occupation hours (00:00 to 08:00) was simulated. When the results for the solid wall (gypsum) were compared to the full control results (see: Figure 112) it was evident that there was a marked increase in RH_{ie} fluctuations, however humidification and dehumidification dwell times were reduced to $t_{lower}/t_{yr} = 0.06$ and $t_{upper}/t_{yr} = 0.14$. This is perhaps due to increased T_{ie} fluctuation from the higher air exchange rate set, particularly during the non-operational hours of the HCHD plant. When compared to the constant HCHD control there was increased dwell time at or above the upper RH limits for all material cases; retrofitted wall ($t_{upper}/t_{yr} = 0.30$), spruce ($t_{upper}/t_{yr} = 0.26$), MS 4.7 ($t_{upper}/t_{yr} = 0.24$), MS 3.3 ($t_{upper}/t_{yr} = 0.18$), and MS 8.3 ($t_{upper}/t_{yr} = 0.08$) due to the elevated RH_{ie} levels during the uncontrolled periods.

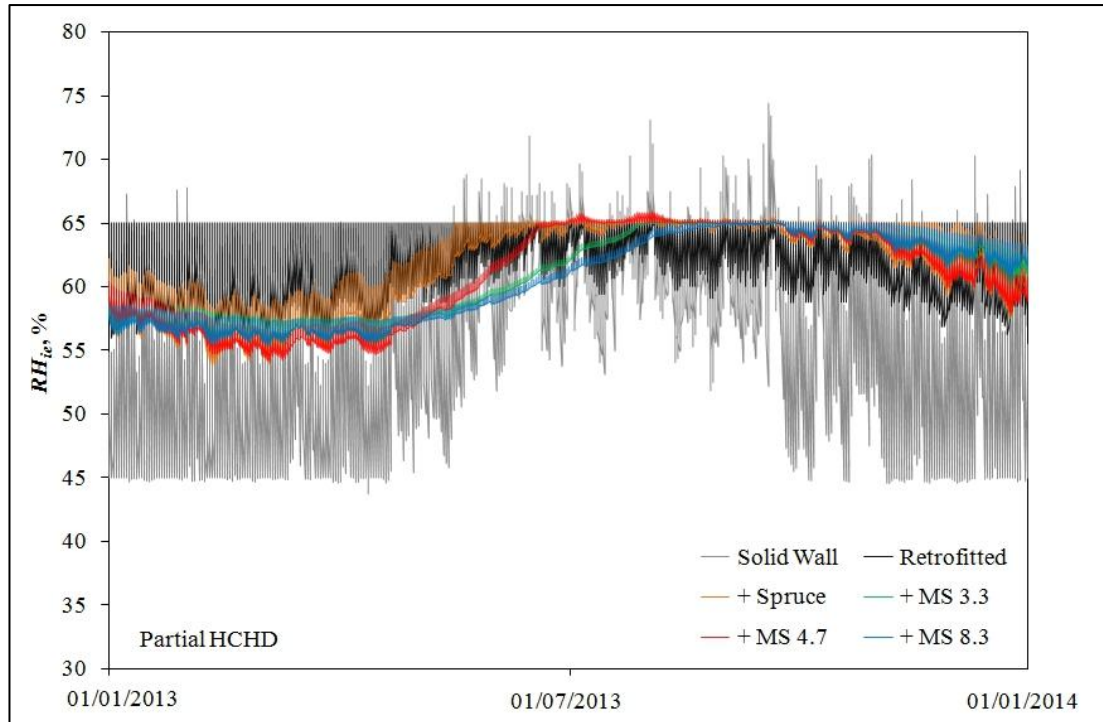


Figure 112 - Graph showing 2nd year RH_{ie} profiles for the six test cases with partial HCHD control at $45\% \leq RH_{ie} \leq 65\%$ and $21\text{ }^{\circ}\text{C} \leq T_{ie} \leq 25\text{ }^{\circ}\text{C}$.

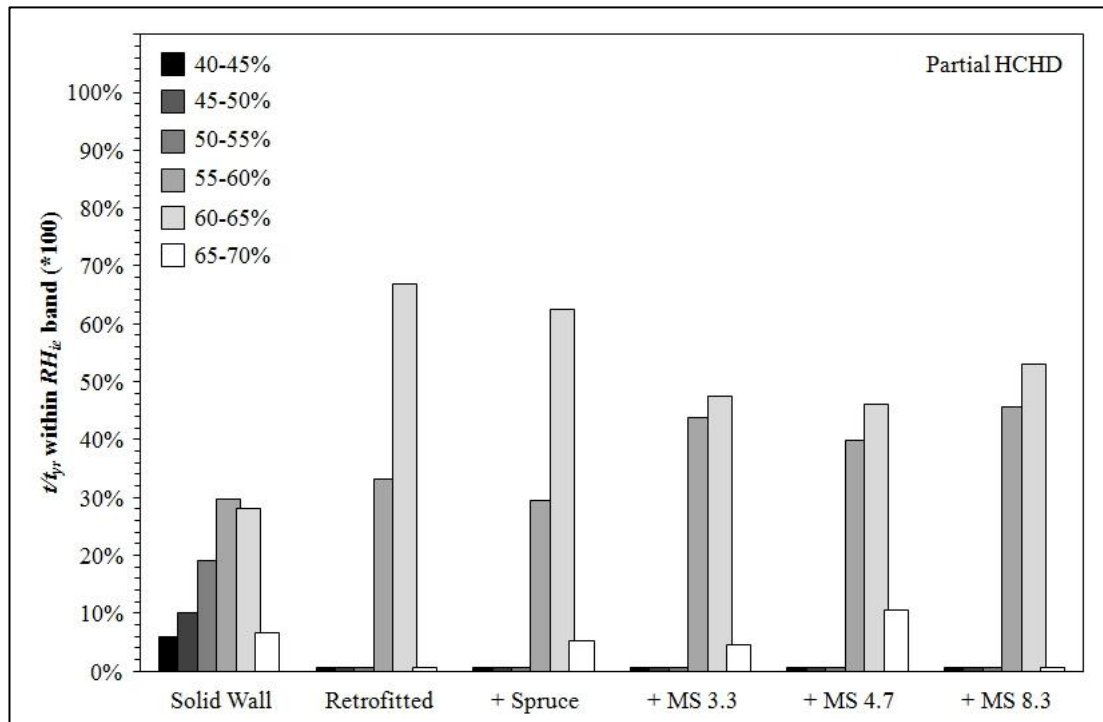


Figure 113 - Graph showing RH_{ie} dwell time for the six test cases with partial HCHD control at $45\% \leq RH_{ie} \leq 65\%$ and $21\text{ }^{\circ}\text{C} \leq T_{ie} \leq 25\text{ }^{\circ}\text{C}$.

Figure 113 shows the distribution of dwell time (t/t_{yr}) for the six material cases in stepped RH_{ie} bands for the partial HCHD control. When compared to the full control

results it can be seen that whilst there were increased fluctuations in RH_{ie} levels for the solid wall, as mentioned previously, the distribution appears more evenly spread across all RH_{ie} bands. In general the distribution of all other cases remained the same as for the full control simulations with the exception of MS 4.7, which appears to have shifted upwards, having increased dwell time in the higher bands (*i.e.* 55 to 70%).

6.8.4 Partial HCHD Control at ASHRAE Limits

For Stage 5 of the representative modelling, the resultant levels of RH_{ie} within the ASHRAE comfort limits (*i.e.* $40\% \leq RH_{ie} \leq 70\%$ and $T_{ie} = 23\text{ }^{\circ}\text{C}$) under partial HCHD control conditions were analysed. The results presented in Figure 114 showed that the maximum predicted RH_{ie} levels for the solid, retrofitted, spruce and MS 4.7 cases, all increased towards the upper limit over levels presented for the previous model (Stage 4). However, upper limit dwell time ratio significantly decreased for the retrofitted wall ($t_{upper}/t_{yr} = 0.20$), and also for spruce ($t_{upper}/t_{yr} = 0.08$) and MS 4.7 ($t_{upper}/t_{yr} = 0.06$). This was probably due to the increase in upper HCHD limit from 65%RH to 70%RH. In the solid wall case there were pronounced daily fluctuations of RH_{ie} , regularly above 70% during HCHD non-operational hours with a maximum RH_{ie} value of 76% and a consequent increased dehumidification ratio ($t_{upper}/t_{yr} = 0.14$). Both MS 3.3 and MS 8.3 remained below the limit throughout the 2nd year with maximum RH_{ie} values of 67% and 65%, respectively.

The distribution of dwell time (t/t_{yr}) for the six cases in stepped RH_{ie} bands for the partial ASHRAE HCHD control is shown in Figure 115. When compared to the distribution observed for Stage 4 there is a clear shift in dwell time, t/t_{yr} for all cases towards the upper RH_{ie} bands. The solid and retrofitted walls along with spruce

showed up to 50% of yearly RH_{ie} distribution above 65%RH. MS 3.3 and MS 4.7 both showed distribution above 65%RH at $t/t_{yr} = 0.33$ and 0.19, respectively. MS 8.3 remained within the range $50\% < RH_{ie} < 65\%$ throughout the full year.

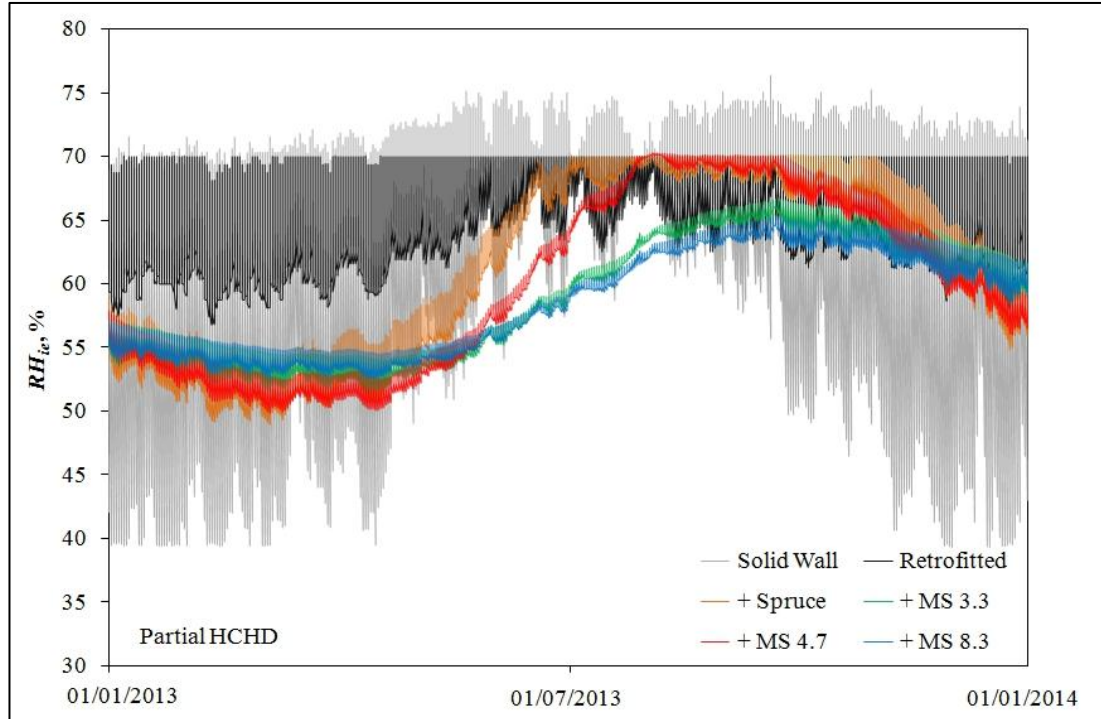


Figure 114 - Graph showing 2nd year RH_{ie} profiles for the six test cases with partial HCHD control at ASHRAE limits.

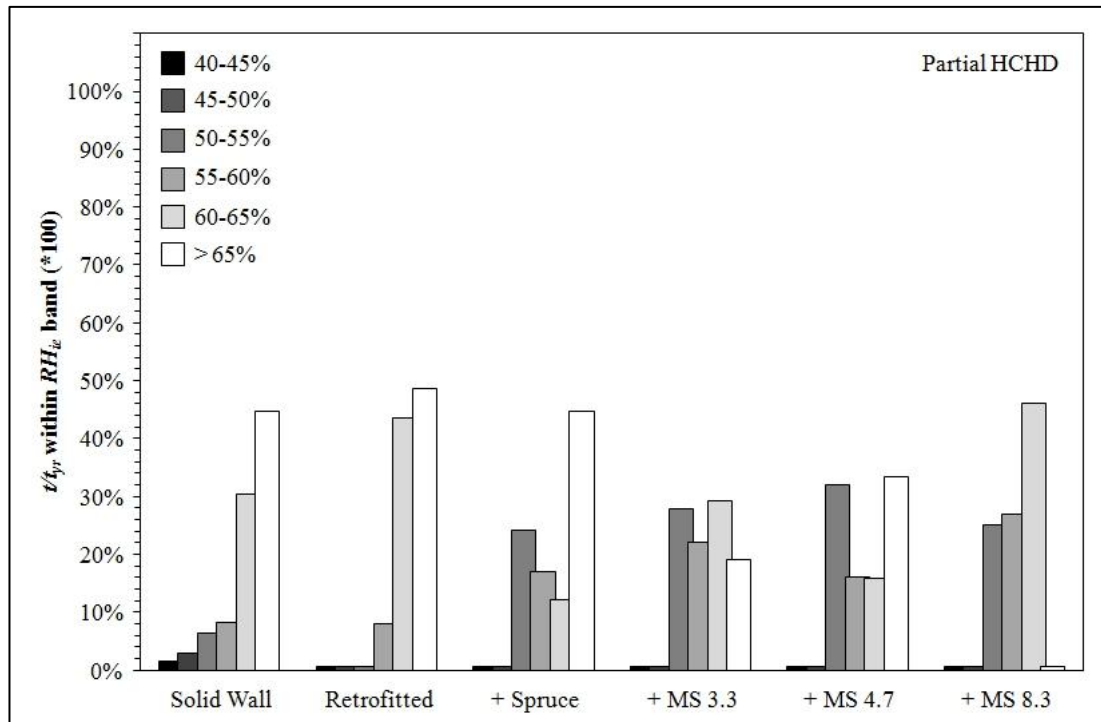


Figure 115 - Graph showing RH_{ie} dwell time for the six test cases with partial HCHD control at ASHRAE limits.

6.8.5 Energy Analysis

As outlined in Section 3.5.2.6 a comparative yearly analysis of HCHD conditioning energy was undertaken and the results are presented here. The potential energy savings shown were only calculated for the post-retrofitting cases (*i.e.* spruce and the three MS materials) and compared against the standard retrofitted case in order to determine the influence of the hygrothermal finishes.

As expected from the results discussed in Section 6.8.3 for the continuous HCHD control at $45\% \leq RH_{ie} \leq 65\%$ and $21\text{ }^{\circ}\text{C} \leq T_{ie} \leq 25\text{ }^{\circ}\text{C}$, the solid wall showed a substantially higher yearly energy usage for humidification of 6.73 KWh when compared to dehumidification of 0.36 KWh (see: Table 49). This was due to a combination of the increased vapour resistance of the painted gypsum and increased air exchange rate (ACH). All other cases required some level of dehumidification energy only and, when compared against the retrofitted wall (gypsum) it was shown that the spruce cladding provided a 33.9% saving, MS 4.7 53.2% whilst the MS 3.3 and MS 8.3 coatings provided substantial savings of 85.7% and 97.4%, respectively.

Full HCHD		Solid Wall	Retrofitted Wall	Spruce Cladding	MS 3.3	MS 4.7	MS 8.3
Latent heat of humidification	KWh	6.73	0.00	0.00	0.00	0.00	0.00
Latent heat of dehumidification	KWh	0.36	3.51	2.32	0.50	1.64	0.09
Total Energy	KWh	7.10	3.51	2.32	0.50	1.64	0.09
Saving on humidification	%	----	0.0%	0.0%	0.0%	0.0%	0.0%
Saving on dehumidification	%	----	0.0%	33.9%	85.7%	53.2%	97.4%
Total Saving	%	----	0.0%	33.9%	85.7%	53.2%	97.4%

Table 49 - Comparative energy usage and potential savings for the four post-retrofitted cases under constant HCHD control at $45\% \leq RH_{ie} \leq 65\%$ and $21\text{ }^{\circ}\text{C} \leq T_{ie} \leq 25\text{ }^{\circ}\text{C}$.

With only partial HCHD control for eight hours at the same psychrometric limits the

energy analysis (see: Table 50) showed a reduction in savings across all post retrofitted cases with the spruce cladding and MS 4.7 achieving the same reductions (24.9%), but with MS 3.3 achieving 61.7% and MS 8.3 achieving 81.4%. When compared to the constant HCHD control there were reductions in operational energy for the solid wall (1.06 KWh), retrofitted wall (1.93 KWh), spruce (1.45 KWh) and MS 4.7 (1.45 KWh). From Section 6.8.4 there was an increase in RH_{ie} dwell time (t/t_{yr}) observed at or above 65%RH when compared with the full HCHD control however, based on the reduction in operational energy this must occur during non-operational HCHD hours.

Partial HCHD - A		Solid Wall	Retrofitted Wall	Spruce Cladding	MS 3.3	MS 4.7	MS 8.3
Latent heat of humidification	KWh	0.58	0.00	0.00	0.00	0.00	0.00
Latent heat of dehumidification	KWh	0.48	1.93	1.45	0.74	1.45	0.36
Total Energy	KWh	1.06	1.93	1.45	0.74	1.45	0.36
Saving on humidification	%	----	0.0%	0.0%	0.0%	0.0%	0.0%
Saving on dehumidification	%	----	0.0%	24.9%	61.7%	24.9%	81.4%
Total Saving	%	----	0.0%	24.9%	61.7%	24.9%	81.4%

Table 50 - Comparative energy usage and potential savings for the four post-retrofitted cases under partial HCHD control at $45\% \leq RH_{ie} \leq 65\%$ and $21^\circ\text{C} \leq T_{ie} \leq 25^\circ\text{C}$.

Table 51 shows the results from the operational energy analysis from the partial HCHD control at the ASHRAE comfort limits ($40\% \leq RH_{ie} \leq 70\%$ and $T_{ie} = 23^\circ\text{C}$). Due to the decreasing dwell times at or above the upper HCHD limit presented in Section 6.8.5, operational energy usage is consequently reduced when compared to the levels generated using the previous limits (see: Table 50). Based on energy savings calculated with respect to the retrofitted wall, the spruce cladding gives a saving of 77.2%, MS 4.7 (88.6%) and both MS 3.3 and MS 8.3, having no humidification/ dehumidification energy usage, provides reductions of 100%.

Partial HCHD - B		Solid Wall	Retrofitted Wall	Spruce Cladding	MS 3.3	MS 4.7	MS 8.3
Latent heat of humidification	KWh	0.14	0.00	0.00	0.00	0.00	0.00
Latent heat of dehumidification	KWh	0.51	1.86	0.80	0.00	0.40	0.00
Total Energy	KWh	0.66	1.86	0.80	0.00	0.40	0.00
Saving on humidification	%	----	0.0%	0.0%	0.0%	0.0%	0.0%
Saving on dehumidification	%	----	0.0%	77.2%	100.0%	88.6%	100.00%
Total Saving	%	----	0.0%	77.2%	100.0%	88.6%	100.00%

Table 51 - Comparative energy usage and potential savings for the four post-retrofitted cases under partial HCHD control at the ASHRAE limits.

6.9 Summary

The main conclusions for this chapter are:

1. The physical modelling results showed lower peak RH_{ie} levels when compared to the numerical models predicted results however, final RH_{ie} levels (day two) appear very similar. For the aluminium foil, gypsum, MS 3.3 and MS 8.3 better agreement was found with excellent matching of both day one and two RH_{ie} levels
2. The correlation of variance against occurrence within limits for the numerical model was deemed acceptable and allowed further 3D numerical models to be simulated within these statistical confidence limits
3. Sensitivity analysis showed that there was a positive linear relationship between ΔRH_{ie} and ΔRH_{oe} suggesting extensive linearity across the ΔRH_{ie} and ACH range within WUFI Plus
4. MS 3.3 and MS 8.3 RH_{ie} levels always remained within the ASHRAE limits under both morning and evening occupancy overloading schedules
5. MS 3.3 and MS 8.3 displayed a marked decrease in ΔRH_{ie} levels when compared to the traditional envelope materials under both morning and

evening increased ventilation schedules

6. Under representative exterior climate conditions, two year MS 3.3 and MS 8.3 RH_{ie} levels remained within the ASHRAE limits at depths greater than 4mm under both occupied and unoccupied scenarios
7. For partial and constant HCHD control, MS 3.3 and MS 8.3 showed minimal RH_{ie} dwell time (t/t_{yr}) outside the control limits.

In summary, the MS materials and particularly MS 3.3 and MS 8.3, displayed outstanding passive buffering performance across a range of exterior climate conditions combined with numerous internal moisture and ventilation overloading scenarios. The MS materials show consistent reduction in fluctuating RH_{ie} levels under both partial and full HCHD control in daily and annual cycles, providing constant humidity buffering within ASHRAE comfort limits. When compared against a retro-fitted gypsum-lined indoor environment there was a potential reduction in humidification/ dehumidification energy demand of up to 100% when using an MS material coating.

CHAPTER 7: Discussion

To counteract heat losses, reduce emissions and energy consumption there has been a push in recent years to internally retrofit high performance thin insulation technologies coupled with vapour barriers to the interior of solid wall UK buildings. This retro-fitting can have adverse effects on the indoor environment by giving rise to amplified relative humidity variations when the spaces are occupied. Energy penalties can be incurred due to the additional interior climate HCHD control required from mechanical systems.

The literature review (see: Chapter 2) sets out how hygrothermal materials can be used to reduce the HCHD load by somewhat reducing relative humidity variations *i.e.* creating a passive buffering effect. The behaviour of these hygrothermal materials is dictated by the materials functional properties including dry-state thermal conductivity, specific heat capacity, bulk density, apparent porosity, water vapour permeability and water absorption coefficient. The aim for this research was to design the functional properties of inorganic, nano-structured surface coatings to produce desired hygrothermal behavioural responses to climatic variables in these closed environments.

To establish a link between material behaviour under set psychrometric conditions and the material's pore network geometry, experimental analysis to characterise the hygrothermal functional properties and the pore network of the materials using a range of techniques as outlined in the methodology (see: Sections 3.2 and 3.3). As expected from the literature (see: Section 2.4.2), the results from N₂ physisorption analysis (see: Table 31) show that the MS materials are all variants of Type IV isotherms indicating a mesoporous network with MS 4.7 displaying pronounced

hysteresis suggestive of type IIb pores with narrow openings leading to the 'ink bottle' effect. The specific surface areas (SSA) of the MS 4.7, MS 8.3 and MMS 4.8 materials were significantly higher than the conventional desiccants, whilst MS 3.3 and silica gel appear to be similar. There was a positive relationship between mesopore diameter and pore volume in the MS/MMS samples, but not to SSA which may suggest that the mesopores have varying degrees of corrugation contributing to an increased SSA for the MMS 4.8 and MS 4.7 samples. From the sorption isotherm tests (see: Figure 80), the MS materials displayed both higher EMC and faster response rates when compared to the conventional desiccants with vapour transfer to/from the material dominated by the macropore geometry.

Initially there does not appear to be any correlation between the hygrothermal behaviour and pore network characteristics of the MS materials with MS 3.3 and MS 8.3 displaying very similar moisture storage functions, ζ_u when compared to MS 4.7 and MMS 4.8 (see: Table 36). As discussed in Section 2.6.1.2 however, it is rarely the moisture capacity of a material that governs its hygric performance but its moisture kinetics, specifically within the ASHRAE comfort range ($40\% \leq RH \leq 70\%$). From figure 87 it can be seen that the DVS response time, t_{emc} has a positive logarithmic relationship with both the mesopore diameter and mesopore volume. This implies that the pore network and specifically mesopore geometry can be tuned in order to give the desired dynamic vapour sorption/ desorption response rate and possibly storage capacity to suit a given set of interior psychrometric conditions.

The next stage of research, as outlined in Sections 3.4.1 and 3.5.1 utilised 1D physical and validated numerical models to parametrically analyse material behaviour based on the hygrothermal properties obtained during Section 4.3, to determine the applicability of using the 1D WUFI numerical model as a material

selection tool by ‘tuning’ material properties and linking with the pore network characteristics and simulate envelope moisture levels under representative psychrometric conditions.

The 1D model validation results (see: Figure 90) show that there was a slight decline in maximum water content, $w_{coat, max}$ in the numerically predicted results on the second cycle for all cases, with no evidence of similar decline in the physical model as was suggested in Section 5.2. As there is currently no provision to couple dynamic t_{emc} timings to EMC levels within the numerical model, WUFI can predict final EMC values accurately, however there may be some level of variance between measured and predicted levels of w for RH fluctuations with shorter time periods (*i.e.* $t < t_{emc}$). In the representative climate modelling (see: Figures 94, 95), the MS materials displayed increased moisture uptake, Δw_{coat} (up to 353 kg/m^3) compared to gypsum (4.72 kg/m^3). This coupled with the close tracking of RH_{ie} by w_{coat} suggests the MS materials are well suited to provide rapid response interior humidity buffering (more than two orders of magnitude greater than that of traditional interior building materials).

In Section 5.6, each hygrothermal property was altered to ascertain its contributing factor to the materials overall behaviour and it was shown that the sorption isotherm, and in particular adjustment of the $w_{50} - w_{80}$ gradient of the adsorption branch isotherm is by far the most sensitive parameter when using WUFI as a design tool for material functional properties (see: Figure 93). This coupled with the relationship between MS mesopore diameter and t_{emc} suggests it is possible to tune an MS material to suit a particular set of psychrometric conditions using WUFI as a design tool.

Chapter 6 presented the results of the 3D physical and validated numerical modelling designed to parametrically analyse the effect of changes to internal climate conditions, ventilation, occupancy and HCHD control on occupant comfort resulting from the presence of the hygrothermal materials under representative moisture generation schedules and external climates. There was some divergence between the numerically-predicted and physical modelling results for all the materials in the validation tests (see: Figure 98), which again could be due to the coupling of dynamic response data (t_{emc}) to EMC levels and variance between measured and predicted levels of w_{coat} for RH fluctuations with time periods shorter than those needed to reach EMC (*i.e.* $t < t_{emc}$) in WUFI. In general however the variance between the numerically-predicted and physical modelling results was acceptable (see: Figure 99).

Under both occupied and unoccupied conditions, the reduction in ΔRH_{ie} levels, $\% \Delta RH_{ie,red}$ for different area/ volume ratios of hygrothermal materials compared to an aluminium lined volume was less effective as the air exchange rate increased, with unoccupied ΔRH_{ie} levels approaching exterior ΔRH_{oe} levels. At the highest air exchange rate ($ACH = 1.0$) the MS materials still achieved a $\% \Delta RH_{ie,red}$ of $> 85\%$ at a relatively low 40% area/ volume ratio (see: Figure 101).

The MS materials and particularly MS 3.3 and MS 8.3, consistently displayed outstanding passive buffering performance across numerous internal moisture and ventilation overloading scenarios providing exceptional occupant comfort. For moisture overloading (*i.e.* increased occupancy) RH_{ie} levels for the MS materials remained within the ASHRAE limits under both morning and evening overloading schedules and across the full range of air exchange. MS 8.3 had a maximum ΔRH_{ie} of 7.5% fluctuating about a mean RH_{ie} of 53% (for $ACH = 1.0$). These simulations

demonstrate the ability of the MS materials to continually buffer RH_{ie} fluctuations even when subjected to repeated moisture overloading scenarios. In the increased ventilation simulations, both the MS 3.3 and MS 8.3 cases remained within the ASHRAE limits during the early schedule, but dropped below the lower limit during the later ventilation schedule for air exchange rates greater than 2.0 (*i.e.* windows and doors fully open) due to the increasing influence of the lower exterior RH_{oe} . In contrast, the traditional building envelope materials (spruce and gypsum) RH_{ie} levels exceeded the upper and lower ASHRAE comfort limits for both scenarios and across all air exchange rates.

The MS materials show consistent reduction in fluctuating RH_{ie} levels under both partial and full HCHD control in daily and annual cycles, providing constant humidity buffering within ASHRAE comfort limits. When compared against a retrofitted gypsum-lined indoor environment there was a potential reduction in humidification/ dehumidification energy demand of up to 100% when using an MS material coating, however when taken as an absolute measure (KWh) this may not be as significant. In terms of occupant comfort however, the MS materials provide exceptional passive buffering performance providing a comfortable environment (within ASHRAE comfort limits) in enclosed, retrofitted spaces.

CHAPTER 8: Conclusions & Further Research

8.1 Concluding Remarks

The conclusions stated here address the overall aim and the specific objectives of this research as outlined in Chapter 1. A range of experimental techniques were utilised to characterise the functional properties and pore networks of all the candidate materials to meet Objective 2. The MS materials displayed Type IV moisture vapour isotherms with significantly higher equilibrium moisture contents (EMC) and faster response rates, t_{emc} in the multi-molecular region when compared to other conventional desiccants. Both MBV and cyclic testing showed the increased moisture capacity of the MS materials with $MBV_{practical}$ levels for MS 8.3 and MS 8.3 of $\approx 8.9 \text{ g/m}^2\%RH$ representing an increase over gypsum boards of $\approx 800\%$. MS mesopore volume increases as pore diameter increases whilst total volume and macropore volume both decrease. This suggests that pore wall thickness reduces as mesopore diameter increases during synthesis. The inverse relationship between vapour permeability and mesopore diameter suggests that vapour transfer to and from the MS materials is dominated by the macropore geometry ($\varnothing > 50 \text{ nm}$) via Fickian diffusion. The DVS response time, t_{emc} has significant and positive logarithmic relationships with both the mesopore diameter and the mesopore volume implying that it is possible to alter or ‘tune’ the MS materials mesopore geometry during synthesis in order to give the desired DVS response rate and storage capacity to suit a given set of interior psychrometric conditions. However, as the macropore geometry dominates bulk vapour transfer, this could also affect bulk DVS response rates (t_{emc}) at material depths greater than those tested ($d = 2 \text{ mm}$).

A series of 1D physical and validated numerical models using the building

performance simulation software WUFI Pro v5.1 were designed and conducted to meet Objective 3. During the representative climate modelling on retrofitted building cases, the MS material coatings displayed increased moisture levels, w_{coat} over the traditional building materials (gypsum and spruce). Yearly moisture uptake range, Δw_{coat} for MS 3.3 and 8.3 were 194 kg/m^3 and 394 kg/m^3 respectively compared to gypsum (5 kg/m^3) and spruce (45 kg/m^3). This increased performance, coupled with the tracking of RH_{ie} by w_{coat} suggests that the MS materials are able to provide rapid response humidity buffering more than two orders of magnitude greater than that of traditional interior building materials.

By determining the contributing factor of each hygrothermal property to material behaviour (within the numerical model), the possibility of using WUFI Pro as a design tool for tuning material functional properties was investigated. The hygrothermal properties of one MS material were sequentially altered to match those of another MS material. The sorption isotherm, and in particular adjustment of the $w_{50} - w_{80}$ gradient of the absorption branch of the isotherm, is by far the most sensitive parameter in the tuning process. As there is a positive logarithmic relationship between MS mesopore diameter and t_{emc} , it is therefore shown that it is possible to tune an MS material to have a designed mesopore geometry and hygrothermal behaviour to suit a particular set of psychrometric conditions using WUFI Pro as a design tool.

A series of 3D physical and validated numerical simulations using the whole-building energetic hygrothermal simulation software WUFI Plus v2.1.1.73 were modelled to meet Objectives 4 and 5. Under moisture loading the MS materials and particularly MS 3.3 and MS 8.3 provided a reduction in ΔRH_{ie} of $> 90\%$ at a total internal surface ratio of 10% when compared to an aluminium lined test room. When

subjected to moisture and ventilation overloading scenarios, the MS materials displayed outstanding passive buffering performance with marked reductions in ΔRH_{ie} and remaining within the ASHRAE comfort limits ($40\% \leq RH_{ie} \leq 70\%$) when compared to the traditional envelope materials.

Under representative external climate simulations, the MS materials show consistent reduction in fluctuating RH_{ie} levels under full HCHD control with limits of $45\% \leq RH_{ie} \leq 65\%$ and $21^\circ\text{C} \leq T_{ie} \leq 25^\circ\text{C}$. MS 3.3 and MS 8.3 displayed the best performances requiring only 9% and 3% dehumidification, respectively over the entire year compared to a traditional solid wall structure that has been retrofitted that required 31% dehumidification. Under partial HCHD control at the same limits where the HCHD plant was timed to operate only during occupation hours (00:00 to 08:00) there was increased dwell dehumidification required for all material cases with MS 3.3 requiring 18%, and MS 8.3 8% due to the elevated RH_{ie} levels during the uncontrolled periods. When the control limits were set to the ASHRAE comfort limits (*i.e.* $40\% \leq RH_{ie} \leq 70\%$ and $T_{ie} = 23^\circ\text{C}$) both MS 3.3 and MS 8.3 remained below the upper limit throughout the year with maximum RH_{ie} values of 67% and 65%, respectively, requiring no dehumidification and passively providing a comfortable environment for occupants.

8.2 Recommendations for future research

With reference to the results obtained from this research, suggestions for future work are presented here:

- In both the 1D and energetic 3D modelling carried out for this research there was some level of variance observed between the physical and numerically predicted results. This variance may be reduced by coupling t_{emc} and EMC

data within the numerical model.

- Whilst a number of the 3D numerical models were simulated under different levels of air exchange, this was not validated through physical modelling. In this respect, the 3D physical models presented could be expanded by utilising the ventilation assembly to experimentally assess the resultant RH_{ie} levels under various air exchange levels.
- There is potential to couple the MS materials used in this research with materials that display passive temperature buffering potential. Some research was conducted into phase change materials (PCM's) in this respect. Combining the latent heat capacity of a PCM with increased heat transfer due to convection in the vapour and latent transport when the vapour condenses within the MS could provide a substantial increase in thermal buffering potential.
- Further research is required with respect to the synthesis of the MS materials. All MS materials used for this research were novel and prepared in minimal quantities under strict laboratory conditions by the team at the University of Oxford. The development of methods to reduce the synthesis time and increase production capacity would be advantageous for future research.
- Whilst the MS materials simulated during the numerical modelling in this research were considered as interior wall coatings, no research was undertaken in respect of the mechanical and structural properties of the materials, such as stiffness, compressive strength etc. As any mounting technique would include some bonding (*i.e.* gluing, sintering), further research investigating bonding effects on MS behaviour should be considered.

REFERENCES

- AKGÜN, H. 2009. Geotechnical characterization and performance assessment of bentonite/sand mixtures for underground waste repository sealing. *Applied Clay Science*, 49, 394-399.
- ALLINSON, D. & HALL, M. 2010. Hygrothermal analysis of a stabilised rammed earth test building in the UK. *Energy and Buildings*, 42, 845-852.
- ALMEIDA, T. 2010. *Hydrothermal Synthesis and Characterisation of α -Fe₂O₃ Nanorods*. University of Nottingham, Thesis (PhD).
- ARFVIDSSON, J. 1999. A new algorithm to calculate the isothermal moisture penetration for periodically varying relative humidity at the boundary. *Nordic Journal of Building Physics*, 2.
- ASHRAE 2009a. *2009 ASHRAE Handbook - Fundamentals (SI Edition)*, Atlanta, American Society of Heating, Refrigerating and Air-Conditioning Engineers, Inc.
- ASHRAE 2009b. Standard 160-2009, Criteria for Moisture-Control Design Analysis in Buildings. *Atlanta, GA: American Society of Heating, Refrigerating and Air-conditioning Engineers, Inc.*
- ATKINS, P. & DE PAULA, J. 2006. *Atkins' physical chemistry*, Oxford, Oxford University Press.
- BAEHR, H. D. & STEPHAN, K. 2006. *Heat and mass transfer*, New York, Springer.
- BAETENS, R., JELLE, B. P., THUE, J. V., TENPIERIK, M. J., GRYNNING, S., UVSLØKK, S. & GUSTAVSEN, A. 2009. Vacuum insulation panels for building applications: A review and beyond. *Energy and Buildings*, 42, 147-172.
- BARNES, G. E. 2000. *Soil Mechanics: Principles and Practice*, London, Macmillan Publishers Limited.
- BECK, J. S., VARTULI, J. C., ROTH, W. J., LEONOWICZ, M. E., KRESGE, C. T., SCHMITT, K. D., CHU, C. T. W., OLSON, D. H. & SHEPPARD, E. W. 1992. A new family of mesoporous molecular sieves prepared with liquid crystal templates. *Journal of the American Chemical Society*, 114, 10834-10843.
- BIRD, STEWART & LIGHTFOOT 2001. *Transport phenomena, 2nd Ed*, New York, John Wiley & Sons Inc.
- BSI 1981. BS 1339:1965 - Definitions, formulae and constants relating to the humidity of the air. London: BSi Group.
- BSI 1996. BS 4359-1: 1996: Determination of the specific surface area of powders. BET method of gas adsorption for solids (including porous materials) London: BSi Group.
- BSI 1998. BS EN 1097-3:1998: Tests for mechanical and physical properties of aggregates. Determination of loose bulk density and voids. London: BSi Group.
- BSI 2000a. BS EN ISO 12570:2000: Hygrothermal performance of building materials and products. Determination of moisture content by drying at elevated temperature. London: BSi Group.

REFERENCES

BSI 2000b. BS EN ISO 12571: 2000: Hygrothermal performance of building materials and products. Determination of hygroscopic sorption properties. London: BSI Group.

BSI 2001a. BS EN ISO 10551:2001: Ergonomics of the thermal environment. Assessment of the influence of the thermal environment using subjective judgement scales. London: BSi Group.

BSI 2001b. BS EN ISO 12572:2001: Hygrothermal performance of building materials and products. Determination of water vapour transmission properties. London: BSI Group.

BSI 2002a. BS EN ISO 13788:2002: Hygrothermal performance of building components and building elements. Internal surface temperature to avoid critical surface humidity and interstitial condensation. Calculation methods. London: BSI Group.

BSI 2002b. BS EN ISO 15148:2002: Hygrothermal performance of building materials and products. Determination of water absorption coefficient by partial immersion. London: BSI Group.

BSI 2005a. BS EN ISO 7730:2005: Ergonomics of the thermal environment. Analytical determination and interpretation of thermal comfort using calculation of the PMV and PPD indices and local thermal comfort criteria. London: BSI Group.

BSI 2005b. BS EN ISO 11357-4:2005: Differential scanning calorimetry (DSC). Determination of specific heat capacity. London: BSI Group.

BSI 2007a. BS EN 15026 2007: Hygrothermal performance of building components and building elements. Assessment of moisture transfer by numerical simulation. London.: BSI Group.

BSI 2007b. BS EN ISO 13786: 2007: Thermal performance of building components. Dynamic thermal characteristics. Calculation methods. London: BSi Group.

BSI 2007c. BS ISO 21687 2007: Carbonaceous materials used in the production of aluminium. Determination of density by gas pycnometry (volumetric) using helium as the analysis gas. Solid materials. London: BSi Group.

BSI 2008. BS EN ISO 16814: 2008: Building environment design - Indoor air quality - Methods of expressing the quality of indoor air for human occupancy. London: BSi Group.

BSI 2011. BS 5250:2011: Code of practice for control of condensation in buildings. London: BSi Group.

BSI 2012. BS EN ISO 22007 - 2: 2012: Plastics. Determination of thermal conductivity and thermal diffusivity. Transient plane heat source (hot disc) method. London: BSi Group.

BZA. 2006. What are Zeolites? . Available: <http://www.bza.org/zeolites.html> [Accessed 05.06.10].

CALEBRE. 2010. CALEBRE: Background. Available: <http://www.calebre.org.uk/background.php> [Accessed 21.03.12].

CATURLA, F., MOLINA-SABIO, M. & RODRIGUEZ-REINOSO, F. 1999. Adsorption-desorption of water vapor by natural and heat-treated sepiolite in ambient air. *Applied Clay Science*, 15, 367-380.

- CEROLINI, S., D'ORAZIO, M., DI PERNA, C. & STAZI, A. 2009. Moisture buffering capacity of highly absorbing materials. *Energy and Buildings*, 41, 164-168.
- CHAROENVAI, S., KHEDARI, J., HIRUNLABH, J., ASASUTJARIT, C., ZEGHMATI, B., QUENARD, D. & PRATINTONG, N. 2005. Heat and moisture transport in durian fiber based lightweight construction materials. *Solar Energy*, 78, 543-553.
- CIBSE 2006. *Guide A - Environmental Design, 7th edn*, London, Chartered Institute of Building Service Engineers.
- CIBSE. 2008. WC08NOT - Current CIBSE TRY/DSY Hourly Weather Data Set - Nottingham. Available: <https://www.cibseknowledgeportal.co.uk/weather-data> [Accessed 13.05.12].
- COLLET, F., ACHCHAQ, F., DJELLAB, K., MARMORET, L. & BEJI, H. 2011. Water vapor properties of two hemp wools manufactured with different treatments. *Construction and Building Materials*, 25, 1079-1085.
- CRUMP, D., RAW, G., UPTON, S., SCIVYER, C., HUNTER, C. & HARTLESS, R. 2002. *A protocol for the assessment of indoor air quality in homes and office buildings*, London, BRE bookshop.
- D'ORAZIO, M. & QUAGLIARINI, E. 2009. Study on some sorption properties of treated bentonites for their potential use as a moisture regulating system for the preservation of historical wooden elements. *Journal of Cultural Heritage*, 11, 185-195.
- DAOU, K., WANG, R. Z. & XIA, Z. Z. 2006. Desiccant cooling air conditioning: a review. *Renewable and Sustainable Energy Reviews*, 10, 55-77.
- DCLG 2007. Building a Greener Future: policy statement.
- DELGADO, J., RAMOS, N. M. M. & DE FREITAS, V. P. 2006. Can Moisture Buffer Performance be Estimated from Sorption Kinetics? *Journal of Building Physics*, 29, 281-299.
- DESTA, T. Z., LANGMANS, J. & ROELS, S. 2011. Experimental data set for validation of heat, air and moisture transport models of building envelopes. *Building and Environment*, 46, 1038-1046.
- DIENG, A. O. & WANG, R. Z. 2001. Literature review on solar adsorption technologies for ice-making and air-conditioning purposes and recent developments in solar technology. *Renewable and Sustainable Energy Reviews*, 5, 313-342.
- DUECK, A., BÖRGESSON, L., GOUDARZI, R., LÖNNQVIST, M. & AKESSON, M. 2008. Humidity-induced water absorption and swelling of highly compacted bentonite in the project KBS-3H. *Physics and Chemistry of the Earth, Parts A/B/C*, 33, S499-S503.
- EDSL. 2010. EDSL TAS, Industry-Leading Building Modelling and Simulation. Available: <http://www.edsl.net/main/Software.aspx> [Accessed 14.07.10].
- FENG, N.-Q. & PENG, G.-F. 2005. Applications of natural zeolite to construction and building materials in China. *Construction and Building Materials*, 19, 579-584.
- FRICKE, J., HEINEMANN, U. & EBERT, H. P. 2008. Vacuum insulation panels: From research to market. *Vacuum*, 82, 680-690.

- GAO, N. F., KUME, S. & WATARI, K. 2005. Zeolite-carbon composites prepared from industrial wastes: (II) evaluation of the adaptability as environmental materials. *Materials Science and Engineering: A*, 404, 274-280.
- GAO, N. F., WATARI, K. & KUME, S. 2006. Fabrication and Characterization of Zeolite-Carbon Composite from Industrial Wastes. *Key Engineering Materials - The Science of Engineering Ceramics III*, 317 - 318, 743-746.
- GARCIA, I. & BULBULIAN, S. 1991. Zeolites for the separation of fission products. *International Journal of Radiation Applications and Instrumentation. Part C. Radiation Physics and Chemistry*, 38, 251-252.
- GUGGENHEIM, S. & MARTIN, R. T. 1995. Definition of clay and clay mineral; joint report of the AIPEA and CMS nomenclature committees. *Clay Minerals*, 30, 257-259.
- GURGEL, J. M. & KLÜPPEL, R. P. 1996. Thermal conductivity of hydrated silica-gel. *The Chemical Engineering Journal and The Biochemical Engineering Journal*, 61, 133-138.
- HAIXIN, C. 2010. *Molecular sieve - Dalian Haixin Chemical Industrial Co. Ltd.* [Online]. Available: <http://www.molecular-sieve.net/ProductClassEn-22-1.html> [Accessed 02.08.12].
- HALL, C. & HOFF, W. D. 2002. *Water transport in brick, stone, and concrete*, London, Taylor & Francis.
- HALL, M. 2010. *Materials for energy efficiency and thermal comfort in buildings*, London, Woodhead Publishing Ltd.
- HALL, M. & ALLINSON, D. 2008. Assessing the moisture-content-dependent parameters of stabilised earth materials using the cyclic-response admittance method. *Energy and Buildings*, 40, 2044-2051.
- HALL, M. & ALLINSON, D. 2009a. Analysis of the hygrothermal functional properties of stabilised rammed earth materials. *Building and Environment*, 44, 1935-1942.
- HALL, M. & ALLINSON, D. 2009b. Assessing the effects of soil grading on the moisture content-dependent thermal conductivity of stabilised rammed earth materials. *Applied Thermal Engineering*, 29, 740-747.
- HALL, M., LINDSAY, R. & KRAYENHOFF, M. 2012a. *Modern Earth Buildings Materials, Engineering, Constructions and Applications*, London, Woodhead Publishing Ltd.
- HALL, M. R. & ALLINSON, D. 2010. Transient numerical and physical modelling of temperature profile evolution in stabilised rammed earth walls. *Applied Thermal Engineering*, 30, 433-441.
- HALL, M. R., TSANG, S. C. E., CASEY, S. P., KHAN, M. A. & YANG, H. 2012b. Synthesis, characterization and hygrothermal behaviour of mesoporous silica high-performance desiccants for relative humidity buffering in closed environments. *Acta Materialia*, 60, 89-101.
- HAMEURY, S. 2005. Moisture buffering capacity of heavy timber structures directly exposed to an indoor climate: a numerical study. *Building and Environment*, 40, 1400-1412.

- HARJULA, R. & LEHTO, J. 1986. Effect of sodium and potassium ions on cesium absorption from nuclear power plant waste solutions on synthetic zeolites. *Nuclear and Chemical Waste Management*, 6, 133-137.
- HEMMINGWAY, B. S. & ROBIE, R. A. 1984. Thermodynamic properties of zeolites: low-temperature heat capacities and thermodynamic functions for phillipsite and clinoptilolite. Estimates of the thermochemical properties of zeolitic water at low temperature. *American Mineralogist*, 69, 692-700.
- HINES, A. L., GHOSH, T. K., LOYALKA, S. K. & WARDER, R. C. 1993. *Indoor air : quality and control*, Englewood Cliffs, N.J., PTR Prentice Hall.
- HOLM, A. H. & KÜNZEL, H. M. 2002. Practical application of an uncertainty approach for hygrothermal building simulations--drying of an AAC flat roof. *Building and Environment*, 37, 883-889.
- HONG, S. H., ORESZCZYN, T. & RIDLEY, I. 2006. The impact of energy efficient refurbishment on the space heating fuel consumption in English dwellings. *Energy and Buildings*, 38, 1171-1181.
- IBP. 2012a. WUFI Plus®: PC-Program for the calculation of transient internal climatic conditions and heat losses. Available: http://www.wufi.de/index_e.html [Accessed 01.03.12].
- IBP. 2012b. WUFI Pro®: PC-Program for calculating the coupled heat and moisture transfer in building components. Available: http://www.wufi.de/index_e.html [Accessed 01.03.12].
- INAGAKI, S. & FUKUSHIMA, Y. 1998. Adsorption of water vapor and hydrophobicity of ordered mesoporous silica, FSM-16. *Microporous and Mesoporous Materials*, 21, 667-672.
- INAGAKI, S., FUKUSHIMA, Y., KURODA, K. & KURODA, K. 1996. Adsorption Isotherm of Water Vapor and Its Large Hysteresis on Highly Ordered Mesoporous Silica. *Journal of Colloid and Interface Science*, 180, 623-624.
- INCROPERA, F. P., DEWITT, D. P., BERGMAN, T. L. & LAVINE, A. S. 2007. *Fundamentals of heat and mass transfer*, New York, John Wiley and Sons.
- IUPAC 1994. Recommendations for the characterization of porous solids. *Pure and Applied Chemistry*, 66, 1739-1758.
- IUPAC 2004. Recommendations for the characterization of porous solids
- JANA, S. K., MOCHIZUKI, A. & NAMBA, S. 2004. Progress in Pore-Size Control of Mesoporous MCM-41 Molecular Sieve Using Surfactant Having Different Alkyl Chain Lengths and Various Organic Auxiliary Chemicals. *Catalysis Surveys from Asia*, 8, 1-13.
- JAYAMAHA, L. 2006. *Energy-efficient building systems : green strategies for operation and maintenance*, New York, McGraw-Hill.
- KALAMEES, T., KORPI, M., VINHA, J. & KURNITSKI, J. 2009. The effects of ventilation systems and building fabric on the stability of indoor temperature and humidity in Finnish detached houses. *Building and Environment*, 44, 1643-1650.
- KALAMEES, T. & VINHA, J. 2003. Hygrothermal calculations and laboratory tests on timber-framed wall structures. *Building and Environment*, 38, 689-697.

- KALOGIROU, S. A., FLORIDES, G. & TASSOU, S. 2002. Energy analysis of buildings employing thermal mass in Cyprus. *Renewable Energy*, 27, 353-368.
- KARAGIOZIS, A. N. 2001. Advanced hygrothermal models and design models. *The Canadian Conference on Building Simulation*. Ottawa, Canada: International Building Performance Simulation Association (IBPSA).
- KAYE & LABY. 1995. Table of Physical & Chemical Constants: Thermal Conductivities, . Available: http://www.kayelaby.npl.co.uk/general_physics/2_3/2_3_7.html [Accessed 25.01.10].
- KAYE & LABY. 2012. The atmosphere: Variation of pressure, density and temperature with altitude. Available: http://www.kayelaby.npl.co.uk/general_physics/2_7/2_7_8.html [Accessed 01.08.12].
- KENJO, T. 1982. A Rapid-Response Humidity Buffer Composed of Nikka Pellets and Japanese Tissue. *Studies in Conservation*, 27, 19-24.
- KHARE, P. & SWARUP, A. 2010. *Engineering physics : fundamentals & modern applications*, Sudbury, Mass., Jones and Bartlett Publishers.
- KINGSPAN. 2011. Thermafloor TF70 - Insulation for solid concrete and suspended ground floors. Available: <http://www.kingspaninsulation.co.uk/Products/Therma/Thermafloor-TF70/Overview.aspx> [Accessed 20.06.12].
- KOCH., P. 1972. *Utilization of the southern pines: the raw material: USDA Agriculture Handbooks*, Washington, USDA Forest Service.
- KORONTHALYOVA, O. 2011. Moisture storage capacity and microstructure of ceramic brick and autoclaved aerated concrete. *Construction and Building Materials*, 25, 879-885.
- KOUGHIA, C., KASAP, S. & CAPPER, P. 2006. *Springer handbook of electronic and photonic materials*, USA, Springer.
- KÜNZEL, H., ZIRKELBACH, D. & SEDLBAUER, K. Predicting indoor temperature and humidity conditions including hygrothermal interactions with the building envelope. 2003.
- KÜNZEL, H. M. 1995. *Simultaneous heat and moisture transport in building components*. Fraunhofer Institute of Building Physics. Thesis (PhD)
- KÜNZEL, H. M., HOLM, A., SEDLBAUER, K., ANTRETTER, F. & ELLINGER, M. 2004. Moisture buffering effects of interior linings made from wood or wood based products: IBP Report HTB-04/2004/e. IBP, Institutsteil Holzkirchen, Germany.
- KÜNZEL, H. M., HOLM, A., ZIRKELBACH, D. & KARAGIOZIS, A. N. 2005. Simulation of indoor temperature and humidity conditions including hygrothermal interactions with the building envelope. *Solar Energy*, 78, 554-561.
- KÜNZEL, H. M. & KIESSL, K. 1996. Calculation of heat and moisture transfer in exposed building components. *International Journal of Heat and Mass Transfer*, 40, 159-167.
- KURNITSKI, J., KALAMEES, T., PALONEN, J., ESKOLA, L. & SEPPÄNEN, O.

2007. Potential effects of permeable and hygroscopic lightweight structures on thermal comfort and perceived IAQ in a cold climate. *Indoor Air*, 17, 37-49.
- LA, D., DAI, Y. J., LI, Y., WANG, R. Z. & GE, T. S. 2010. Technical development of rotary desiccant dehumidification and air conditioning: A review. *Renewable and Sustainable Energy Reviews*, 14, 130-147.
- LAL, R. & SHUKLA, M. 2004. *Principles of soil physics*, New York, Marcel Dekker Inc.
- LI, Q., RAO, J. & FAZIO, P. 2009. Development of HAM tool for building envelope analysis. *Building and Environment*, 44, 1065-1073.
- LI, Z., BARNES, J. C., BOSOI, A., STODDART, J. F. & ZINK, J. I. 2012. Mesoporous silica nanoparticles in biomedical applications. *Chem. Soc. Rev.*
- LIDDAMENT, M. W. & ORME, M. 1998. Energy and ventilation. *Applied Thermal Engineering*, 18, 1101-1109.
- MAEDA, H. & ISHIDA, E. H. 2009a. Water vapor adsorption and desorption of mesoporous materials derived from metakaolinite by hydrothermal treatment. *Ceramics International*, 35, 987-990.
- MAEDA, H. & ISHIDA, E. H. 2009b. Water Vapor Adsorption and Desorption on Materials Hydrothermally Solidified from Clay Minerals. *Journal of the American Ceramic Society*, 92, 2125-2128.
- MARONI, M., SEIFERT, B. & LINDVALL, T. 1995. *Indoor air quality : a comprehensive reference book*, Amsterdam, Elsevier.
- MCNAUGHT, A. D. & WILKINSON, A. 1997. *Compendium of chemical terminology: IUPAC recommendations, 2nd edn. (Online Version)*, Oxford, MA, Blackwell Science.
- MEISSNER, J. W., MENDES, N., MENDONÇA, K. C. & MOURA, L. M. 2010. A full-scale experimental set-up for evaluating the moisture buffer effects of porous material. *International Communications in Heat and Mass Transfer*, 37, 1197-1202.
- MURASHOV, V. V. & WHITE, M. A. 2002. Thermal properties of zeolites: effective thermal conductivity of dehydrated powdered zeolite 4A. *Materials Chemistry and Physics*, 75, 178-180.
- NG, K. C., CHUA, H. T., CHUNG, C. Y., LOKE, C. H., KASHIWAGI, T., AKISAWA, A. & SAHA, B. B. 2001. Experimental investigation of the silica gel-water adsorption isotherm characteristics. *Applied Thermal Engineering*, 21, 1631-1642.
- NOFAL, M., STRAVER, M. & KUMARAN, K. Comparison of four hygrothermal models in terms of long-term performance assessment of wood-frame constructions. Proceedings of the Eighth Conference On Building Science and Technology—Solutions to moisture problems in building enclosures, February 22-23, 2001 2001 Toronto. 118-138.
- OGOLI, D. M. 2003. Predicting indoor temperatures in closed buildings with high thermal mass. *Energy and Buildings*, 35, 851-862.
- OHASHI, F., MAEDA, M., INUKAI, K., SUZUKI, M. & TOMURA, S. 1999. Study on intelligent humidity control materials: Water vapor adsorption properties of mesostructured silica derived from amorphous fumed silica. *Journal of Materials*

Science, 34, 1341-1346.

ORME, M. 2001. Estimates of the energy impact of ventilation and associated financial expenditures. *Energy and Buildings*, 33, 199-205.

OROSA, J. A. & BAALIÑA, A. 2009. Improving PAQ and comfort conditions in Spanish office buildings with passive climate control. *Building and Environment*, 44, 502-508.

OROSA, J. A. & OLIVEIRA, A. C. 2009. Hourly indoor thermal comfort and air quality acceptance with passive climate control methods. *Renewable Energy*, 34, 2735-2742.

OSANYINTOLA, O. F. & SIMONSON, C. J. 2006. Moisture buffering capacity of hygroscopic building materials: Experimental facilities and energy impact. *Energy and Buildings*, 38, 1270-1282.

OSANYINTOLA, O. F., TALUKDAR, P. & SIMONSON, C. J. 2006. Effect of initial conditions, boundary conditions and thickness on the moisture buffering capacity of spruce plywood. *Energy and Buildings*, 38, 1283-1292.

OZAYDIN, S., KOCER, G. & HEPBASLI, A. 2006. Natural Zeolites in Energy Applications. *Energy Sources, Part A: Recovery, Utilization, and Environmental Effects*, 28, 1425 - 1431.

PADFIELD, T. 1998. *The role of absorbent materials in moderating changes of relative humidity*. Ph.D, The Technical University of Denmark.

PAKSOY, H. Ö. 2007. *Thermal energy storage for sustainable energy consumption fundamentals, case studies and design*, Dordrecht, Springer.

PARSONS, K. C. 2003. *Human thermal environments: the effects of hot, moderate, and cold environments on human health, comfort, and performance*, , London, Taylor & Francis.

PAVLÍK, Z. & CERNÝ, R. 2008. Experimental assessment of hygrothermal performance of an interior thermal insulation system using a laboratory technique simulating on-site conditions. *Energy and Buildings*, 40, 673-678.

PEUHKURI, R., RODE, C. & HANSEN, K. K. 2008. Non-isothermal moisture transport through insulation materials. *Building and Environment*, 43, 811-822.

PLATHNER, P. & WOLOSZYN, M. 2002. Interzonal air and moisture transport in a test house: experiment and modelling. *Building and Environment*, 37, 189-199.

QIU, L., MURASHOV, V. & WHITE, M. A. 2000. Zeolite 4A: heat capacity and thermodynamic properties. *Solid State Sciences*, 2, 841-846.

RAEL, R. 2008. *Earth architecture (Online Version)*, New York, Princeton Architectural Press.

RAMOS, N. M. M., DELGADO, J. M. P. Q. & DE FREITAS, V. P. 2010. Influence of finishing coatings on hygroscopic moisture buffering in building elements. *Construction and Building Materials*, 24, 2590-2597.

RODE, C. & GRAU, K. 2008. Moisture Buffering and its Consequence in Whole Building Hygrothermal Modeling. *Journal of Building Physics*, 31, 333-360.

RODE, C., MENDES, N. & KARL, G. 2004. Evaluation of Moisture Buffer Effects by Performing Whole-Building Simulations. *A S H R A E Transactions*, 110, 783-

794.

RODE, C., PEUHKURI, R. H., MORTENSEN, L. H., HANSEN, K. K., TIME, B., GUSTAVSEN, A., OJANEN, T., AHONEN, J., SVENNBERG, K. & ARFVIDSSON, J. 2005. Moisture buffering of building materials. Department of Civil Engineering, Technical University of Denmark.

ROELS, S., TALUKDAR, P., JAMES, C. & SIMONSON, C. J. 2010. Reliability of material data measurements for hygroscopic buffering. *International Journal of Heat and Mass Transfer*, 53, 5355-5363.

ROQUE-MALHERBE, R. M. A. 2007. *Adsorption and diffusion in nanoporous materials*, London, CRC Press, Taylor & Francis Group.

SAKKA, S. 2005. *Handbook of sol-gel science and technology processing, characterization, and applications* [Online]. Boston: Kluwer Academic Publishers.

SALONVAARA, M., OJANEN, T., HOLM, A., KUNZEL, H. M. & KARAGIOZIS, A. N. Moisture buffering effects on indoor air quality – experimental and simulation results. In: Proceedings (CD) of the Performance of Exterior Envelopes of Whole Buildings IX International Conference, December 5-10 2004 Clearwater Beach, Florida, USA.

SETARAM. 2012. SETARAM Instrumentation - Thermal Conductivity - TCi. Available: <http://www.setaram.com/TCi.htm> [Accessed 28.06.12].

SIMMLER, H. & BRUNNER, S. 2005. Vacuum insulation panels for building application: Basic properties, aging mechanisms and service life. *Energy and Buildings*, 37, 1122-1131.

SIMONSON, C. J., OJANEN, T. & SALONVAARA, M. 2001. Improving indoor climate and comfort with wooden structures. Technical Research Centre of Finland.

SIMONSON, C. J., SALONVAARA, M. & OJANEN, T. 2002. The effect of structures on indoor humidity - possibility to improve comfort and perceived air quality. *Indoor Air*, 12, 243-251.

SING, K., EVERETT, D., HAUL, R., MOSCOU, L., PIEROTTI, R., ROUQUEROL, J. & SIEMIENIEWSKA, T. 1985. Reporting physisorption data for gas/solid systems. *Pure Appl. Chem*, 57, 603-619.

SPENGLER, J. D., SAMET, J. M. & MCCARTHY, J. F. 2001. *Indoor air quality handbook*, New York, McGraw-Hill.

SVENNBERG, K., LENGSELD, K., HARDERUP, L.-E. & HOLM, A. 2007. Previous Experimental Studies and Field Measurements on Moisture Buffering by Indoor Surface Materials. *Journal of Building Physics*, 30, 261-274.

TA. 2012. TA Instruments. Available: <http://www.tainstruments.com/?gclid=CiiljXn8LACFQwjfAodxi1uxQ> [Accessed 28.06.12].

TANG, F., LI, L. & CHEN, D. 2012. Mesoporous Silica Nanoparticles: Synthesis, Biocompatibility and Drug Delivery. *Advanced Materials*.

TAS. 2008. Products - Series 3 range - Specification Available: <http://www.tasltd.co.uk/series3specnew.html> [Accessed 28.06.12].

TENPIERIK, M. & CAUBERG, H. Vacuum Insulation Panel: friend or foe? The

23rd Conference on Passive and Low Energy Architecture, 6-8 September 2006
2006 Geneva, Switzerland.

TINYTAG. 2012. Tinytag Ultra 2. Available:
<http://www.geminaloggers.com/data-loggers/tinytag-ultra-2/tgu-4500> [Accessed
21.06.12].

TOISHI, K. 1959. Humidity Control in a Closed Package. *Studies in Conservation*,
4, 81-87.

TRECHSEL, H. R. 1994. *Moisture control in buildings*, Philadelphia, Astm Intl.

TSUTSUMI, H., TANABE, S., HARIGAYA, J., IGUCHI, Y. & NAKAMURA, G.
2007. Effect of humidity on human comfort and productivity after step changes from
warm and humid environment. *Building and Environment*, 42, 4034-4042.

UOT. 2012. University of Texas: BIO 322 – Structure, Physiology and Reproduction
of Seed Plants. Available: <http://web.biosci.utexas.edu/bio322/images/wood.sem.jpg>
[Accessed 04.08.12].

UPM. 2009. WISA®-Form MDO. Available: [http://w3.upm-](http://w3.upm-kymmene.com/upm/internet/cms/upmma.nsf/lupgraphics/form_mdo_en.pdf/$file/form_mdo_en.pdf)
[kymmene.com/upm/internet/cms/upmma.nsf/lupgraphics/form_mdo_en.pdf/\\$file/f](http://w3.upm-kymmene.com/upm/internet/cms/upmma.nsf/lupgraphics/form_mdo_en.pdf/$file/form_mdo_en.pdf)
[orm_mdo_en.pdf](http://w3.upm-kymmene.com/upm/internet/cms/upmma.nsf/lupgraphics/form_mdo_en.pdf/$file/form_mdo_en.pdf) [Accessed 20.06.12].

USDA 1989. *Handbook of wood and wood-based materials for engineers,*
architects, and builders: USDA Forest Products Laboratory, New York,
Hemisphere Pub. Corp.

USDE. 2007. U.S. Department of Energy, EnergyPlus 2.0 - Major Release - New
Functionality. Available:
http://apps1.eere.energy.gov/buildings/energyplus/pdfs/energyplus_v2_brochure.pdf
[Accessed 14.03.12].

VAN BELLEGHEM, M., STEEMAN, M., WILLOCKX, A., JANSSENS, A. & DE
PAEPE, M. 2011. Benchmark experiments for moisture transfer modelling in air and
porous materials. *Building and Environment*, 46, 884-898.

VAN SCHIJNDEL, A. W. M. 2008. Estimating Values for the Moisture Source
Load and Buffering Capacities from Indoor Climate Measurements. *Journal of*
Building Physics, 31, 319-331.

VIBRA. 2011. HT/HTR Series - tuning-fork sensor analytical balance. Available:
http://www.vibra.co.jp/global/products/analytical/ht_htr/index.html [Accessed
28.06.12].

VILLAR, M. V. & RIVAS, P. 1994. Hydraulic properties of montmorillonite-quartz
and saponite-quartz mixtures. *Applied Clay Science*, 9, 1-9.

WANG, L. W., WANG, R. Z. & OLIVEIRA, R. G. 2009. A review on adsorption
working pairs for refrigeration. *Renewable and Sustainable Energy Reviews*, 13,
518-534.

WANG, S. & PENG, Y. 2010. Natural zeolites as effective adsorbents in water and
wastewater treatment. *Chemical Engineering Journal*, 156, 11-24.

WANG, X., WALLIMAN, N., OGDEN, R. & KENDRICK, C. 2007. VIP and their
applications in buildings: a review. *Construction Materials*, 160, 145-153.

WEBB, P. A. 2001. Volume and density determinations for particle technologists.

Available:

http://www.micromeritics.com/pdf/app_articles/density_determinations.pdf

[Accessed 02.05.2012].

WILSON, J., SAVAGE, D., BOND, A., WATSON, S., PUSCH, R. & BENNETT, D. 2011. Bentonite - A Review of key properties, processes and issues for consideration in the UK context. Available: <http://www.nda.gov.uk/documents/biblio/upload/Bentonite-A-Review-of-key-properties-processes-and-issues-for-consideration-in-the-UK-context.pdf> [Accessed 31.08.12].

WOLOSZYN, M., KALAMEES, T., OLIVIER ABADIE, M., STEEMAN, M. & SASIC KALAGASIDIS, A. 2009. The effect of combining a relative-humidity-sensitive ventilation system with the moisture-buffering capacity of materials on indoor climate and energy efficiency of buildings. *Building and Environment*, 44, 515-524.

YANG, P., QUAN, Z., LU, L., HUANG, S. & LIN, J. 2008. Luminescence functionalization of mesoporous silica with different morphologies and applications as drug delivery systems. *Biomaterials*, 29, 692-702.

YOSHINO, H., MITAMURA, T. & HASEGAWA, K. 2009. Moisture buffering and effect of ventilation rate and volume rate of hygrothermal materials in a single room under steady state exterior conditions. *Building and Environment*, 44, 1418-1425.

YOSHINO, H., YOSHINO, Y., ZHANG, Q., MOCHIDA, A., LI, N., LI, Z. & MIYASAKA, H. 2006. Indoor thermal environment and energy saving for urban residential buildings in China. *Energy and Buildings*, 38, 1308-1319.

ZALBA, P., DEYÁ, C., SANCHEZ, N. V. & AMO, B. D. 2009. Zeolitic rocks used as pigment for ceiling paints. Activation of the rock. *Microporous and Mesoporous Materials*, 117, 148-152.

ZHAO, D., FENG, J., HUO, Q., MELOSH, N., FREDRICKSON, G. H., CHMELKA, B. F. & STUCKY, G. D. 1998. Triblock Copolymer Syntheses of Mesoporous Silica with Periodic 50 to 300 Angstrom Pores. *Science*, 279, 548-552.

APPENDICES

A1 - Photographs of experimental apparatus



Figure A1.1 - The climate chamber with circulation fan detail.



Figure A1.2 - The DSC Q10 apparatus for measuring specific heat capacity.



Figure A1.3 – Desiccator Jar with fan.



Figure A1.4 – Physisorption apparatus.

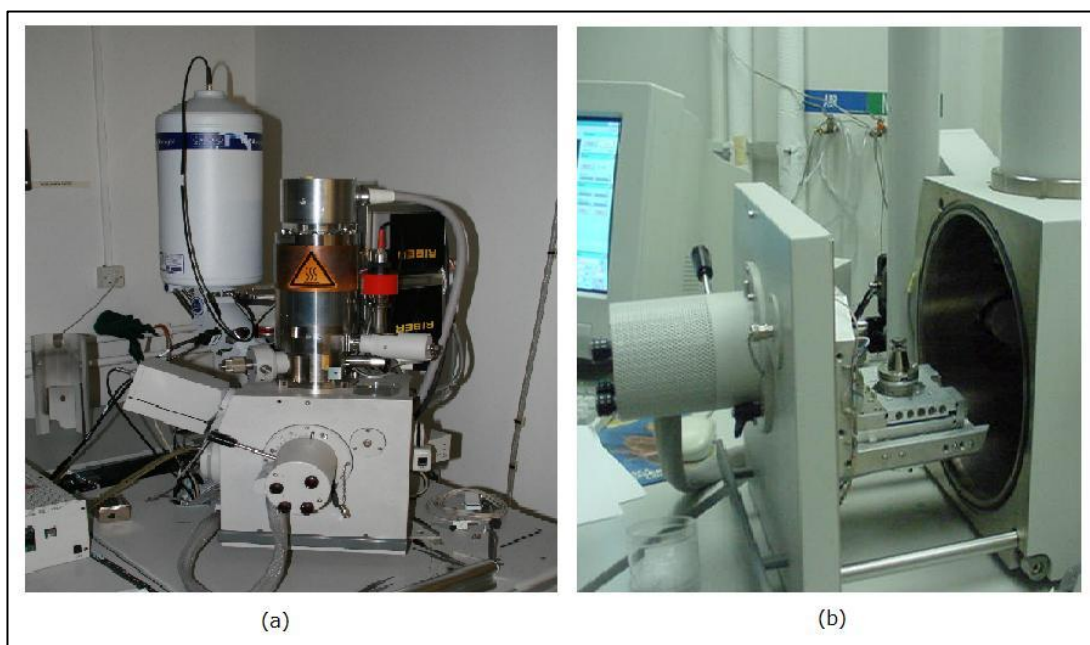


Figure A1.5 – Scanning Electron Microscope.

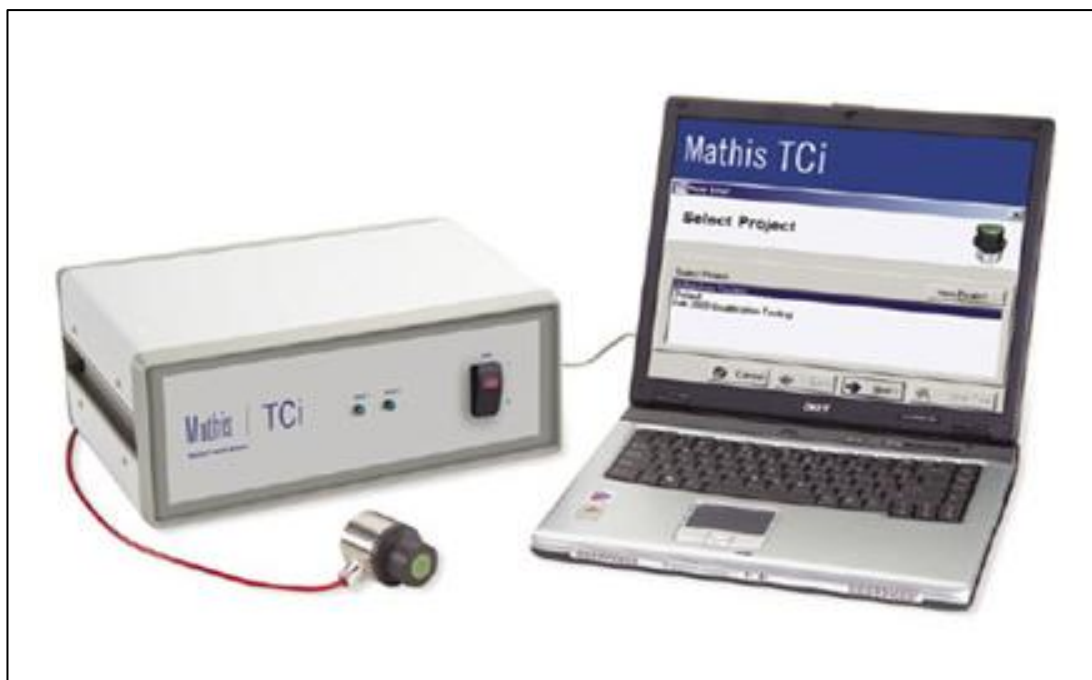


Figure A1.6 – Modified transient plane source apparatus.

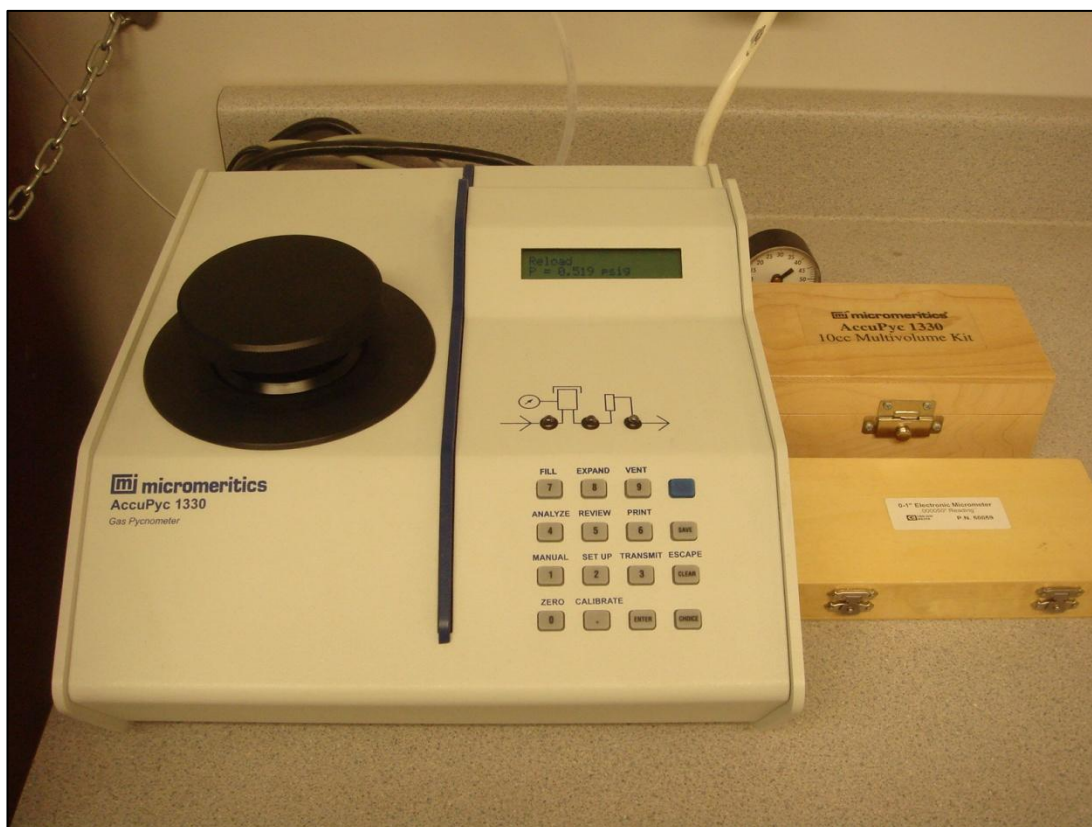


Figure A1.7 – Helium pycnometer.



Figure A1.8 – Vapour permeability cell.



Figure A1.10 – Isolated box for humidity buffering model (Closed).



Figure A1.11 – Isolated box for humidity buffering model (Interior - lids removed).

A2 - WUFI Material Datasheets

Layer/Material Data **MS 3.3nm**

Material Data | Info

Basic Values


Bulk density [kg/m³]	501.27
Porosity [m³/m³]	0.76
Specific Heat Capacity, Dry [J/kgK]	1011.0
Thermal Conductivity, Dry, 10°C [W/mK]	0.05
Water Vapour Diffusion Resistance Factor [-]	4.54

Approximation Parameter

Reference Water Content [kg/m³]	246.83
Free Water Saturation [kg/m³]	346.13
Water Absorption Coefficient [kg/m²s ^{0.5}]	2.112
Moisture-dep. Thermal Cond. Supplement [%/M.-%]	1.5
Temp-dep. Thermal Cond. Supplement [W/mK²]	0.0002

Typical Built-In Moisture [kg/m³] 79.25

Layer thickness [m] 0.002

Color 

Paste into Material Database Import... Export... OK Abort Help

Hygrothermal Functions

Moisture Storage Function

Liquid Transport Coefficient, Suction

Liquid Transport Coefficient, Redistribution

Water Vapour Diffusion Resistance Factor, moisture-depend

Thermal Conductivity, moisture-dependent

Thermal Conductivity, temperature-dependent

Enthalpy, temperature-dependent

Graph Edit Table from File...

☐ Approximate

No.	RH [-]	Water Content [kg/m³]
1	0.0	0.0
2	0.2	11.58
3	0.5	79.25
4	0.8	246.83
5	0.95	268.28
6	1.0	346.13

Copy

Figure A2.1 – WUFI material data for MS 3.3.

Layer/Material Data **MS 4.7nm**

Material Data | Info

Basic Values


Bulk density [kg/m³]	336.31
Porosity [m³/m³]	0.85
Specific Heat Capacity, Dry [J/kgK]	1866.0
Thermal Conductivity, Dry, 10°C [W/mK]	0.05
Water Vapour Diffusion Resistance Factor [-]	7.13

Approximation Parameter

Reference Water Content [kg/m³]	105.13
Free Water Saturation [kg/m³]	363.01
Water Absorption Coefficient [kg/m²s ^{0.5}]	0.561
Moisture-dep. Thermal Cond. Supplement [%/M.-%]	1.5
Temp-dep. Thermal Cond. Supplement [W/mK²]	0.0002

Typical Built-In Moisture [kg/m³] 32.55

Layer thickness [m] 0.002

Color 

Paste into Material Database Import... Export... OK Abort Help

Hygrothermal Functions

Moisture Storage Function

Liquid Transport Coefficient, Suction

Liquid Transport Coefficient, Redistribution

Water Vapour Diffusion Resistance Factor, moisture-depend

Thermal Conductivity, moisture-dependent

Thermal Conductivity, temperature-dependent

Enthalpy, temperature-dependent

Graph Edit Table from File...

☐ Approximate

No.	RH [-]	Water Content [kg/m³]
1	0.0	0.0
2	0.2	8.11
3	0.5	32.55
4	0.8	105.13
5	0.95	137.08
6	1.0	363.01

Copy

Figure A2.2 – WUFI material data for MS 4.7.

Layer/Material Data

Layer/Material Name: MS 8.3nm

Material Data | Info

Basic Values

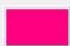
Bulk density [kg/m³]	617,54
Porosity [m³/m³]	0,76
Specific Heat Capacity, Dry [J/kgK]	1691,0
Thermal Conductivity, Dry, 10°C [W/mK]	0,05
Water Vapour Diffusion Resistance Factor [-]	10,52

Approximation Parameter

Reference Water Content [kg/m³]	294,76
Free Water Saturation [kg/m³]	759,69
Water Absorption Coefficient [kg/m²s ^{0.5}]	0,55
Moisture-dep. Thermal Cond. Supplement [%/M.-%]	1,5
Temp-dep. Thermal Cond. Supplement [W/mK²]	0,0002

Typical Built-In Moisture [kg/m³]: 85,81

Layer thickness [m]: 0,002

Color: 

Hygrothermal Functions

- Moisture Storage Function
- Liquid Transport Coefficient, Suction
- Liquid Transport Coefficient, Redistribution
- Water Vapour Diffusion Resistance Factor, moisture-depend
- Thermal Conductivity, moisture-dependent
- Thermal Conductivity, temperature-dependent
- Enthalpy, temperature-dependent

Graph | Edit Table | from File...

☐ Approximate

No.	RH [-]	Water Content [kg/m³]
1	0,0	0,0
2	0,2	4,59
3	0,5	85,81
4	0,8	294,76
5	0,95	576,83
6	1,0	759,69

Copy

Paste into Material Database | Import... | Export... | OK | Abort | Help

Figure A2.3 – WUFI material data for MS 8.3.

Layer/Material Data

Layer/Material Name: Mol Siv 10Å

Material Data | Info

Basic Values


Bulk density [kg/m³]	756,6
Porosity [m³/m³]	0,68
Specific Heat Capacity, Dry [J/kgK]	1929,0
Thermal Conductivity, Dry, 10°C [W/mK]	0,1
Water Vapour Diffusion Resistance Factor [-]	7,55

Approximation Parameter

Reference Water Content [kg/m³]	155,86
Free Water Saturation [kg/m³]	224,33
Water Absorption Coefficient [kg/m²s ^{0.5}]	0,193
Moisture-dep. Thermal Cond. Supplement [%/M.-%]	1,5
Temp-dep. Thermal Cond. Supplement [W/mK²]	0,0002

Typical Built-In Moisture [kg/m³]: 146,02

Layer thickness [m]: 0,002

Color: 

Hygrothermal Functions

- Moisture Storage Function
- Liquid Transport Coefficient, Suction
- Liquid Transport Coefficient, Redistribution
- Water Vapour Diffusion Resistance Factor, moisture-depend
- Thermal Conductivity, moisture-dependent
- Thermal Conductivity, temperature-dependent
- Enthalpy, temperature-dependent

Graph | Edit Table | from File...

☐ Approximate

No.	RH [-]	Water Content [kg/m³]
1	0,0	0,0
2	0,2	136,41
3	0,5	146,02
4	0,8	155,86
5	0,95	170,84
6	1,0	224,33

Copy

Paste into Material Database | Import... | Export... | OK | Abort | Help

Figure A2.4 – WUFI material data for Molecular Sieve 10Å.

Layer/Material Data

Layer/Material Name: Silica Gel

Material Data | Info

Basic Values

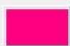
Bulk density [kg/m³]	791.51
Porosity [m³/m³]	0.63
Specific Heat Capacity, Dry [J/kgK]	1500.0
Thermal Conductivity, Dry, 10°C [W/mK]	0.196
Water Vapour Diffusion Resistance Factor [-]	5.57

Approximation Parameter

Reference Water Content [kg/m³]	265.95
Free Water Saturation [kg/m³]	472.29
Water Absorption Coefficient [kg/m²s ^{0.5}]	0.246
Moisture-dep. Thermal Cond. Supplement [%/M.-%]	1.5
Temp-dep. Thermal Cond. Supplement [W/mK²]	0.0002

Typical Built-In Moisture [kg/m³]: 192.16

Layer thickness [m]: 0.002

Color: 

Hygrothermal Functions

- Moisture Storage Function
- Liquid Transport Coefficient, Suction
- Liquid Transport Coefficient, Redistribution
- Water Vapour Diffusion Resistance Factor, moisture-depend
- Thermal Conductivity, moisture-dependent
- Thermal Conductivity, temperature-dependent
- Enthalpy, temperature-dependent

Graph | Edit Table | from File...

☐ Approximate

No.	RH [-]	Water Content [kg/m³]
1	0.0	0.0
2	0.2	60.53
3	0.5	192.16
4	0.8	265.95
5	0.95	274.07
6	1.0	472.29

Copy

Paste into Material Database | Import... | Export... | OK | Abort | Help

Figure A2.5 – WUFI material data for Silica Gel.

Layer/Material Data

Layer/Material Name: Clinoptilolite

Material Data | Info

Basic Values


Bulk density [kg/m³]	706.31
Porosity [m³/m³]	0.69
Specific Heat Capacity, Dry [J/kgK]	1856.0
Thermal Conductivity, Dry, 10°C [W/mK]	0.235
Water Vapour Diffusion Resistance Factor [-]	5.03

Approximation Parameter

Reference Water Content [kg/m³]	46.55
Free Water Saturation [kg/m³]	163.58
Water Absorption Coefficient [kg/m²s ^{0.5}]	0.115
Moisture-dep. Thermal Cond. Supplement [%/M.-%]	1.5
Temp-dep. Thermal Cond. Supplement [W/mK²]	0.0002

Typical Built-In Moisture [kg/m³]: 32.7

Layer thickness [m]: 0.002

Color: 

Hygrothermal Functions

- Moisture Storage Function
- Liquid Transport Coefficient, Suction
- Liquid Transport Coefficient, Redistribution
- Water Vapour Diffusion Resistance Factor, moisture-depend
- Thermal Conductivity, moisture-dependent
- Thermal Conductivity, temperature-dependent
- Enthalpy, temperature-dependent

Graph | Edit Table | from File...

☐ Approximate

No.	RH [-]	Water Content [kg/m³]
1	0.0	0.0
2	0.2	21.19
3	0.5	32.7
4	0.8	46.55
5	0.95	68.58
6	1.0	163.58

Copy

Paste into Material Database | Import... | Export... | OK | Abort | Help

Figure A2.6 – WUFI material data for Clinoptilolite.

Layer/Material Data

Layer/Material Name: Bentonite

Material Data | Info

Basic Values

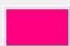
Bulk density [kg/m³]	637,72
Porosity [m³/m³]	0,76
Specific Heat Capacity, Dry [J/kgK]	1941,0
Thermal Conductivity, Dry, 10°C [W/mK]	0,09
Water Vapour Diffusion Resistance Factor [-]	4,71

Approximation Parameter

Reference Water Content [kg/m³]	94,26
Free Water Saturation [kg/m³]	345,65
Water Absorption Coefficient [kg/m²s ^{0.5}]	0,016
Moisture-dep. Thermal Cond. Supplement [%/M.-%]	1,5
Temp-dep. Thermal Cond. Supplement [W/mK²]	0,0002

Typical Built-In Moisture [kg/m³]: 41,96

Layer thickness [m]: 0,002

Color: 

Hygrothermal Functions

- Moisture Storage Function
- Liquid Transport Coefficient, Suction
- Liquid Transport Coefficient, Redistribution
- Water Vapour Diffusion Resistance Factor, moisture-depend
- Thermal Conductivity, moisture-dependent
- Thermal Conductivity, temperature-dependent
- Enthalpy, temperature-dependent

Graph | Edit Table | from File...

☐ Approximate

No.	RH [-]	Water Content [kg/m³]
1	0,0	0,0
2	0,2	9,63
3	0,5	41,96
4	0,8	94,26
5	0,95	148,78
6	1,0	345,65

Copy

Paste into Material Database | Import... | Export... | OK | Abort | Help

Figure A2.7 – WUFI material data for Bentonite.

Layer/Material Data

Layer/Material Name: Solid Brick Masonry

Material Data | Info

Basic Values


Bulk density [kg/m³]	1900,0
Porosity [m³/m³]	0,24
Specific Heat Capacity, Dry [J/kgK]	850,0
Thermal Conductivity, Dry, 10°C [W/mK]	0,6
Water Vapour Diffusion Resistance Factor [-]	10,0

Approximation Parameter

Reference Water Content [kg/m³]	18,0
Free Water Saturation [kg/m³]	190,0
Moisture-dep. Thermal Cond. Supplement [%/M.-%]	15,0
Temp-dep. Thermal Cond. Supplement [W/mK²]	0,0002

Typical Built-In Moisture [kg/m³]: 100,0

Layer thickness [m]: 0,24

Color: 

Hygrothermal Functions

- Moisture Storage Function
- Liquid Transport Coefficient, Suction
- Liquid Transport Coefficient, Redistribution
- Water Vapour Diffusion Resistance Factor, moisture-depend
- Thermal Conductivity, moisture-dependent
- Thermal Conductivity, temperature-dependent
- Enthalpy, temperature-dependent

Graph | Edit Table | from File...

☒ Approximate

No.	RH [-]	Water Content [kg/m³]
1	0,0	0,0
2	0,1	0,55
3	0,2	1,23
4	0,3	2,11
5	0,4	3,26
6	0,5	4,84
7	0,55	5,89

Copy

Paste into Material Database | Import... | Export... | OK | Abort | Help

Figure A2.8 – WUFI material data for Solid Brick.

Layer/Material Data

Layer/Material Name: Interior Plaster (Gypsum Plaster)

Material Data | Info

Basic Values

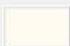
Bulk density [kg/m³]	850,0
Porosity [m³/m³]	0,65
Specific Heat Capacity, Dry [J/kgK]	850,0
Thermal Conductivity, Dry, 10°C [W/mK]	0,2
Water Vapour Diffusion Resistance Factor [-]	8,3

Approximation Parameter

Moisture-dep. Thermal Cond. Supplement [%/M.-%]	8,0
Temp-dep. Thermal Cond. Supplement [W/mK²]	0,0002

Typical Built-In Moisture [kg/m³]: 400,0

Layer thickness [m]: 0,015

Color: 

Hygrothermal Functions

- Moisture Storage Function
- Liquid Transport Coefficient, Suction
- Liquid Transport Coefficient, Redistribution
- Water Vapour Diffusion Resistance Factor, moisture-depend
- Thermal Conductivity, moisture-dependent
- Thermal Conductivity, temperature-dependent
- Enthalpy, temperature-dependent

Graph | Edit Table | from File...

☐ Approximate

No.	RH [-]	Water Content [kg/m³]
1	0,0	0,0
2	0,5	3,6
3	0,65	5,2
4	0,8	6,3
5	0,9	11,0
6	0,93	17,0
7	0,95	19,0

Copy

Paste into Material Database | Import... | Export... | OK | Abort | Help

Figure A2.9 – WUFI material data for Gypsum Plaster.

Layer/Material Data

Layer/Material Name: Spruce, radial

Material Data | Info

Basic Values


Bulk density [kg/m³]	455,0
Porosity [m³/m³]	0,73
Specific Heat Capacity, Dry [J/kgK]	1500,0
Thermal Conductivity, Dry, 10°C [W/mK]	0,09
Water Vapour Diffusion Resistance Factor [-]	130,0

Approximation Parameter

Moisture-dep. Thermal Cond. Supplement [%/M.-%]	1,3
Temp-dep. Thermal Cond. Supplement [W/mK²]	0,0002

Typical Built-In Moisture [kg/m³]: 80,0

Layer thickness [m]: 0,015

Color: 

Hygrothermal Functions

- Moisture Storage Function
- Liquid Transport Coefficient, Suction
- Liquid Transport Coefficient, Redistribution
- Water Vapour Diffusion Resistance Factor, moisture-depend
- Thermal Conductivity, moisture-dependent
- Thermal Conductivity, temperature-dependent
- Enthalpy, temperature-dependent

Graph | Edit Table | from File...

☐ Approximate

No.	RH [-]	Water Content [kg/m³]
1	0,0	0,0
2	0,2	30,0
3	0,5	45,0
4	0,65	57,0
5	0,8	80,0
6	0,9	100,0
7	0,96	125,0

Copy

Paste into Material Database | Import... | Export... | OK | Abort | Help

Figure A2.6 – WUFI material data for Spruce.